

Doctoral Thesis  
博士論文

*Ab initio* prediction of magnetic structures  
(磁気構造の第一原理予測)

フブシ・マリーテレス

Marie-Therese HUEBSCH

Doctoral Thesis

博士論文

*Ab initio* prediction of magnetic structures

(磁気構造の第一原理予測)

フブシ・マリーテレス

Marie-Therese HUEBSCH

Graduate School of Frontier Sciences

The University of Tokyo

磁気構造の

第一原理予測

# Abstract

The grand challenge in first-principles calculation for magnetic materials is whether we can predict the experimental magnetic structure for a given material. Among a variety of possible functional materials, noncollinear magnets are a fascinating playground for materials design [1, 2] as they facilitate a wide range of fundamental phenomena and possible applications.

For example, in the context of antiferromagnetic (AFM) spintronics [3] there is a particular interest in noncollinear antiferromagnetism sparked by (i) its robustness against perturbations due to magnetic fields, (ii) a quasi-absence of magnetic stray fields disturbing for instance nearby electronic devices, and (iii) ultrafast dynamics of AFM domainwalls [4], as well as (iv) its ability to generate large magnetotransport effects [5–7]. Hence, the optimization of AFM materials would open the door for applications such as seamless and low-maintenance energy generation, ultrafast spintronics and robust data retention, as well as be a guide towards advancing fundamental understanding of magnetotransport.

However, first-principles calculations with the generalized gradient approximation (GGA) in the framework of spin-density functional theory (SDFT) for magnetic materials have a problem: It is still an open question how accurately SDFT–GGA can reproduce the experimental magnetic ground state. While SDFT has been widely used in studies on various magnets [8], there has been no systematic benchmark calculation for noncollinear AFM materials. Previous attempts have been restricted to collinear magnetism [9] or even stricter symmetry constraints [10–12]. In regard to noncollinear AFM materials, high-throughput calculations have been limited to setting the experimentally determined magnetic configuration as an initial guess [13]. A recently proposed attempt to predict magnetic structures based on a genetic evolution algorithm [14] strongly relies on the proper prediction of the magnetic ground state by SDFT. The lack of a systematic benchmark calculation is a consequence of the fact that it is a highly non-trivial task to investigate all the local minima in the SDFT energy landscape. Indeed, to search for all the (meta-)stable states, we need an exhaustive list of physically reasonable magnetic configurations for which first-principles calculations can be performed.

To this end, we devise the so-called cluster multipole (CMP) expansion, which enables the expansion of an arbitrary magnetic configuration in terms of an orthogonal basis set of magnetic multipole configurations. By means of the CMP expansion, a list of initial magnetic structures for

self-consistent GGA calculations is efficiently and systematically generated. A comparison with the experimental data collected on MAGNDATA [15] shows that the most stable magnetic configurations in nature are linear combinations of only few CMPs. With this at hand, a high-throughput calculation for all candidate magnetic structures is performed in the scope of this thesis. We benchmark the predictive power of CMP+SDFT with 2935 calculations, which show that (i) the CMP expansion administers an exhaustive list of candidate magnetic structures, (ii) CMP+SDFT can narrow down the possible magnetic configurations to a handful of computed configurations, and (iii) SDFT reproduces the experimental magnetic configurations with an accuracy of  $\pm 0.5 \mu_B$ . For a subset the impact of on-site Coulomb repulsion  $U$  is investigated by means of 1545 CMP+SDFT+ $U$  calculations revealing no further improvement on the predictive power.

The thesis is structured as follows: In Chapter 1, we take a birds eye view on magnetism and in particular motivate the search for novel magnetic structures realized in crystalline compounds, that feature transition metals, lanthanides and actinoides as magnetic sites. In Chapter 2, we introduce the framework of SDFT for noncollinear magnetic structures. In Chapter 3, the multipole theory is first developed generally to expand a vector gauge field characterized by the vector Poisson equation. Subsequently, this theory is applied to magnetic structures in real materials to arrive at a scheme to generate a symmetry-adapted orthogonal basis set of magnetic configurations in the crystallographic point group. This is the so-called CMP theory. In Chapter 4 we present the central results of this thesis. Here, we discuss a benchmark calculation of 131 materials, those magnetic ground state is predicted in a high-throughput CMP+SDFT scheme. Moreover, we investigate the effects of Coulomb repulsion  $U$  on the prediction of the most stable magnetic configuration, as well as the size of the magnetic moment. Based on these practical insights, we revisit SDFT in Chapter 5. This shall set the stage for a new question: Namely, how can we improve existing exchange–correlation functionals in order to accurately reproduce the experimental magnetic ground state in the framework of SDFT. A summary and outlook is presented in Chapter 6.

To my beloved husband.

# Acknowledgements

First and foremost, I would like to thank Professor Dr. Ryotaro Arita. Without his optimism and support in every step throughout my doctoral program, this work would have never been accomplished. He encouraged me to go beyond what I thought is feasible and always trusted in my ability to find a unique approach. I feel privileged to be part of your group and to get challenged every day, in the most positive sense.

I would like to express my gratitude to every member of the committee, which includes Professor Arita, Professor Dr. Takehiko Sasaki, Professor Dr. Kozo Okazaki, Professor Dr. Takashi Koretsune and Professor Dr. Motoaki Hirayama. I know you have kindly allocated your precious time not only to read this thesis, but also to reflect on my work and shared useful comments. Thank you for that indeed. Let me also acknowledge that the academic framework for the doctoral program of Complexity Science and Engineering has been provided by the Graduate School of Frontier Science at the University of Tokyo.

My gratitude also goes to Dr. Takuya Nomoto, who always found time to share his brilliant insights. If this fits the description of a Senpai, then Dr. Shiro Sakai was my Senpai during the first year in Japan. He kindly invited me to join conferences and helped me to overcome a few awkward moments occasionally endured in an unfamiliar culture. In October 2018, I visited Professor Dr. Michi-To Suzuki at the Center for Computational Materials Science at the Institute for Materials Research at Tohoku University. The impact of his work on my own study is obvious throughout this dissertation and I want to sincerely thank him for the inspiration.

Since I entered Professor Arita's groups at RIKEN and the University of Tokyo many members joined, some continued their path elsewhere and some have remained a constant. Thank you all for the spirit of comradeship, Professor Hirayama, Dr. Sakai, Dr. Yuske Nomura, Dr. Nomoto, Dr. Susumu Minami, Mr. Congshan Wu MSc, Mr. Tianchun Wang MSc, Tonghua Yu, Akira Matsui, and Ryota Masuki! It has been truly a pleasure. I am also grateful to have meet Professor Dr. Philipp Werner, Mr. Gauthier Mukerjee MSc, Mr. Niklas Witt MSc and Mr. Yann in 't Veld MSc, who joined the group as visitors; each for a couple of months. Perhaps not usually recognized at this point, yet certainly the backbone of any institution, is the non-academic staff. Let me particularly thank Mrs. Kaori Ichikawa, Mrs. Maya Kobayashi and Mrs. Mutsue Kominami, representative of all the staff who supported me during my doctoral program.

I gratefully recognize a fruitful collaboration with Mr. Ryoma Kaneko MSc, Dr. Hiroshi Shi-naoka, Dr. Kentaro Ueda, Professor Dr. Yoshinori Tokura, and Professor Dr. Jun Fujioka. This can be directly attributed to the superb working environment at RIKEN, where I am privileged to have been accepted as an International Program Associate (IPA) fellow. There, I found ample supply of stimulating talks and an impressive computational infrastructure. I also want to thank Professor Dr. Manfred Fiebig, Dr. Daichi Kurebayashi, and Dr. Tze Tzen Ong for many inspiring coffee breaks.

Furthermore, my appreciation goes to all groups at the Center for Emergent Matter Science (CEMS) at RIKEN, who shared their latest results every Wednesday. Then, to all groups at the Institute of Applied Physics at the University of Tokyo, who treated me as one of their students and where I participated in a weekly joint seminar. And many thanks to Professor Dr. Masatoshi Imada and his group, who allowed me to participate in regular, conference-like meetings to glimpse at their recent work.

At TU Wien, I want to thank my former supervisors Professor Dr. Karsten Held and Professor Dr. Alessandro Toschi for inviting me to visit their groups during my doctoral program. I appreciated all opportunities to foster an active academic exchange between Japan and Austria and to share ideas with my former colleagues, in particular with Professor Dr. Georg Rohringer, Professor Dr. Thomas Schäfer, Dr. Anna Kauch, Dr. Markus Wallerberger, Mr. Severino Adler MSc and Mr. Martin Pimon MSc. I also want to give credit to TU Wien as a whole for providing me with a foundation in physics. Here, I would like to mention Professor Dr. Anton Rebhan, Professor Dr. Daniel Grumiller and Professor Dr. Peter Mohn, whose outstanding teaching has inspired me.

This work is supported by the Center for Computational Materials Science, Institute for Materials Research, Tohoku University for the use of MASAMUNE-IMR (MAterials science Supercomputing system for Advanced MUlti-scale simulations towards NExt-generation - Institute for Materials Research) (Project No. 19S0005), as well as a Grant-in-Aid for Scientific Research (No. 19H05825, and No. 16H06345) from the Ministry of Education, Culture, Sports, Science and Technology, and CREST (JPMJCR18T3) from the Japan Science and Technology Agency, and JSPS KAKENHI Grants Numbers JP15H05883 (J-Physics), JP19H01842, JP20H05262 and JP20K21067, and JST PRESTO Grant number JPMJPR17N8.

Last but not least, I want to thank my family, friends and my husband for bearing with me and to graciously accept my absence, even in times of hardship. Especially my little sister deserves the utmost respect and appreciation, and maybe some sort of medal. My friends supported me in various ways ranging from macrobiotic power food sent to my home in the final stage of writing this thesis, all the way to long philosophical discussions about statistical significance. You are the best!

*Tokyo, December 5, 2020*



# Contents

<b>1</b>	<b>Introduction</b>	<b>1</b>
1.1	A birds eye view on noncollinear magnetism . . . . .	4
1.2	Scope of this thesis . . . . .	8
1.2.1	Outline . . . . .	8
1.2.2	Limitations . . . . .	9
<b>2</b>	<b>A brief introduction to spin-density functional theory</b>	<b>10</b>
2.1	The electronic Hamiltonian . . . . .	10
2.2	The two basic theorems . . . . .	12
2.3	Exchange–correlation functional . . . . .	14
2.3.1	Local spin-density approximation . . . . .	14
2.3.2	Generalized gradient approximation . . . . .	16
2.4	Solving the Kohn–Sham equations . . . . .	17
2.5	Including spin–orbit coupling . . . . .	19
2.6	Including strong electron–electron interactions beyond SDFT . . . . .	20
2.7	Concluding remarks . . . . .	23
<b>3</b>	<b>Multipole theory</b>	<b>24</b>
3.1	The vector Poisson equation and its solution . . . . .	25
3.2	Example of four bar magnets . . . . .	31
3.3	Cluster multipole expansion . . . . .	35
3.3.1	Point group harmonics . . . . .	36
3.3.2	Multipole expansion on a point form . . . . .	38
3.3.3	Multipole expansion in real materials . . . . .	40
3.4	Magnetic domains and linear combinations of cluster multipoles . . . . .	43
3.4.1	Heuristic rule . . . . .	45
3.4.2	Magnetic domains . . . . .	46

<b>4 High-throughput benchmark CMP+SDFT calculation</b>	<b>49</b>
4.1 Methods . . . . .	49
4.1.1 Cluster Multipole expansion . . . . .	50
4.1.2 Setup for SDFT . . . . .	52
4.2 Results and Discussion . . . . .	53
4.2.1 The investigated materials and workflow . . . . .	53
4.2.2 Reproducibility . . . . .	57
4.2.3 The performance of candidate magnetic configurations . . . . .	59
4.2.4 Analysis of CMP+SDFT local minima . . . . .	62
4.2.5 The magnetic moment per site . . . . .	66
4.2.6 CMP+SDFT+U case study . . . . .	73
4.3 Concluding Remarks . . . . .	77
<b>5 Spin-density functional theory revisited</b>	<b>81</b>
<b>6 Summary and Outlook</b>	<b>86</b>
6.1 Future perspective . . . . .	88
<b>Appendices</b>	<b>90</b>
<b>A Dirac theory</b>	<b>91</b>
A.1 Solution of the Dirac equation . . . . .	92
A.2 Electromagnetic coupling . . . . .	93
A.3 Pauli Hamiltonian . . . . .	95
A.4 Relativistic corrections . . . . .	97
A.5 Radial Dirac equation and spinor harmonics . . . . .	98
<b>B Details of solving the vector Poisson equation</b>	<b>101</b>
B.1 General form of the vector gauge field . . . . .	101
B.2 Green's function method . . . . .	108
B.3 General form of multipole coefficients . . . . .	110
B.4 Why there are no monopole gauge fields or monopole magnetic fields . . . . .	115
B.5 Multipole coefficients for an electron cloud . . . . .	116
B.6 Magnetic field of a general vector gauge field . . . . .	117
B.7 Generating vector spherical harmonics . . . . .	118
<b>C Experimental data</b>	<b>124</b>



# Chapter 1

## Introduction

水晶の一面光り渡り鳥

---

小川軽舟

Magnetism is a truly ubiquitous phenomenon and we humans seem to be one of the few specimens blind to it. For example, migratory birds, common chickens, honeybees, turtles, a number of mammals, for instance horses, as well as fish and even bacteria have a sense called *magnetoreception*. In other words, they can consciously perceive the direction of the magnetic field. This has already been hunched upon by zoologists observing migratory birds in the wild. Perhaps the earliest record of that is given by Alexander Theodor von Middendorff in 1855, who writes [16]

(...), es möge die erstaunliche Unbeirrbarkeit der Zugvögel — trotz Wind und Wetter, trotz Nacht und Nebel — eben darauf beruhen, dass das Geflügel immerwährend der Richtung des Magnetspoles sich bewusst ist, (...). Was dem Schiffe die Magnetnadel ist, wäre dann diesen ‹‹Seglern der Lüfte›› das innere magnetische Gefühl, (...).

The scientific proof [17] is provided by W. Wiltschko and coworkers in 1968. However, the exact biological mechanism of detecting the magnetic field is still discussed with controversy [18] and may differ between species. In case of migratory birds, the leading hypothesis describes photoexcitation of cryptochrome proteins to create radical pairs in the retina. This so-called radical pair mechanism is thus expected to be located in the birds eyes and one might even coin the phrase *birds see magnetic fields*.

A recent study on human magnetoreception [19] suggests humans may also unconsciously be able to detect changes in the magnetic field surrounding them. Nevertheless, without a doubt the true multitude of magnetic field arrangements is only accessible to humans thanks to the experimental advances [20] made in recent decades. In particular, with the advent of neutron scattering in the 1950s, it became possible to characterize and analyze the static and dynamic spin structure of

polymers, ferrofluids, bulk magnetic materials, superconductors, disordered and porous materials, ceramics, biological structures etc. This long list hints towards the fact, that the magnetism is far from a subject *sui generis*. Here, we shall not attempt to cover magnetism as a whole. Instead, we focus our attention on the magnetic structures present in crystals<sup>1</sup>. In particular, compounds featuring transition metals, lanthanides and actinoides as magnetic sites. The goal is to predict the magnetic ground state from first-principles, therefore we must begin our discussion at the origin of magnetism: The *spin*.

In realistic materials, the electronic spin is fundamentally responsible for magnetism. The origin of the electronic spin has been discovered in 1928 by P. Dirac, when formulating his relativistic quantum theory of the electron [21]. One might be tempted to imagine each electron simply carrying a small bar magnet, however this picture is too classical. Already in 1919 H. van Leeuwen, a Ph.D. student of N. Bohr, formulates the proof [22, 23] that magnetism is a quantum mechanical phenomenon and cannot be explained by means of classical Boltzmann statistics rigorously applied to moving particles, even if they carry spin and charge. Thus, in addition to spin, proper *quantum mechanical statistics* is necessary to explain magnetism in crystals. In fact, there is one more necessary ingredient: *electron–electron interaction*. Only the specific details of the interaction between electrons leads to the emergence of a finite magnetic moment, otherwise any crystal would be magnetic [8].

Given that magnetism is a *collective, quantum electrodynamic* phenomenon, we need to at least briefly recall Dirac’s theory to properly account for the spin and then solve the quantum mechanical many-body problem with the appropriate relativistic corrections. However, as P. Dirac puts it [24],

For dealing with atoms involving many electrons the accurate quantum theory, involving a solution of the wave equation in many-dimensional space, is far too complicated to be practicable. One must therefore resort to approximate methods.

The way for this practical, approximate method is paved by P. Hohenberg and W. Kohn in 1964 [25] by formulating *density functional theory* (DFT). They show that the ground state energy can be expressed in terms of an energy functional of the electron density only. In a second paper [26], W. Kohn and L. Sham obtain the now called *Kohn–Sham equations*, which are effective one-electron Schrödinger-type equations, by means of the variational principle. This represents the groundwork for the so-called *local spin-density approximation* (LSDA) for exchange and correlation energies in the framework of spin-density functional theory (SDFT), that is formulated in the early 1970s [27–30]. The tremendous progress in the last five decades is largely dominated by extensions of LSDA in order to account for specific correlation effects. The perhaps most widely used exchange–correlation energy functional is the so-called generalized gradient approximation (GGA). However, there is truly a zoo of exchange–correlation functionals among which no clear winner has emerged in terms of applicability to real materials. Besides that, in the last five decades, advances have been

---

<sup>1</sup>A crystal is a highly regular solid in which atoms occupy fixed atomic positions on an underlying crystal lattice.

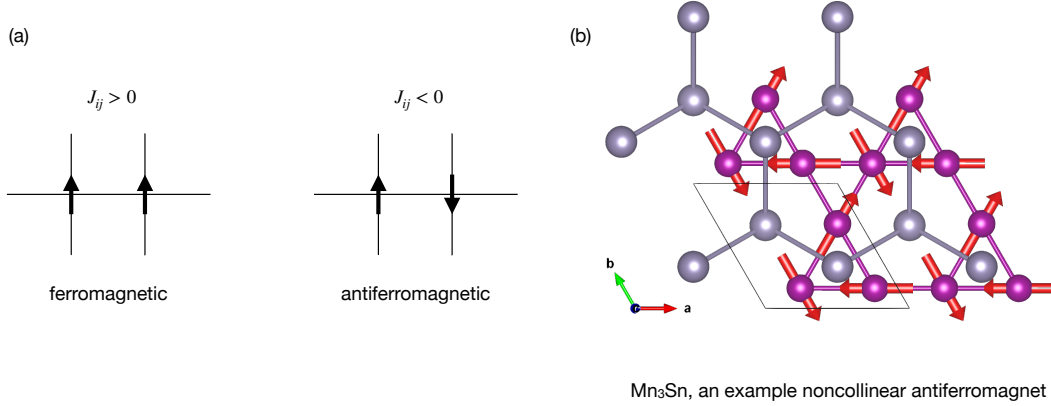


Figure 1.1: (a) Schematic ground state for positive and negative exchange coupling  $J_{ij}$  in the Heisenberg model yielding ferromagnetic and antiferromagnetic alignment of the spins, respectively. (b) The magnetic structure of  $\text{Mn}_3\text{Sn}$  visualized using VESTA1001[31]. *Mn has a non-collinear magnetic dipole moment.*

made due to the increase in computational capabilities, improvement of numerical methods and a remarkable, ever increasing material survey provided by experimentalists.

Especially the experimental insights supply a continuous stream of new, intriguing phenomena in magnetism. One of the major sources for newly observed magnetotransport effects in crystals is the specific alignment of magnetic moments on neighboring sites. The interaction between neighboring magnetic sites is determined by the so-called *exchange coupling*, which can be computed from first-principles by means of SDFT. In order to illustrate the effects of exchange coupling, let us consider the arguably simplest model system of coupling spins: Namely, the Heisenberg Hamiltonian, which reads

$$\mathcal{H}_{Heis} = -\frac{1}{2} \sum_{i,j} J_{ij} \mathbf{S}_i \cdot \mathbf{S}_j. \quad (1.1)$$

In this example, positive (negative) exchange coupling  $J_{ij}$  leads to parallel (antiparallel) alignment of neighboring spins  $\mathbf{S}_i$  and  $\mathbf{S}_j$ . As depicted in Figure 1.1 (a), this corresponds to *collinear* ferromagnetic (FM) and antiferromagnetic (AFM) ordering, respectively. Collinearity implies that site  $i$  and  $j$  have a common spin-quantization axis.

In a realistic material however the interplay between the arrangement of magnetic sites on the crystal lattice and the details of the exchange coupling, may lead to more complex, *noncollinear* magnetic structures. One example of a noncollinear antiferromagnet is  $\text{Mn}_3\text{Sn}$ , as shown in Figure 1.1 (b). Here, we show only one of the two layers of magnetic Mn-sites that each form a Kagome lattice<sup>2</sup> in this material. In the magnetic ground state, the on-site magnetic moments are rotated

<sup>2</sup>The word *kagome* 籠目 refers to a traditional Japanese pattern for woven bamboo baskets that resembles stars

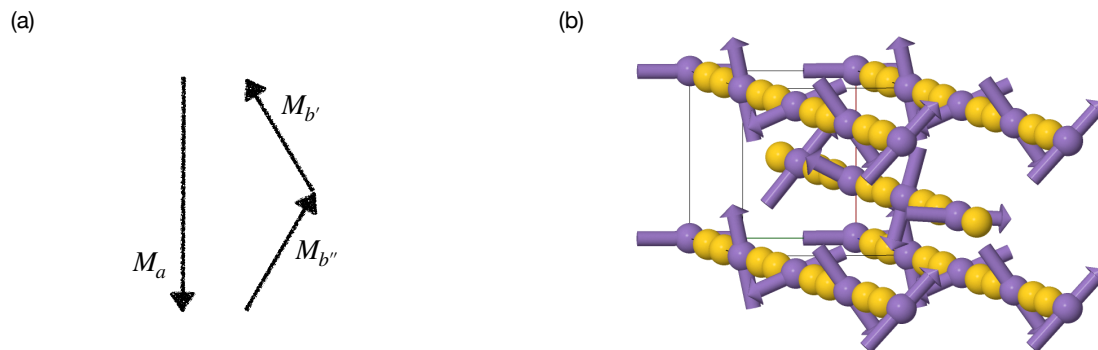


Figure 1.2: (a) Yafet–Kittel spin structure. (b) First ever reported [35] spiral magnetic structure realized in  $\text{MnAu}_2$ . Visualized using tools provided on MAGNDATA [15].

by  $120^\circ$  with respect to their neighbour and add up to zero net magnetization. It is noncollinear magnetic structures like this, that give rise to novel observations and which are at the heart of this work.

In the next section, we will give a birds eye view on noncollinear magnetism. However before that, the novice reader may appreciate some introductory works on magnetism, which cover different aspects of the subject: *Magnetism in the solid state—an introduction* [32] by P. Mohn, *Magnetism and magnetic materials* [33] by J. M. D. Coey, *Physical inorganic chemistry: a coordination chemistry approach* [34] by S. F. A. Kettle and *Theory of itinerant electron magnetism* [8] by J. Kübler.

## 1.1 A birds eye view on noncollinear magnetism

For a long time the discussion of magnetic order has been dominated by magnets with a collinear ferromagnetic (FM) order, and the closely related phenomena of collinear antiferromagnetic (AFM) and ferrimagnetic ordering. Clearly, collinear ferromagnetism is most easily observed due to its macroscopic magnetization. In 1936 L. Néel, who was a student of P. Weiss, is famously the first to discuss two equal, FM sublattices that are opposing each other such that the net magnetization vanishes. The presence of a magnetic order without a resultant macroscopic magnetization is the defining feature of antiferromagnetism. If the sublattices do not perfectly cancel each others magnetization, one speaks of ferrimagnetism.

In hindsight, it seems curious that no earlier than 1952 Y. Yafet and C. Kittel [36] first propose a triangular arrangement of spins, as shown in Figure 1.2 (a). Starting point of their discussion is L. Néel’s mean-field treatment of two sublattices  $a$  and  $b$ , where one of the sublattices is further divided into two sublattices  $b'$  and  $b''$ , each on its own being FM. The magnetic moments of  $b'$  and  $b''$  are canted to each other such that their combined total magnetization still fully compensates the

---

made up of a central hexagon and adjacent triangular.

magnetization of sublattice  $a$ . In their paper, they suggest some materials for which an experimental confirmation should be possible by means of the back then still rather new method of neutron diffraction.

Indeed, neutron diffraction itself has been developed around the same time and subsequently experiences a huge improvement in the 1970s with the advent of high-brilliance neutron sources and the development of dedicated small-angle neutron scattering instruments [37]. Since then, many materials have been identified to exhibit the long overlooked *noncollinear* magnetic ordering. The possible alignments range from small canting with respect to a dominant FM axis to fully AFM configurations, such that the total magnetization is zero. For the latter, we have already seen two examples (i) the theoretically proposed Yafet–Kittel structure in Figure 1.2 (a), and (ii) the experimentally determined magnetic structure of  $\text{Mn}_3\text{Sn}$  in Figure 1.1. Moreover, Figure 1.2 (b) shows an even more involved spiral structure spanning across multiple crystallographic unit cells in  $\text{MnAu}_2$  [35,38]. In fact, this is the first spiral structure ever reported in 1961. There have been some early reviews by F. Keffer [39] in the Encyclopedia of Physics in 1966 and in the late 1980 by J. Coey [40] aimed at to provide an overview of compounds exhibiting noncollinear magnetism. Nowadays, many of these measurements can be found on the database MAGNDATA [15]. In addition to a convenient quick-look, MAGNDATA offers access to the corresponding magnetic *cif*-files [41]. This is a standard file format since 2014, which enables efficient handling of magnetic structure data. The curious reader is invited to check out the latest entries at the database’ web page: [www.webbdcrista1.ehu.es/magnadata](http://www.webbdcrista1.ehu.es/magnadata).

The *origin of noncollinear magnetic ordering* is quite generally the competition between different ordering (disordering) exchange coupling mechanisms. At this point, we want to highlight that in addition to the symmetric Heisenberg-type exchange interaction, one might encounter antisymmetric exchange coupling, the so-called *Dzyaloshinskii–Moriya interaction* of the form

$$\mathcal{H}_{DM} = \frac{1}{2} \sum_{ij} D_{ij} \cdot (\mathbf{S}_i \times \mathbf{S}_j). \quad (1.2)$$

Generally, in realistic materials we expect symmetric and antisymmetric exchange coupling to be present. If these exchange interactions can be appeased, the system relaxes to a magnetically ordered ground state.

This stands in contrast with *magnetic disorder*, which is introduced by randomly distributed magnetic impurities. These can cause *random* spin canting, which is categorized as *spin glass*. Note however, that even systems without magnetic disorder—that feature anisotropic AFM exchange coupling—have been shown<sup>3</sup> to exhibit a spin glass ground state. The underlying effect, that leads to a lack of ordering even at the ground state of the so-called Kitaev model, is found in many realistic materials: *magnetic frustration*.

---

<sup>3</sup>This has been first proven by A. Kitaev in 2015 in one of his lectures at Caltech “*A simple model of quantum holography*”, which is available for streaming.



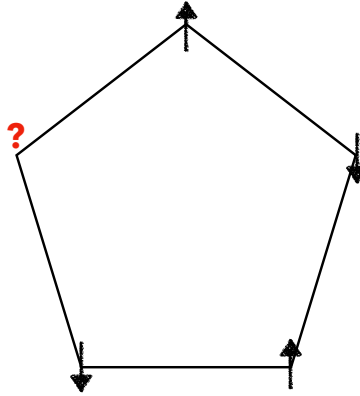


Figure 1.3: Magnetic frustration. A loop of five magnetic sites which couple antiferromagnetically. One site cannot be chosen to be spin up or down without violating one antiferromagnetic bond.

Magnetic frustration arises when all AFM exchange interactions cannot be easily appeased. For instance, odd-membered loops with isotropic AFM exchange coupling give rise to an increased degeneracy of the magnetic ground state. In other words, any of the bonds between neighbors is equally likely to be the only one that is forced to remain ferromagnetically coupled, while all the rest couples AFM. This is illustrated in Figure 1.3. As a consequence the Néel temperature, at which the magnetic moments order antiferromagnetically, is much smaller than the absolute value of the Curie temperature [33]. It is said [33] that systems featuring magnetic frustration have a tendency towards exhibiting a noncollinear magnetic ground state. Other possible sources for noncollinear ordering include a mixture of AFM and FM exchange coupling, electron–electron correlation etc.

Some reader might be already intrigued by this collective, quantum electrodynamic phenomenon taking on all kind of shapes and beautiful patterns, while others pose the well-vested question: *How is this useful, if we are barely able to detect it?* So let us discuss new phenomena that have been discovered in the context of noncollinear magnetism by looking at two concrete examples. Firstly, the ability to experimentally detect magnetic domains and magnetic space groups without devising neutrons. And secondly, the observation of large magneto-transport effects in  $\text{Mn}_3\text{Sn}$ .

In the 1990s, M. Fiebig and coworkers develop an experimental technique [42], where by means of *second harmonic generation* in laser light magneto-optical properties are detected. In particular, the shape of the linear response tensor is determined. Based on analysis done by W. Kleiner [6,43], which have been recently extended by M. Seemann and coworkers [7], the magnetic space group can be inferred from the shape of the linear response tensor. While this method lacks the ability to determine the exact size of the on-site magnetic moment, it reveals the magnetic symmetry with much lower effort compared to neutron diffraction. In view of material design, this method can be used as a filter in order to identify promising magnetic structures. Further, the prior knowledge

of the magnetic space group, when post-processing neutron scattering spectra, may give additional guidance for the interpretation. Most noteworthy, this method can detect the relative orientation of magnetic domains with respect to each other. This might be the key step towards application of noncollinear magnetism in a technical device.

We have mentioned that the allowed shape of linear response might be inferred from the magnetic space group. It should be highlighted that usually in linear response theory only the coupling of external magnetic fields to the magnetization is considered, where the magnetization is the macroscopic magnetic dipole moment emerging as a sum of all on-site magnetic dipole moments. The discussion by W. Kleiner [6, 43] and M. Seemann *et al.* [7] is exceptional, as it allows—without explicitly phrasing it in the language of multipole theory—linear response to occur as a result of *higher order moments*, because it is based on symmetry considerations only. For instance, the *magneto-optical Kerr effect* [44] describes the rotation of the spin-polarization axis of light upon reflection off a magnetic surface. Naively, one might expect AFM surfaces generally fail to generate Kerr rotation, because the spin-polarization interacts with the magnetization. However, in principle, higher magnetic moments could interact with the light.

Let us point out one practical example: Starting with a nature paper [45] by S. Nakatsuji *et al.* in 2015 a number of works discover large *anomalous*<sup>4</sup> response in  $\text{Mn}_3\text{Sn}$ . Besides a large anomalous Hall effect [45], also an anomalous Nernst effect [46] and a large magneto-optical Kerr effect [47] are reported. As mentioned above, in Figure 1.1 the magnetic structure of  $\text{Mn}_3\text{Sn}$  is shown. Clearly, there is no total magnetization, when adding all magnetic moments in the unit cell, which is encompassed by a black line. So naively one would not expect Kerr rotation to occur. However it has been demonstrated [48] that the magnetic structure corresponds to a magnetic octupole on the inter-atomic scale, which—like the magnetic dipole—couples to an external magnetic field. This is one of many examples, where multipoles on the inter-atomic length scale have recently proven to be important in order to explain emergent phenomena. Others include the toroidal magnetic moments to explain *anomagnetism* [49], magnetic quadrupole in  $\text{Cr}_2\text{O}_3$  [50–53] and  $\text{Co}_4\text{Nb}_2\text{O}_9$  [54–58], the magnetic toroidal dipole in  $\text{UNi}_4\text{B}$  [59–61], magnetic toroidal octupole [62], electric and magnetic toroidal dipoles in  $\text{BiTeBr}$  [63] and  $\alpha\text{-Cu}_2\text{V}_2\text{O}_7$  [64–68] etc.

Finally, we allow ourselves to envision what might be possible with just the right magnet. A recent review by V. Baltz [3] has laid out a number of promising applications in the field of AFM spintronics. The main obstacle in detecting noncollinear AFM materials is simultaneously the main advantages for technological application: It is quite hard to manipulate AFM structures by means of magnetic fields and, thus, it is robust against perturbation due to external magnetic fields. These might otherwise involuntarily interfere with the system. Inversely, there are no significant stray fields that could potentially disturb nearby circuits or electronic devices. In technical applications the information is not stored within the magnetic structure itself, but rather in the magnetic

---

<sup>4</sup>Anomalous refers to the fact that, the magnetic structure of the material—rather than an applied magnetic field—causes other transport phenomena such as electric current.

domain walls. Thus, the timescale at which domain walls can be switched, fundamentally limits the speed at which information can be written. In case of FM domain walls the so-called Walker breakdown [69] describes a precession motion above a critical magnetic field and the appearance of a periodic component in the forward motion of the domain wall. This fundamental limit is absent in AFM domain walls and hence AFM materials allow for ultra-fast domain wall dynamics [4]. Lastly, as we have mentioned, noncollinear AFM materials have the potential to generate large magneto-transport effects [7]. One example is indeed  $\text{Mn}_3\text{Sn}$ , where the octupole gives rise to a magneto-optical Kerr effect, which is usually exclusively viewed as a response to a magnetic dipole. Hence, the optimization of AFM materials would open the door for applications such as seamless and low-maintenance energy generation, ultra-fast spintronics and robust data retention, as well as be a guide towards advancing fundamental understanding of magneto-transport.

## 1.2 Scope of this thesis

So far we have briefly motivated the search for novel magnetic structures. In particular, we have turned our attention to crystalline compounds, that feature transition metals, lanthanides and actinoides. We have argued that magnetism is a collective, quantum electrodynamical many-body problem, which can be discussed from first-principles in the framework of spin-density functional theory (SDFT). Now, **the grand challenge in first-principles calculation for magnetic materials is whether we can predict the experimental magnetic structure for a given material.**

This challenge stands in a context, where we witness a paradigm shift from computational science to data-driven science. As eluded in the last section, antiferromagnetic (AFM) compounds are a fascinating playground for material design as they facilitate a wide range of fundamental phenomena and possible applications. However, first-principles calculations with the generalized gradient approximation (GGA) in the framework of spin-density functional theory (SDFT) for magnetic materials have a problem: It is still an open question how accurately SDFT-GGA can reproduce the experimental magnetic ground state. While SDFT has been widely used in studies on various magnets [8], there has been no systematic benchmark calculation for noncollinear AFM materials. In the scope of this thesis such a systematic high-throughput calculation with 2935 calculations has been performed.

To this end, we devise the so-called cluster multipole (CMP) expansion, which enables the expansion of an arbitrary magnetic configuration in terms of an orthogonal basis set of magnetic multipole configurations. By means of the CMP expansion, a list of initial magnetic structures for self-consistent GGA calculations is efficiently and systematically generated. With this at hand, a systematic high-throughput calculation with 2935 calculations has been performed.

### 1.2.1 Outline

The thesis is structured as follows: In Chapter 1, we take a birds eye view on magnetism and in particular motivate the search for novel magnetic structures realized in crystalline compounds, that

feature transition metals, lanthanides and actinoides as magnetic sites. In Chapter 2, we introduce the framework of SDFT for noncollinear magnetic structures. In Chapter 3, the multipole theory is first developed generally to expand a vector gauge field characterized by the vector Poisson equation. Subsequently, this theory is applied to magnetic structures in real materials to arrive at a scheme to generate a symmetry-adapted orthogonal basis set of magnetic configurations in the crystallographic point group. This is the so-called CMP theory. In Chapter 4 we present the central results of this thesis. Here, we discuss a benchmark calculation of 131 materials, whose magnetic ground state is predicted in a high-throughput CMP+SDFT scheme. Moreover, we investigate the effects of Coulomb repulsion  $U$  on the prediction of the most stable magnetic configuration, as well as the size of the magnetic moment. Based on these practical insights, we revisit SDFT in Chapter 5. This shall set the stage for a new question: Namely, how can we improve existing exchange–correlation functionals in order to accurately reproduce the experimental magnetic ground state in the framework of SDFT. A summary and outlook is presented in Chapter 6.

### 1.2.2 Limitations

While we have made it a priority to formulate our scheme in the most general way, there are still a number of effects that have been excluded in our considerations and may play an important role in some materials. For instance, by taking the Born–Oppenheimer approximation [70] we effectively neglect electron–phonon coupling. Moreover, we only aim to predict the magnetic ground state, so the treatment of all finite temperature effects has been omitted. One rather surprising choice to the expert reader might be that in most calculations no electron–electron correlation effects beyond SDFT are considered. However, we deem a benchmark for GGA to be an appropriate first step and in fact perform GGA+ $U$  calculations for specific materials. Lastly, we have constrained ourselves to discussing commensurate,  $\mathbf{q} \equiv 0$  bulk magnetism without any disorder and thus surface effects, layered materials, random magnetic impurities etc. are overlooked entirely throughout this thesis.

## Chapter 2

# A brief introduction to spin-density functional theory

In this chapter, we introduce the many-body problem and its treatment, which is underlying noncollinear magnetism and, thus, the phenomena outlined in Section 1.1. The starting point is that, electrons move in the adiabatic field produced by nuclei in solids, which is known as Born–Oppenheimer approximation. We shall arrive at the generalized gradient approximation (GGA) in the framework of spin-density functional theory (SDFT) and get familiar with its ingredients.

Complete derivations have been the subject of many textbooks and shorter works of which we may list a few for the interested reader: *A bird's-eye view of density-functional theory* [71] by K. Capelle, *Theory of itinerant electron magnetism* by J. Kübler and *Current density functional theory* by H. Eschrig.

### 2.1 The electronic Hamiltonian

Let us consider  $N$  interacting electrons that carry a spin  $\sigma = \uparrow$  or  $\downarrow$  with kinetic energy  $T_{\sigma'\sigma}$  in an external potential  $V_{\sigma'\sigma}$ , which in the Born–Oppenheimer approximation [70] consists of the potential  $v_{\sigma'\sigma}^{\text{ion}}(\mathbf{r} - \mathbf{R}_\mu)$  due to the ions located at static positions  $\mathbf{R}_\mu$  and other external fields  $v_{\sigma'\sigma}^{\text{field}}(\mathbf{r})$ . Then, considering the relativistic Dirac theory up to third order in powers of the kinetic energy relative to the rest mass as it follows from the Foldy–Wouthuysen transformation [72], we recall that the simplest version of the theory of magnetic materials can be written with electronic states expressed by two-component spinor functions and with the electronic Hamiltonian expressed by a  $2 \times 2$  matrix [8]. Now, let us use  $m = 1/2$ ,  $\hbar = 1$  and  $e^2 = 2$  for notational simplicity—particularly of the Coulomb interaction  $U_{\sigma'\sigma}$  of the electrons. This allows us to write the Hamiltonian of  $N$

interacting electrons in a crystal as

$$\mathcal{H}_{\sigma'\sigma} = T_{\sigma'\sigma} + V_{\sigma'\sigma} + U_{\sigma'\sigma}, \quad (2.1)$$

$$T_{\sigma'\sigma} = -\delta_{\sigma'\sigma} \sum_{i=1}^N \nabla_i^2, \quad (2.2)$$

$$V_{\sigma'\sigma} = \sum_{i=1}^N v_{\sigma'\sigma}^{\text{ext}}(\mathbf{r}_i), \quad (2.3)$$

$$v_{\sigma'\sigma}^{\text{ext}}(\mathbf{r}) = \sum_{\mu} v_{\sigma'\sigma}^{\text{ion}}(\mathbf{r} - \mathbf{R}_{\mu}) + v_{\sigma'\sigma}^{\text{field}}(\mathbf{r}), \quad (2.4)$$

$$U_{\sigma'\sigma} = \sum_{\substack{i,j=1 \\ i \neq j}}^N \frac{\delta_{\sigma'\sigma}}{|\mathbf{r}_i - \mathbf{r}_j|}. \quad (2.5)$$

The only neglect at this point is the motion of nuclei and core electrons bound to that nuclei, which can be summarized in the term *ionic vibrations*. We note that, neglecting the effect of ionic vibrations translates to omitting the treatment of *electron–phonon coupling*. In the context of magnetism, electron–phonon coupling is in fact the driving effect underlying structure transitions caused by magnetic ordering. Although this is an intriguing phenomenon it is beyond the scope of this thesis.

Here, we are particularly interested in noncollinear magnetism, which implies that the spin state cannot be described by a single, global quantization axis. Such a mixed quantum mechanical state can be described by a density matrix of the form

$$\begin{aligned} & \rho(\mathbf{r}'_1\sigma'_1, \mathbf{r}'_2\sigma'_2, \dots, \mathbf{r}'_N\sigma'_N | \mathbf{r}_1\sigma_1, \mathbf{r}_2\sigma_2, \dots, \mathbf{r}_N\sigma_N) \\ &= \sum_{\alpha} c_{\alpha} \Psi_{\alpha}(\mathbf{r}'_1\sigma'_1, \mathbf{r}'_2\sigma'_2, \dots, \mathbf{r}'_N\sigma'_N) \Psi_{\alpha}^*(\mathbf{r}_1\sigma_1, \mathbf{r}_2\sigma_2, \dots, \mathbf{r}_N\sigma_N), \end{aligned} \quad (2.6)$$

where  $\alpha$  sums over all degenerate many-particle wave functions  $\Psi_{\alpha}$ . Here, the sum rule  $\sum_{\alpha} c_{\alpha} = 1$  and restriction  $0 \leq c_{\alpha} \leq 1$  applies. A salient ingredients of SDFT is the electron density  $n$

$$n(\mathbf{r}) = \text{Tr}\{\rho \hat{n}(\mathbf{r})\}, \quad (2.7a)$$

$$\hat{n}(\mathbf{r}) = \sum_{i=1}^N \delta(\mathbf{r} - \mathbf{r}_i), \quad (2.7b)$$

where we have defined the electron-density operator  $\hat{n}$  in the last line. The trace entails a summation over all spins and integration over all but one spacial coordinate. Even more important for SDFT is the definition of a  $2 \times 2$  *spin-density matrix*  $\underline{n}^{(s)}$

$$\underline{n}^{(s)}(\mathbf{r}) = \begin{pmatrix} n_{\uparrow\uparrow}^{(s)}(\mathbf{r}) & n_{\uparrow\downarrow}^{(s)}(\mathbf{r}) \\ n_{\downarrow\uparrow}^{(s)}(\mathbf{r}) & n_{\downarrow\downarrow}^{(s)}(\mathbf{r}) \end{pmatrix}, \quad (2.8)$$

where the elements are obtained by sparing one spin index of being traced out, such that we obtain

$$n_{\sigma'\sigma}^{(s)}(\mathbf{r}) = N \sum_{\sigma_2, \dots, \sigma_N} \int d\mathbf{r}_2 \dots d\mathbf{r}_N \rho(\mathbf{r}\sigma', \mathbf{r}_2\sigma_2, \dots, \mathbf{r}_N\sigma_N | \mathbf{r}\sigma, \mathbf{r}_2\sigma_2, \dots, \mathbf{r}_N\sigma_N). \quad (2.9)$$

Note that, the spin-density matrix  $\underline{n}^{(s)}$  is not diagonal in general. We can establish the connection to the electron density by introducing the trace over the remaining spin indices  $\text{tr}$  and yield

$$n(\mathbf{r}) = \text{tr} \left\{ \underline{n}^{(s)}(\mathbf{r}) \right\} = n_{\uparrow\uparrow}^{(s)}(\mathbf{r}) + n_{\downarrow\downarrow}^{(s)}(\mathbf{r}). \quad (2.10)$$

So far we have introduced the many-body problem of Equation (2.1) and the spin-density matrix  $\underline{n}^{(s)}$  as one of the key quantities. We shall now consider how to determine the ground state of this problem.

## 2.2 The two basic theorems

In 1973 U. von Barth and L. Hedin [29], shortly followed by A. Radgopal and J. Callaway [30] modified the proof of the basic theorem by P. Hohenberg and W. Kohn [25] to include spin-polarization in a matrix formalism. They proved a direct correspondence of the ground state spin-densities to the ground state itself for non-degenerate ground states.

We proceed by stating the two basic theorems that SDFT builds upon:

- The total energy of a many-body electron system in an external potential  $V$  is a unique functional of the spin-density  $\underline{n}^{(s)}(\mathbf{r})$ :  $E = E[\underline{n}^{(s)}]$ .
- For any many-electron system the energy functional  $E[\underline{n}^{(s)}(\mathbf{r})]$  has a minimum at exactly the ground state spin-density  $\underline{n}_0^{(s)}(\mathbf{r})$ . Hence, it is possible to apply the variational principle to find  $E_0 = E[\underline{n}_0^{(s)}(\mathbf{r})]$ .

Let us devise the electronic Hamiltonian of Equation (2.1) and show above theorems intuitively by an argument of contradiction in an back-of-the-envelope calculation. We assume some non-degenerate ground state of the system defined by  $\mathcal{H}$  exists and has energy  $E_0$ . It shall be described by the density matrix  $\rho_0$  with

$$E_0 = \text{Tr}\{\rho_0 \mathcal{H}\}. \quad (2.11)$$

Now, let us assume there was another external potential  $V'$  to yield a different density matrix  $\rho'_0$ , but the same spin-density  $\underline{n}^{(s)}$ :

$$\underline{\mathcal{H}}' = \underline{T} + \underline{V}' + \underline{U}, \quad (2.12)$$

$$E'_0 = \text{Tr}\{\rho'_0 \mathcal{H}'\}. \quad (2.13)$$

Because of the general variational principle, we know that any variation to  $\rho'_0$  will increase the total energy of the system defined by  $\mathcal{H}'$ . Thus, we obtain

$$E'_0 < \text{Tr}\{\rho_0 \mathcal{H}'\} = \text{Tr}\{\rho_0 (\mathcal{H} + V' - V)\} \quad (2.14)$$

$$E'_0 < E_0 + \text{Tr}\{\rho_0 (V' - V)\}. \quad (2.15)$$

Let us write these expressions more explicitly in terms of the spin-density and the external potential with Equation (2.4). This yields

$$\text{Tr}\{\rho_0(V' - V)\} = \int d\mathbf{r} \text{tr} \left\{ \underline{n}^{(s)}(\mathbf{r}) [\underline{v}^{ext'}(\mathbf{r}) - \underline{v}^{ext}(\mathbf{r})] \right\} \quad (2.16)$$

And repeating the same argument with primed and unprimed quantities exchanged, yields

$$E'_0 < E_0 - \int d\mathbf{r} \text{tr} \left\{ \underline{n}^{(s)}(\mathbf{r}) [\underline{v}^{ext'}(\mathbf{r}) - \underline{v}^{ext}(\mathbf{r})] \right\}, \quad (2.17)$$

with the same spin-density  $\underline{n}^{(s)}$ . However, combining Equation (2.15) and Equation (2.17) leads to the following contradiction:

$$E'_0 + E_0 < E_0 + E'_0. \quad (2.18)$$

We therefore conclude that  $\underline{n}^{(s)}$  cannot be the same for two different external potentials  $\underline{V}$  and  $\underline{V}'$ . Or inversely, the ground state energy is uniquely determined by a total energy functional of the spin-density  $E[\underline{n}^{(s)}(\mathbf{r})]$ .

The Kohn–Sham equations [26], that look like single-particle Schrödinger equations, can be derived by applying the variational principle. The effective single particle equations of noncollinear magnets have been derived by J. Kübler and coworkers [73, 74] in 1988. Their work pointed out that there exists a well-defined set of directions for the spins, already in the absence of spin–orbit coupling. The latter merely couples the set of directions for the spins to the underlying lattice. We will now introduce a central concept of DFT: the exchange–correlation energy functional.

First, let us assume we can determine single-particle functions  $\{\psi_{i\sigma}\}$  with eigenenergies  $\varepsilon_i$  below the Fermi energy, that allow us to express the spin-density matrix as

$$n_{\sigma\sigma'}^{(s)}(\mathbf{r}) = \sum_{i=1}^N \psi_{i\sigma} \psi_{i\sigma'}^*. \quad (2.19)$$

The kinetic energy can be split into the kinetic energy  $T_0$  of the non-interacting system

$$T_0[\underline{n}^{(s)}] = \sum_{i=1}^N \int d\mathbf{r} \text{tr} \{ \nabla \psi_{i\sigma}^*(\mathbf{r}) \nabla \psi_{i\sigma}(\mathbf{r}) \} \quad (2.20)$$

and the part  $T_{xc}$  that is the remainder. The Coulomb interaction can also be split into the so-called *Hartree term*

$$v_{\sigma'\sigma}^H(\mathbf{r}) = 2\delta_{\sigma'\sigma} \int d\mathbf{r}' \frac{n(\mathbf{r}')}{|\mathbf{r} - \mathbf{r}'|}, \quad (2.21)$$

that explicitly depends on the electron density and the remainder  $U_{xc}$ . These two remainder together define the *exchange–correlation energy functional*  $E_{xc}[\underline{n}^{(s)}(\mathbf{r})]$  of SDFT:

$$E_{xc}[\underline{n}^{(s)}(\mathbf{r})] = T_{xc}[\underline{n}^{(s)}(\mathbf{r})] + U_{xc}[\underline{n}^{(s)}(\mathbf{r})]. \quad (2.22)$$



And the *exchange–correlation potential* when varied w.r.t. the elements of the spin-density matrix  $\underline{n}^{(s)}(\mathbf{r})$ :

$$v_{\sigma'\sigma}^{xc}(\mathbf{r}) = \frac{\delta E_{xc}[\underline{n}^{(s)}(\mathbf{r})]}{\delta n_{\sigma'\sigma}^{(s)}(\mathbf{r})}. \quad (2.23)$$

The choice of the exchange–correlation functional  $E_{xc}[\underline{n}^{(s)}(\mathbf{r})]$  has evolved to be a large field in itself and will be discussed in the next section.

Finally, we complete the reduction to an effective single-particle problem by stating the *Kohn–Sham equations*

$$\sum_{\sigma} [-\delta_{\sigma'\sigma} \nabla^2 + v_{\sigma'\sigma}^{\text{eff}}(\mathbf{r})] \psi_{i\sigma} = \varepsilon_{i\sigma'} \psi_{i\sigma'}, \quad (2.24)$$

with the *effective potential*

$$v_{\sigma'\sigma}^{\text{eff}}(\mathbf{r}) = v_{\sigma'\sigma}^{\text{ext}}(\mathbf{r}) + v_{\sigma'\sigma}^H(\mathbf{r}) + v_{\sigma'\sigma}^{xc}(\mathbf{r}), \quad (2.25)$$

where we recall that  $v^{\text{ext}}$  is the external potential due to the nuclei and any applied field as given in Equation (2.4),  $v^H$  is the usual Hartree potential given in Equation (2.21) and  $v^{xc}$  is the exchange–correlation potential, that is defined in Equation (2.23) through the exchange–correlation energy functional  $E_{xc}$  discussed in the next section. Note that, the Equations (2.19), (2.24) and (2.25) can be solved iteratively until self-consistency is reached.

## 2.3 Exchange–correlation functional

The simplest, yet astonishingly useful [75], exchange–correlation functional is modeled after the homogeneous, interacting electron gas and only takes into account the local-density. It is thus called local-density approximation (LDA).

### 2.3.1 Local spin-density approximation

The generalization of LDA to magnetic systems in the case of a global spin-axis, i.e. collinear magnetism, leads to local spin-density approximation (LSDA) [29]. The exchange–correlation energy functional of LSDA is written as

$$E_{xc}^{\text{LSDA}}[\underline{n}^{(s)}(\mathbf{r})] = \int d\mathbf{r} n(\mathbf{r}) \epsilon_{xc}^{\text{LSDA}}(n_{\uparrow}^{(s)}(\mathbf{r}), n_{\downarrow}^{(s)}(\mathbf{r})), \quad (2.26)$$

where  $n_{\uparrow}^{(s)}(\mathbf{r}) = n_{\uparrow\uparrow}^{(s)}$  and  $n_{\downarrow}^{(s)}(\mathbf{r}) = n_{\downarrow\downarrow}^{(s)}$ , while  $n_{\uparrow\downarrow}^{(s)} = n_{\downarrow\uparrow}^{(s)} = 0$ . This defines the exchange–correlation potential of LSDA as

$$v_{\alpha}^{xc, \text{LSDA}}(\mathbf{r}) = \frac{\partial}{\partial n_{\alpha}^{(s)}} \left[ n \epsilon_{xc}^{\text{LSDA}}(n_{\uparrow}^{(s)}, n_{\downarrow}^{(s)}) \right]_{\substack{n_{\uparrow}^{(s)} = n_{\uparrow}^{(s)}(\mathbf{r}), \\ n_{\downarrow}^{(s)} = n_{\downarrow}^{(s)}(\mathbf{r})}}, \quad (2.27)$$

with  $\alpha = \uparrow, \downarrow$ .

Now, the explicit expression for  $\epsilon_{xc}^{\text{LSDA}}$  can be determined numerically<sup>1</sup>. In a nutshell, the exchange part is calculated from the Hartree–Fock approximation of a spin-polarized gas and then the correlation part is estimated by supplementing such that one obtains the total energy of a homogeneous, interacting spin-polarized electron gas. The main difference among LSDA functionals by different authors lies in the approach to the underlying numerical problem.

The key assumption of J. Kübler and coworkers [73] is that even in the case of noncollinear magnetism, it is possible to locally diagonalize the spin-density. This leads to the generalized LSDA for noncollinear magnetism (gLSDA). It is based on a unitary transformation  $\underline{U}(\mathbf{r})$  of the form

$$\underline{U}(\mathbf{r}) = \exp\left\{\left(\frac{1}{2}i\theta(\mathbf{r})\underline{\sigma}_y\right)\right\} \exp\left\{\left(\frac{1}{2}i\varphi(\mathbf{r})\underline{\sigma}_z\right)\right\}, \quad (2.28)$$

with

$$\tan \varphi(\mathbf{r}) = -\frac{\text{Im}(n_{\uparrow\downarrow}^{(s)}(\mathbf{r}))}{\text{Re}(n_{\uparrow\downarrow}^{(s)}(\mathbf{r}))}, \quad (2.29a)$$

$$\tan \theta(\mathbf{r}) = 2 \frac{\sqrt{\left[\text{Re}(n_{\uparrow\downarrow}^{(s)}(\mathbf{r}))\right]^2 + \left[\text{Im}(n_{\uparrow\downarrow}^{(s)}(\mathbf{r}))\right]^2}}{n_{\uparrow\uparrow}^{(s)}(\mathbf{r}) - n_{\downarrow\downarrow}^{(s)}(\mathbf{r})}, \quad (2.29b)$$

where  $\underline{\sigma}_i$  with  $i = x, y, z$  are the Pauli matrices. This transformation rotates the spin-axis locally by means of

$$\tilde{\underline{\sigma}}_z(\mathbf{r}) = \underline{U}^\dagger(\mathbf{r}) \underline{\sigma}_z \underline{U}(\mathbf{r}). \quad (2.30)$$

Finally, the exchange–correlation functional of the generalized LSDA can be written as a diagonal matrix as follows:

$$\underline{v}^{xc, \text{gLSDA}}(\mathbf{r}) = v_0^{xc}(\mathbf{r}) \underline{1} + \Delta v^{xc, \text{LSDA}}(\mathbf{r}) \tilde{\underline{\sigma}}_z(\mathbf{r}), \quad (2.31a)$$

$$v_0^{xc}(\mathbf{r}) = \frac{1}{2} \left( v_{\uparrow}^{xc, \text{LSDA}}(\mathbf{r}) + v_{\downarrow}^{xc, \text{LSDA}}(\mathbf{r}) \right), \quad (2.31b)$$

$$\Delta v^{xc}(\mathbf{r}) = \frac{1}{2} \left( v_{\uparrow}^{xc, \text{LSDA}}(\mathbf{r}) - v_{\downarrow}^{xc, \text{LSDA}}(\mathbf{r}) \right), \quad (2.31c)$$

where  $\underline{1}$  is a  $2 \times 2$  unit matrix. Here, again Equation (2.27) is used to compute  $v_{\alpha}^{xc, \text{LSDA}}(\mathbf{r})$  and  $\epsilon_{xc}^{\text{LSDA}}(n_{\uparrow}^{(s)}, n_{\downarrow}^{(s)})$  is modeled after homogeneous, interacting spin-polarized electron gas.

In order to emphasize the connection to magnetism in general, let us present an alternative terminology. We introduce the usual vector of Pauli matrices  $\underline{\sigma} = (\underline{\sigma}_x, \underline{\sigma}_y, \underline{\sigma}_z)^T$ , that together with the unit matrix  $\underline{1}$  clearly forms a basis for  $\underline{v}^{xc}(\mathbf{r})$ . Then, the exchange–correlation energy  $E_{xc}^{\text{gLSDA}}[\underline{n}^{(s)}(\mathbf{r})]$  can be written in terms of the electron density  $n(\mathbf{r}) = n_{\uparrow}^{(s)}(\mathbf{r}) + n_{\downarrow}^{(s)}(\mathbf{r})$  and the

<sup>1</sup>A didactically valuable demonstration can be found in Ref. [8].

spin-magnetization  $m^{(s)}(\mathbf{r})$ . The latter can be seen as the length of a vector, which reads [76]

$$\mathbf{m}^{(s)}(\mathbf{r}) = -\mu_B \sum_{\alpha\beta} n_{\alpha\beta}^{(s)}(\mathbf{r}) \boldsymbol{\sigma}_{\alpha\beta} \quad (2.32)$$

$$= \text{Tr} \left\{ \rho \hat{\mathbf{m}}^{(s)}(\mathbf{r}) \right\}, \quad (2.33)$$

which defines the *spin-magnetization operator*

$$\hat{\mathbf{m}}^{(s)}(\mathbf{r}) = -\mu_B \sum_{i=1}^N \delta(\mathbf{r} - \mathbf{r}_i) \boldsymbol{\sigma}. \quad (2.34)$$

There are different sign conventions in the literature, however here we chose the spin-magnetization to oppose the spin, as is most natural from a physical perspective.

In case of LSDA and gLSDA—without loss of generality—we may construe

$$E_{xc}^{gLSDA}[n(\mathbf{r}), m^{(s)}(\mathbf{r})]. \quad (2.35)$$

It is now possible to define the *exchange–correlation magnetic field*  $\mathbf{B}_{xc}(\mathbf{r})$ . In analogy to the Zeeman term in the Pauli Hamiltonian, that is derived in Section A.3, the variation of  $E_{xc}$  with respect to the spin-magnetization  $\mathbf{m}^{(s)}(\mathbf{r})$ , yields the components of  $\mathbf{B}_{xc}(\mathbf{r})$ :

$$B_{xc,i}(\mathbf{r}) = \frac{\delta E_{xc}[n, m^{(s)}]}{\delta m_i^{(s)}(\mathbf{r})}. \quad (2.36)$$

In this alternative formulation, the effective potential in Equation (2.25) is replaced by

$$v_{\sigma'\sigma}^{\text{eff}}(\mathbf{r}) = v_{\sigma'\sigma}^{\text{ext}}(\mathbf{r}) + v_{\sigma'\sigma}^H(\mathbf{r}) + v_0^{xc}(\mathbf{r}) \delta_{\sigma'\sigma} - \mu_B \boldsymbol{\sigma} \cdot \mathbf{B}_{xc}(\mathbf{r}). \quad (2.37)$$

Here, the contributions to the exchange–correlation potential is split into  $v_0^{xc}(\mathbf{r})$  and a term containing  $\mathbf{B}_{xc}(\mathbf{r})$ . These contributions correspond exactly to the two contributions in Equation (2.31a). The assumption of J. Kübler and coworkers [73], that it is possible to locally diagonalize the spin-density, can then be reformulated saying that the exchange–correlation magnetic field  $\mathbf{B}_{xc}(\mathbf{r})$  is collinear to the local spin-magnetic moment  $\mathbf{m}^{(s)}(\mathbf{r})$  everywhere in space:  $\mathbf{m}^{(s)}(\mathbf{r}) \parallel \mathbf{B}_{xc}(\mathbf{r})$ .

### 2.3.2 Generalized gradient approximation

The *homogeneous*, interacting spin-polarized electron gas is a good approximation, as long as the spin-density is slowly varying. In a realistic material, this assumption does not generally hold and in an effort to incorporate the leading nonlocal corrections the exchange–correlation energy functional is chosen to be not just dependent on the local spin-density, but also its gradient. Interestingly, attempts to simply compose the exchange–correlation energy functional based on two contributions, the original LSDA contribution and one arising from the gradient of the spin-density, fail. In particular, this is because a number of scaling relations and sum rules are violated by this attempt.

A more general ansatz leads to the so called *generalized gradient approximation* (GGA). It can be written as

$$E_{xc}^{\text{GGA}}[n^{(s)}(\mathbf{r})] = \int d\mathbf{r} f(n_{\uparrow}^{(s)}(\mathbf{r}), n_{\downarrow}^{(s)}(\mathbf{r}), \nabla n_{\uparrow}^{(s)}(\mathbf{r}), \nabla n_{\downarrow}^{(s)}(\mathbf{r})), \quad (2.38)$$

where the function  $f$  is unknown and *cannot* be modeled after some numerically known system, in contrast to  $\varepsilon_{xc}^{\text{LSDA}}$  for LSDA, which is modeled after the homogeneous electron gas. In fact, there is no model system after which the GGA functional could be uniquely constructed, instead the so-called *conservative philosophy of approximations* has been adopted [77]. I.e., a number of conservation laws and scaling relations are used to obtain a suitable, but not uniquely defined GGA functional starting from the unpolarized uniform electron gas.

In the scope of this thesis, we use the GGA functional introduced in 1996 by J. Perdew, K. Burke and M. Ernzerhof [78]. This flavor of GGA, the so-called PBE–GGA, is presently the standard choice particularly in condensed matter physics for multiple reasons. One of which might be that among different proposals it is the most local [79] and another might be that it is the standard setting<sup>2</sup> in the Vienna *ab initio* Simulation Package (VASP) [80, 81], which is todate the most widely used program to perform *ab initio* calculations.

## 2.4 Solving the Kohn–Sham equations

In the last section, we have roughly outlined how to arrive at an explicit expression for the exchange–correlation energy functional and, thus, the effective potential in Equation (2.25) is fully defined given some spin-density  $\underline{n}^{(s)}$ . Recall that, if we make an educated guess for the single-particle spinor wave functions  $\{\psi_{i\sigma}\}$ , the spin-density follows from Equation (2.19). The next step is solving the Kohn–Sham equations given in Equation (2.24) and finding a new set of single-particle functions  $\{\psi_{i\sigma}\}$ . This is an iterative process that forms a self-consistency loop as illustrated in Figure 2.1 and can be solved numerically.

Hence, we need an appropriate ansatz for the single-particle wave functions  $\{\psi_{i\sigma}\}$ . However, the popular plane wave ansatz is bound to fail, because one needs to simultaneously cope with a diverging potential near the ions and a rather flat potential in between. This lead to the development of *pseudopotentials* [82]. The basic idea is to replace the strong potential near the nuclei with a well-behaved potential that accommodates the overall behaviour of the wave function, but neglects strong oscillations. A generalization [83] of the early ideas from both Vanderbilt-type [84] ultrasoft-pseudopotentials [85] (USPP) and the linear-augmented plane waves [86] (LAPW) yields the *projector augmented-wave method* (PAW) [87]. In 2000, D. Hobbs, G. Kresse and J. Hafner generalized the PAW method [76] to account for noncollinear magnetism in the framework<sup>3</sup> proposed by J. Kübler and coworkers [73]. The formalism described in Ref. [76] is implemented in the Vienna *ab initio* Simulation Package (VASP) [80, 81] and, thus, it is underlying calculations performed in the scope of this thesis.

<sup>2</sup>Standard setting are chosen based on a broad applicability of the selected method.

<sup>3</sup>This has been discussed in the Section 2.3.1.

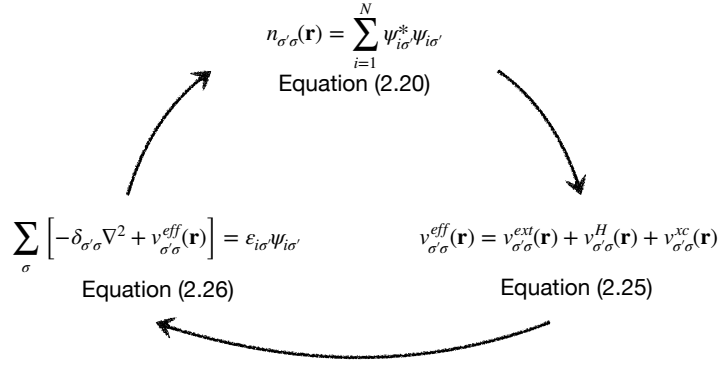


Figure 2.1: Spin-density functional theory self-consistency loop to solve the Kohn–Sham equations. The Hartree potential is given in Equation (2.21) and the external potential is given in Equation (2.4).

The reader is encouraged to access one of the many pedagogical tutorials that can be found in text and video-format provided by VASP. However, in order to be complete, let us formally introduce the ansatz for the *single-particle two-component spinor wave functions*<sup>4</sup>  $\psi_{i\sigma}$ , that are eigenfunctions of the Kohn–Sham equation in Equation (2.24) with eigenenergy  $\epsilon_{i\sigma}$ , i.e.,

$$|\psi_{i\sigma}\rangle = |\tilde{\psi}_{i\sigma}\rangle + \sum_{\eta} \left( |\phi_{\eta}\rangle - |\tilde{\phi}_{\eta}\rangle \right) \langle \tilde{p}_{\eta} | \tilde{\psi}_{i\sigma} \rangle. \quad (2.39)$$

Here,  $\eta$  is shorthand for the atomic site  $\mathbf{R}_{\mu}$ , the quantum numbers  $n$ ,  $l$  and  $m$  that label the *local basis functions*<sup>5</sup>  $\phi_{\eta}$ , which are solutions of the spherical (scalar relativistic) Schrödinger equation for a nonspinpolarized atom with reference energy  $\epsilon_{nl}$ .  $\tilde{\phi}_{\eta}$  are additional local basis functions called *pseudo partial waves*, that are constructed to be dual to the projector functions  $\tilde{p}_{\eta}$ , i.e.,

$$\langle \tilde{p}_{\eta} | \tilde{\phi}_{\eta'} \rangle = \delta_{\eta\eta'}. \quad (2.40)$$

They serve as a continuous transition from the local basis  $\phi_{\eta}$ , that is nonzero within the so-called *PAW sphere* in a core radius  $r_c$  around  $\mathbf{R}_{\mu}$ , and a non-local, plane wave *pseudo-wave functions*  $\tilde{\psi}_{i\sigma}$ , that serves as the variational quantity in the minimization of the total energy. These can be written as plane plane waves as follows

$$\langle \mathbf{r} | \tilde{\psi}_{i\sigma} \rangle = \frac{1}{\sqrt{\Omega_r}} \sum_{\mathbf{k}} C_{i\mathbf{k}}^{\sigma}(\mathbf{r}) e^{i\mathbf{k}\cdot\mathbf{r}}, \quad (2.41)$$

where  $\sqrt{\Omega_r}$  is the volume of the Wigner–Seitz cell.

<sup>4</sup>The single-particle two-component spinor wave functions are also referred to as all-electron (AE) wave functions.

<sup>5</sup>The local basis functions  $\phi_{\eta}$  are also referred to as all-electron partial waves.

For any term that we would like to include into the Hamiltonian, we will henceforth need to consider, how the operator  $\hat{O}$ , which is associated with the term we want to include, acts on  $\psi_{i\sigma}$  defined in Equation (2.39). This will be the starting point of the next section, where we will discuss spin-orbit coupling.

## 2.5 Including spin-orbit coupling

The Hamiltonian introduced in Section 2.1 does not contain any relativistic corrections. In 2016, S. Steiner and coworkers [88] published a paper<sup>6</sup> describing the details of the spin-orbit coupling (SOC) implementation in VASP. It constitutes the most important relativistic correction, as discussed in the context of Dirac theory in Section A.4.

The relativistic corrections to the  $2 \times 2$  Hamiltonian in Equation (2.1) can be derived by means of different perturbative methods [89]. Most commonly, the Foldy-Wouthuysen transformation [72] is performed in orders of  $E_{\text{kin}}/(mc^2)$ , where the kinetic energy reads  $E_{\text{kin}} = \sqrt{m^2c^4 + \mathbf{p}^2c^2} - mc^2$ . However, for  $\mathbf{r} \rightarrow \mathbf{0}$  this is not a well regularized expansion in a Coulomb potential  $v(r)$ . Thus, E. van Lenthe and coworkers [90] have proposed to expand in orders of  $(E_{\text{kin}} + v)/(mc^2 - v)$  instead.

The  $2 \times 2$  SOC-term can then be written as

$$\underline{\mathcal{H}}^{SO} = \frac{1}{c^2} \frac{K(r)}{r} \frac{dv^{\text{ion}}(r)}{dr} \boldsymbol{\sigma} \cdot \mathbf{L}, \quad (2.42)$$

where  $\mathbf{L}$  is the angular momentum operator,  $\boldsymbol{\sigma}$  is the vector of Pauli matrices,  $v^{\text{ion}}(r)$  is the Coulomb potential of a nonspinpolarized atom and we use the units  $m = 1/2$ ,  $\hbar = 1$  as in Section 2.1. The factor  $K(r)$  appears due to the less common choice of the expansion parameter and is given by

$$K(r) = \left(1 - \frac{v^{\text{ion}}(r)}{c^2}\right)^{-2}. \quad (2.43)$$

Here,  $r$  can be thought to be the distance between an electron at  $\mathbf{r}$  and a nucleus at  $\mathbf{R}_\mu$ , i.e.,  $r = |\mathbf{r} - \mathbf{R}_\mu|$ . This already anticipates that SOC is expected to be only relevant locally in close vicinity of the nuclei.

Within the PAW method any (semi-)local operator  $\hat{O}$  acting on  $\psi_{i\sigma}$  has a corresponding *pseudo operator*  $\hat{\hat{O}}$  of the form [87]

$$\hat{\hat{O}} = \hat{O} + \sum_{\eta\eta'} |\tilde{p}_\eta\rangle \left( \langle \phi_\eta | \hat{O} | \phi_{\eta'} \rangle - \langle \tilde{\phi}_\eta | \hat{O} | \tilde{\phi}_{\eta'} \rangle \right) \langle \tilde{p}_{\eta'}|. \quad (2.44)$$

---

<sup>6</sup>In the same paper [88], they performed a magnetic anisotropy energy calculation for  $\text{Fe}_{1-x}\text{Co}_x$  and concluded that their results prove,

hopefully beyond doubt, that magnetic anisotropy calculations are feasible within the PAW methodology and compare very well with other methods.

The outcome of our benchmark in Chapter 4 will strongly rely on their conjecture to hold for other compounds apart from  $\text{Fe}_{1-x}\text{Co}_x$ .

It is assumed that the effect can be neglected outside the PAW sphere and, consequently, only the second term in Equation (2.44), that is the local contribution by construction, must be considered. We obtain

$$\tilde{\mathcal{H}}^{SO} = \sum_{\eta\eta'} |\tilde{p}_\eta\rangle \langle \phi_\eta | \mathcal{H}^{SO} | \phi_{\eta'} \rangle \langle \tilde{p}_{\eta'}|. \quad (2.45)$$

Further following Ref. [88], the local basis functions, i.e.,

$$\phi_\eta(\mathbf{r} - \mathbf{R}_\mu) = R_{nl}(|\mathbf{r} - \mathbf{R}_\mu|) Y_{lm}(\Omega_\mu) \quad (2.46)$$

are written in terms of the radial-dependence  $R_{nl}$  and angle-dependence by means of spherical harmonics  $Y_{lm}$ , where  $\eta$  is shorthand for the atomic site  $\mathbf{R}_\mu$ , the quantum numbers  $n$ ,  $l$  and  $m$  that label the solutions of the spherical (scalar relativistic) Schrödinger equation for a nonspin-polarized atom with reference energy  $\varepsilon_{nl}$ . That allows us to obtain<sup>7</sup> the SOC pseudo Hamiltonian of Equation (2.42), which reads

$$\tilde{\mathcal{H}}_{\sigma\sigma'}^{SO} = \frac{1}{c^2} \sum_{\eta\eta'} |\tilde{p}_\eta\rangle R_{\eta\eta'} \boldsymbol{\sigma}_{\sigma\sigma'} \cdot \mathbf{L}_{\eta\eta'} \langle \tilde{p}_{\eta'}|, \quad (2.47a)$$

$$R_{\eta\eta'} = \int_0^{r_c} dr r^2 R_{nl}^*(r) \frac{K(r)}{r} \frac{dv^{\text{ion}}(r)}{dr} R_{n'l'}(r) \quad (2.47b)$$

$$\mathbf{L}_{\eta\eta'} = \int d\Omega Y_{lm}^*(\Omega) \mathbf{L} Y_{l'm'}(\Omega). \quad (2.47c)$$

With Equation (2.47a), we know how the SOC Hamiltonian acts on the variational pseudo wave functions

$$|\tilde{\psi}_{i\sigma}\rangle = \sum_{\sigma'} \tilde{\mathcal{H}}_{\sigma\sigma'}^{SO} |\tilde{\psi}_{i\sigma'}\rangle, \quad (2.48)$$

which concludes this section. In the next section, we will discuss strong electron–electron correlation effects that cannot be easily accounted for in SDFT.

## 2.6 Including strong electron–electron interactions beyond SDFT

The strongly varying spin-density that lead to the development of GGA is not the only nonrelativistic correction to LSDA in order to satisfactorily reproduce experimental observations. Another effect that is difficult to account for by exchange–correlation functionals is strong electron–electron correlation that arise particularly in  $3d$  and  $4f$ -orbitals, where electrons tend to be localized. For

<sup>7</sup>We note that Eq. (8) of Ref. [88] compared to Equation (2.47b) contains a factor of  $4\pi$  and lacks a factor  $r^2$ , those origin we do not understand. Moreover, in the source code of VASP version 5.4.4, the factor  $4\pi$  seems not to appear, however the factor  $r^2$ , which we believe appears as Jacobi determinant, seems to be not included.

instance,  $\text{La}_2\text{CuO}_4$  [91],  $\text{NiO}$  [92] and  $\text{Eu}_2\text{Ir}_2\text{O}_7$  [93] are falsely predicted to be metallic for temperatures above the AFM phase.

In fact, LSDA and GGA represent a substantial approximation to the treatment of the Coulomb interaction given in Equation (2.5). In order to reduce the full many-body problem to a set of single-electron problems in a local or semi-local effective potential, it is necessary to condone a crude approximation: An electron at position  $\mathbf{r}$  sees only a time-averaged local spin-density  $\underline{n}^{(s)}(\mathbf{r})$  and the gradient  $\nabla \underline{n}^{(s)}(\mathbf{r})$  of the other electrons. One of said examples, where DFT fails, is  $(\text{Eu}_{1-x}\text{Ca}_x)_2\text{Ir}_2\text{O}_7$  [93]. At  $x = 0$  the strong electronic correlation in the  $5d$  Ir orbitals drives a so-called Mott–Hubbard metal-to-insulator transition [94–96]. Upon doping  $x > 0$  the filling of the  $d$ -bands can be finely tuned experimentally, which leads to the realization of a doped Mott-insulating phase.

Both phases, the Mott–Hubbard insulating phase and the *doped* Mott–Hubbard insulating phase, are successfully described by a different branch in the condensed matter community that also tries to solve the electronic Hamiltonian introduced in Section 2.1. By means of equally crude approximations the problem is rewritten in terms of a kinetic term with hopping amplitude  $-t$  and on-site Coulomb interaction Hubbard  $U$  [97]. In a commendable effort of these two communities to join forces, methods beyond SDFT to include strong electron–electron correlation effects on top of first-principles calculations have been developed. For instance, one approach is to include a Hubbard correction term directly in the exchange–correlation functional (SDFT+U) [98], another approach combines SDFT with the dynamical mean field theory (DMFT) [99–102] which leads to the SDFT+DMFT [103–108] approach. The DMFT Hamiltonian based on SDFT can be written as [108]

$$\begin{aligned} \hat{\mathcal{H}} = & - \sum_{i\sigma jm\sigma'} t_{iljm}^{\sigma\sigma'} \hat{c}_{il,\sigma}^\dagger \hat{c}_{jm,\sigma'} + U \sum_{i\sigma} \hat{n}_{il}^\sigma \hat{n}_{il}^{\bar{\sigma}} + \sum_{\substack{i\sigma\sigma' \\ l \neq m}} (U' - \delta_{\sigma\sigma'} J) \hat{n}_{il}^\sigma \hat{n}_{im}^{\sigma'} \\ & - \frac{J}{2} \sum_{\substack{i\sigma \\ l \neq m}} \hat{c}_{il,\sigma}^\dagger \hat{c}_{jl,\bar{\sigma}} \hat{c}_{im,\bar{\sigma}}^\dagger \hat{c}_{im,\sigma} - \frac{\tilde{J}}{2} \sum_{\substack{i\sigma \\ l \neq m}} \hat{c}_{il,\sigma}^\dagger \hat{c}_{il,\bar{\sigma}} \hat{c}_{im,\sigma} \hat{c}_{im,\bar{\sigma}} - \sum_{i\sigma} \Delta \epsilon \hat{n}_{il}^\sigma \end{aligned} \quad (2.49)$$

where  $\bar{\sigma} = \uparrow (\downarrow)$  for  $\sigma = \downarrow (\uparrow)$ , the creation (annihilation) operator  $\hat{c}_{il,\sigma}^\dagger$  ( $\hat{c}_{il,\sigma}$ ) correspond to electron  $i$  in a localized<sup>8</sup>  $d$ - or  $f$ -orbital  $\varphi_{il,\sigma}^*(\mathbf{r})$  with spin  $\sigma$  and orbital quantum number  $l$ , the hopping amplitude  $t_{iljm}^{\sigma\sigma'}$  is given by

$$t_{iljm}^{\sigma\sigma'} = - \int d\mathbf{r} \varphi_{il,\sigma}^*(\mathbf{r}) [-\delta_{\sigma\sigma'} \nabla^2 + v_{\sigma\sigma'}^{\text{eff}}] \varphi_{jm,\sigma'}(\mathbf{r}) \quad (2.50)$$

and the density operator reads  $\hat{n}_{il}^\sigma = \hat{c}_{il,\sigma}^\dagger \hat{c}_{jm,\sigma}$ .

<sup>8</sup>Depending on the basis in which the Kohn–Sham equations are solved, these orbitals may not be inherently defined. Indeed, the PAW method employed here would need a projection onto Wannier orbitals [109] before doing DMFT calculations:  $\{\psi_{i\sigma}\} \mapsto \{\varphi_{il,\sigma}\}$ . That allows us to define the many-body state in second quantised form:  $\hat{\Psi}_\sigma^\dagger(\mathbf{r}) = \sum_{il} \hat{c}_{il,\sigma}^\dagger \varphi_{il,\sigma}^*$ . For details see Ref. [108].



The reason for explicitly stating Equation (2.49) at this point is to emphasize the different terms that appear and their fundamental connection to magnetism. Although we mentioned that magnetism is a collective phenomenon, it might not be immediately obvious how strong electron–electron correlations induce magnetic ordering. The first term in Equation (2.49) corresponds to the kinetic energy with the material specific dispersion relation given by SDFT through Equation (2.50). The second term is the intra-orbital Coulomb interaction commonly referred to as Hubbard  $U$ -term. If  $U$  is large, electrons avoid to occupy the same orbital and tend to be localized, which ultimately leads to the Mott–Hubbard transition mentioned above. The third term introduces the inter-orbital Coulomb repulsion  $U'$ , that describes the interaction of two opposing spins in different orbitals at the same site. If the spins are aligned, we need to avoid double counting of the Hund’s exchange coupling  $J$ , which is properly accounted for in the fourth term. It contains a spin-flip term, that prefers to align spins all up (or down) across orbitals. Next, the fifth term is a pair hopping with amplitude  $\tilde{J}$ , which is only the same as  $J$ , if the wave functions can be chosen real. This process is often neglected since the presence of  $U$  makes double occupation unlikely and in respect to magnetism it has no influence. The last term is the double counting term, that has the nontrivial task of subtracting all correlation effects already accounted for in SDFT by an appropriate choice of  $\Delta\epsilon$ .

All of these parameters ( $U$ ,  $J$ , and  $\tilde{J}$ ) present tuneable parameters in a Hamiltonian that is, in fact, not exactly solvable in dimensions less than infinity. Powerful, though computationally expensive, numerical methods can treat this model to some extent by first mapping it to the Anderson impurity model [110, 111] and then employing a suitable impurity solver [103]. Furthermore, in an effort to avoid the parameters to be adjustable, the so-called GW approximation [112] and resulting GW+DMFT [113, 114], as well as constraint random phase approximation (cRPA) [115–117] have been developed. More recently diagrammatic extensions of DMFT [118, 119] are able to account for non-local correlations that arise in low-dimensional systems and have shown some success in describing critical behaviour in the vicinity of AFM phase transitions [120–124] and accounting for vertex corrections e.g. corresponding to incommensurate spin-fluctuations in the pseudo-gap phase of the single-band Hubbard model on a  $2d$  square lattice investigated by the present author in Ref. [125]. So far the applications of diagrammatic extensions of DMFT have been limited to model calculations, but most recently fully self-consistent *ab initio* dynamical vertex approximation (DVA) [126] has been implemented.

In practice, the computational cost of these corrections increases rapidly. It is therefore practical to start from GGA, in order to avoid the tuning parameter  $U$  in SDFT+U and only go beyond SDFT if some observation cannot be explained otherwise. For instance, in the case of  $(\text{Eu}_{1-x}\text{Ca}_x)_2\text{Ir}_2\text{O}_7$ , the present author performed a DFT+DMFT calculation [93] in order to explain an unexpected sign change in the Seebeck coefficient. And in the present thesis, we will perform a case study on Mn-compounds and half-filled  $4f$ -compounds in order to understand the importance of strong electronic correlations in the context of magnetic structure prediction, see Section 4.2.6.

## 2.7 Concluding remarks

In this chapter, we have introduced the electronic Hamiltonian, which lead to the first crude approximation: We neglected ionic vibrations. Therefore, all structure transitions that might accompany a magnetic phase transition are neglected. Next, we have outlined the strategy to define and solve the Kohn–Sham equations for systems featuring noncollinear magnetism. Here, we briefly reviewed the basic ideas, that were pioneered by J. Kübler *et al.* [8, 73]. The key assumption—which should be seen as an approximation—is that the spin-density can always be diagonalized locally. The most important relativistic correction in the context of magnetism, i.e., spin–orbit coupling, has been introduced in Section 2.5. Subsequently, in Section 2.6, we emphasized that SDFT imposes additional approximations involved in the treatment of the electron–electron interaction. Nevertheless, the sum of all these approximations has produced quantitative results in good agreement with experimental observations in many instances and, thus, we believe they represent a good starting point in predicting the magnetic ground state.

Still, the reader is encouraged to critically keep track of these approximations, as only their application to realistic materials can prove whether or not they are indeed appropriate. In Chapter 4, we will present a high-throughput benchmark of 131 materials including many noncollinear compounds. Any lack of accuracy in assigning the correct energy to the magnetic ground state should be occasion to question the approximations introduced in the present chapter. In the following chapter, we will introduce the multipole theory with a focus on magnetic multipoles.

## Chapter 3

# Multipole theory

The expansion of fields in orders of multipole moments is a widely used concept in electromagnetism and consequently it finds applications in many areas of physics. For instance, in classical electromagnetism it is used to characterize radiation [127, 128], in particle physics it is exploited to describe a particle's motion in various fields [129–131], in nuclear physics it enables the calculation of form factors [132–138] and in solid-state physics it is increasingly devised to characterize many-body states [139–150].

The arguably most widely known application of multipole theory is the discussion of *atomic orbitals*. They can be found in many text books [152, 153] and their angle dependencies, i.e., the real spherical harmonics, are shown in Figure 3.1. Let us recall that the solution of the *scalar Poisson equation* with a point charge acting as a source is found by separation of variables into a *radial* and a *spherical problem*. The *scalar potential* can subsequently be expressed in terms of *electric multipole moments*<sup>1</sup> of order<sup>2</sup>  $l$  and integer  $m$  with  $-l \leq m \leq l$ . This result leads to the well-known atomic orbitals, which describe the probability density of an electron with *angular momentum* quantum number  $l$  and *magnetic* quantum number  $m$ .

In this chapter, we want to apply the multipole theory to magnetic structures in crystallographic unit cells. In contrast to the discussion of electric multipoles of atomic orbitals, we need to consider the vector gauge field instead of the scalar potential and arrive at *time-reversal odd multipole*

---

<sup>1</sup>Also referred to as *scalar*, *polar* or *tensor* multipoles. The multitude of names for electric multipole moments arises from its symmetry properties: It transforms like a tensor of rank  $l$  under both *proper* and *improper* rotation. Improper rotations are rotation followed by reflection. In other words, the electric multipole moments have a *parity* of  $(-1)^l$ . Such quantities are called scalar for rank 0, polar vector for rank 1 and (polar) tensors for rank greater 1. The parity is merely a result of the symmetry properties of spherical harmonics at the corresponding expansion order. On the other hand the name electric implicitly carries the meaning of the most important symmetry property: The electric multipole moment is invariant under time-reversal symmetry. Nevertheless, all names can be found in literature and it is useful to know their correspondence.

<sup>2</sup>Also referred to as *rank*. Again, this refers to the fact that a multipole of expansion order  $l$  transforms like a tensor of rank  $l$ .

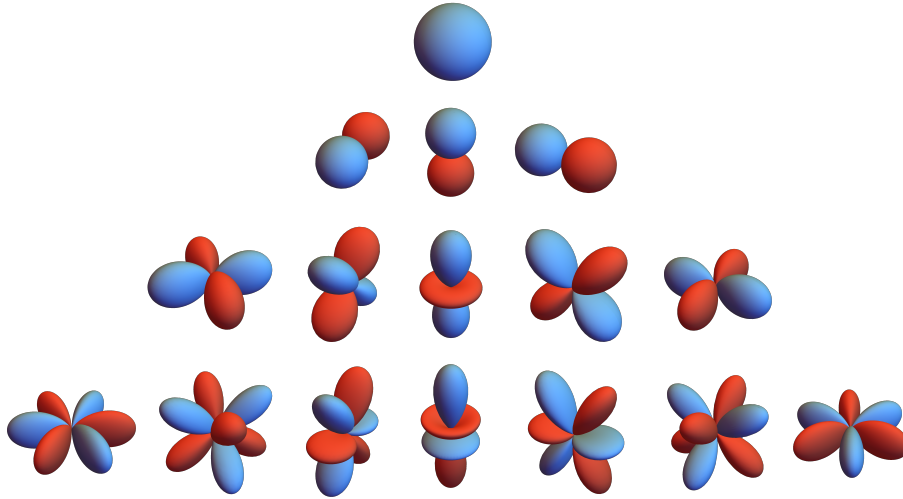


Figure 3.1: Atomic orbitals. Order is increasing from top to bottom with  $l = 0, 1, 2, 3$  corresponding to  $s, p, d$  and  $f$ . These are real harmonics as defined in Equation (3.38). Columns to the left (right) correspond to  $Y_{lm}^{(s)}$  ( $Y_{lm}^{(c)}$ ) with increasing  $m$  to the left.  $Y_{l0}$  is always real. Visualized using Mathematica [151].

*moments*<sup>3</sup>. Here, we are primarily interested in multipoles on an inter-atomic length scale. In fact, as mentioned in Section 1.1, the discussion of magnetic structures in terms of multipole moments has recently proven to be useful in order to explain a multitude of phenomena. Here, we will discuss the derivation of the general form of vector gauge fields starting from Maxwell's equations. Then, we will arrive at specific expressions for the time-reversal odd multipoles and examine the so-called *cluster multipole theory*. In the last section, we will show a complete cluster multipole expansion for some representative structures.

### 3.1 The vector Poisson equation and its solution

The Maxwell equations read

$$\nabla \times \mathbf{B}(\mathbf{r}, t) = 4\pi \mathbf{j}_{\text{tot}}(\mathbf{r}, t) + \frac{\partial}{\partial t} \mathbf{E}(\mathbf{r}, t), \quad (3.1a)$$

$$\nabla \cdot \mathbf{E}(\mathbf{r}, t) = 4\pi \rho_{\text{tot}}(\mathbf{r}, t), \quad (3.1b)$$

$$\nabla \times \mathbf{E}(\mathbf{r}, t) = -\frac{\partial}{\partial t} \mathbf{B}(\mathbf{r}, t), \quad (3.1c)$$

$$\nabla \cdot \mathbf{B}(\mathbf{r}, t) = 0, \quad (3.1d)$$

<sup>3</sup>The time-reversal odd, magnetic multipole moments have been called *axial* or *pseudotensor* multipole moments in analogy to the terms used for electric multipoles.

where the  $\mathbf{B}$  and  $\mathbf{E}$  are the magnetic and electric fields with sources  $\mathbf{j}_{\text{tot}}$  and  $\rho_{\text{tot}}$ . In general, the charge and current densities have convective contributions, i.e., external and orbital, and bound contributions<sup>4</sup>:

$$\rho_{\text{tot}}(\mathbf{r}, t) = \rho_{\text{conv}}(\mathbf{r}, t) + \nabla \cdot \mathbf{P}(\mathbf{r}, t), \quad (3.4a)$$

$$\mathbf{j}_{\text{tot}}(\mathbf{r}, t) = \mathbf{j}_{\text{ext}}(\mathbf{r}, t) + \mathbf{j}_{\text{orb}}(\mathbf{r}, t) + \frac{\partial}{\partial t} \mathbf{P}(\mathbf{r}, t) + \nabla \times \mathbf{M}(\mathbf{r}, t), \quad (3.4b)$$

with convective charge density  $\rho_{\text{conv}}$ , polarization  $\mathbf{P}$ , magnetization  $\mathbf{M}$  and external current  $\mathbf{j}_{\text{ext}}$ . Here, we are interested in the *static limit with no external sources* such that  $\mathbf{j}_{\text{tot}}$  in Equation (3.1a) becomes

$$\mathbf{j}(\mathbf{r}) = \mathbf{j}_{\text{orb}}(\mathbf{r}) + \nabla \times \mathbf{M}(\mathbf{r}). \quad (3.5)$$

Motivated by Equation (3.1d), we now make an ansatz for the magnetic field  $\mathbf{B}(\mathbf{r}) = \nabla \times \mathbf{A}(\mathbf{r})$  in terms of a vector gauge field  $\mathbf{A}(\mathbf{r})$ . By inserting into Equation (3.1a), we readily find<sup>5</sup>

$$\nabla^2 \mathbf{A}(\mathbf{r}) = -4\pi \mathbf{j}(\mathbf{r}) \quad (3.6)$$

in the so-called Coulomb gauge  $\nabla \cdot \mathbf{A}(\mathbf{r}) = 0$ . This is the *vector Poisson equation* that shall be solved in this section. Here, we merely sketch the main steps, while for details on solving Equation (3.6) we refer the reader to Appendix B.

First, the homogeneous vector Poisson equation is solved by rewriting the problem in terms of spherical components and performing a separation in radial and spherical variables for each component of the vector gauge field. Note that,  $\mathbf{A}(\mathbf{r})$  is a vector and, thus, it is a rank 1 tensor with three components. Each component is found to have a spherical dependence given in terms of spherical harmonics  $Y_{lm}(\Omega)$ . We then formally couple the spherical harmonics—that describe the spherical dependence of each spherical component of the vector gauge field—with the spherical unit vector, that describes the three degrees of freedom of coordinate space. This yields a general form of the vector gauge field in terms of so-called *vector spherical harmonics*. The latter are defined as

$$\mathbf{Y}_{pq}^{l1}(\Omega) = \sum_{m=-l}^l \sum_{m'=-1}^1 \langle lm1m'|pq \rangle Y_{lm}(\Omega) \mathbf{e}_{1m'}, \quad (3.7)$$

$$l^2 \mathbf{Y}_{pq}^{l1}(\Omega) = l(l+1) \mathbf{Y}_{pq}^{l1}(\Omega). \quad (3.8)$$

<sup>4</sup>For instance, for a Dirac spinor  $\Psi$  as introduced in Section A.2, the convective contributions read

$$\rho_{\text{conv}} = \mu_B \left[ \bar{\Psi} \frac{\partial \Psi}{\partial t} - \left( \frac{\partial \bar{\Psi}}{\partial t} \right) \Psi \right] + \frac{e^2 \phi}{m} \bar{\Psi} \Psi, \quad (3.2)$$

and

$$\mathbf{j}_{\text{orb}} = i \mu_B \left[ \bar{\Psi} \nabla \Psi - (\nabla \bar{\Psi}) \Psi \right], \quad \mathbf{j}_{\text{ext}} = \frac{e^2 \mathbf{A}}{m} \bar{\Psi} \Psi. \quad (3.3)$$

<sup>5</sup> $\nabla \times \nabla \times \mathbf{A} = \epsilon_{ijk} \partial_j \epsilon_{klm} \partial_l A_m = (\delta_{il} \delta_{jm} - \delta_{im} \delta_{jl}) \partial_j \partial_l A_m = \nabla(\nabla \cdot \mathbf{A}) - \nabla^2 \mathbf{A}$

Here,  $Y_{lm}(\Omega)$  are spherical harmonics and  $\mathbf{e}_{1m'}$  are spherical unit vectors, which are coupled to each other via the *Clebsch–Gordon coefficient*  $\langle lm1m'|pq \rangle$  [154]. Note that, by construction the *angular momentum quantum number*  $l = p - 1, p, p + 1$ , as  $p$  is the “total angular momentum” resulting from coupling the rank 1 tensor  $\mathbf{e}_{1m'}$  and the eigenstate of the angular momentum operator  $\mathbf{l}$ . The Coulomb gauge acts as an additional constraint on the form of the general solution  $\mathbf{A}(\mathbf{r})$ , and contributions  $l = p - 1$  are found to always vanish in this gauge. The vector gauge field takes on the following general form<sup>6</sup>:

$$\mathbf{A}(\mathbf{r}) = \sum_{p=1}^{\infty} \sum_{q=-p}^p \left[ M_{pq}^{p1} \frac{1}{r^{p+1}} \mathbf{Y}_{pq}^{p1}(\Omega) + T_{pq}^{p+1,1} \frac{1}{r^{p+2}} \mathbf{Y}_{pq}^{p+1,1}(\Omega) \right]. \quad (3.9)$$

Here,  $M_{pq}^{p1}$  are *magnetic* (M) multipole coefficients,  $T_{pq}^{p+1,1}$  are *magnetic toroidal* (MT) multipole coefficients. Physically, both, M and MT, multipole moments are magnetic, i.e., as we will see momentarily they have a time-reversal odd behaviour  $\mathcal{T} = -1$ . However, they are fundamentally distinct in the sense that at expansion order  $p$ , the M multipole has a parity  $\mathcal{P} = (-1)^{p+1}$  as can be seen from Equation (3.7), while the MT multipole has a parity  $\mathcal{P} = (-1)^{p+2}$  or equally  $(-1)^p$ . The significance of such MT multipoles is a matter of continued discussion [155]. Let us point out here, that the observable magnetic field is expressed in terms of M multipoles only, because  $\nabla \times \frac{1}{r^{p+2}} \mathbf{Y}_{pq}^{p+1,1}(\Omega) \equiv 0$ . The *magnetic field*  $\mathbf{B}(\mathbf{r}) = \nabla \times \mathbf{A}(\mathbf{r})$  generally reads

$$\mathbf{B}(\mathbf{r}) = -i \sum_{p=0}^{\infty} \sum_{q=-p}^p \sqrt{p(2p+1)} M_{pq}^{p1} \frac{1}{r^{p+2}} \mathbf{Y}_{pq}^{p+1,1}(\Omega). \quad (3.10)$$

An equivalent expression is given in Ref. [155]. Consequently, we want to broach that any magnetic density  $\mathbf{M}(\mathbf{r})$  that causes the emergence of a surrounding magnetic field carries an M multipole moment  $M_{pq}^{p1}$ .

More insight can be gained by determining explicit expressions for the M multipole coefficients  $M_{pq}^{p1}$  and the MT multipole coefficients  $T_{pq}^{p+1,1}$ . To this end, the Green’s function method and an appropriate ansatz is employed, as discussed in Section B.3. Let us highlight some intricacies of the derivation: Due to the general orthogonality relation for vector spherical harmonics the problem immediately falls apart into M multipole and MT multipole solutions. The Green’s function method yields a simple result for both types of multipoles, that reads

$$M_{pq}^{p1} = \frac{4\pi}{2p+1} \int d^3\mathbf{r} r^p \mathbf{Y}_{pq}^{*p1}(\Omega) \cdot \mathbf{j}(\mathbf{r}), \quad (3.11)$$

$$T_{pq}^{p+1,1} = \frac{4\pi}{2p+3} \int d^3\mathbf{r} r^{p+1} \mathbf{Y}_{pq}^{*p+1,1}(\Omega) \cdot \mathbf{j}(\mathbf{r}), \quad (3.12)$$

where  $\mathbf{j}(\mathbf{r})$  is given by Equation (3.5).

In principle, there is no need to further rewrite these expressions, however in practice it is useful to arrive at a formulation where the fundamental source of magnetization, i.e., the spin and

---

<sup>6</sup>See Appendix B.

angular momentum, are the source of the multipoles. A lengthy exercise of algebra and partial integration—that can be found in Section B.3—leads to the following expressions

$$M_{pq}^{p1} = -\frac{4\pi i}{2p+1} \int d^3\mathbf{r} \nabla (r^p Y_{pq}^*(\Omega)) \cdot \left[ \frac{\mathbf{r} \times \mathbf{j}_{\text{orb}}(\mathbf{r})}{\sqrt{p(p+1)}} + \sqrt{\frac{p+1}{p}} \mathbf{M}(\mathbf{r}) \right], \quad (3.13)$$

and

$$T_{pq}^{p+1,1} = \frac{-4\pi}{\sqrt{(p+1)(2p+1)}} \int d^3\mathbf{r} \nabla (r^p Y_{pq}^*(\Omega)) \cdot \left[ \mathbf{r} \times \frac{\mathbf{j}_{\text{orb}}(\mathbf{r})}{p+2} + \mathbf{r} \times \mathbf{M}(\mathbf{r}) \right]. \quad (3.14)$$

The first terms in brackets, that is in terms of the orbital current  $\mathbf{j}_{\text{orb}}(\mathbf{r})$ , in Equation (3.13) and Equation (3.14), are used to describe convective contributions. For instance, one should avoid only considering the magnetic dipole<sup>7</sup> arising due to the orbital angular momentum operator  $\hat{\mathbf{l}}$  acting on the  $i$ th electron at position  $\mathbf{r}_i$  and instead use the definition of the convective current operator<sup>8</sup>, which yields

$$\mathbf{r} \times \hat{\mathbf{j}}_{\text{orb}}(\mathbf{r}) = -\mu_B \sum_{i=1}^N [\mathbf{l}\delta(\mathbf{r} - \mathbf{r}_i) + \delta(\mathbf{r} - \mathbf{r}_i)\mathbf{l}]. \quad (3.15)$$

The second terms in brackets, on the other hand, that is in terms of magnetization  $\mathbf{M}(\mathbf{r})$ , in Equation (3.13) and Equation (3.14), are useful to describe fields arising from bound currents  $\mathbf{j}_m(\mathbf{r}) = \nabla \times \mathbf{M}(\mathbf{r})$ . For instance, a set of magnetic dipoles distributed in space or a set of  $N$  intrinsic magnetic moments due to the electronic spin give rise to the spin-magnetization  $\mathbf{M}(\mathbf{r}) = \mathbf{m}^{(s)}(\mathbf{r})$  defined in Equation (2.32). We recall that the spin-magnetization operator is defined as given in Equation (2.34), i.e.

$$\hat{\mathbf{m}}^{(s)}(\mathbf{r}) = -\mu_B \sum_{i=1}^N \delta(\mathbf{r} - \mathbf{r}_i) \boldsymbol{\sigma}.$$

Combining the last two equations with Equation (3.13) and Equation (3.14), we can write the quantum mechanical M multipole operator  $\hat{M}_{pq}^{p1}$  and the MT multipole operator  $\hat{T}_{pq}^{p+1,1}$  for an electron cloud as

$$\hat{M}_{pq}^{p1} = \frac{4\pi i \mu_B}{2p+1} \sqrt{\frac{p+1}{p}} \int d^3\mathbf{r} \nabla (r^p Y_{pq}^*(\Omega)) \cdot \sum_{i=1}^N \left[ \frac{[\mathbf{l}\delta(\mathbf{r} - \mathbf{r}_i) + \delta(\mathbf{r} - \mathbf{r}_i)\mathbf{l}]}{p+1} + \delta(\mathbf{r} - \mathbf{r}_i) \boldsymbol{\sigma} \right], \quad (3.16)$$

$$\hat{T}_{pq}^{p+1,1} = \frac{4\pi \mu_B}{\sqrt{(p+1)(2p+1)}} \int d^3\mathbf{r} \nabla (r^p Y_{pq}^*(\Omega)) \cdot \sum_{i=1}^N \left[ \mathbf{r} \times \frac{[\mathbf{l}\delta(\mathbf{r} - \mathbf{r}_i) + \delta(\mathbf{r} - \mathbf{r}_i)\mathbf{l}]}{p+2} + \mathbf{r} \times \delta(\mathbf{r} - \mathbf{r}_i) \boldsymbol{\sigma} \right]. \quad (3.17)$$

<sup>7</sup>Note that  $\mathbf{M}_l(\mathbf{r}) = -\mu_B \mathbf{L}(\mathbf{r})$  with  $\mathbf{L}(\mathbf{r}) = \frac{1}{2} \text{Tr} \left\{ \sum_{i=1}^N [\hat{\mathbf{l}}\delta^{(3)}(\mathbf{r} - \mathbf{r}_i) + \delta^{(3)}(\mathbf{r} - \mathbf{r}_i)\hat{\mathbf{l}}] \right\}$  would neglect higher order multipoles arising from the orbital angular momentum.

<sup>8</sup>See Section A.2 and Section B.5.

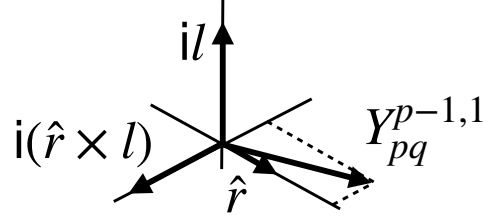


Figure 3.2: Schematic view of the direction of  $\mathbf{Y}_{pq}^{p-1,1}$  in the space spanned by  $\hat{\mathbf{r}} = \mathbf{r}/r$ ,  $i\mathbf{l} = \mathbf{r} \times$  and  $i(\hat{\mathbf{r}} \times \mathbf{l})$ . Inspired by Fig. A 1 in Ref. [140].

Here, the only reason we refrain from integrating over  $d^3\mathbf{r}$  by making use of the delta function to evaluate the integral kernel at  $\mathbf{r}_i$  is that  $\nabla(r^p Y_{pq}^*(\Omega))$  contains an operator that has not been applied, though this step can be explicitly done in practice without hesitation. On a different note, this is a good opportunity to check our claim that  $\hat{M}_{pq}^{p1}$  and  $\hat{T}_{pq}^{p+1,1}$  are time-reversal odd. We recall that, the spin magnetization and the orbital angular momentum are time-reversal odd and, thus, Equations (3.16) and (3.17) are too. Analogous expressions have been first derived by H. Kusunose and S. Hayami [59, 140].

Let us further emphasize that  $\nabla(r^p Y_{pq}^*(\Omega))$  is a vector, which is directly connected to a vector spherical harmonic. It is instructive to consider the direction of this vector spherical harmonic in coordinate space. To this end, we recall the following relations

$$\nabla(r^p Y_{pq}) = \sqrt{p(2p+1)} r^{p-1} \mathbf{Y}_{pq}^{p-1,1}, \quad (3.18)$$

$$\mathbf{Y}_{pq}^{p-1,1}(\Omega) = \frac{1}{\sqrt{p(2p+1)}} (p\hat{\mathbf{r}} - i\hat{\mathbf{r}} \times \mathbf{l}) Y_{p,q}(\Omega), \quad (3.19)$$

where  $\hat{\mathbf{r}} = \mathbf{r}/r$ . The direction, which is schematically shown in Figure 3.2, hence depends on the expansion order  $p$ . Based on that, it is possible to carefully construct an MT density  $\mathbf{M}^{MT}(\mathbf{r}; p, p')$  for given expansion orders  $p$  and  $p'$  that satisfy the following MT conditions

$$\mathbf{Y}_{pq}^{p-1,1}(\Omega) \cdot \mathbf{M}^{MT}(\mathbf{r}; p, p') = 0, \quad (3.20a)$$

$$\mathbf{Y}_{p'q'}^{p'-1,1}(\Omega) \cdot (\mathbf{r} \times \mathbf{M}^{MT}(\mathbf{r}; p, p')) \neq 0, \quad (3.20b)$$

such that the bound M multipole moment in Equation (3.13) at  $p$  vanishes, but the bound MT moments in Equation (3.14) at  $p'$  is finite. This is an intriguing observation, because it grants access to the manipulation of  $\mathbf{A}(\mathbf{r})$  by means of a magnetic configuration with concomitant stray fields with minimal coupling to the surrounding. An article by N. Papasimakis *et al.* [150] discusses the toroidal excitations on a rudimentary level and draws a picture of a new field in its infancy. Applications might be found in combination with the Aharonov–Bohm effect [156] in the field of spintronics [3] and skyrmion dynamics [157, 158].



Let us emphasize that the direction of  $\nabla (r^p Y_{pq}^*(\Omega))$  depends on the order  $p$ , as can be readily seen from Equation (3.19). Hence, the *MT condition* given in Equation (3.20) can only be satisfied for specified orders  $p$  and  $p'$ . In other words, every magnetic toroidal multipole moment has a corresponding finite M multipole moment at some expansion order. Consequently, it is not possible to define a magnetic density, whose gauge vector field consists of only MT moments, although it is possible to carefully choose at which expansion order M multipoles appear. This can be exploited in connection with the discussion of the shape of the linear response tensor by W. Kleiner, M. Seemann and coworkers [5, 6, 43, 159].

A pure M multipole moment, on the other hand, can be easily constructed, invoking

$$\mathbf{r} \times \mathbf{M}^M(\mathbf{r}) = \mathbf{0}. \quad (3.21)$$

Here,  $\mathbf{M}^M(\mathbf{r})$  is the magnetic density corresponding to a pure magnetic multipole with no toroidal contribution at any order in the vector gauge field.

In the scope of this thesis, we are interested in constructing all possible magnetic structures, which can be expressed in terms of  $\mathbf{M}(\mathbf{r})$ . In general, it is true that M multipole gauge fields  $\mathbf{A}^M$  and MT multipole gauge fields  $\mathbf{A}^{MT}$  are orthogonal to each other by construction:

$$\mathbf{A}^M \perp \mathbf{A}^{MT}, \quad (3.22)$$

with

$$\mathbf{A}^M = \sum_{p=0}^{\infty} \sum_{q=-p}^p M_{pq}^{p1} \frac{1}{r^{p+1}} \mathbf{Y}_{pq}^{p1}(\Omega), \quad (3.23)$$

$$\mathbf{A}^{MT} = \sum_{p=0}^{\infty} \sum_{q=-p}^p T_{pq}^{p+1,1} \frac{1}{r^{p+2}} \mathbf{Y}_{pq}^{p+1,1}(\Omega). \quad (3.24)$$

This is a result of the orthogonality of vector spherical harmonics, which reads

$$\int d\Omega \mathbf{Y}_{PQ}^{*L1}(\Omega) \cdot \mathbf{Y}_{pq}^{L1}(\Omega) = \delta_{Ll} \delta_{Pp} \delta_{Qq}. \quad (3.25)$$

Yet,  $\mathbf{A}^M$  and  $\mathbf{A}^{MT}$  have different sources as seen in Equation (3.13) and Equation (3.14). The magnetic structures associated to these sources, i.e., the magnetic structures giving rise to M multipoles  $\mathbf{M}^M$  and MT multipoles  $\mathbf{M}^{MT}$ , are NOT generally orthogonal to each other:

$$\mathbf{M}^M \not\perp \mathbf{M}^{MT}. \quad (3.26)$$

One might therefore choose to construct a basis for magnetic configurations either by expanding in magnetic multipoles *or* in magnetic toroidal multipoles<sup>9</sup>. We recall that, it is possible to construct

---

<sup>9</sup>With this the present thesis follows a different approach than the pioneering work by M.-T. Suzuki *et al.* in Ref. [48].

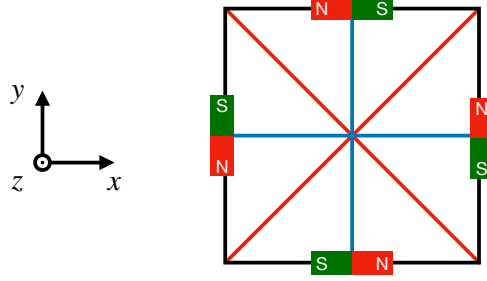


Figure 3.3: The magnetic density  $\mathbf{M}^{\text{cl}}$  given in Equation (3.27) composed of four magnets pointing counterclockwise with their north pole. The red and blue axis are symmetry axis, when reflection is followed by time reversal operation.

magnetic densities, which completely lack MT coefficients, hence we should not construct magnetic densities based on MT sources. In order to avoid a blind spot, we believe it is better to create all possible magnetic densities based on the M multipole expansion. In the next section, we will solve a toy model, which is meant to build intuition before constructing the so-called cluster multipole expansion for magnetic structures.

### 3.2 Example of four bar magnets

As a little warm up exercise, let us consider four bar magnets arranged in the  $xy$ -plane such that they obey the point group  $C_4$ . As shown in Figure 3.3, the northpole of each magnet points counterclockwise. Applying the time-reversal operation flips all magnets and reflection at any of the four planes also flips all magnets. Hence, this system has  $\mathcal{T} = -1$  and  $\mathcal{P} = -1$ .

Let us compute the vector gauge field  $\mathbf{A}(\mathbf{r})$  and the magnetic field  $\mathbf{B}(\mathbf{r})$  surrounding this configuration of magnets. To this end, we determine the M multipole coefficients and the MT multipole coefficients devising Equation (3.13) and Equation (3.14). The proposed arrangement of bar magnets can be expressed by the following magnetization density:

$$\mathbf{M}^{\text{b}}(\mathbf{r}) = \sum_{i=1}^4 \mathbf{m}_i \delta^{(3)}(\mathbf{r} - \hat{\mathbf{r}}_i), \quad (3.27\text{a})$$

$$\mathbf{m}_i = (\hat{\mathbf{r}}_i \times \hat{\mathbf{z}}) \mu_{\text{B}}, \quad (3.27\text{b})$$

$$\hat{\mathbf{r}}_1 = -\hat{\mathbf{r}}_3 = (1, 0, 0)^T, \quad (3.27\text{c})$$

$$\hat{\mathbf{r}}_2 = -\hat{\mathbf{r}}_4 = (0, 1, 0)^T. \quad (3.27\text{d})$$

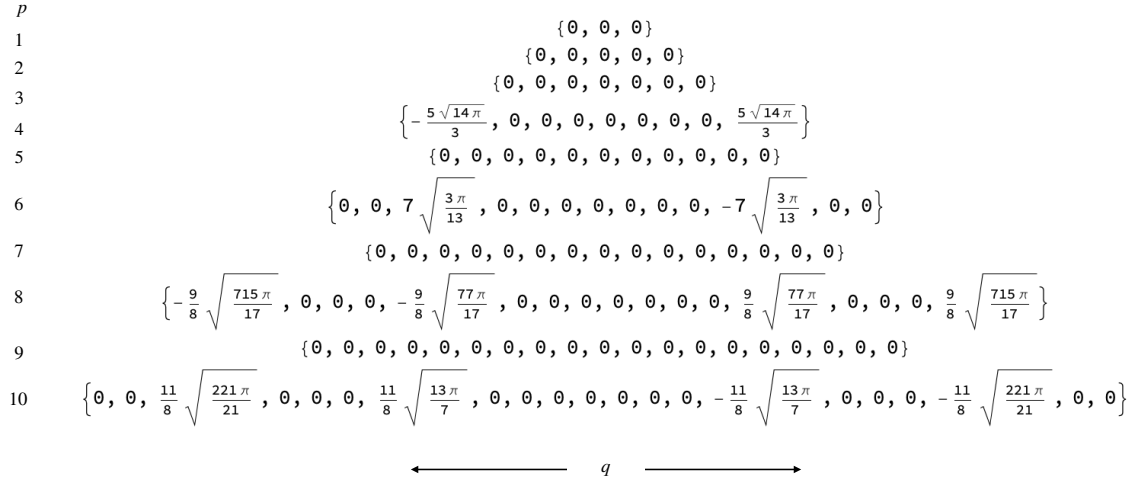


Figure 3.4: Quantitative solution of Equation (3.28) corresponding to the magnetic multipole coefficients for the arrangement shown in Figure 3.3.

We compute the coefficients

$$M_{pq}^{p1} = -\frac{4\pi i}{2p+1} \sqrt{\frac{p+1}{p}} \int d^3\mathbf{r} \nabla (r^p Y_{pq}^*(\Omega)) \cdot \mathbf{M}^b(\mathbf{r}), \quad (3.28)$$

$$T_{pq}^{p+1,1} = \frac{-4\pi}{\sqrt{(p+1)(2p+1)}} \int d^3\mathbf{r} \nabla (r^p Y_{pq}^*(\Omega)) \cdot (\mathbf{r} \times \mathbf{M}^b(\mathbf{r})) \quad (3.29)$$

using for instance **Mathematica** [151]. The lowest order  $M$  multipole coefficients, that are nonzero, are obtained for the tuples  $(p, q) = (4, 4)$  and  $(4, -4)$ :

$$M_{44}^{41} = -M_{4,-4}^{41} = -\frac{5}{3} \sqrt{14\pi}. \quad (3.30)$$

Higher orders appear systematically, in analogy to higher order harmonics in a Fourier analysis of a discrete function, see Figure 3.4.

The magnetic field up to corrections  $\mathcal{O}(1/r^8)$  is obtained using Equation (3.10) and Equation (3.30):

$$\mathbf{B}(\mathbf{r}) = -i6 \frac{M_{44}^{41}}{r^6} [\mathbf{Y}_{44}^{51}(\Omega) - \mathbf{Y}_{4,-4}^{51}(\Omega)] + \mathcal{O}(1/r^8) \quad (3.31a)$$

$$= -20\sqrt{7}\pi \frac{1}{r^6} \underbrace{\frac{i}{\sqrt{2}} [\mathbf{Y}_{44}^{51}(\Omega) - \mathbf{Y}_{4,4}^{51*}(\Omega)]}_{\in \mathbb{R}} + \mathcal{O}(1/r^8). \quad (3.31b)$$

Here, we used that the complex conjugate of a vector spherical harmonic is given by

$$[\mathbf{Y}_{pq}^{l1}(\Omega)]^* = (-1)^{p+q+l+1} \mathbf{Y}_{p-q}^{l1}(\Omega). \quad (3.32)$$

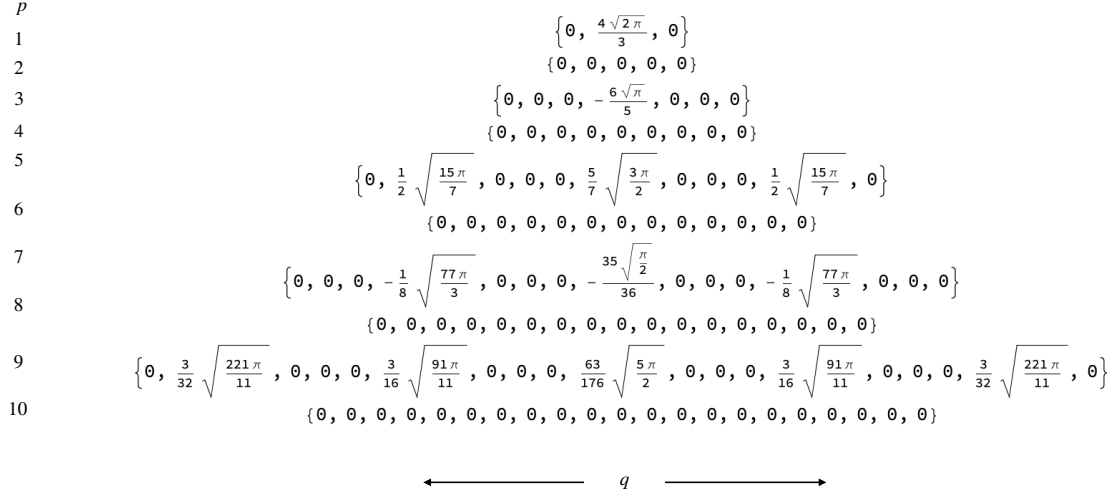


Figure 3.5: Quantitative solution of Equation (3.29) corresponding to the magnetic toroidal multipole coefficients for the arrangement shown in Figure 3.3.

Therefore, the magnetic field in Equation (3.31) is indeed real. Next, let us compute the leading order MT multipole coefficient. The reader might have guessed that this arrangement of magnets yields an MT contribution for  $p = 1$ . It renders as

$$T_{10}^{21} = \frac{4}{3}\sqrt{2\pi}. \quad (3.33)$$

Again, there are higher order harmonics of this MT multipole coefficient up to infinite order, as shown in Figure 3.5.

In summary, the vector gauge field of the configuration of magnets shown in Figure 3.3 is given by

$$\mathbf{A}(\mathbf{r}) = \mathbf{A}^M(\mathbf{r}) + \mathbf{A}^{MT}(\mathbf{r}), \quad (3.34a)$$

$$\mathbf{A}^M(\mathbf{r}) = M_{44}^{41} \frac{1}{r^5} [\mathbf{Y}_{44}^{41}(\Omega) + \mathbf{Y}_{44}^{41*}(\Omega)] + \mathcal{O}(1/r^7) \quad (3.34b)$$

$$\mathbf{A}^{MT}(\mathbf{r}) = T_{10}^{21} \frac{1}{r^3} \mathbf{Y}_{10}^{21}(\Omega) + T_{30}^{41} \frac{1}{r^5} \mathbf{Y}_{30}^{41}(\Omega) + \mathcal{O}(1/r^7). \quad (3.34c)$$

It is thus dominated by its MT contribution. The leading order multipole gauge field and magnetic field is shown in Figure 3.6. In particular, Figure 3.6 (a) shows the magnetic hexadecapole gauge field corresponding to  $p = 4$  in Equation (3.34b). We see that  $\mathbf{A}^M$  points in  $z$ -direction and is the vector analog of the real spherical harmonic  $Y_{lm}^s$  with  $l = 4$  and  $m = 4$  of Equation (3.38), which is shown in Figure 3.7 (a). In other words, Figure 3.7 (a) presents the  $g_{xy(x^2-y^2)}$ -orbital. The scalar analogs of higher order contributions that can be extracted from Figure 3.4 are shown in Figure 3.7 (b)-(d).

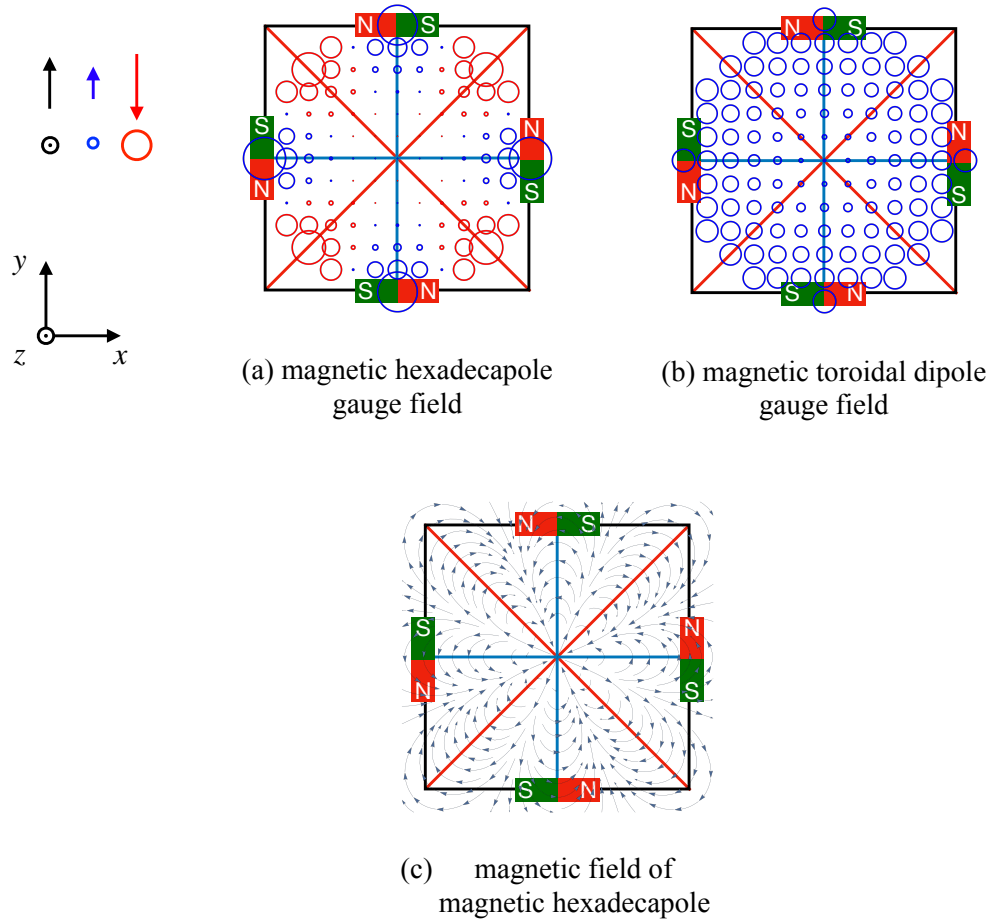


Figure 3.6: The leading order fields emerging from the arrangement of four bar magnets. (a) Magnetic hexagonal gauge field given in Equation (3.34b), (b) magnetic toroidal dipole gauge field given by the first term in Equation (3.34c), and (c) Magnetic field of a magnetic hexadecapole given in Equation (3.31).

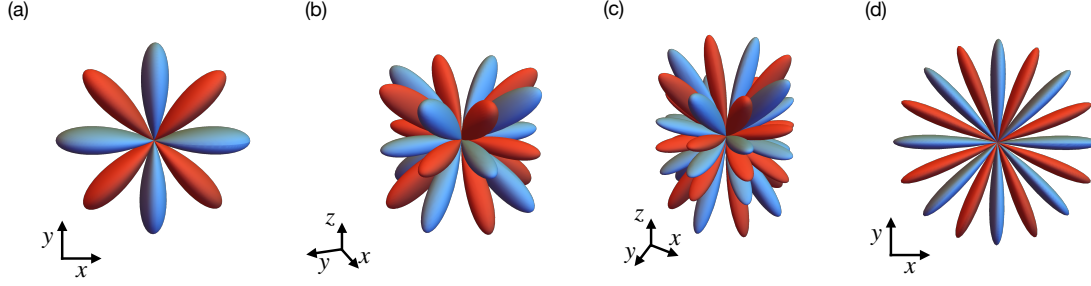


Figure 3.7: Real harmonics defined by Equation (3.38), that are related to the non-zero multipole coefficients in Figure 3.4. (a)  $g_{xy(x^2-y^2)}$ -orbital with  $l = 4$   $m = 4$ , (b)  $l = 6$   $m = 4$ , (c)  $l = 8$   $m = 4$ , and (d)  $l = 8$   $m = 8$ . Visualized using Mathematica [151].

The MT dipole gauge field in Equation (3.34c) also points in  $z$ -direction, yet integrated over all angles it is orthogonal to the M multipole as expected. As already mentioned in the paragraph below Equation (3.44), the symmetry properties for M multipoles are given by

$$\mathcal{T} = -1, \quad \mathcal{P} = (-1)^{p+1}, \quad (3.35)$$

while the symmetry properties for MT multipole moments are given by

$$\mathcal{T} = -1, \quad \mathcal{P} = (-1)^p. \quad (3.36)$$

Hence, due to the parity of the arrangement of magnets, only every second order of multipoles is allowed to be nonzero. Consequently, the correction terms in Equation (3.34) are one order higher than one might naively expect. We note that the calculated leading order  $p = 4$  and 1 for M and MT multipole gauge field, respectively, agree with the observation we made when explicitly applying time-reversal and parity transformation to Figure 3.3 at the beginning of this section.

Let us highlight that, clearly, the same magnetic configuration gives rise to both magnetic multipoles and magnetic toroidal multipoles. This illustrates the argument we gave in the end of the previous section about why we focus on the magnetic multipole moments and neglect the magnetic toroidal moments in the cluster multipole expansion, which will be the focus of the succeeding section. Furthermore, this example illustrated that very specific linear combinations of spherical harmonics appear in the expansion of the vector gauge field. In the subsequent section, we will continue by generalizing this idea.

### 3.3 Cluster multipole expansion

In Section 3.1, we have derived the explicit form of magnetic (M) and magnetic toroidal (MT) multipoles and applied it to an electron cloud. In the previous section, we have applied the multipole theory to a discrete system of four bar magnets as a little warm up exercise. In the present section,

we want to apply multipole theory to real materials and, hence, our main focus is the point group symmetry of the underlying crystal.

### 3.3.1 Point group harmonics

A *point group* is a group of symmetry operations that leave a finite object invariant. The elements are confined to rotations and their combinations with inversion about a fixed point of that object [160]. There are 32 crystallographic point groups, which all derive from the cubic ( $O_h$ ) or hexagonal ( $D_{6h}$ ) point group.

*Point group harmonics* [161] are linear combinations of spherical harmonics that are invariant under the action of elements of a given point group:

$$\mathcal{Y}_{p\Gamma\gamma}(\Omega) = \sum_{q=-p}^p c_{pq}^{(\Gamma\gamma)} Y_{pq}(\Omega) \quad (3.37)$$

The determination of these linear combinations, i.e. the coefficients  $c_{lm}^{(\Gamma\gamma)}$ , can be derived systematically from the reduction of all irreducible representations (irrep's) of the rotation group  $O(3)$ . Depending on the dimension of the irrep  $\Gamma$ , there are correspondingly many point group harmonics—also referred to as basis functions or components—that are labeled by  $\gamma$  in Equation (3.37).

Commonly, one distinguishes *cubic harmonics* and *hexagonal harmonics*, that are invariant under  $O_h$  and  $D_{6h}$ , respectively. Note that neither of them are exactly equivalent to the well-known *real harmonics*, which read

$$Y_{lm}^{(c)}(\Omega) = \frac{1}{\sqrt{2}} (Y_{l-m}(\Omega) + (-1)^m Y_{lm}(\Omega)) = \sqrt{2}(-1)^m \text{Re} [Y_{lm}(\Omega)] \quad (3.38a)$$

$$Y_{lm}^{(s)}(\Omega) = \frac{i}{\sqrt{2}} (Y_{l-m}(\Omega) - (-1)^m Y_{lm}(\Omega)) = \sqrt{2}(-1)^m \text{Im} [Y_{lm}(\Omega)], \quad (3.38b)$$

with  $m > 0$  in the Condon–Shortley phase convention. Instead, they are often defined as a linear combinations of real harmonics, though being real is not a necessary condition for point group harmonics. Another crucially different property of point group harmonics compared to real harmonics is their behaviour in a sum of products [140]

$$\sum_{m=-l}^l Y_{lm}(\Omega) Y_{lm}^*(\Omega) = \sum_{m=1}^l \left[ Y_{lm}^{(c)}(\Omega) Y_{lm}^{(c)*}(\Omega) + Y_{lm}^{(s)}(\Omega) Y_{lm}^{(s)*}(\Omega) \right] + Y_{l0}(\Omega) Y_{l0}^*(\Omega) \quad (3.39)$$

$$\sum_{q=-p}^p Y_{pq}(\Omega) Y_{pq}^*(\Omega) \xrightarrow{O(3) \rightarrow \text{point group}} \sum_{\Gamma\gamma} \mathcal{Y}_{p\Gamma\gamma}(\Omega) \mathcal{Y}_{p\Gamma\gamma}^*(\Omega) \quad (3.40)$$

In 1929, H. Bethe [162] published a method to deduce cubic harmonics and a table up to order  $p = 4$ . Since then, many iterative methods have been proposed and tables published [161, 163–171]. For a recent version—in direct connection with the multipole formalism discussed in this thesis—see Table 1 and 2 for cubic harmonics and Table 12 and 13 for hexagonal harmonics in Ref. [155] by

order	irrep	$\gamma$	definition	linear combination
1	$T_{1u}$	1	$x$	(11)
		2	$y$	(11)'
		3	$z$	(10)
2	$E_g$	1	$\frac{1}{2}(3z^2 - r^2)$	(20)
		2	$\frac{\sqrt{3}}{2}(x^2 - y^2)$	(22)
	$T_{2g}$	1	$\sqrt{3}yz$	(21)'
		2	$\sqrt{3}zx$	(21)
		3	$\sqrt{3}xy$	(22)'
3	$A_{2u}$	1	$\sqrt{15}xyz$	(32)'
	$T_{1u}$	1	$\frac{1}{2}x(5x^2 - 3r^2)$	$\frac{1}{2\sqrt{2}} [\sqrt{5}(33) - \sqrt{3}(31)]$
		2	$\frac{1}{2}y(5y^2 - 3r^2)$	$-\frac{1}{2\sqrt{2}} [\sqrt{5}(33)' - \sqrt{3}(31)']$
		3	$\frac{1}{2}z(5z^2 - 3r^2)$	(30)
	$T_{2u}$	1	$\frac{\sqrt{15}}{2}x(5y^2 - z^2)$	$-\frac{1}{2\sqrt{2}} [\sqrt{3}(33) + \sqrt{5}(31)]$
		2	$\frac{1}{2}y(5z^2 - x^2)$	$-\frac{1}{2\sqrt{2}} [-\sqrt{3}(33)' - \sqrt{5}(31)']$
		3	$\frac{\sqrt{15}}{2}z(x^2 - y^2)$	(32)

Table 3.1: Cubic harmonics sorted by expansion order and irreducible representation (irrep) with components ( $\gamma$ ).  $(lm)$  and  $(lm)'$  correspond to real harmonics  $Y_{lm}^{(c)}$  and  $Y_{lm}^{(s)}$  given in Equation (3.38). See Ref. [155] for higher orders.



S. Hayami and coworker. In Table 3.1 we provide the first three orders of the cubic harmonics for the reader's convenience and better understanding without immediately referring to Ref. [155].

Finally, we can make liberal use of Equation (3.40) in all expressions we have derived thus far, because the point group harmonics are defined to be complete and orthogonal:

$$\sum_{p=1}^{\infty} \sum_{\Gamma\gamma} \mathcal{Y}_{p\Gamma\gamma}(\Omega) \mathcal{Y}_{p\Gamma\gamma}^*(\Omega') = \delta(\Omega - \Omega') \quad (3.41)$$

$$\int d\Omega \mathcal{Y}_{p\Gamma\gamma}(\Omega) \mathcal{Y}_{p'\Gamma'\gamma'}^*(\Omega) = \delta_{pp'} \delta_{\Gamma\Gamma'} \delta_{\gamma\gamma'}, \quad (3.42)$$

for all expansion orders  $p$ , irreducible representations  $\Gamma$  and components  $\gamma$ .

### 3.3.2 Multipole expansion on a point form

According to the International Tables for Crystallography [172] a *point form* is a set of all symmetrically equivalent points for a given point group. All possible point forms for a given point group are classified into *Wyckoff positions* of point forms. This name has been chosen in analogy to the Wyckoff positions of space groups. The *multiplicity* is the number of points in a point form. For a *general* point form, the multiplicity is equal to the order of the point group. For *special* point forms, on the other hand, the multiplicity is lower than the order of the point group.

A crystal may contain multiple inequivalent sites and thus multiple point forms. In the following we will define a *magnetic cluster* to be a magnetic site on a point form. We can write a general magnetization density of a magnetic cluster as

$$\mathbf{M}(\mathbf{r}) = \sum_{i=1}^N \mathbf{m}_i \delta^{(3)}(\mathbf{r} - \mathbf{r}_i), \quad (3.43)$$

where  $\mathbf{m}_i$  is the on-site magnetic dipole moment at position  $\mathbf{r}_i$ . The sum goes over all points of a magnetic site in a point form—or in other words over all points in the magnetic cluster—where  $N$  is the multiplicity.

The gauge field can now be written as

$$\mathbf{A}(\mathbf{r}) = \sum_{p=0}^{\infty} \sum_{\Gamma\gamma} \left[ M_{p\Gamma\gamma}^{p1} \frac{1}{r^{p+1}} \mathcal{Y}_{p\Gamma\gamma}^{p1}(\Omega) + T_{p\Gamma\gamma}^{p+1,1} \frac{1}{r^{p+2}} \mathcal{Y}_{p\Gamma\gamma}^{p+1,1}(\Omega) \right]. \quad (3.44)$$

Here, we introduced vector point group harmonics in analogy to vector spherical harmonics and the point group magnetic multipole moment  $M_{p\Gamma\gamma}^{p1}$  and the point group MT multipole moment  $T_{p\Gamma\gamma}^{p+1,1}$ . These can be explicitly computed by means of

$$M_{p\Gamma\gamma}^{p1} = \frac{4\pi}{2p+1} \sqrt{\frac{p+1}{p}} \int d^3\mathbf{r} \sum_{i=1}^N \nabla \cdot (r^p \mathcal{Y}_{p\Gamma\gamma}(\Omega)) \cdot \mathbf{m}_i \delta^{(3)}(\mathbf{r} - \mathbf{r}_i), \quad (3.45a)$$

$$T_{p\Gamma\gamma}^{p+1,1} = \frac{4\pi}{\sqrt{(p+1)(2p+1)}} \int d^3\mathbf{r} \sum_{i=1}^N \nabla \cdot (r^p \mathcal{Y}_{p\Gamma\gamma}(\Omega)) \cdot (\mathbf{r} \times \mathbf{m}_i) \delta^{(3)}(\mathbf{r} - \mathbf{r}_i). \quad (3.45b)$$

The imaginary unit in the definition of  $M_{p\Gamma\gamma}^{p1}$  is absorbed into the point group harmonics as we saw in the example of four bar magnets in Section 3.2. Furthermore, the point group harmonics are chosen real, such that we can drop the complex conjugation of  $\mathcal{Y}_{p\Gamma\gamma}(\Omega)$ .

It is possible to compute all point group M and MT multipoles for an arbitrary magnetic configuration using Equation (3.45). For notational simplicity, we express the magnetic configuration as a ket-vector

$$|m\rangle = (\mathbf{m}_1, \mathbf{m}_2, \dots, \mathbf{m}_N)^T, \quad (3.46)$$

where  $\mathbf{m}_i$  is the  $i$ th on-site magnetic dipole moment, which is experimentally directly observable by e.g. neutron diffraction and arises due to the spin and/or the angular momentum. Hence, here we take on a simplified view, that ignores higher order magnetic moments and convective effects on the atomic scale. This is because from an experimental viewpoint we cannot measure the spin and orbital contribution to the on-site magnetic dipole moment separately.  $|m\rangle$  defines the magnetic structure well-enough for our purpose, but should *not* be mistaken as a many-body state of  $N$  particles with good quantum number  $\mathbf{m}_i$  or the spin-magnetization  $\mathbf{m}(\mathbf{r})$  as it was introduced in Chapter 2. Instead, the state  $|m\rangle$  lives in the *space of all possible uniform magnetic configurations*.

We can formally span this space of all possible uniform magnetic configurations by means of a *complete set of orthogonal magnetic configurations*:

$$\left\{ |n\rangle = \left( \mathbf{e}_1^{(n)}, \mathbf{e}_2^{(n)}, \dots, \mathbf{e}_N^{(n)} \right)^T \right\}, \quad (3.47a)$$

$$\frac{1}{N} \sum_{n=1}^{3N} |n\rangle \langle n| = \mathbf{1}_{3N \times 3N}, \quad (3.47b)$$

$$\langle n|n'\rangle = \sum_{i=1}^N \mathbf{e}_i^{(n)} \cdot \mathbf{e}_i^{(n')} = N \delta_{nn'}. \quad (3.47c)$$

Here, we define the basis vector  $\mathbf{e}_i^{(n)}$  at position  $\mathbf{r}_i$ . We will refer to this basis as a *cluster multipole (CMP) basis of a single cluster*. In contrast to a traditional multipole expansion, the cluster multipole expansion suspends all higher harmonics. Therefore, the maximum expansion order of the CMP expansion and, thus, the number of elements in the CMP basis is  $3N$ , which corresponds to three rotational degrees of freedom of the on-site magnetic moment on  $N$  points in the point form.

It is now our task to find a suitable choice of  $|n\rangle$  in order to span the space of all possible uniform magnetic configurations. To this end, let us compute the inner product of a CMP basis element and an arbitrary magnetic configuration:

$$\langle n|m\rangle = \sum_{i=1}^N \mathbf{e}_i^{(n)} \cdot \mathbf{m}_i. \quad (3.48)$$

The inner product is defined through Equation (3.47c). Let us compare this expression to a slightly rearranged Equation (3.45a):

$$M_{p\Gamma\gamma}^{p1} = \sum_{i=1}^N \frac{4\pi}{2p+1} \sqrt{\frac{p+1}{p}} \int d^3\mathbf{r} \delta^{(3)}(\mathbf{r} - \mathbf{r}_i) \nabla (r^p \mathcal{Y}_{p\Gamma\gamma}(\Omega)) \cdot \mathbf{m}_i. \quad (3.49)$$

We now identify the projection of a magnetic configuration onto a CMP basis element with the point group M multipole moment  $M_{p\Gamma\gamma}^{p1}$ . However additionally, we want to invoke the normalization we have imposed on the CMP basis in Equation (3.47). Let us introduce a dummy vector  $|u_{p\Gamma\gamma}\rangle$  as a first step. The components of  $|u_{p\Gamma\gamma}\rangle$  are taken from Equation (3.49):

$$|u^{1\Gamma\gamma}\rangle = \left( \mathbf{u}_1^{1\Gamma\gamma}, \mathbf{u}_2^{1\Gamma\gamma}, \dots, \mathbf{u}_N^{1\Gamma\gamma} \right)^T, \quad (3.50)$$

$$\mathbf{u}_i^{p\Gamma\gamma} = \frac{4\pi}{2p+1} \sqrt{\frac{p+1}{p}} \int d^3\mathbf{r} \delta^{(3)}(\mathbf{r} - \mathbf{r}_i) \nabla (r^p \mathcal{Y}_{p\Gamma\gamma}(\Omega)). \quad (3.51)$$

The next step is a Gram–Schmidt orthonormalization of  $|u^{p\Gamma\gamma}\rangle$  starting from the lowest order  $p = 1$ :

$$|v_1^{p\Gamma\gamma}\rangle = \frac{|u^{p\Gamma\gamma}\rangle}{\sqrt{\langle u^{p\Gamma\gamma} | u^{p\Gamma\gamma} \rangle}}, \quad (3.52)$$

$$|w_n^{p\Gamma\gamma}\rangle = |u^{p\Gamma\gamma}\rangle - \sum_{n'=1}^{n-1} \langle v_{n'}^{p\Gamma\gamma} | u^{p\Gamma\gamma} \rangle |v_{n'}^{p\Gamma\gamma}\rangle, \quad (3.53)$$

$$|v_n^{p\Gamma\gamma}\rangle = \frac{|w_n^{p\Gamma\gamma}\rangle}{\sqrt{\langle w_n^{p\Gamma\gamma} | w_n^{p\Gamma\gamma} \rangle}}. \quad (3.54)$$

This orthonormalization procedure yields  $3N$  basis elements  $|v_n^{p\Gamma\gamma}\rangle$  of spanning the space of all possible uniform magnetic configurations. However, we want to avoid the on-site magnetic moment to be smaller with increasing number of magnetic sites. So we invoke Equation (3.47c) to finally obtain

$$|n\rangle = \sqrt{N} |v_n^{p\Gamma\gamma}\rangle. \quad (3.55)$$

This procedure defines the CMP basis for a single point form. This method has been originally proposed by M.-T. Suzuki and coworkers [48, 173]. In the subsequent section, we will extend this idea to multiple point forms.

### 3.3.3 Multipole expansion in real materials

A real material may have multiple inequivalent magnetic sites that form independent clusters  $c_1, c_2, \dots, c_d$ . The space of all possible uniform magnetic configurations is then spanned by the product space of the CMP bases of all contained point forms:

$$\{|n_{c_1}\rangle \otimes |n_{c_2}\rangle \otimes \dots \otimes |n_{c_d}\rangle\}, \quad (3.56)$$

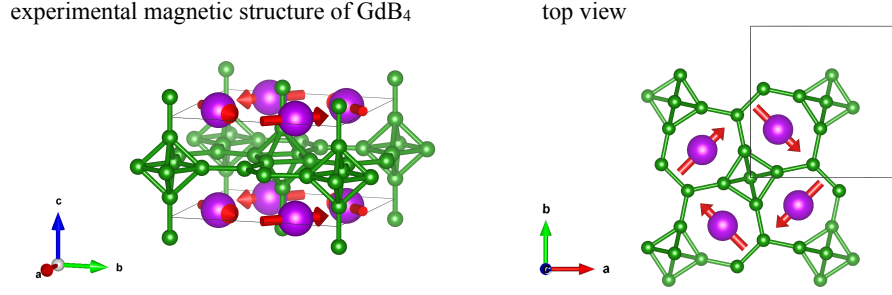


Figure 3.8: The experimental magnetic configuration of  $\text{GdB}_4$  as reported in Ref. [174]. The black box indicates the boundaries of the unit cell. The structure is shown from two viewpoints visualized using VESTA [31].

where  $|n_{c_j}\rangle$  is the CMP basis for the  $j$ th cluster with multiplicity  $N^{(c_j)}$ .

Let us now define the CMP coefficient

$$M_n^{(c_j)} = \langle m | n_{c_j} \rangle, \quad (3.57)$$

that is closely related to the point group M multipole coefficient  $M_{p\Gamma\gamma}^{p1}$  as can be seen by comparison of Equation (3.48) and Equation (3.49). Based on the above, an arbitrary uniform magnetic configuration in a crystal can be expanded as

$$|m\rangle = |m_{c_1}\rangle \otimes |m_{c_2}\rangle \otimes \cdots \otimes |m_{c_d}\rangle, \quad (3.58)$$

$$|m_{c_j}\rangle = \frac{1}{N^{(c_j)}} \sum_{n=1}^{3N^{(c_j)}} M_n^{(c_j)} |n_{c_j}\rangle. \quad (3.59)$$

At last, let us devise the CMP expansion to characterize a magnetic structures that has been measured experimentally. We look at entry 0.9.mcif on MAGNDATA, which correspond to  $\text{GdB}_4$ . The magnetic structures has been reported in Ref. [174] and can be seen in Figure 3.8 from two viewpoints. At first glance the magnetic configuration of  $\text{GdB}_4$ , shown in Figure 3.8, closely resembles the example of four bar magnets we have discussed in Section 3.2. There are 4 points in a Gd-cluster with position  $\mathbf{r}_i$  and on-site magnetic moment  $\mathbf{m}_i$ :

$$\mathbf{r}_1 = (0.31746, 0.81746, 0), \quad \mathbf{m}_1 = (-0.49576, -0.49576, 0) \quad (3.60a)$$

$$\mathbf{r}_2 = (0.18254, 0.31746, 0), \quad \mathbf{m}_2 = (0.49576, -0.49576, 0) \quad (3.60b)$$

$$\mathbf{r}_3 = (0.81746, 0.68254, 0), \quad \mathbf{m}_3 = (-0.49576, 0.49576, 0) \quad (3.60c)$$

$$\mathbf{r}_4 = (0.68254, 0.18254, 0), \quad \mathbf{m}_4 = (0.49576, 0.49576, 0). \quad (3.60d)$$

The ambitious reader may have implemented the calculation of the M multipole coefficients and is able to quickly verify the result shown in Figure 3.9. This is achieved using Equation (3.28)

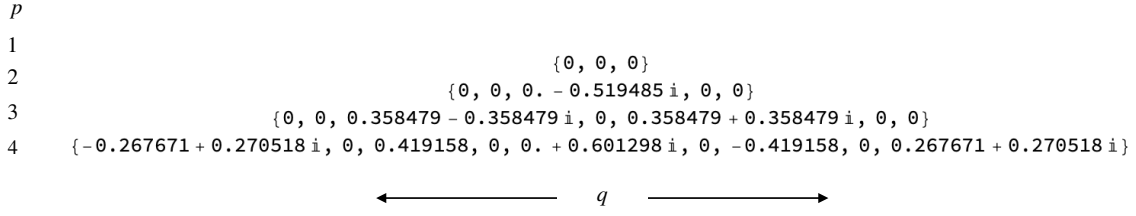


Figure 3.9: The magnetic multipole moments at different order  $p$  and magnetic quantum number  $q$  as defined in Equation (3.28) for the experimental magnetic configuration of  $\text{GdB}_4$  as reported in Ref. [174] shown in Figure 3.8 and stated in Equation (3.60).

for the M multipole coefficient  $M_{pq}^{p1}$ . Interestingly, the leading order M multipole coefficient corresponds to a quadrupole gauge field, instead of a hexadecapole as in the toy model despite the superficial resemblance. And notably the coefficients  $M_{pq}^{p1}$  are complex. The M quadrupole gauge field  $\mathbf{A}^M(\mathbf{r})$ —as defined in Equation (3.23)—is real, which can be checked by inserting  $M_{20}^{21}$  from Figure 3.9 to find

$$\mathbf{A}^M(\mathbf{r}) = M_{20}^{21} \frac{1}{r^3} \mathbf{Y}_{20}^{21}(\Omega) + \mathcal{O}\left(\frac{1}{r^5}\right), \quad (3.61)$$

and noting that  $\mathbf{Y}_{p0}^{p1}$  is purely imaginary. This can be inferred from some useful identities, which are extensively used in Appendix B:

$$\mathbf{Y}_{pq}^{p-1,1}(\Omega) = \frac{1}{\sqrt{p(2p+1)}} (p\hat{\mathbf{r}} - i\hat{\mathbf{r}} \times \mathbf{l}) Y_{p,q}(\Omega), \quad (3.62)$$

$$\mathbf{Y}_{pq}^{p,1}(\Omega) = \frac{1}{\sqrt{p(p+1)}} \mathbf{l} Y_{p,q}(\Omega), \quad (3.63)$$

$$\mathbf{Y}_{pq}^{p+1,1}(\Omega) = \frac{-1}{\sqrt{(p+1)(2p+1)}} ((p+1)\hat{\mathbf{r}} + i\hat{\mathbf{r}} \times \mathbf{l}) Y_{p,q}(\Omega), \quad (3.64)$$

These are derived step-by-step in Section B.7. One may also check that the leading order magnetic field is real-valued, i.e., physical, by inserting  $M_{20}^{21}$  from Figure 3.9 into Equation (3.10) and this time noting that  $\mathbf{Y}_{p0}^{p+1,1}$  is purely real.

Turning our attention back to the CMP expansion of  $\text{GdB}_4$ , we find that  $N = 4$  Gd atoms must yield 12 magnetic configurations in the CMP basis. These are computed by means of the Gram-Schmidt procedure outlined in the previous section, see Equation (3.54). The complete CMP basis for  $\text{GdB}_4$  is shown in Figure 3.10. By a closer look, one may identify  $|4\rangle$  to be exactly the experimental magnetic configuration shown in Figure 3.8. Consequently, the CMP coefficient of the Gd-cluster, i.e.,  $M_n^{(\text{Gd})} = \langle m_{(\text{GdB}_4)_4} | n_{\text{Gd}} \rangle$ , vanishes for all  $n \neq 4$  for the experimental magnetic structure  $|m(\text{GdB}_4)\rangle$ , i.e.,

$$|m_{(\text{GdB}_4)}\rangle = M_4^{(\text{Gd})} |4\rangle. \quad (3.65)$$

expansion order ( $p$ )	$2^p$	multipole
1	2	dipole
2	4	quadrupole
3	8	octupole
4	16	hexadecapole
5	32	32-pole
6	64	64-pole

Table 3.2: The naming convention of multipoles according to their expansion order  $p$ .

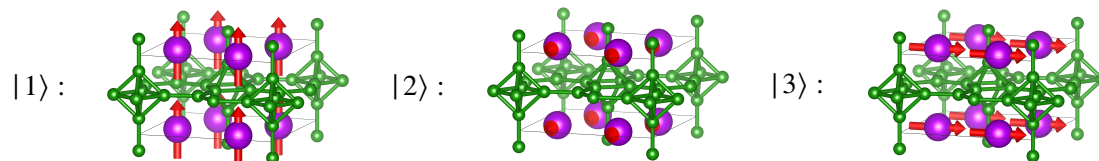
Compared to the M multipole coefficient  $M_{pq}^{p1}$ , the CMP coefficient  $M_n$  cannot immediately be used to compute the gauge field or the magnetic field. Only the closely related point group M multipole coefficients  $M_{p\Gamma\gamma}^{p1}$  given in Equation (3.45a) could be used to compute physical fields using Equation (3.44). This is the price paid for the CMP elements to be orthogonal and must be kept in mind, when considering the interaction of CMPs with M and MT multipoles in future projects. Recall, that the close relation between  $M_n$  and  $M_{p\Gamma\gamma}^{p1}$  allows each  $n$  to be traced back to an expansion order  $p$ , irreducible representation  $\Gamma$  and component  $\gamma$ . This allows the CMP basis elements to be categorized. Conventionally, multipoles are named by the  $2^p$ -nomenclature shown in Table 3.2, where  $2^p$  is often replaced by the Greek number up to  $p = 16$ . In Figure 3.10 the CMP basis elements of  $\text{GdB}_4$  are categorized by the corresponding multipole order, where by construction the multipole order increases with  $n$ . And again we confirm that  $|4\rangle$  in Figure 3.10 corresponds to a quadrupole.

### 3.4 Magnetic domains and linear combinations of cluster multipoles

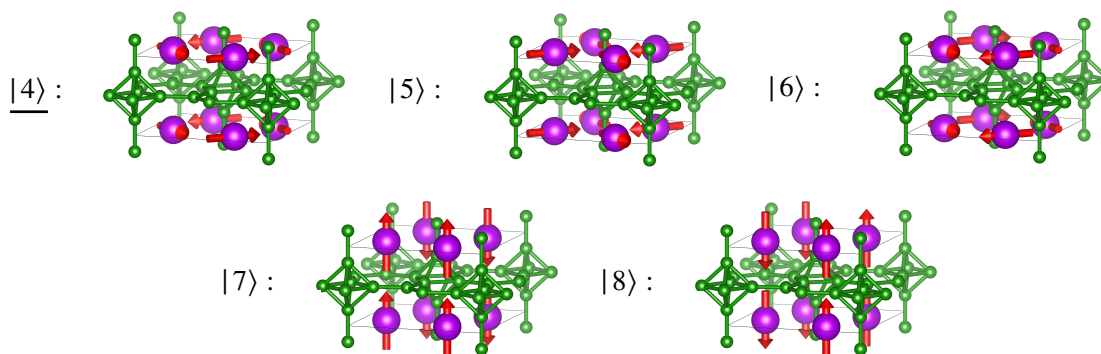
In the previous section, we have introduced the cluster multipole (CMP) basis in a pedagogical way. This scheme to span the space of all uniform magnetic structures in a crystal is deeply rooted in the symmetry properties of the corresponding crystal. Another concept, that is entrenched with the crystal symmetry of a magnetic structures, is the idea of magnetic domains. Magnetic domain walls have been shortly touched upon in Chapter 1 and shall be connected to CMPs in the present section. Furthermore, we will postulate a heuristic rule, which will play a key role in Chapter 4. Here, we need to condone some hand waving arguments, but ultimately our heuristic rule will be statistically validated. We resume on a more or less pedagogical path and introduce these concepts with the help of a practical example.

Let us consider  $\text{YMnO}_3$ , whose experimental details can be found on MAGNDATA in entry 0.3.mcif. Figure 3.11 shows 18 magnetic configurations that correspond to the CMP basis of  $\text{YMnO}_3$ . Hence, these 18 magnetic configurations span the space of possible uniform magnetic configurations on the Mn-cluster in  $\text{YMnO}_3$ . The basis elements are categorized by their expansion

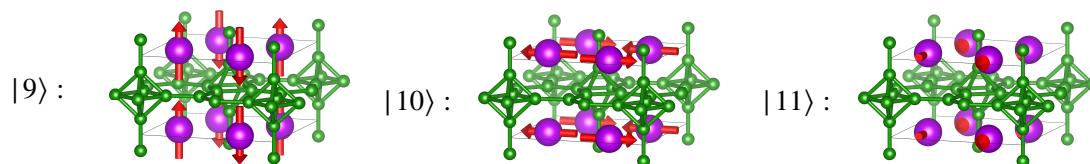
## Dipole



## Quadrupole



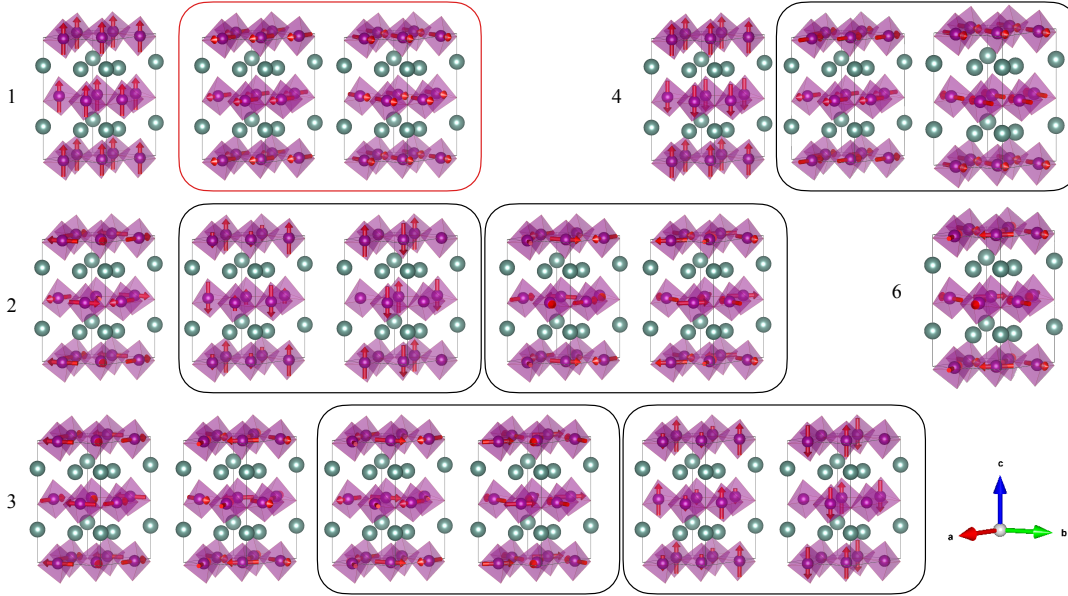
## Octupole



## Hexadecapole



Figure 3.10: The complete cluster multipole basis for  $GdB_4$  categorized by expansion order. Visualized by Vesta.

Figure 3.11: Magnetic configurations in the CMP basis of  $\text{YMnO}_3$ .

order from 1 to 6, i.e. from dipole to 64-pole, yet the Gram–Schmidt procedure leads to no 32-pole. The magnetic configurations within one box—additionally to having the same expansion order—also share the same irreducible representation (irrep).

### 3.4.1 Heuristic rule

We now postulate that *the magnetic ground state favors either pure CMPs or linear combinations of CMPs that combine equally weighted CMPs of the same order and same irrep.*

This heuristic rule is based on the following physical intuition. From the Landau–Lifshitz theory of second-order phase transitions we know that the change of the spin-density  $\delta n_{\sigma\sigma'}^{(s)}$ , that lowers the symmetry during a phase transition, can be written as a sum over physical irreducible representations  $\Gamma$  and its components  $\gamma$ :

$$n_{\sigma\sigma'}^{(s)} = n_{0\sigma\sigma'}^{(s)} + \delta n_{\sigma\sigma'}^{(s)}, \quad (3.66)$$

$$\delta n_{\sigma\sigma'}^{(s)} = \sum_{\Gamma\gamma} \eta_{\gamma}^{(\Gamma)} \phi_{\gamma}^{(\Gamma)}. \quad (3.67)$$

The total free energy  $F$  can then be written in even powers of an order parameter  $\eta$ :

$$F(p, T, \eta) = F_0(p, T) + \sum_{\Gamma} A^{(\Gamma)}(p, T) \underbrace{\sum_{\gamma} \eta_{\gamma}^{(\Gamma)2}}_{\eta^2} + \mathcal{O}(\eta^4), \quad (3.68)$$



where  $p$  is pressure,  $T$  is temperature, and  $\eta^2$  can be expressed by a sum of squares over components  $\gamma$ . According to the standard Landau theory, there is one  $\Gamma$  for which  $A^{(\Gamma)}(p, T)$  must change sign and vanish at the transition point. Therefore it is usually enough to consider the linear combination of components  $\gamma$  within one irrep at least when  $T$  or  $p$  is close to the transition point. However, as a counterexample, within the lower symmetry phase (i.e., far away from the transition point), mixing among components with different irreps may occur if no further symmetry breaking is induced.

It remains the question why we also expect CMPs of equal *expansion order* to be more likely to mix. First, we recall that the point group harmonics  $\mathcal{Y}_{l\Gamma\gamma}(\Omega)$  underlying the CMP expansion are structured as linear combinations of spherical harmonics  $Y_{lm}(\Omega)$  of the same order  $l$ , such that they are invariant under the action of elements given a point group with irrep  $\Gamma$ :

$$\mathcal{Y}_{l\Gamma\gamma}(\Omega) = \sum_{m=-l}^l c_{lm}^{(\Gamma\gamma)} Y_{lm}(\Omega), \quad (3.69)$$

so that the CMP basis elements corresponding to a specific order  $l$  and irrep  $\Gamma$  always feature all components at that expansion order. Nevertheless, at different orders the same irrep might appear. We believe it is more likely that components of the same order mix, because the complexity of the magnetic configuration increases with the expansion order. Counterexamples are materials where the magnetic structure has a large collinear contribution and a small tilt introducing noncollinearity.

Following our proposed heuristic rule, we now construct equally weighted linear combinations of CMP basis elements that have the same order and same irrep. As we have 6 pairs that fulfill this condition, this leads to additional 12 magnetic configurations. In each instance we consider the sum and the difference. The resulting configurations for the dipolar magnetic configurations, i.e., the red box in Figure 3.11, are shown in Figure 3.12. The upper (lower) row shows the addition (subtraction) of CMPs. The last column provides a top view of the resulting magnetic configuration.

In the following we will see that the top and the bottom configurations are actually expected to yield the same total energy and in that sense they are redundant. This is because they are different domains of the same underlying magnetic configuration. Let us use this example to understand the notion of magnetic domains.

### 3.4.2 Magnetic domains

A magnetic domain corresponds to one possible realization of a magnetic structure. Given the paramagnetic unit cell of a material, the set of all possible symmetry operations yields the space group (spg). In a magnetic material the spg of the paramagnetic system is often called parent spg, in contrast to the magnetic space group (mspg). The mspg contains all symmetry operations that consist of rotations, translations and time reversal, which leave the magnetic unit cell invariant. When we apply an spg operation, which is not element of the mspg, we obtain a different magnetic domain, but we explicitly do not change the magnetic structure.

Figure 3.13 presents all possible domains—or magnetic configurations obtained for one magnetic structure. The starting point is the magnetic configuration we obtained in the top row of Figure 3.12.

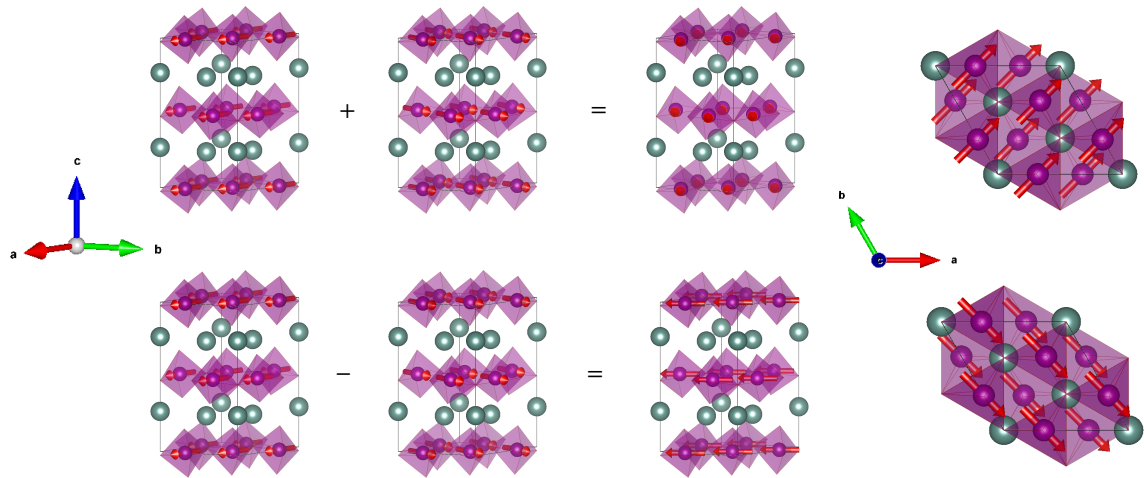


Figure 3.12: Magnetic configurations corresponding to equally weighted linear combinations of CMPs with order 1 and same irreducible representation for  $\text{YMnO}_3$ .

Then, an operation which is element of the parent spg combined with both positive and negative time reversal symmetry is applied. The specific operation is written on top of each resulting magnetic configuration. Here, the operation is given in BNS convention as used by the Bilbao Crystallographic Server [175]. The careful reader may have noticed that the magnetic configuration obtained by application of  $(x - y, -y, z, -1)$  exactly agrees with the magnetic configuration we obtained in the bottom row of Figure 3.12. In other words, these two magnetic configurations correspond to two domains of the same magnetic structure and we expect the total energy for both of these magnetic configurations to be exactly the same.

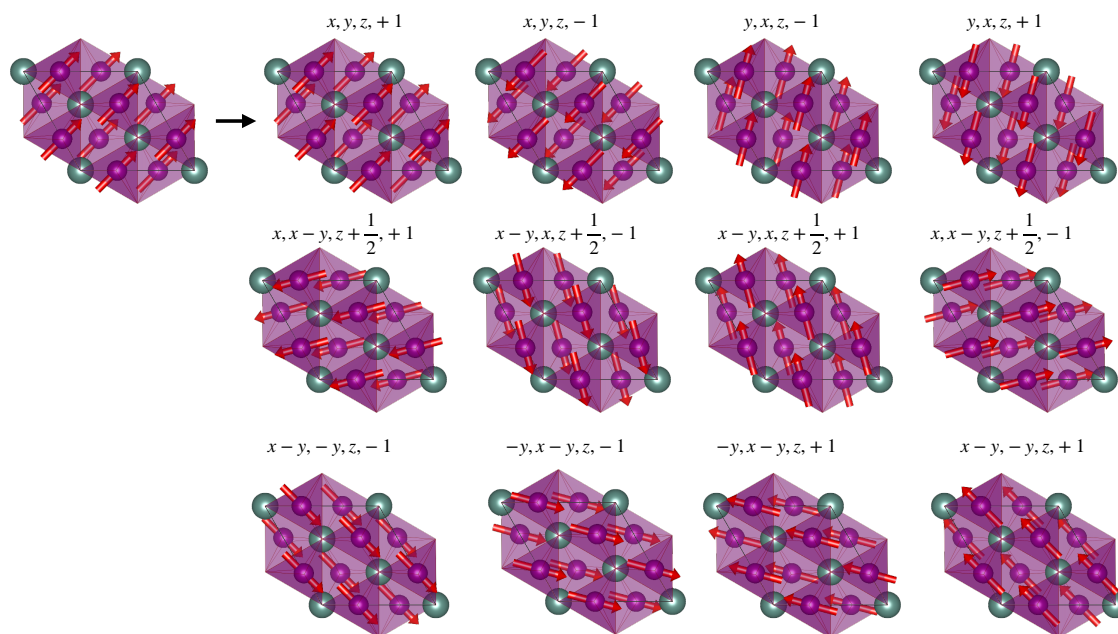


Figure 3.13: Magnetic configurations corresponding to domains derived from the upper left configuration by application of the operation labeling the resulting magnetic configuration. The example material is  $\text{YMnO}_3$ .

## Chapter 4

# High-throughput benchmark CMP+SDFT calculation

The cluster multipole (CMP) expansion for magnetic structures provides a scheme to systematically generate candidate magnetic structures specifically including noncollinear magnetic configurations adapted to the crystal symmetry of a given material. A comparison with the experimental data collected on MAGNDATA shows that the most stable magnetic configurations in nature are linear combinations of only few CMPs. Furthermore, a high-throughput calculation for all candidate magnetic structures was performed in the framework of spin-density functional theory (SDFT). We benchmark the predictive power of CMP+SDFT with 2935 calculations, which show that (i) the CMP expansion administers an exhaustive list of candidate magnetic structures, (ii) CMP+SDFT can narrow down the possible magnetic configurations to a handful of computed configurations, and (iii) SDFT reproduces the experimental magnetic configurations with an accuracy of  $\pm 0.5 \mu_B$ . For a subset the impact of on-site Coulomb repulsion  $U$  is investigated by means of 1545 CMP+SDFT+ $U$  calculations revealing no further improvement on the predictive power.

This chapter is almost identical to our manuscript “Benchmark for *ab initio* prediction of magnetic structures based on cluster multipole theory” [176], which is co-authored by T. Nomoto, M.-T. Suzuki and R. Arita. Text that is clarifying details or needed adjustment to be integrated in this thesis and, thus, is not part of the published manuscript uses a different font typeface.

### 4.1 Methods

In this section we shortly discuss the employed methods, namely the CMP expansion and SDFT. As the CMP expansion is a rather novel approach [48, 145, 177], it has been motivated and set out in some detail in Chapter 3. However, it will be briefly summarized once again. For more background and details of the algorithm we refer the reader to Ref. [173]. SDFT, on the other hand, is a well established method [8, 178]. It is available as part of many *ab initio* packages [179–184] in its

generalized version [185, 186], which is applicable to noncollinear AFM configurations. Here, we chose to use VASP [80, 81, 179] and hence we merely elaborate on the setup details employed in this study.

#### 4.1.1 Cluster Multipole expansion

The reader unfamiliar with the CMP expansion may want to refer to Chapter 3. Here, we recall that the cluster multipole (CMP) expansion for magnetic structures [48, 173] provides an orthogonal basis set of magnetic configurations, which are symmetrized based on the crystallographic point group. In order to motivate the expansion, let us consider the vector Poisson equation:

$$\nabla^2 \mathbf{A}(\mathbf{r}) = -\frac{4\pi}{c} \mathbf{j}(\mathbf{r}), \quad (4.1)$$

where  $\mathbf{j}(\mathbf{r}) = c\nabla \times \mathbf{M}(\mathbf{r})$  is the current density and  $\mathbf{M}(\mathbf{r})$  is the magnetization density. Here, the Coulomb gauge  $\nabla \cdot \mathbf{A}(\mathbf{r}) = 0$  is invoked and the potential outside of the magnetization density is considered. The rotational invariance of  $\nabla^2$  allows the vector gauge potential  $\mathbf{A}(\mathbf{r})$  to be expanded w.r.t. vector spherical harmonics  $\mathbf{Y}_{pq}^{l1}$  [140]. Accordingly, the magnetic field  $\mathbf{B}(\mathbf{r}) = \nabla \times \mathbf{A}(\mathbf{r})$  can be written in terms of magnetic multipole moments  $M_{lm}^{l1}$  as follows [155]

$$\mathbf{B}(\mathbf{r}) = -i \sum_{l=1}^{\infty} \sum_{m=-l}^l \sqrt{l(2l+1)} M_{lm}^{l1} \frac{1}{r^{l+2}} \mathbf{Y}_{lm}^{l+1,1}(\Omega), \quad (4.2)$$

where  $l$  is the orbital angular momentum quantum number and  $m$  magnetic quantum number.

Following M.-T. Suzuki *et al.* in Ref. [173] the magnetic multipole coefficients for a magnetic configuration on a point form  $|m\rangle = (\mathbf{m}_1, \mathbf{m}_2, \dots, \mathbf{m}_N)^T$  read

$$M_{lm}^{l1} = -\frac{4\pi i}{2l+1} \sqrt{\frac{p+1}{p}} \int d^3\mathbf{r} \sum_{i=1}^N \mathbf{m}_i \cdot [\nabla (r^l Y_{lm}^*(\Omega))] \delta^{(3)}(\mathbf{r} - \mathbf{r}_i). \quad (4.3)$$

$\mathbf{m}_i$  is a local magnetic moment on the magnetic site  $i$  at position  $\mathbf{r}_i$ . For a given point group the point form is a set of all symmetrically equivalent points and can be classified into Wyckoff positions [172] in analogy to the Wyckoff positions of space groups. Here,  $N$  is the multiplicity of the Wyckoff position of the point form, that constitutes the magnetic configuration. As introduced by Ref. [173] a point form carrying a magnetic configuration is referred to as (magnetic) cluster in the context of the CMP expansion for magnetic structures. In contrast to Ref. [173], here we do not introduce toroidal moments.

Symmetrization according to irreducible representations of the crystallographic point group allows for a physically meaningful expansion w.r.t. point group harmonics

$$\mathcal{Y}_{l\Gamma\gamma} = \sum_m c_{lm}^{(\Gamma\gamma)} Y_{lm}, \quad (4.4)$$

where  $\Gamma$  indicates the irreducible representation and  $\gamma$  its components. Here, the tabulated coefficients [155]  $c_{lm}^\gamma$  are chosen to be real valued. With this a *virtual cluster* [173] is constructed, where

each magnetic site is assigned a magnetic moment. By mapping  $l\gamma \rightarrow n$  through a Gram-Schmidt orthonormalization scheme the CMP basis is computed.

The CMP basis can be written as

$$\left\{ |n\rangle = \left( \mathbf{e}_1^{(n)}, \mathbf{e}_2^{(n)}, \dots, \mathbf{e}_N^{(n)} \right)^T \right\}, \quad (4.5)$$

where  $\mathbf{e}_i^{(n)}$  is a unit vector of a local magnetic moment on the magnetic site  $i$ . By convention  $n = 1, 2, 3$  corresponds to ferromagnetism, while  $n \geq 4$  corresponds to more complicated higher order magnetic configurations including noncollinear magnetism. The definition of  $|n\rangle$  coincides with  $\left\{ \mathbf{e}_{l\gamma}^\mu \right\}$  in Ref. [173] up to the choice of normalization<sup>1</sup>.

In case that the period of the magnetic order coincides with that of the crystal structure, the propagation vector of the magnetic order  $\mathbf{q}$  is zero. The magnetic structure is said to exhibit  $\mathbf{q} = \mathbf{0}$  magnetism. Note that 3 continuous degrees of freedom of rotation of the magnetic moment per magnetic site for a total of  $N$  magnetic sites yields  $3N$  linearly independent magnetic configurations and thus  $n = 1, \dots, 3N$ . In this work, the configuration space of  $\mathbf{q} = \mathbf{0}$  magnetic structures is explored.

The CMP basis defined in Equation (3.47) is complete

$$\frac{1}{N} \sum_{n=1}^{3N} |n\rangle \langle n| = \mathbb{1}_{3N \times 3N}, \quad (4.6)$$

and obeys the orthogonality relation

$$\langle n|n'\rangle = N \delta_{nn'}. \quad (4.7)$$

Furthermore, the symmetry-adapted CMP coefficient reads

$$M_n = \sum_{i=1}^N \mathbf{m}_i \cdot \mathbf{e}_i^{(n)} = \langle m|n\rangle = \langle n|m\rangle. \quad (4.8)$$

In case of more than one inequivalent site exhibiting a magnetic moment, the space of all possible magnetic configurations is spanned by

$$\left\{ |n_{c_1}\rangle \otimes |n_{c_2}\rangle \otimes \dots \otimes |n_{c_d}\rangle \right\}, \quad (4.9)$$

where  $d$  is the number of clusters. Based on the above, an arbitrary magnetic configuration can be

---

<sup>1</sup>In other words,  $\mathbf{e}_i^{(n)}$  correspond to components of  $\left\{ \mathbf{e}_{l\gamma}^\mu \right\}$  in Ref. [173] except that here  $\sum_i^N \mathbf{e}_i^{(n)} \mathbf{e}_i^{(n')} = N \delta_{nn'}$ , while in Ref. [173]  $\left( \left\{ \mathbf{e}^n \right\} \cdot \left\{ \mathbf{e}^{n'} \right\} \right) = \delta_{nn'}$ . Also note that  $\left\{ \mathbf{e}_{l\gamma}^\mu \right\}$  is labeled by  $\mu = 1, 2$  representing magnetic (M) and magnetic toroidal (MT) multipoles, respectively. As we do not expand in terms of MT multipoles, those components appear as higher order magnetic multipoles here, and thus completeness is still ensured.

expanded as

$$|m\rangle = |m_{c_1}\rangle \otimes |m_{c_2}\rangle \otimes \cdots \otimes |m_{c_d}\rangle, \quad (4.10)$$

$$|m_{c_j}\rangle = \frac{1}{N^{(c_j)}} \sum_{n=1}^{3N^{(c_j)}} M_n^{(c_j)} |n_{c_j}\rangle. \quad (4.11)$$

Any two magnetic configurations on the same magnetic sites can be compared by an overlap, which we define as

$$\mathcal{O}_{mm'} = \left( \frac{\langle m|m'\rangle}{\sqrt{\langle m|m\rangle}\sqrt{\langle m'|m'\rangle}} \right)^2. \quad (4.12)$$

Lastly, notice that each CMP carries a definite order and irreducible representation (irrep).

### 4.1.2 Setup for SDFT

The *ab initio* calculations are performed by the Vienna Ab initio Simulation Package (VASP) in version 5.4 [80, 81, 179] and the flags are set appropriate to noncollinear SDFT-GGA calculation including spin-orbit coupling. In practice, the flags in the INCAR file are set as follows:

- First try: ENCUT= 520, EDIFF =  $10^{-8}$ , ISMEAR = 0, SIGMA = 0.02, NELM = 999, LSORBIT = True, LNONCOLLINEAR = True, NPAR = 4, LORBIT = 11, LORBMOM = True, MAGMOM= (*material dependent*)
- Second try: IALGO = 58, AMIX\_MAG = 0.1, BMIX\_MAG = 0.0001, ENCUT= 520, EDIFF =  $10^{-8}$ , ISMEAR = 0, SIGMA = 0.02, NELM = 999, LSORBIT = True, LNONCOLLINEAR = True, NPAR = 4, LORBIT = 11, LORBMOM = True, MAGMOM= (*material dependent*)
- Third try: IALGO = 58, ENCUT= 520, EDIFF =  $10^{-6}$ , ISMEAR = 0, SIGMA = 0.02, NELM = 999, LSORBIT = True, LNONCOLLINEAR = True, NPAR = 4, LORBIT = 11, LORBMOM = True, MAGMOM= (*material dependent*)
- Fourth try: IALGO = 58, AMIX\_MAG = 0.1, BMIX\_MAG = 0.0001, ENCUT= 520, EDIFF =  $10^{-6}$ , ISMEAR = 0, SIGMA = 0.02, NELM = 999, LSORBIT = True, LNONCOLLINEAR = True, NPAR = 4, LORBIT = 11, LORBMOM = True, MAGMOM= (*material dependent*)

Finally, in the rare cases that none of the above converge we chose the most stable setting by visual inspection of the OSZICAR file and reduced EDIFF as needed. We note that there has been no material, where this procedure failed to find a converged magnetic result with  $\text{EDIFF} \leq 10^{-5}$ .

The pseudopotentials are chosen such that *d*-electrons in transition metals and *f*-electrons in lanthanides and actinoides are treated as valence electrons. The default exchange correlation functional, i.e. generalized gradient approximation [187] by Perdew, Burke and Ernzerhof (PBE), is used.

The VASP input is created by the aid of the Python Materials Genomics (pymatgen) package [188]. In particular, we use subroutines based on `spglib` [189]. The magnetic configurations

of the CMP basis are created by a code authored by M.-T. Suzuki, which employs the TSPACE library [190].

## 4.2 Results and Discussion

In this Section, we want to explore the following two main aspects:

(i) Is the CMP expansion a physically meaningful description of magnetic configurations? Namely, here the premise for a physically meaningful description constitutes that naturally occurring magnetic configurations can be characterized by one or few symmetrically related CMPs. It can be understood in the same sense as atomic orbitals are a meaningful basis to describe electrons bound to a free atom, i.e. the probability distribution of one electron is described by one or few degenerate atomic orbitals. In fact, this analogy extends to molecular orbitals in a complex, where the underlying spherical harmonics are symmetrized according to site symmetry.

(ii) Can SDFT predict the most stable magnetic configuration by the aid of an exhaustive list of candidate magnetic configurations for a given crystal? In fact, the predictive power of the combination of the CMP expansion and SDFT (CMP+SDFT) ought to be seen as a composition of the following issues: (a) Is there evidence to assume that the list of candidate magnetic configurations generated by the CMP basis is exhaustive?

(b) Can the experimentally determined magnetic configuration be found among all SDFT results? Note that the similarity between two magnetic configurations is expressed by the overlap defined in Equation (4.12). In addition, we compare the magnetic space group, which crucially influences physical properties.

(c) Can SDFT correctly assign the lowest total energy to the experimental magnetic configuration?

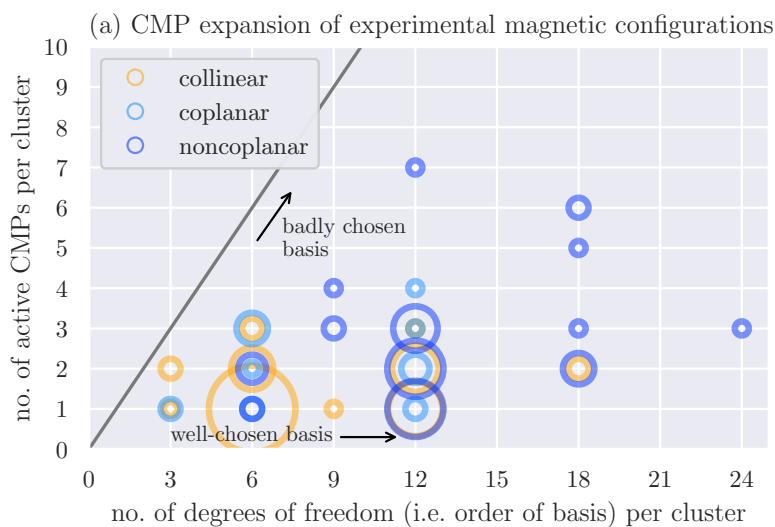
### 4.2.1 The investigated materials and workflow

After precluding these questions, let us start by focusing on the experimental data found on MAGNDATA [15]. This commendable collection of meticulously gathered neutron diffraction measurements and other measurements, e.g. optomagnetic response, is still growing and by no means complete. The MAGNDATA entries used in this study were personally double-checked with the experimental references [174, 191–194, 194–208, 208–214, 214–220, 220–231, 231–238, 238, 239, 239, 239–285, 285–297, 297–300, 300–306, 306–310] and the specific compounds are listed in Appendix C.

These materials explicitly contain transition metals, lanthanides and actinoides with on-site magnetic moments and most data entries are fully AFM or show only weak ferromagnetism. The magnetic configurations considered here possess zero propagation vector, which limits the available data to about 400 entries in MAGNDATA. Moreover, entries corresponding to duplicates in respect to higher temperature, pressure or external magnetic field phases are excluded from this study. Finally, some large unit cells are omitted for efficiency reasons.

The still evolving nature of this database inclined us to take a differentiated perspective on each entry: For some materials the size of the magnetic moment is well-determined, while the





(b) orbital character

(c) crystal system

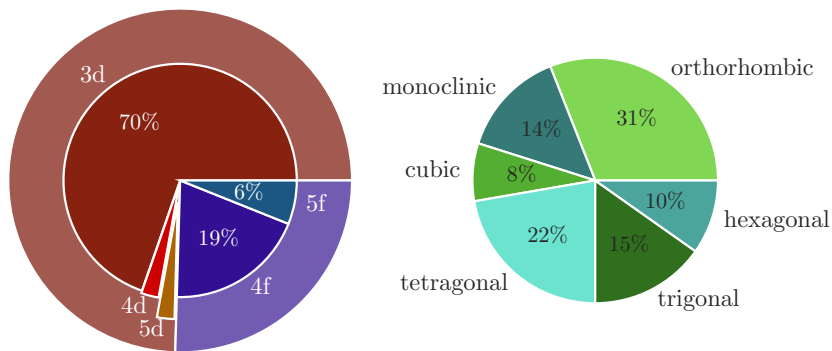


Figure 4.1: Properties of 122 experimental magnetic configurations. (a) The number of CMPs needed to expand the experimental magnetic configuration—active CMPs—over the number of degrees of freedom per magnetic cluster. There are  $3N$  degrees of freedom for  $N$  sites in a magnetic cluster, which coincides with the order of the CMP basis. The size of the circle indicates the frequency of occurrence. (b) Orbital character of the magnetic site. (c) Crystal system.

magnetic order could not be uniquely identified. And conversely, some materials have a well-known symmetry, despite the lack of an exactly determined size of the magnetic moment. Therefore, in this study a total of 131 materials are analyzed, albeit they are distinguished in 122 entries with known magnetic order and 116 entries with known on-site magnetic moment.

Figure 4.1 (a) presents the number of CMPs needed to describe a magnetic cluster featured in the experimental magnetic configuration over the total number of degrees of freedom in the corresponding magnetic cluster. Here, a non-zero CMP component is a so-called *active* CMP in analogy to the terminology used w.r.t. irreducible representations. The number of degrees of freedom per cluster is naturally equivalent to the order of the CMP basis.

The data shown in Figure 4.1 (a) comprises 162 magnetic clusters in 122 materials, among which 69 are classified to be collinear, 53 are noncollinear. In particular, 10 are coplanar and 43 are noncoplanar, as indicated by the color of the circles. Meanwhile, the size of the circle indicates the rate of occurrence.

A well-chosen basis is able to express a configuration in terms of few non-zero components. In this regard, remarkably 48.77% of all clusters are characterized by a single active CMP. And only 6 clusters, i.e. 3.70%, of the clusters in the experimental configurations are linear combinations of more than three CMPs.

The construction of the CMP basis [173] might intuitively wake the expectation that the number of active CMPs per cluster for a *collinear* magnetic structure is equal or less than three. Nevertheless, that could not have been generally expected for the *noncollinear* case. This intuition is empirically confirmed in Figure 4.1 (a), where all collinear circles are as expected reported below three active CMPs. In the case of *noncollinear* magnetic configurations, on the other hand,  $\leq 3$  contributing CMPs per cluster strongly suggests that the basis is particularly well-chosen. Thus, the CMP expansion of experimental configurations in Figure 4.1 (a) establishes the CMP basis to be a particularly suitable basis.

The pie charts in Figure 4.1 give an overview of the composition of all 131 materials. In particular, Figure 4.1 (b) shows the orbital character of the valence electrons on the magnetic site. The majority of the materials features transition metals with emerging *d*-orbital magnetism, while a minority of 25% observes *f*-orbital magnetism. Secondly, the pie chart in Figure 4.1 (c) presents the underlying Bravais lattice and fortifies a balanced mixture comprising of all lattice types.

After we have discussed the known experimental properties, let us move on to setting up a predictive scheme. In Figure 4.2 the computational workflow is organized in four steps: input, setup, calculation, and analysis. The input is taken in form of (magnetic) CIF files [41] from the database MAGNDATA.

Step 2 in Figure 4.2, the setup, includes reading the magnetic CIF files, creating the list of candidate magnetic configurations and writing the input files for VASP by the aid of pymatgen. Crucially, in this step the CMP basis is obtained as described in ??, which does not require the experimental magnetic configuration as an input, but merely the choice of magnetic clusters.

We presume the following heuristic rule holds:

*The magnetic ground state favors either pure CMPs or linear combinations of CMPs that combine equally weighted CMPs of the same order and same irrep.*

We try to provide some physical intuition, why it holds in Section 3.4.1. However, more importantly, we will present statistical evidence in the discussion of Figure 4.5 (b) and (c). Nevertheless, let us first continue focusing on the computational workflow, that presents the core of our prediction scheme.

This heuristic rule prompts us to extend the list of initial candidate magnetic configurations by linear combinations of same order and same irrep. Neglecting linear combinations of pairs yields  $(Y - 1)Y$  additional guesses, for  $Y$  being the number of CMPs with same order and same irrep.

In the case of more than one magnetic cluster,  $d \geq 2$ , this would lead to too many additional guesses. For the 73 materials in concern, where  $d \geq 2$ , we chose to combine only the exact same multipole projected onto a different magnetic cluster. In other words, the linear combination of CMPs with same order, same irrep and same  $y$  is taken, c.f. the last paragraph of ???. Now this similarly leads to  $(Y - 1)Y$  additional guesses, but  $Y$  is the number of CMPs, which are distinct only w.r.t.  $c_j$ .

Step 3 in Figure 4.2, the VASP calculation, is performed as described in ??. The total number of SDFT calculations necessary is equal to the number of candidates. The list of candidates is composed of in total  $\left(\sum_j^d 3N^{(c_j)}\right)$  CMP basis magnetic configurations and accordingly many times  $(Y - 1)Y$  additional guesses. This amounts to a total of 2935 calculations including all 131 materials in this study.

Step 4 in Figure 4.2, the analysis, involves determining characteristic quantities of each calculation. First, all possible domains of the converged magnetic configuration are computed. To that end each space group operation combined with time reversal operations  $\pm 1$  is applied, which leads to either (a) covering the magnetic configuration and thus the operation is element of the magnetic space group, or (b) a new magnetic domain. Considering the set of operations that leave the magnetic configuration invariant, we determine the magnetic space group devising the IDENTIFY MAGNETIC GROUP application on the Bilbao Crystallographic Server [175].

All calculations of a given material and their domains are cross-checked with each other in order to filter how many distinct magnetic configurations and, thus, distinct local minima in the SDFT total energy landscape have been identified. Quantities such as the total energy and the size of the magnetic moment per site are averaged over all calculation corresponding to the same local minimum. The calculation with the lowest total energy among all SDFT calculations of a given material is the CMP+SDFT global minimum.

Note that the list of candidates created as discussed in step 3 is not free of duplicates corresponding to different domains of the same magnetic configuration. In Section 3.4 the CMP basis for  $\text{YMnO}_3$  is constructed. Then, linear combinations of CMPs and magnetic domains are eluded by hands of that example. The candidates corresponding to different domains could be excluded to avoid unnecessary numerical cost. This amounts to a total of 2313 unique calculations for all 131

materials in this study, which comprise of 35.75% additional guesses.

To conclude step 4 in Figure 4.2, all possible domains are considered when computing the overlaps of (i) the experimental and the initial candidate’s magnetic configuration,  $\mathcal{O}_{\text{exp,init}}$ , (ii) the experimental and the converged SDFT calculation’s final magnetic configuration,  $\mathcal{O}_{\text{exp,fin}}$ , and (iii) the initial candidate’s and the converged SDFT calculation’s final magnetic configuration,  $\mathcal{O}_{\text{fin,init}}$ , as defined in Equation (4.12).

In total this study identifies 2005 CMP+SDFT local minima starting from 2313 unique candidates. As mentioned, we performed 2935 calculations including some redundant candidates in this study. Instead of excluding these redundant candidates that correspond to different domains of the same magnetic structure, we used them to statistically analyze the reproducibility. In a nutshell, the reproducibility is the probability to converge to the same local minimum, when repeating the SDFT calculation. More details are described in the subsequent section. In this study the reproducibility reaches 0.79 on a scale from 0 to 1, where 1 refers to perfect reproducibility.

### 4.2.2 Reproducibility

One of the core values of science as a whole is the reproducibility of a result. Especially in big data and high-throughput calculations, the meaning of reproducibility is different than in fields such as classical mechanics. Therefore, let us define reproducibility in the context of this study.

In Section 3.4 we have discussed that SDFT calculations starting from the same magnetic configuration are expected to yield the same converged result up to numerical uncertainty. Furthermore, we have introduced the notion of redundant candidates, that is two magnetic configurations which correspond to different magnetic domains of the same underlying magnetic structure. Neither the CMP basis nor the additional linear combinations that are introduced to create an exhaustive list of candidate magnetic configurations is generally free of such a redundancy. Without loss of exhaustiveness it is possible to avoid additional computational cost by excluding redundant candidates and only perform SDFT calculations for unique candidates. In other words, it is sufficient to pick one realization of a magnetic structure and include it in the list of candidate magnetic configurations.

In this study, we did not filter the redundant candidates. This offers the opportunity to measure the reproducibility. We define reproducibility as the probability to end up in the same local minimum under the condition that the initial candidates are equivalent up to their domain. Figure 4.3 visualizes how the reproducibility is computed.

For a given material, the list of candidates is generated, represented by yellow circles. Then each magnetic structure is given a unique number. Candidates with the same number hence correspond to different domains of the same magnetic structure. In the following this is referred to as candidate group. Independent SDFT calculations let each candidate fall into a local minimum in the SDFT total energy landscape. For the converged magnetic configuration, again all possible domains are constructed. If two SDFT results are equivalent up to their domain, they are said to have fallen into the same local minimum. This is represented by boxes in Figure 4.3.

If we assume a bond between each candidate within a candidate group, then we expect these bonds

**1. Input**

- obtain experimental magnetic configuration from MAGNDATA as .mcif file

**2. Setup**

- perform CMP expansion using Fortran code authored by M.-T. Suzuki (uses TSPACE library)
- read experimental magnetic configurations and CMP basis configurations as pymatgen structure
- create list of initial candidate magnetic configurations incl. linear combinations of same CMP order and irreducible representation
- write VASP input

**3. Calculation**

- run GGA for noncollinear magnetic magnetism in VASP

**4. Analysis**

- read final converged magnetic configuration as pymatgen structure
- determine key quantities:
  - CMP+SDFT local minima
  - compare total energy to obtain CMP+SDFT global minimum
  - domains
  - overlaps btw. initial, final, and experimental magnetic configurations
  - magnetic space groups

Figure 4.2: Computational workflow divided in 4 steps: input, setup, calculation and analysis.

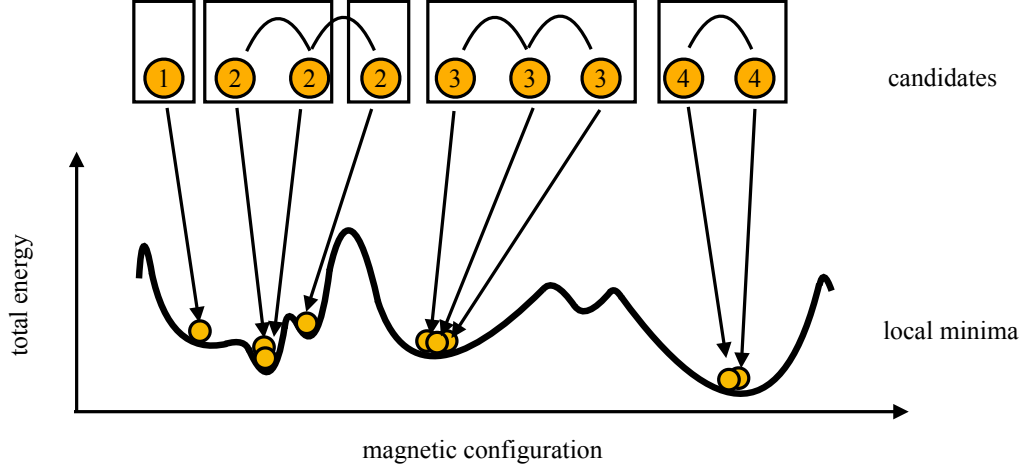


Figure 4.3: An illustration of the reproducibility.

to hold even after the SDFT calculation. In other words, each candidate group should map to one local minimum. This is the case for the magnetic structures labeled 3 and 4 in Figure 4.3. On the other hand, if candidates are at a very unstable initial position or many narrow local minima are present, then numerical uncertainty might indeed be enough impetus to converge to different magnetic structures. This is shown for the magnetic structures labeled 2 in Figure 4.3, where one of the bonds is severed. The reproducibility of one candidate group ( $g$ ) is defined as

$$r_g = \frac{b_{\text{us}}^{(g)}}{b_{\text{tot}}^{(g)}}, \quad (4.13)$$

where  $b_{\text{tot}}$  is the total number of bonds and  $b_{\text{us}}$  is the number of unsevered bonds. Clearly, the magnetic structure labeled 1 in Figure 4.3 is not a candidate group of its own and is disregarded in the discussion about reproducibility. Finally, for the whole database we compute the expectation value of the reproducibility by summing over all entries and all candidate groups

$$\langle r \rangle = \sum_{\text{entries}} \left( \sum_g r_g \right) \quad (4.14)$$

### 4.2.3 The performance of candidate magnetic configurations

The high computational cost is justified, only if the list of candidates can be expected to be exhaustive. Let us recall that the CMP basis defined in Equation (4.5) spans the space of all possible magnetic configurations. Each CMP is characterized by its order and irrep. First, we want to argue that the candidate's irrep is likely to prevail throughout the SDFT calculation. As the CMP basis

is complete and, thus, any irrep that could be active in a given system explicitly appears in the CMP basis, the former corroborates that the CMP basis is a good starting point.

Figure 4.4 (a) shows a histogram of the overlap of the final magnetic configuration and the initial candidate,  $\mathcal{O}_{\text{fin,init}}$ . In particular,  $\mathcal{O}_{\text{fin,init}} \approx 1$  corresponds to the candidate's magnetic configuration remaining almost identical during the iterations. In that case, the candidate appears to be in close vicinity to a local minimum in the total energy landscape of SDFT. We see that the uppermost bin, with 46.54% of all calculations, accounts for more calculations than any other bin.

On the other hand, if the candidate does not correspond to a minimum in the total energy, the calculation is expected to yield a small overlap:  $\mathcal{O}_{\text{fin,init}} \ll 1$ . If the system converges to a magnetic configuration, which is a linear combination of the initial candidate and another magnetic configuration, a finite  $\mathcal{O}_{\text{fin,init}}$  occurs.

There is a related scenario in which the system converges to a magnetic configuration that is of the same irrep, but does not including the CMP of the initial candidate. That case can be characterized by  $\mathcal{O}_{\text{fin,init}} \approx 0$  and  $\sigma_{\text{irrep}} = 0$ , warranted the definition of the variance of the irrep reads

$$\sigma_{\text{irrep}} = \sum_{j,j'}^d \sum_{n,n'}^{3N^{(c_j)}} |\hat{M}_n^{(c_j,\text{init})}| B_{nn'} |\hat{M}_{n'}^{(c_j,\text{fin})}| \quad (4.15)$$

with

$$\hat{M}_n^{(c_j,\text{init}/\text{fin})} = \frac{M_n^{(c_j,\text{init}/\text{fin})}}{\sum_{j=1}^d \sum_{n'=1}^{3N^{(c_j)}} |M_{n'}^{(c_j,\text{init}/\text{fin})}|}, \quad (4.16a)$$

$$B_{nn'} = \begin{cases} 1, & \text{irrep}_n \neq \text{irrep}_{n'} \\ 0, & \text{irrep}_n = \text{irrep}_{n'} \end{cases}. \quad (4.16b)$$

Here,  $\sigma_{\text{irrep}}$  is defined such that, if the same irreps appear with the same weight in the candidate's CMP expansion and in the CMP expansion of the converged calculation, then  $\sigma_{\text{irrep}} = 0$ . In a nutshell,  $|\hat{M}_n|$  indicates to what percentage the  $n$ -th CMP contributes to the expansion and  $B_{nn'}$  is a boolean giving zero weight to equal irreps.

The colorbar in Figure 4.4 (a) corresponds to  $\sigma_{\text{irrep}}$  defined in Equation (4.15). The variance of the irrep is less than 10%,  $\sigma_{\text{irrep}} < 0.1$ , in 78.16% of all SDFT calculations. In other words, the initial irrep is highly likely to be active in the final magnetic configuration.

The inset of Figure 4.4 (a) emphasizes this observation: The variance of the irrep for the lowermost bin of Figure 4.4 (a) is shown as a histogram. Notably, the initial irrep has less than 10% deviation, i.e.  $\sigma_{\text{irrep}} < 0.1$ , in 53.95% of the calculations with  $\mathcal{O}_{\text{fin,init}} \approx 0$ .

As a more general statement, we have shown that the candidate's irrep is statistically likely to prevail throughout the SDFT calculation. Conversely, the most stable magnetic configuration is less likely to be found, if the irrep is not among the list of candidates. Hence, creating a list of candidates building upon the CMP basis is an efficient solution to assure all possible irreps are among the candidates.

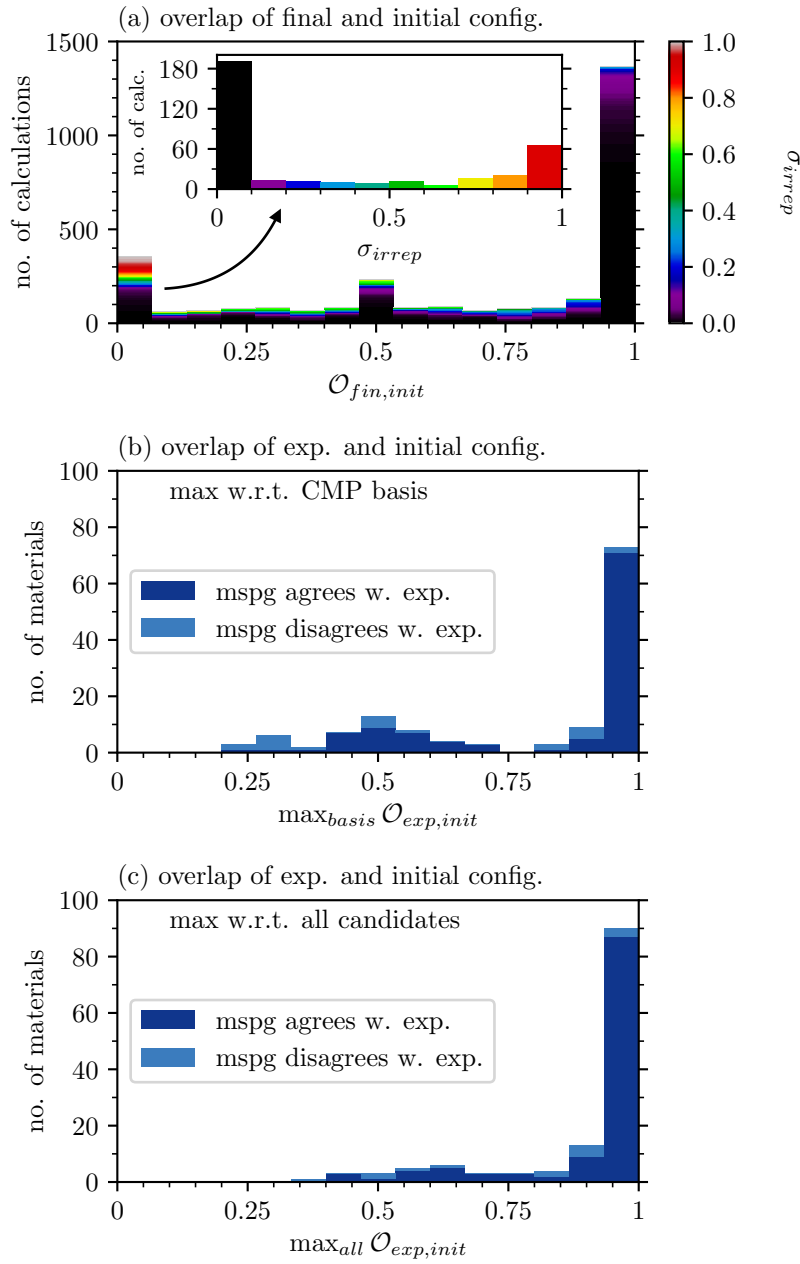


Figure 4.4: (a) Overlap of the candidate and the final SDFT result. The overlap is defined in Equation (4.12). The color scale indicates the variance of the irreducible representation. Inset: The variance of the irreducible representation for the lowermost bin (see arrow). (b) The maximum overlap of the experiment and the initial candidate w.r.t. the CMP basis. (c) The maximum overlap of the experiment and the initial candidate w.r.t. all candidates incl. the CMP basis and additional guesses. The color classifies if the magnetic space group (mspg) agrees with the experimentally determined mspg.



From this point of view, it seems unnecessary to introduce additional guesses as candidates that are equally weighted CMPs of same order and same irrep. However, using the experimental data as a guide once more, the advantages of including additional guesses into the list of candidates becomes clear.

Figure 4.4 (b) presents the maximum overlap of the CMP basis and the experiment,  $\max_{\text{all}} \mathcal{O}_{\text{init,exp}}$ . The histogram shows a probability density strongly peaked close to one. Additionally, there are side peaks at  $1/3$  and  $1/2$ . This bias towards  $1/3$  and  $1/2$  can be appreciated when considering the aforementioned heuristic rule once again.

Namely, the magnetic ground state favors either pure CMPs or linear combinations of CMPs that combine equally weighted CMPs of the same order and same irrep. An irrep can have a dimension of 1, 2 or 3 and accordingly at each CMP order CMPs basis configurations occur in sets of 1, 2 or 3 configurations in the expansion. Hence, favored linear combinations projected onto a CMP basis configuration are prone to yield overlap of 1,  $1/2$  or  $1/3$ .

In comparison, Figure 4.4 (c), displays the maximum overlap of initial candidate and the experiment,  $\max_{\text{all}} \mathcal{O}_{\text{init,exp}}$ , w.r.t. the complete list of candidates, which contains the CMP basis configurations as well as additional guesses. The introduction of additional guesses, following the heuristic rule, can effectively avoid side peaks at  $1/3$  and  $1/2$  and thus takes into account linear combinations common in materials existing in nature.

As Figure 4.4 (a) showed, most magnetic configurations remain close to the initial magnetic configuration. Therefore it is paramount to start from an exhaustive list of magnetic configurations.

The dark blue and light blue colors in Figure 4.4 (b) and (c) indicate, that the magnetic space group found experimentally is identical to the magnetic space group of the candidate or not, respectively. Considering all candidates, as in Figure 4.4 (c), 117 of 122 magnetic space groups agree. This is an improved agreement rate compared to considering only the CMP basis, as in Figure 4.4 (b), where 110 magnetic space groups agree. It is noteworthy that some magnetic space groups only enter the list of candidates through the additional guesses.

A final argument in favor of introducing additional guesses is that in total we find 655 of 2005, hence 32.67%, of the local minima in the SDFT energy landscape only thanks to the additional guesses. Even among the CMP+SDFT minima with the minimum total energy 23 are thanks to the additional guesses, as well as 15 of the (local) minima most similar to the experiment.

Therefore, with the collection of arguments mentioned above, we have justified expectation that the list of candidate magnetic configurations is exhaustive. In the following, let us investigate whether the experimentally determined magnetic configuration is present among all SDFT results and how we might predict the likely experimental magnetic configuration for an unknown material.

#### 4.2.4 Analysis of CMP+SDFT local minima

Following the workflow in Figure 4.2 all final SDFT results are scrutinized for their similarity. Some SDFT results correspond to the same local minimum in the SDFT total energy landscape and as such they are grouped in CMP+SDFT local minima. The overlap of each CMP+SDFT local minimum

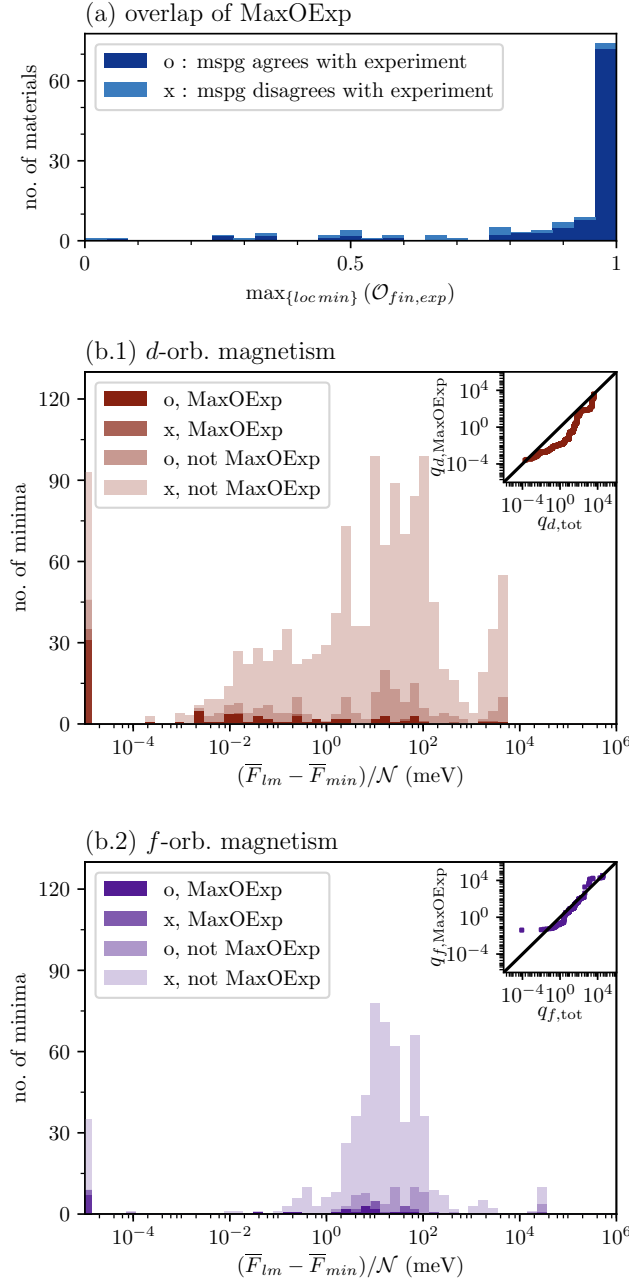


Figure 4.5: (a) Overlap of experiment and CMP+SDFT minimum most similar to experiment (MaxOExp). Overlap is defined in Equation (4.12). o/x classifies if the magnetic space group (mspg) agrees/disagrees with the experimental mspg. (b.1) total energy distribution w.r.t. materials feature *d*-orbital magnetism. The minima are classified in MaxOExp and remainder “not” MaxOExp, and mspg agrees/disagrees. Inset: Q-Q plot, where  $q_{d,MaxOExp}$  w.r.t. the distribution of MaxOExp is compared to  $q_{d,tot}$  w.r.t. the distribution of all local minima of materials feature *d*-orbital magnetism. (b.2) total energy distribution w.r.t. materials feature *f*-orbital magnetism. Inset: Q-Q plot, where  $q_{f,MaxOExp}$  w.r.t. the distribution of MaxOExp is compared to  $q_{f,tot}$  w.r.t. the distribution of all local minima of materials featuring *f*-orbital magnetism.

with the experimental magnetic configuration is computed according to Equation (4.12). The CMP+SDFT minimum that yields the maximum overlap with the experiment  $\max_{\{loc\ min\}} \mathcal{O}_{fin,exp}$  (MaxOExp) is termed to be the most similar CMP+SDFT local minimum to the experiment. A worthwhile run should yield  $\max_{\{loc\ min\}} \mathcal{O}_{fin,exp} \approx 1$ , entailing that MaxOExp is indeed very similar to the experiment. Additionally, the magnetic space group (mspg) should agree with the experimentally detected symmetry.

Figure 4.5 (a) presents  $\max_{\{loc\ min\}} \mathcal{O}_{fin,exp}$ , i.e. the overlap of MaxOExp for 122 materials with known experimental magnetic order. The distribution features a substantial peak at  $\max_{\{loc\ min\}} \mathcal{O}_{fin,exp} \approx 1$ . In fact, 82.44% of MaxOExp mark  $\max_{\{loc\ min\}} \mathcal{O}_{exp,vasp} > 0.75$ , verifying good agreement of one CMP+SDFT local minimum with the experiment.

Despite the large overlap, some mspg do not agree. In particular 70.99% of MaxOExp agree w.r.t. their mspg, despite yielding  $\max_{\{loc\ min\}} \mathcal{O}_{exp,vasp} > 0.75$ , see the dark blue labeled “o”.

The upper most bin in Figure 4.5 (a) accumulates 54.96% and corresponds to

$$\max_{\{loc\ min\}} \mathcal{O}_{exp,vasp} > 0.96. \quad (4.17)$$

Even in the upper most bin not all mspg agree, while on the other hand most CMP+SDFT local minima with rather inadmissible

$$\max_{\{loc\ min\}} \mathcal{O}_{exp,vasp} < 0.75 \quad (4.18)$$

still agree w.r.t. their mspg. For instance,  $\text{Fe}_2\text{O}_3$  has a collinear AFM structure with a small tilting [299]. While the parent spg is  $\text{R}\bar{3}\text{c}$  (167) the small tilting results in  $\text{P}\bar{1}$  (2.4) for the mspg. In the CPM expansion, the experimental configuration is described by two CMP basis configurations of order 5. However, they do not observe the same irreducible representation. In particular, the main contribution is  $\text{A}_{1g}$  and the tilting is due to contributions of  $\text{E}_u$ . In CMP+SDFT the most stable configuration is pure  $\text{A}_{1g}$  without any tilting. So that, although the overlap  $\max_{\{loc\ min\}} \mathcal{O}_{exp,vasp} = 0.9658$ , the mspg predicted by CMP+SDFT is  $\text{R}\bar{3}\text{c}$  (167.103) not  $\text{P}\bar{1}$  (2.4) as found experimentally.

In total 84.43% among MaxOExp yield the correct mspg. This is to say that neither the overlap nor the mspg alone are a sufficient criterion whether the experimental configuration is correctly predicted or not.

In comparison, only 16.17% of all CMP+SDFT minima yield the experimental mspg. However, for 90.16% of the materials at least one CMP+SDFT minima yields the experimental mspg. As mentioned among MaxOExp 84.43% yield the experimental mspg.

Another characteristic CMP+SDFT minimum is the CMP+SDFT global minimum, which observes the minimum total energy in SDFT. Among all CMP+SDFT global minima only 37.70% yield the experimental mspg. This shows that the mspg of the CMP+SDFT global minima is more likely to agree with the experimental mspg than a random CMP+SDFT minimum, but the CMP+SDFT global minima is not adequately predicting the mspg.

Let us continue by analyzing the SDFT total energy of the CMP+SDFT minima in more detail. Each CMP+SDFT minimum is attributed one or more SDFT results, as multiple candidates might converge to the same minimum. An average over these attributed SDFT results leads to the material dependent and magnetic configuration dependent total energy of a specific CMP+SDFT minimum  $\bar{E}_{lm}$ . The CMP+SDFT global minimum observes the minimum total energy  $\bar{E}_{min}$ .

In order to compare the total energy across materials, we take a normalized relative total energy that reads

$$(\bar{E}_{lm} - \bar{E}_{min})/\mathcal{N}. \quad (4.19)$$

Here,  $\mathcal{N}$  is the total number of degrees of freedom, i.e. the sum of the order of basis over all clusters that observe a magnetic moment in SDFT in that material.

Figure 4.5 (b.1) and (b.2) present the distribution of CMP+SDFT minima over the normalized relative total energy of materials featuring  $d$ -orbital magnetism and  $f$ -orbital magnetism, respectively. The energy scale is logarithmic in units of meV. And the lowermost bin, representing the CMP+SDFT global minima, would theoretically lie precisely at zero. However, for the obvious practical reasons, namely that  $\log(0) \rightarrow -\infty$ , it is added at the lower edge. The remaining bins represent the distribution of CMP+SDFT local minima  $\rho_{d/f,tot}$ . A key question is, whether MaxOExp tends to be close to the total energy minimum.

In Figure 4.5 (b.1) and (b.2) the color intensity classifies all CMP+SDFT minima according to agreement/disagreement with the experimental mspg labeled by o/x, respectively. Additionally, the minima are classified according to being MaxOExp or not. Overall the total energy distributions  $\rho_{d/f,tot}$  span across many orders of magnitude. Albeit,  $\rho_{f,tot}$  is more concentrated in the energy range 1 meV up to 1000 meV.

The data shows that in total 43 of 122 (35.25%) of the CMP+SDFT global minima coincide with MaxOExp. Hence, the magnetic configuration with the minimum total energy in this study does not, at this point, identify the expected experimental configuration. Nevertheless, MaxOExp might tend towards smaller total energy. In order to gain more insight, we ask if MaxOExp data points follow the same distribution as an arbitrary local minimum in  $\rho_{d/f,tot}$ .

Two distributions can be compared in terms of a Q-Q plot [311], where the  $x$ -axis represents the quantile of the reference distribution and the  $y$ -axis represents the quantile of the sample distribution. Let us define the quantile,  $q_{s/r}$  for a sample/reference distribution of local minima  $\{lm_k\}$ , where  $k = 0, \dots, K - 1$  and the local minima (lm) are ordered by  $\bar{E}_{lm_k} \leq \bar{E}_{lm_{k+1}}$ . The  $k/(K - 1)$  quantile  $q_k$  is given by

$$q_k = (\bar{E}_{lm_k} - \bar{E}_{min})/\mathcal{N}. \quad (4.20)$$

Hence, the 0.5 quantile is simply the median value and the 0.1 quantile is the point that divides the distribution such that 90% of the local minima have greater total energy.

The Inset of Figure 4.5 (b.1) shows the Q-Q plot comparing quantiles of  $\rho_{d,MaxOExp}$ , as the sample distribution, with  $\rho_{d,tot}$ , as the reference distribution. For each data point in the smaller

sample distribution the quantile is computed, as explained above. Subsequently,  $q_{d,\text{MaxOExp}}$  is juxtaposed against  $q_{d,\text{tot}}$ .

If the two datasets are sampled from the same underlying distribution  $\rho_{d,\text{MaxOExp}} = \rho_{d,\text{tot}}$ , all points align on the median. The quantile is defined on the same axis as the original distribution, i.e.  $q_{d,\text{MaxOExp}}$  and  $q_{d,\text{tot}}$  are defined on  $(\overline{E}_{lm_k} - \overline{E}_{min})/\mathcal{N}$ .

The Q-Q plot in the inset of Figure 4.5 (b.1) shows significant deviation from the median. Indeed, the slow incline up to approximately 10 meV reveals an accumulation of MaxOExp towards lower total energy. For  $d$ -orbital magnetism we find 77.66% of MaxOExp below 1 meV. On average each material has 4.45 CMP+SDFT local minima below 1 meV. In particular, in this dataset the material with the maximum number of CMP+SDFT local minima has 18 minima below 1 meV. This shows that CMP+SDFT successfully narrows down the possible magnetic configurations for a new material featuring  $d$ -orbital magnetism to a handful of CMP+SDFT local minima, that are highly likely to be close to the experimental observation.

The inset of Figure 4.5 (b.2) shows the analogous Q-Q plot for  $f$ -orbital magnetism. Here, the quantiles basically align on the median suggesting that  $\rho_{f,\text{MaxOExp}} = \rho_{f,\text{tot}}$ . Moreover, for  $f$ -orbital magnetism we find only 32.43% of MaxOExp below 1 meV. Although in case of  $f$ -orbital magnetism the consideration of the total energy seems to fail in narrowing down the number of possible magnetic configurations, at least the CMP+SDFT run itself proposes a set of 10 – 15 possible magnetic configurations.

The presented data opens a gateway to identifying a handful of magnetic configurations as CMP+SDFT local minima for a given material among which the experimentally stable magnetic space group and exact configuration is highly likely to be found. Yet it has not been possible to uniquely identify the ground state based on the SDFT total energy. Although CMP+SDFT yield local minima with the experimental mspg and local minima with large overlap with the experimental magnetic configuration, SDFT fails to assign a low total energy compared to other local minima.

### 4.2.5 The magnetic moment per site

Besides the magnetic configuration, the size of the on-site magnetic moment crucially influences the magnetic properties of a material. Hence, it is interesting to ask, if the magnetic moment estimated by SDFT is close to the experimentally determined magnetic moment per site. In the literature [34] it is well-known that complexes containing first row transition metals with open  $3d$  orbitals are dominated by crystal field splitting. This is referred to as *strong field regime*. Further, the ground state of complexes containing Lantanides with open  $4f$  orbitals are dominated by spin-orbit coupling. Complementary, this is referred to as *weak field regime*. Let us explore the implications by looking closer at the element-dependence of the on-site magnetic moment.

Figure 4.6 presents the on-site magnetic moment averaged over sites within one magnetic cluster as a function of elements sorted by increasing no. of electrons. In particular, the average magnetic

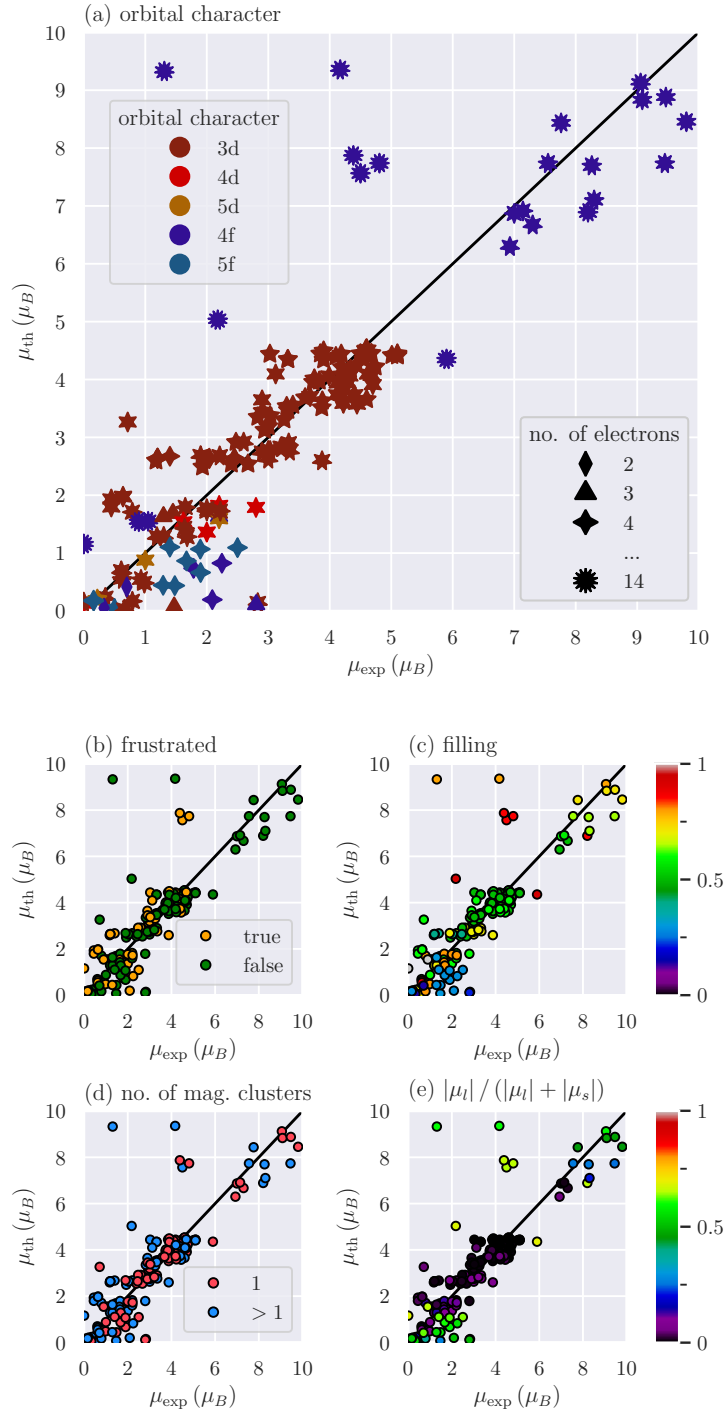


Figure 4.6: The magnetic moment per site as a function of electrons per atom for  $3d$ - and  $4f$ -orbital magnetism. (a.1) and (b.1), the experimental magnetic moment per site  $\mu_{\text{exp}}$ . (a.2) and (b.2), the magnetic moment per site of the CMP+SDFT minimum most similar to experiment w.r.t. its magnetic configuration  $\mu_{\text{th}}$ . (a.3) and (b.3), absolute values of the orbital angular momentum contribution  $\mu_l$  and the spin contribution  $\mu_s$  to  $\mu_{\text{th}}$ .

moment per site reads

$$\mu_{c_j} = \frac{1}{N(c_j)} \sum_{i=1}^{N(c_j)} |\mathbf{m}_i| \quad (4.21)$$

and, thus, the average is taken within each magnetic cluster  $c_j$ , only. The columns show the case of  $3d$ -orbital magnetism and  $4f$ -orbital magnetism, respectively.

Figure 4.6 (a.1) gives an overview of the experimental results  $\mu_{\text{exp}}$  for  $3d$ -orbital magnetism. We see that within compounds featuring the same magnetic element vastly different on-site magnetic moments are reported. This is referred to as *compound dependence* in the following discussion. Overall, the maximum on-site magnetic moment per element frames a dome shape with a clear maximum at Mn closely followed by Fe. In comparison, Figure 4.6 (a.2) shows the on-site magnetic moment  $\mu_{\text{th}}$  predicted by CMP+SDFT. Here,  $\mu_{\text{th}}$  is taken to be the magnetic moment of the magnetic configuration with MaxOExp, which has the most similar magnetic order compared to the experiment. We can see very good agreement in the overall tendency between experiment and CMP+SDFT.

A strong crystal field represents a real and time reversal invariant perturbation that forces a real-valued ground state which effectively quenches the orbital angular momentum operator ( $\mathbf{L} \equiv \mathbf{0}$ ) as discussed in many text books, see e.g. Ref. [312]. Therefore the spin contribution alone is expected to constitute the on-site magnetic moment. Fortunately, in contrast to the experiment the numeric calculation grants direct access to the spin contribution  $\boldsymbol{\mu}_{s,th}$  and the angular momentum contribution  $\boldsymbol{\mu}_{l,th}$  to the on-site magnetic moment

$$\boldsymbol{\mu}_{th} = \boldsymbol{\mu}_{s,th} + \boldsymbol{\mu}_{l,th}. \quad (4.22)$$

Figure 4.6 (a.3) presents the absolute values  $\mu_{s,th}$  and  $\mu_{l,th}$ . The data clearly confirms that the angular momentum is almost entirely quenched in SDFT. Only for the heavier elements, where spin-orbit coupling becomes more relevant <sup>2</sup>, a small contribution is given by  $\mu_{l,th}$ . In other words, SDFT supports that for compounds with more than half-filled  $3d$  bands the angular momentum is only partially quenched.

The dominant  $\mu_{s,th}$  can be directly compared to the spin-only magnetic moment in the ionic limit. It is computed within the Russel-Saunders (or L-S) coupling scheme and is given by

$$\mu_{s,\text{ion}}^{(3d)} = 2\sqrt{s(s+1)} \mu_B \quad (4.23)$$

with spin quantum number  $s$  for the total spin operator  $\mathbf{S}$ . The total spin  $\mathbf{S}$  of the electronic configuration  $3d^n$  with  $n$  electrons is essentially constructed by following Hund's first rules. Albeit in real complexes the electron configuration can be in the high spin (hs) or the low spin (ls) configuration depending on the crystal field strength compared to the intra-orbital Coulomb repulsion. This

<sup>2</sup>The spin-orbit coupling is proportional to  $dV/dr$ , where  $V$  is the potential due to the ions. Hence, heavier elements exhibit stronger spin-orbit coupling. See e.g. Ref. [8].

yields different spin-only magnetic moments  $\mu_{s,\text{ion}}^{(3d)}$  in the ionic limit for electronic configurations of the form  $3d^n$  (hs/l<sub>s</sub>).

In Figure 4.6 (a.3)  $\mu_{s,\text{ion}}^{(3d)}$  is displayed as a reference for various possible electronic configurations. Here, we assumed octahedral complexes for the crystal field splitting. The maximum magnetic moment is consistent with the experiment and CMP+SDFT calculation realized for  $\text{Mn}^{2+}$  or  $\text{Fe}^{3+}$  in the ionic limit. Additionally, the ionic limit already hints towards possible reasons for the observed compound dependence. Namely, we expect the formal oxidation state and the crystal field strength to introduce compound dependence. Further compound dependence arises due to the exact symmetry including small distortions as introduced by the Jahn-Teller effect and the choice of ligands via the nephelauxetic effect, which describes the delocalization of metal electrons through covalent bonds with the ligands.

Let us now move on to the case of compounds featuring lanthanides shown in the right column of Figure 4.6. As mentioned, in the weak field regime spin-orbit coupling is strong compared to the crystal field effect. Therefore the orbital angular momentum operator  $\mathbf{L}$  cannot be neglected and the magnetic moment is computed in the  $j$ - $j$  coupling scheme in terms of the total angular momentum  $\mathbf{J}$ . In the ionic limit, the electronic ground state can be determined following all three Hund's rules<sup>3</sup> for a given shell configuration  $4f^n$  with  $n$  electrons. The magnetic moment in terms of the total angular momentum quantum number  $j$  then reads

$$\mu_j = g_j \sqrt{j(j+1)} \mu_B \quad (4.24)$$

with the Landé  $g$ -factor ( $g_j$ ). Representative, we compute the magnetic moment  $\mu_{\text{III-ion}}^{(4f)}$  for all 3+ ions. Note that in fact,  $\text{Eu}^{2+}$  for instance is expected to resemble  $\text{Ga}^{3+}$  because both have a  $4f^7$  electronic configuration.

Figure 4.6 (b.1) shows the experimental results  $\mu_{\text{exp}}^{(4f)}$  for  $4f$ -orbital magnetism in comparison to  $\mu_{\text{III-ion}}^{(4f)}$ . Similar to the  $3d$ -orbital magnetism, different compounds featuring the same magnetic element observe vastly different  $\mu_{\text{exp}}^{(4f)}$ , however the origin must be different as we will see. A comparison to the CMP+SDFT results presented in Figure 4.6 (b.2) shows good agreement of the overall characteristic behaviour. In both, experiment and CMP+SDFT, the magnetic moment is just below the ionic limit and a small (large) dome forms in the less (more) than half-filled region.

Noticeably, the compound dependence in the CMP+SDFT results is reduced compared to the experiment. By a more detailed analysis of the experimental data, the compound dependence in  $4f$ -orbital magnetism is revealed to arise when long-range order cannot be established very well experimentally. SDFT naturally assumes a well-established long-range order by design as it is a zero temperature method. Specific cases are considered in the discussion of Figure 4.7.

<sup>3</sup>For instance, the 3+-ion for Er has  $4f^{11}$  and thus 3 unpaired spins yielding  $s = 3/2$ . The orbital angular momentum is maximized when orbitals with magnetic quantum number  $m_l = 3, 2, 1$  are singly occupied yielding  $l = 6$  and  $L=I$ . Finally the total angular momentum  $\mathbf{J} = \mathbf{S} + \mathbf{L}$  for more than half-filling, i.e. quantum number  $j = 15/2$ . The ground state term-symbol reads  $4I_{15/2}$ .



Figure 4.6 (b.3) shows the absolute value of the spin and orbital contributions ( $\mu_{s,th}^{(4f)}$  and  $\mu_{l,th}^{(4f)}$ ) in SDFT. As a reference, we plot a fictitious spin-only  $\mu_{s,III-ion}^{(4f)}$  and orbital-only magnetic moment  $\mu_{l,III-ion}^{(4f)}$  in the ionic limit for 3+ ions:

$$\mu_{s,III-ion}^{(4f)} = 2\sqrt{s(s+1)}\mu_B, \quad (4.25)$$

$$\mu_{l,III-ion}^{(4f)} = \sqrt{l(l+1)}\mu_B. \quad (4.26)$$

Prominently, the destructively (constructively) coupling for less (more) than half-filling is confirmed and visualized. Further, the spin contribution  $\mu_{s,th}^{(4f)}$  very closely aligns with the ionic limit. This can be expected as 4*f* electrons barely delocalize by covalently bonding with the surrounding ligands. The orbital contribution  $\mu_{l,th}^{(4f)}$  shows a clearly reduced value compared to  $\mu_{l,III-ion}^{(4f)}$ . This might be interpreted as partial quenching of  $\mathbf{L}$  in SDFT, which is supported by the observation that the reduction of  $\mu_{l,III-ion}^{(4f)}$  is stronger for lighter elements.

So far it has become clear that there is no systematic overestimation of the on-site magnetic moment by CMP+SDFT. However naively one might anyways expect a general underestimation due to the lack of treatment of strong electronic correlation effects in SDFT, albeit strong electronic correlation is expected in particular in 3*d* and 4*f*-bands. As we will see in the following, the data defies this general expectation of an underestimated on-site moment. To this end, let us compare  $\mu_{th}$  and  $\mu_{exp}$  compound-wise, or rather cluster-wise for all compounds.

Figure 4.7 juxtaposes the average magnetic moment per site  $\mu_{th}$  of the magnetic configuration with MaxOExp and the experimentally measured magnetic moment per site  $\mu_{exp}$ . If for a magnetic cluster  $\mu_{th} \approx \mu_{exp}$ , the data point is in close vicinity to the median and the size of the magnetic moment per site is well-estimated. In Figure 4.7 (a), each cluster  $c_j$  is represented by a star, whose color indicates the orbital character of the magnetic site and the number of points indicates which magnetic element forms the cluster. For instance, the 5-pointed dark red star corresponds to a Mn-cluster, since Mn atom has five 3*d* electrons. At first sight, there is no general over- or underestimation seen in the scatter plot.

Moreover, the data suggests that the uncertainty of SDFT is reflected in the absolute deviation of  $|\mu_{th} - \mu_{exp}|$ , rather than some relative deviation of the magnetic moment  $|\mu_{th} - \mu_{exp}|/|\mu_{th} + \mu_{exp}|$ . Indeed, 51.90% of the magnetic moments are within  $\pm 0.5\mu_B$ , and beyond 77.22% obey  $|\mu_{th} - \mu_{exp}| \leq 1\mu_B$ . Concomitantly, in the small magnetic moment regime, that is approximately  $\mu \lesssim 2\mu_B$ , no reliable prediction is possible. In the mid to high magnetic moment regime, on the other hand, a mostly accurate prediction is made.

There is an accumulation of 3*d* data points within  $2\mu_B < \mu_{th} < 5\mu_B$ , whose center of mass closely aligns with the median. However, an apparent lack of precision leads to a wide spread around the median. Despite another accumulation of 4*f* data points in the range of  $6\mu_B < \mu_{th} < 10\mu_B$  showing similarly a high accuracy with a center of mass near the median, we also see many outliers with 4*f*-orbital character across the entire range of the on-site magnetic moments.

The specific group of three outliers at  $4\mu_B < \mu_{exp} < 5\mu_B$  and  $7\mu_B < \mu_{th} < 8\mu_B$  correspond to

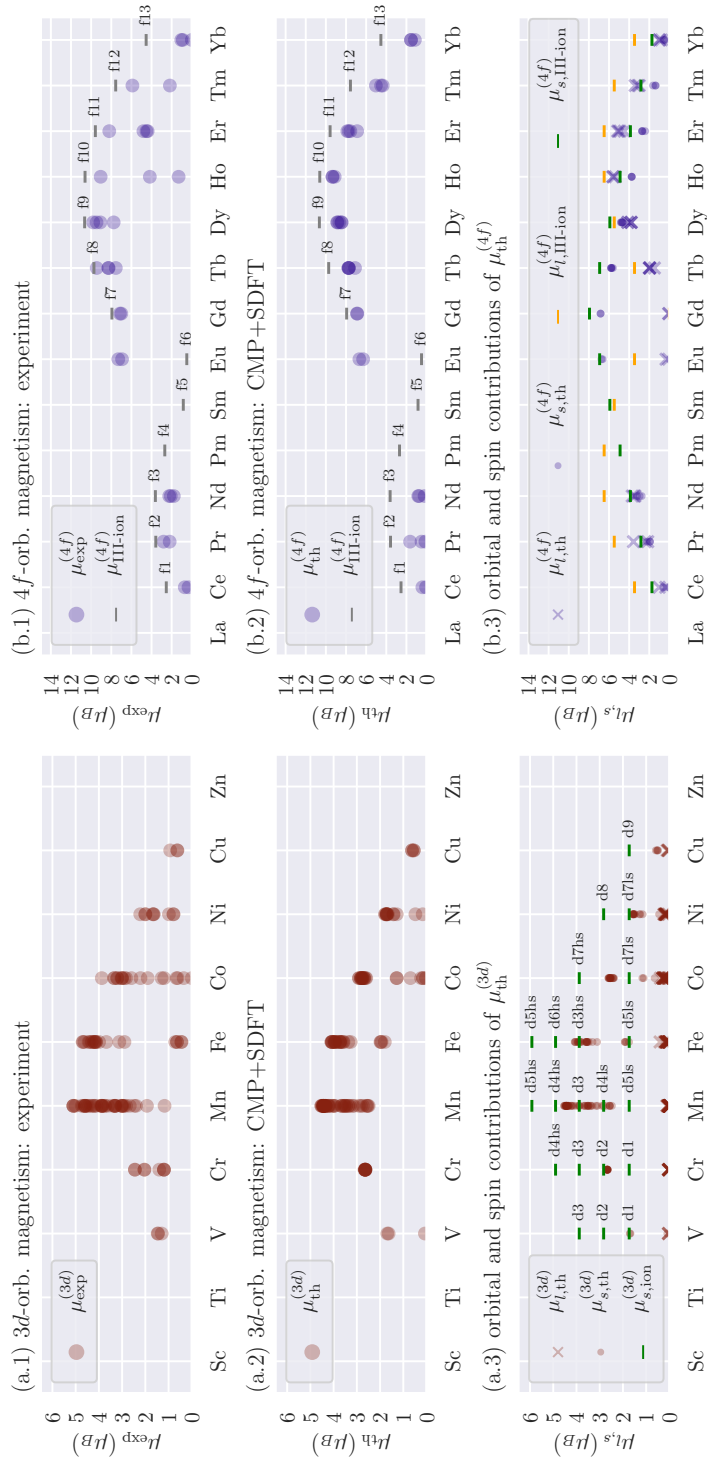


Figure 4.7: Average magnetic moment per site of the CMP+SDFT minimum most similar to experiment w.r.t. its magnetic configuration  $\mu_{th}$  compared to the experimentally measured magnetic moment per site  $\mu_{exp}$ . (a) Color indicates the valence orbital character of the magnetic site. The no. of points on a star mark equals no. of electrons. (b) Color indicates if the material is expected to be frustrated due to odd numbered rings of antiferromagnetic bonds. (c) The color bar shows the filling of the valence orbital of the magnetic site. (d) Color indicates if a single cluster or multiple clusters are magnetic in the material. (e) The color bar shows the normalized orbital angular momentum contribution  $|\mu_l|/(|\mu_l| + |\mu_s|)$ .

Er-clusters in  $\text{Er}_2\text{Sn}_2\text{O}_7$ ,  $\text{Er}_2\text{Ru}_2\text{O}_7$  and  $\text{Er}_2\text{Pt}_2\text{O}_7$ , listed from left to right. In the ionic limit, the ground state electronic configuration of  $\text{Er}^{3+}$  is  $^4I_{15/2}$  with the Landé  $g$ -factor ( $g_j$ ) of  $6/5$ . Therefore,  $\mu_{\text{III-ion}}^{(\text{Er})}$  is estimated to be  $9.58 \mu_{\text{B}}$  using Equation (4.24). We see that  $\mu_{\text{th}}$  of the three outliers are considerably less than  $\mu_{\text{III-ion}}$ . In fact, the three outliers are known candidates for realizing a spin liquid phase due to the presence of magnetic frustration, as described in Ref. [273], [226] and [274] and hence present highly non-trivial cases.

The two outliers with  $\mu_{\text{th}} > 9 \mu_{\text{B}}$  correspond to Ho-clusters. Both data points are contributed by the same material  $\text{HoMnO}_3$ , which contains two inequivalent Ho-sites on top of a Mn-cluster. The latter orders at  $T = 78.5 \text{ K}$  and is well-estimated by CMP+SDFT with  $\mu_{\text{exp}}^{(\text{Mn})} = 3.32 \mu_{\text{B}}$  and  $\mu_{\text{th}}^{(\text{Mn})} = 3.47 \mu_{\text{B}}$ . On the other hand, experimental ordering of the two Ho-clusters is subject to controversy [285, 313–316]. It seems unclear from an experimental perspective whether one or both Ho-sites order even down to approximately 2 K. Generally, the long range ordering of magnetic moments on Ho-sites is suggested to occur at much lower temperature compared to Mn-sites. As mentioned above, a strict comparison of the SDFT result to  $\mu_{\text{exp}}$  is inappropriate in the case that proper long-range ordering cannot be established experimentally. Nevertheless, SDFT can be compared to the ionic limit, similar to the discussion on the three materials containing Er. The ground state electronic configuration of  $\text{Ho}^{3+}$  is  $^5I_8$ , which yields  $\mu_{\text{III-ion}}^{(\text{Ho})} = 10.61 \mu_{\text{B}}$  as an estimate. To conclude, in  $\text{HoMnO}_3$  the  $\mu_{\text{th}}^{(\text{Ho})}$  of the Ho-clusters lie below  $\mu_{\text{III-ion}}^{(\text{Ho})}$  and a strict comparison to  $\mu_{\text{exp}}^{(\text{Ho})}$  is inappropriate.

In Figure 4.7 (b), again  $\mu_{\text{th}}$  and  $\mu_{\text{exp}}$  are compared, but additionally the color indicates whether or not the compound is expected to be frustrated. Here, the expectation of frustration is based on whether nearest neighbors form rings of odd number of magnetic sites. Assuming AFM coupling this geometrically leads to magnetic frustration. Hence, we take advantage of the database being specifically focused on antiferromagnets. Furthermore, rings of even number of magnetic sites could potentially also yield a magnetically frustrated system, if the AFM coupling is anisotropic, such as in the Kitaev model. We hence note, that the definition of expected frustration used here is imprecise and only suitable for a quick superficial classification.

Figure 4.7 (b) shows that indeed the well-estimated  $4f$ -clusters in the large magnetic moment regime are not expected to feature magnetic frustration. The discussed group of three outliers on the other hand are expected to be frustrated. Data points with  $4f$ -orbital character in the small magnetic moment regime  $\mu_{\text{th}} < 2 \mu_{\text{B}}$  are likewise expected to be magnetically frustrated and are not particularly well-estimated. Although, we expect that  $\mu_{\text{th}}$  is overestimated when the system is frustrated, many clusters that are expected to be magnetically frustrated are not necessarily overestimated. And some outliers are—at least in the approximate definition employed here—not expected to be frustrated. However, as we have seen for  $\text{HoMnO}_3$  there might be other non-trivial phenomena preventing a proper long-range order. Hence, the geometrically expected magnetic frustration is not a sufficient indicator for overestimation of the magnetic moment.

Figure 4.7 (c) displays the filling on a colormap from 0 to 1, where 0.5 correspond to half-filling.

Here, the filling is defined as the ratio between the number of  $d$  or  $f$  electrons in each magnetic atom and the number of orbitals. For the number of electrons, we consider the charge neutral state, i.e., the ionized state is not taken account. Less (more) than half-filled  $4f$  and  $5f$ -clusters appear in the underestimated (overestimated) region.

Figure 4.7 (d) addresses the number of magnetic clusters present in a specific compound. The data points corresponding to single cluster (red), and multiple clusters (blue) appear to be evenly distributed. Let us divert the attention towards data points with  $\mu_{\text{th}} \approx 0$ . It should be noted that these are not paramagnetic solutions. Two scenarios can yield  $\mu_{\text{th}} \approx 0$ : Either another cluster bears most of the on-site magnetic moment, or the spin contribution to the magnetic moment  $\mu_s$  is canceled by the orbital contribution to the magnetic moment  $\mu_l$ .

Figure 4.7 (e) shows the normalized orbital contribution

$$\frac{\mu_l}{|\mu_l| + |\mu_s|} \quad (4.27)$$

in SDFT to the total magnetic moment  $\mu_{\text{th}} = |\mu_s + \mu_l|$ . Below the median in the small magnetic moment regime, indeed many clusters with less than half-filled orbitals observe  $\mu_l/(|\mu_l| + |\mu_s|) \approx 0.5$ . In these instances,  $\mu_s$  and  $\mu_l$  adopt opposing signs and thus the contributions in fact cancel. Clusters of heavier lanthanides are well-estimated solely as a result of including  $\mu_l$ . Considering, once more Figure 4.6 (b.3) and a comparison of Figure 4.6 (a.1) and Figure 4.6 (a.2), the agreement between experiment and SDFT could be improved, if the orbital angular momentum would be less quenched in SDFT.

#### 4.2.6 CMP+SDFT+U case study

Hitherto we have discussed the effects of spin-orbit coupling and crystal field splitting on magnetism in compounds with  $3d$  and  $4f$ -orbital character and omitted the careful treatment of another important energy scale in these systems: the electron-electron correlation due to intra-orbital Coulomb repulsion  $U$ . There are various extensions to include electronic correlation beyond SDFT: For instance, SDFT+U [98], SDFT+DMFT [103–108], self-consistent *ab initio* DGA [126] and other diagrammatic extensions beyond DMFT [118, 119]. In fact, these methods have brought important insight in the properties of many compounds closely related to the ones under investigation here [93, 317–319], in particular w.r.t. Mott–Hubbard localization.

A full treatment of electron-electron correlations from first-principles for all materials introduces various challenges and is beyond the scope of this paper. While it is in principle possible to estimate the parameter  $U$  from first-principles by means of constraint random phase approximation (cRPA) [116, 117], the computational cost of this procedure is immense. Therefore, albeit we aim at the prediction of the magnetic ground state from first-principles, we must resort to introducing  $U$  as an adjustable parameter in this section. In particular, we will screen  $U = 2, 3, 4$  eV for  $d$ -orbitals in Mn and  $U = 4, 6, 8$  eV for  $f$ -orbitals of Eu and Gd in accordance with the range of typical  $U$ -values used in literature [317, 319]. Although this amounts to 1545 additional CMP+SDFT+U calculations, we caution the reader, that our efforts to include  $U$  may not be conclusive enough to

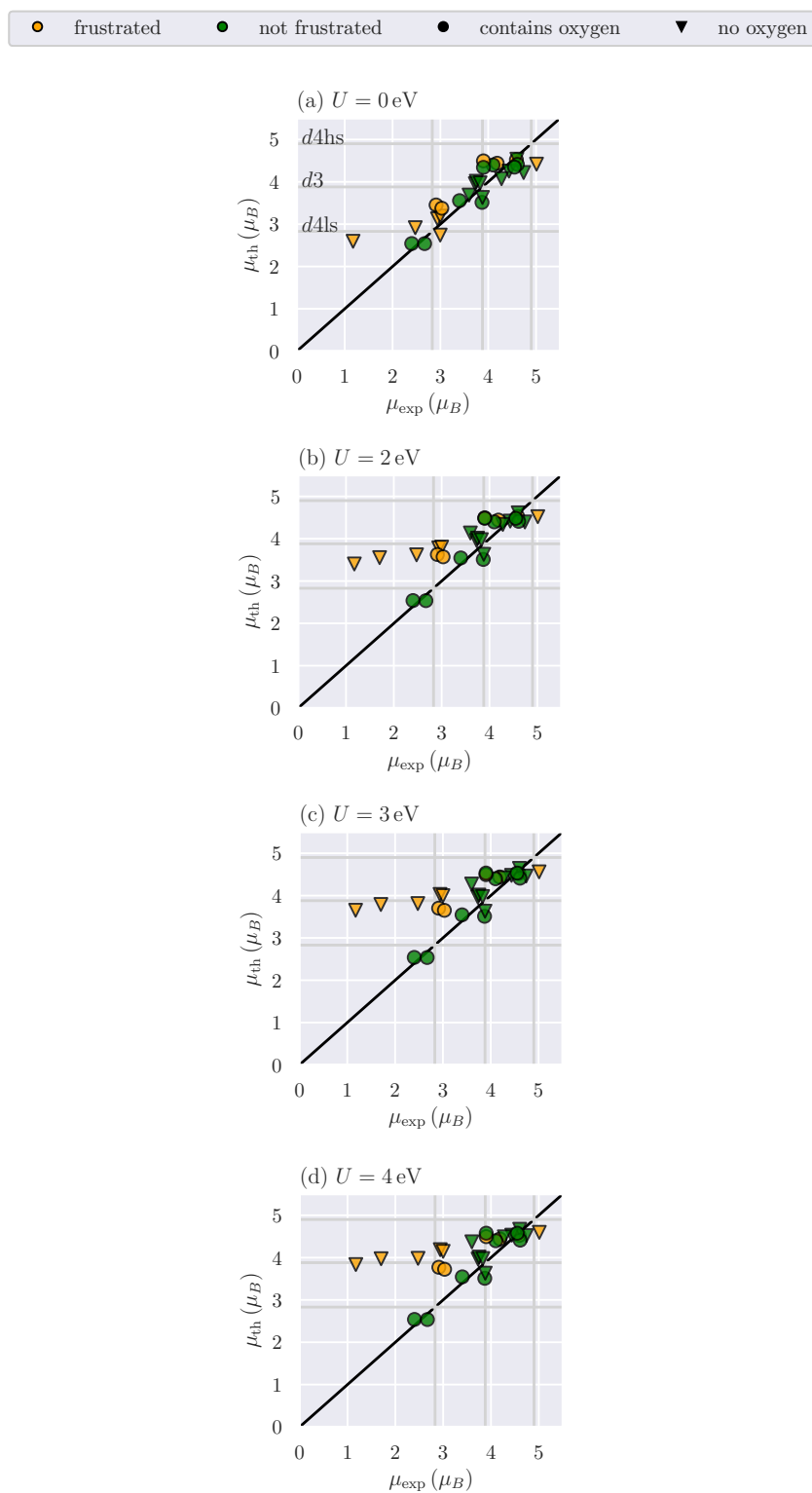


Figure 4.8: Average magnetic moment per Mn-site of the CMP+SDFT+U minimum most similar to the experiment w.r.t. its configuration  $\mu_{th}$  compared to the experimentally measured magnetic moment per site  $\mu_{exp}$ . (a)  $U = 0$  eV, (b)  $U = 2$  eV, (c)  $U = 3$  eV, (d)  $U = 4$  eV.

be generalized to statements about the importance of strong electronic correlations in regard to the prediction of the magnetic ground state.

We have chosen to perform CMP+SDFT+U calculations for all materials containing a single Mn-cluster, because of the following reasons: (i) It is a well-defined subgroup of 28 materials, which is near the minimum sample size necessary to obtain statistically significant results. (ii) The compounds are *not* prone to poor localization due to magnetic frustration in connection with strong spin-orbit coupling, so that the comparison with the experiment stands on solid grounds. (iii) For  $U = 0$  the size of the magnetic moment is over- or underestimated depending on the material, as shown in Figure 4.8 (a). Therefore, we can clearly distinguish if the theoretical magnetic moment  $\mu_{\text{th}}$  gets closer to the experimental value  $\mu_{\text{exp}}$  with increasing  $U$  or if  $\mu_{\text{th}}$  increases regardless of whether it was already overestimated for  $U = 0$ . (iv) The total energy distribution  $\rho_{\text{Mn,MaxOExp}}$  of the CMP+SDFT minimum that yields the maximum overlap with the experiment (MaxOExp) for  $U = 0$  has a strong bias towards the energy minimum. In other words, there is room to improve if MaxOExp were to always agreed with the CMP+SDFT global minimum and also room to deteriorate if  $\rho_{\text{Mn,MaxOExp}}$  were to spread across a wider range of energy.

Furthermore, we have chosen to perform CMP+SDFT+U calculations for all materials containing Eu and Gd, which are the following four compounds:  $\text{EuTiO}_3$ ,  $\text{EuZrO}_3$ ,  $\text{GdVO}_4$ ,  $\text{GdB}_4$ . That is because these  $4f$ -elements are close to half-filling, where the orbital contribution to the on-site magnetic moment  $\mu_l$  vanishes, as can be confirmed in Figure 4.6 (b.3). Thus, spin-orbit coupling is of no importance in these systems and furthermore the crystal field splitting is expected to be small, because the strongly localized  $4f$ -orbitals are well-shielded by the outer  $3d$  and  $4s$ -orbitals. Hence, we expect the Coulomb interaction  $U$  to predominantly determine the dynamics of  $f$ -electrons in these compounds.

The two main questions are as follows: (i) Does including  $U$  improve the prediction of the most stable magnetic structure, and (ii) will the estimation of the on-site magnetic moment improve upon introducing  $U$ ? Without further ado let us present the results of CMP+SDFT+U for compounds containing Mn, Eu and Gd.

We find that CMP+SDFT+U identifies the same local minima as CMP+SDFT with different relative total energy to each other. Thus, MaxOExp is the same at any value of  $U$ . Moreover, the range of the total energy distribution  $\rho_{\text{Mn,tot}}$  is  $U$ -independent and ranges from 0 meV to 1000 meV. Hence, we ask if MaxOExp tends to have the lowest total energy and if this tendency is increased by increasing  $U$ . We note that for the limited number of materials investigated the total energy distribution of MaxOExp  $\rho_{\text{Mn,MaxOExp}}$  for  $U = 0, 2$  eV ranges from 0 meV to approximately 5 meV. Additionally the distribution of  $\rho_{\text{Mn,MaxOExp}}$  is skewed towards lower total energy compared to  $\rho_{\text{Mn,tot}}$ . On the other hand, for  $U = 3, 4$  eV  $\rho_{\text{Mn,MaxOExp}}$  reaches close to 1000 meV, while it remains skewed towards lower total energy. In other words, introducing  $U$  does not assign the correct total energy to the true magnetic ground state found in the experiment in this data. In fact, increasing  $U$  reduces the tendency for MaxOExp to have a particularly low total energy.

Let us now discuss the estimation of the on-site magnetic moment. Figure 4.8 (a) - (d) shows the average on-site magnetic moment  $\mu_{\text{th}}$  of MaxOExp for all materials containing a single Mn-cluster for  $U = 0, 2, 3$  and  $4$ , respectively. The grey lines labeled  $d4\text{hs}$  (high spin),  $d3$  and  $d4\text{ls}$  (low spin) correspond to the spin-only contribution of Mn with formal oxidation  $3+$  and  $4+$ , i.e.  $4$  and  $3$   $d$ -electrons, in an octahedral ligand-field [34], same as in Figure 4.6 (a.3). We see that increasing  $U$  never decreases  $\mu_{\text{th}}$ . For each compound we distinguish whether the crystal contains loops of odd number of magnetic sites and is thus expected to be frustrated. This is indicated by the color of the marker. The shape of the marker implies if the compound contains oxygen. Note that GGA is known to cause overbinding of oxygen to transition metals [320–323]. The effect of increasing  $U$  most strongly increases  $\mu_{\text{th}}$  of frustrated compounds containing no oxygen that are far away from the high spin state for  $U = 0$  eV. The increase of  $\mu_{\text{th}}$  also seems to occur—though less pronounced—in compounds that satisfy only one of the conditions. That is either compounds that are expected to be frustrated albeit containing oxygen or compounds lacking oxygen, although they are not expected to be frustrated.

We speculate that the overbinding of the ligand oxygen could lead to a very strong crystal field splitting. This may protect the low spin state for instance of the compounds near  $\mu_{\text{th}} \approx 2.5 \mu_{\text{B}}$ . Furthermore, we intuitively expect frustration to reduce the size of the magnetic moment, because not all AFM bonds can be satisfied simultaneously and the cost of not satisfying a bond is proportional to the size of the on-site magnetic moment. Introducing  $U$  has a localizing effect and might cause intra-atomic effects to become prevalent over frustration. The on-site magnetic moment is reduced compared to the ionic limit due to delocalization of the Mn-electrons for instance onto the ligands. Moreover, itinerancy may lead to a reduced  $\mu_{\text{th}}$  compared to the ionic limit depending on the partial density of states. Thus, there are various reasons for the on-site magnetic moment ranging from  $1 \mu_{\text{B}}$  to  $5 \mu_{\text{B}}$ . In the investigated Mn-compounds the agreement of  $\mu_{\text{th}}$  with  $\mu_{\text{exp}}$  corroded by introducing  $U$  by means of GGA+U.

The CMP+SDFT+U results for  $\text{EuTiO}_3$ ,  $\text{EuZrO}_3$ ,  $\text{GdVO}_4$ ,  $\text{GdB}_4$  similarly show no improvement by introducing  $U$ . In fact, for  $\text{EuTiO}_3$ ,  $\text{EuZrO}_3$ ,  $\text{GdVO}_4$  the magnetic ground state is falsely predicted to be ferromagnetic for  $U > 4$  eV. Again the same local minima are found, so that in these cases MaxOExp observes increasing total energy by increasing  $U$  relative to the CMP+SDFT+U global minimum at each  $U$ -value. For  $\text{GdB}_4$  the CMP+SDFT+U global minimum is AFM along  $\mathbf{c}$ -direction for all  $U$ -values, while the experimental structure is a hexadecapole in the  $\mathbf{ab}$ -plane. However,  $U = 0$  eV these two magnetic structures are almost degenerate with  $0.5$  meV difference in total energy and for increasing  $U$  the system increasingly prefers the out-of-plane magnetic structure.

The on-site magnetic moment is increased with increasing  $U$  for all four compounds containing Eu and Gd. As can be seen in Figure 4.7 (a) around  $\mu_{\text{exp}} \approx 7 \mu_{\text{B}}$ , the size of  $\mu_{\text{th}}$  is slightly underestimated for  $U = 0$  for all four compounds. Thus, the estimates of  $\mu_{\text{th}} = 6.95 \mu_{\text{B}}$ ,  $6.98 \mu_{\text{B}}$ ,  $7.04 \mu_{\text{B}}$  and  $7.10 \mu_{\text{B}}$  for  $U = 8$  eV for  $\text{EuTiO}_3$ ,  $\text{EuZrO}_3$ ,  $\text{GdVO}_4$  and  $\text{GdB}_4$ , respectively, are closer to

the experimental values  $\mu_{\text{exp}} = 6.93 \mu_{\text{B}}, 7.30 \mu_{\text{B}}, 7.00 \mu_{\text{B}}$  and  $7.14 \mu_{\text{B}}$  than for  $U = 0 \text{ eV}$   $\mu_{\text{th}} = 6.30 \mu_{\text{B}}, 6.67 \mu_{\text{B}}, 6.87 \mu_{\text{B}}$  and  $6.91 \mu_{\text{B}}$ . Let us note that other  $4f$ -compounds observe slightly overestimates on-site magnetic moment and we suspect for these compounds increasing  $U$  would also increase  $\mu_{\text{th}}$ .

Instead of focusing on effects of strong electronic correlations, we speculate that the prediction of the true experimental magnetic ground state could be improved by a different choice of exchange–correlation functional. We would like to point out one recent example of a detailed SDFT+ $U$  study [324] on  $\text{LiOsO}_3$  and  $\text{NaOsO}_3$  testing other exchange–correlation functionals thus far implemented in VASP, including local spin-density approximation (LSDA), PBE’s improved version for solids (PBEsol), the strongly constrained appropriately normed (SCAN) meta-GGA functional and hybrid functional HSE06. By means of scanning different  $U$ -values including predicted ones from cRPA, Liu *et al.* found that none of the considered functionals is capable to simultaneously predict the correct magnetic ground state for  $\text{LiOsO}_3$  and  $\text{NaOsO}_3$  comparing the total energy of two energetically favorable configurations. The treatment of exchange–correlation effects in all of these functionals hitherto implemented in VASP have the underlying assumption that locally the spin-density can be diagonalized. Schematically, an electron thus only couples to an exchange–correlation magnetic field ( $\mathbf{B}_{xc}$ ) that is parallel to its own magnetization. In the last two decades, some—perhaps too poorly noticed—work [325–337] has been done to extend SDFT to include the so-called spin-torque effect, which couples the electron’s spin to  $\mathbf{B}_{xc}$  including antisymmetric terms.

### 4.3 Concluding Remarks

This study is a benchmark of an *ab initio* prediction of the magnetic ground state using a novel approach termed CMP+SDFT. This scheme devises a combination of the cluster multipole (CMP) expansion and the spin-density functional theory (SDFT) for noncollinear magnetism. We find that materials existent in nature are well-described in terms of only few CMPs and infer the CMP basis to be a suitable basis for magnetic configurations. Additionally, the experimental data suggests that the magnetic ground state favors either pure CMPs or linear combinations of CMPs having the same expansion order and same irreducible representation. Guided by this heuristic rule an exhaustive list of initial candidate magnetic configurations for *ab initio* calculations in the framework of SDFT is created.

A high-throughput calculation of 2935 *ab initio* calculations using VASP led to a handful of CMP+SDFT local minima corresponding to different possible magnetic configurations for each material. 90.16% of materials yield the experimental magnetic space group for at least one of the CMP+SDFT local minima. Furthermore, the maximum overlap between the experimental magnetic configuration and the CMP+SDFT local minima exceeds 0.75—with 1 corresponding to equivalence—in 70.99% of all materials.

An *ab initio* prediction of the most stable magnetic configuration in the experiment is guided by a comparison of the total energy in SDFT using GGA of the the possible magnetic configurations



for each material. In particular, the local minimum with the largest overlap with the experiment (MaxOExp) is expected to yield the lowest total energy. Indeed, for materials featuring magnetic sites with  $d$ -orbital magnetism, MaxOExp is in great majority of the cases less than 1 meV above the so-called CMP+SDFT global minimum. On the other hand, the same could not be confirmed for  $f$ -orbital magnetism. In fact, MaxOExp for  $f$ -orbital magnetism shows no tendency towards lower total energy. The implementation of GGA–PBE [76] used in this study did not necessarily assign the lowest total energy to the local minimum with the largest overlap with the experiment.

We have further investigated the effect of including strong electronic correlations on the level of SDFT+ $U$  for materials containing a single Mn-cluster, Eu-cluster or Gd-cluster. Our results show that for the materials we investigated introducing  $U$  has a rather unfavorable influence on the prediction for both, the magnetic ground state and the size of the magnetic moment. In the end of 4.2 E, we speculate that the prediction of the true experimental magnetic ground state could be improved by a different choice of exchange–correlation functional that accounts for the spin-torque effect [325–337], as opposed to focusing on effects of strong electronic correlations.

As far as we know, the only other scheme that aims at the prediction of noncollinear magnetic structures is based on a genetic algorithm by Zheng and Zhang [14]. In their approach only the fittest magnetic structures of each generation survive, which is decided based on the total energy of the magnetic structure. Thus, currently it converges to the global minimum corresponding to a theoretical magnetic ground state that is not necessarily the true magnetic ground state found in the experiment. On the other hand, in CMP+SDFT we yield a set of magnetic configurations that are local minima of the total energy, which is very likely to include the magnetic ground state as we have demonstrated in this paper. Hence, we want to emphasize that CMP+SDFT succeeded to significantly narrow down the number of possible magnetic ground states. This is achieved thanks to a list of candidate magnetic configurations that is tailored to account for details of the symmetry of the crystallographic unit cell. In fact, CMP theory enables SDFT to identify local minima from a feasible number of candidate magnetic configurations, that put data screening and AFM material design within reach. On average, in this study we performed only  $2935/131 = 22.4$  for each material, while in Ref. [14] they performed 30 calculations in each generation. In order to ensure convergence, they ran the evolution for 30 generations which amounts to 900 calculations for one material. This comparison of the number of calculations that are necessary to find the theoretical magnetic ground state, emphasizes that our list of candidates—the CMP basis combined with our heuristic rule and omitting the magnetic configurations corresponding to different magnetic domains of the same magnetic structure—is well-suited to search the space of all possible magnetic configurations.

In addition, this study showed that the on-site magnetic moment could be estimated surprisingly well by GGA without including  $U$ . The precision of the predicted magnetic moment is estimated to be roughly  $\pm 0.5 \mu_B$ . Some outliers arise from a lack of long-range order in the experiment. This can be due to extremely low transition temperatures and magnetic frustration. Despite some explainable outliers, the prediction shows no major systematic over- or underestimation of the on-site magnetic

moment in GGA. In contrast to the experiment, the SDFT calculation grants additional insight into the balance of spin contribution and orbital angular momentum contribution to the total magnetic moment. The first row transition metals prove to be well-described by Russell-Saunders coupling applicable within the strong field regime. In other words, the orbital angular momentum is quenched and the spin-only ionic limit can be used as a reference. The case of lanthanides, on the other hand, is representative for systems in the weak field regime. The on-site magnetic moment is well-described in the  $j$ - $j$  coupling scheme. In the end of 4.2 D, we speculate that GGA might have slightly overestimates the crystal field effects compared to the strength of spin-orbit coupling. Some related discussions of GGA causing an overbinding of ligand oxygen can be found in the literature [320–323]. This could explain why materials governed by crystal field splitting—such as the compounds with  $d$ -orbital magnetism—are assigned more appropriate total energy by GGA. Yet, materials governed by spin-orbit coupling—such as lanthanides—the experimental magnetic configuration is not assigned the lowest total energy by GGA. The balance between spin-orbit coupling and crystal field splitting becomes particularly crucial for lighter  $4f$ -elements and heavier  $3d$ -elements, where the orbital angular momentum is only partially quenched.

We want to end by putting this study into a bigger context and providing an outlook into future works. The starting point of this study was the experimental database MAGNDATA [15]. It conveniently facilitated testing and benchmarking of our *ab initio* scheme to predict the magnetic ground state. Generally, experimental databases [338–347] not only facilitate testing and benchmarking of theoretical methods, but also data mining in the experimentally explored chemical space. Indeed, for some nonmagnetic functional materials an informed search and optimization has led to promising discoveries [348–360]. However so far, apart from few pioneering works [9–13] that are constrained to specific cases, these breakthroughs in material design have not yet been matched by similar advances with respect to AFM materials. Certainly one of the major obstacles is that compared to databases of crystal structures with more than 200 000 entries, MAGNDATA has to date a modest amount of about 1 130 entries. This is because the experimental determination of the magnetic configuration is much more involved than that of the crystal structure. Given this situation, it is an urgent challenge to construct a large-scale computational database of AFM materials. The presented benchmark provides a crucial step in laying a solid foundation for the construction of such a computational database of AFM materials. We are optimistic that *ab initio* calculations will soon be able to reliably predict the magnetic ground state. Based on that, our CMP+SDFT scheme will be able to construct a computational database of magnetic materials with a feasible amount of computational effort. On top of that database, model calculations—using for instance the Liechtenstein method [361–363]—can lead to useful insights in particular w.r.t. the spin wave dispersion and critical temperatures of magnetic phase transitions. Finally, let us note that many magnetic transitions are accompanied by structural transitions. And it might prove imperative to follow a scheme of successively relaxing the atomic position and the magnetic ground state. In the current study we avoided this obstacle by using the atomic positions obtained experimentally.

However, in view of material design, the ability to treat experimentally unknown crystal structures will be of great use.

## Chapter 5

# Spin-density functional theory revisited

In Chapter 2, the basic concept of spin-density functional theory (SDFT) has been introduced. It represents a practical approximation in order to solve the  $2 \times 2$  Hamiltonian derived from Dirac's theory of the relativistic electron briefly presented in Appendix A. We have continuously tried to caution the reader that the approximations must stand the test of time, and should not be accepted without skepticism. The benchmark presented in Chapter 4 indeed reveals that first-principles calculations with the generalized gradient approximation (GGA) in the framework of SDFT for noncollinear magnetism could not accurately reproduce the total energy landscape when varying the magnetic structure. In this chapter, we want to review some literature on first-principles approaches to noncollinear magnetism, which has not received much attention by the community.

We start by recalling that in 1988 J. Kübler and coworkers [73, 74] have extended the local spin-density approach (LSDA) to noncollinear magnetism by assuming that the spin-density could always be diagonalized locally, see Section 2.3.1. That is, an electron at position  $\mathbf{r}$  with spin-magnetic moment  $\mathbf{m}^{(s)}(\mathbf{r})$  sees only a time-averaged local *exchange-correlation* (xc) magnetic field  $\mathbf{B}_{xc}(\mathbf{r})$ , which happens to be always parallel to the magnetic moment:  $\mathbf{m}^{(s)}(\mathbf{r}) \parallel \mathbf{B}_{xc}(\mathbf{r})$ .

In 1999, this assumption is criticized by L. Kleinman [325] because neither LSDA nor GGA can reproduce the experimental wave vector of the spiral-spin-density-wave ground state in  $\gamma$ -Fe [364–366]. Due to this limitation, he proposes an additional term for the xc energy functional, which introduces off-diagonal elements to the xc correlation potential  $v^{xc}$  in Equation (2.31a). While this early work discusses the connection between spiral-spin-density-waves and the off-diagonal elements of the spin-density, the first numerical results of GGA with the proposed correction term [367] fail to improve the results for the ground state of  $\gamma$ -Fe [367]. Thus, there remained a lack of convincing data or any proof that these terms are important. We recall that in 2000, J. Kübler's approach to noncollinear magnetism has been implemented in VASP [76], which we use in our calculations.

Still in 2000, K. Capelle and L. N. Oliveira [368] also propose an xc correlation potential with off-diagonal elements and bring these in connection with the local spin-magnetization. They provide some theoretical arguments reasoning that the Kleinman functional is incomplete and probably fails because of that. In fact, shortly before that, in 1997, K. Capelle and E. K. U. Gross [369] have shown that the xc functional of SDFT is identical to current-DFT on a certain set of densities. A followup work in 2001 [326] combines these findings [368, 369] and K. Capelle, G. Vignale and B. L. Györfy derive the equation of motion for the spin degrees of freedom within time-dependent SDFT in the absence of relativistic effects. They formulated the so-called *zero-torque theorem*:

$$\int d^3r \mathbf{m}^{(s)}(\mathbf{r}, t) \times \mathbf{B}_{xc}(\mathbf{r}, t) \equiv 0, \quad (5.1)$$

that states that  $\mathbf{B}_{xc}$  cannot give rise to a net torque on the system. The zero-torque theorem can be used as an exact constraint when constructing new xc functionals. Perhaps even more interestingly, in the same paper [326], they show that in the static limit with no external magnetic field the divergence of the tensor-valued *xc spin-current*  $\mathbf{J}_{xc}$  is generated by the component of  $\mathbf{B}_{xc}(\mathbf{r})$  perpendicular to  $\mathbf{m}^{(s)}(\mathbf{r})$ , i.e.,

$$\nabla \cdot \mathbf{J}_{xc}(\mathbf{r}) = 2\mu_B(\mathbf{m}^{(s)}(\mathbf{r}) \times \mathbf{B}_{xc}(\mathbf{r})). \quad (5.2)$$

Here, we have introduced the xc spin-current  $\mathbf{J}_{xc}(\mathbf{r})$ , which is defined as the difference between the expectation value of the spin-current operator

$$\hat{J}_{\alpha\beta} = -i\frac{\mu_B^2}{e} \sum_{i=1}^N [\partial_\beta \sigma_\alpha \delta(\mathbf{r} - \mathbf{r}_i) + \delta(\mathbf{r} - \mathbf{r}_i) \sigma_\alpha \partial_\beta], \quad (5.3)$$

with respect to the Kohn–Sham (KS) wave functions  $\psi_{i\sigma}$  and with respect to the many-body state defined by the density matrix  $\rho$  in Equation (2.6):  $\mathbf{J}_{xc}(\mathbf{r}) = \mathbf{J}^{KS}(\mathbf{r}) - \mathbf{J}(\mathbf{r})$ . In other words, the xc spin-current is the anomalous orbital current that carries spin instead of electric charge. The inner product  $\nabla \cdot \mathbf{J}$  is thereby defined to act on the second index of  $\mathbf{J}$ , i.e.  $\partial_\beta J_{\alpha\beta}$ . Equation (5.2) proves that J. Kübler’s assumption, i.e.,  $\mathbf{m}^{(s)}(\mathbf{r}) \parallel \mathbf{B}_{xc}(\mathbf{r})$ , holds exactly for compounds with zero xc spin-current everywhere, i.e.,  $\mathbf{J}_{xc}(\mathbf{r}) \equiv 0$ . This renders any xc functional that assumes  $\mathbf{m}^{(s)}(\mathbf{r}) \parallel \mathbf{B}_{xc}(\mathbf{r})$  improper for the study of spin dynamics.

In order to overcome this serious limitation, the community has been working towards a generalized xc functional [327, 370–374] for noncollinear magnetism, which has lead to a noteworthy publication [328] by S. Sharma, E. K. U. Gross and coworkers in 2007. They employ the *optimized effective potential* (OEP) method, where the xc functional depends explicitly on the KS single-particle functions<sup>1</sup>. In their implementation they formulate a so-called *exact exchange* (EXX) functional, which is an *exchange-only* treatment that employs the Fock energy:

$$E_{xc} = E_x^{EXX}[\psi_{i\sigma}] = -\frac{1}{2} \int d^3r \int d^3r' \sum_{ij}^{occ} \frac{\psi_i^\dagger(\mathbf{r})\psi_i^\dagger(\mathbf{r})\psi_j(\mathbf{r}')\psi_i(\mathbf{r}')}{|\mathbf{r} - \mathbf{r}'|}. \quad (5.4)$$

<sup>1</sup>Consequently, the xc functional implicitly depends on the spin-density.

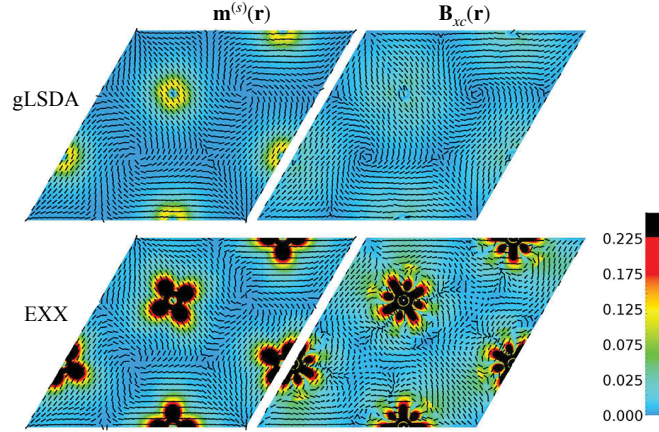


Figure 5.1: Sin-magnetization density  $\mathbf{m}(\mathbf{r})$  and exchange–correlation magnetic field  $\mathbf{B}_{xc}(\mathbf{r})$  field obtained using the local spin-density approximation (LSDA) and exchange-only exact exchange (EXX) functionals for an unsupported Cr-monolayer in Néel state. Reprinted figure with permission from S. Sharma *et al.*, Phys. Rev. Let., vol. 98, no. 19, p. 196405, 2007. [328]

This is then applied to a Cr-monolayer and compared to the gLSDA results, as shown in Figure 5.1: The top row shows the spin-magnetization  $\mathbf{m}^{(s)}(\mathbf{r})$  and the xc magnetic field  $\mathbf{B}_{xc}(\mathbf{r})$  in gLSDA. We see that the magnetization is large in the vicinity of the nuclei indicated by the color code. The inter-atomic non-collinearity is obtained by a change of direction in  $\mathbf{B}_{xc}(\mathbf{r})$  mainly located in the interstitial regions. Overall  $\mathbf{B}_{xc}(\mathbf{r})$  appears quite homogeneous in gLSDA, which is indicated by a monotonous color. The bottom row of Figure 5.1 shows the  $\mathbf{m}^{(s)}(\mathbf{r})$  and  $\mathbf{B}_{xc}(\mathbf{r})$  of the EXX result. First of all, the spin-magnetization is not locally aligned with the xc magnetic field, i.e.,  $\mathbf{m}^{(s)}(\mathbf{r}) \not\parallel \mathbf{B}_{xc}(\mathbf{r})$ . Then,  $|\mathbf{m}^{(s)}(\mathbf{r})|$  and  $|\mathbf{B}_{xc}(\mathbf{r})|$  show flower-like patterns in the magnitude around the nuclei, that remind us of the shape of vector spherical harmonics. To our knowledge, there has been no work on combining the magnetic multipole description with the formulation of exchange–correlation functionals. In view of this result, this might be worth pursuing in future works. Lastly, we note that  $\mathbf{B}_{xc}(\mathbf{r})$  of EXX is much less homogenous compared to gLSDA and that the change of direction is not restricted to the interstitial regions of the Cr-monolayer.

Even with this intriguing result, the search for an appropriate xc functional for noncollinear magnetism is far from over [329,330,375,376] and is continuously fueled by the increasing importance of the spin-torque in spintronics [377]. We want to highlight works by F. G. Eich, S. Pittalis, G. Vignale and E. K. U. Gross [331, 332] in 2013, that discuss the extension of xc functionals including the gradient of the spin-magnetization  $\nabla \cdot \mathbf{m}^{(s)}(\mathbf{r})$ . Then, in 2017, S. Pittalis, G. Vignale and F. G. Eich have published a complete formalism [333] for combining spin-DFT and current-DFT to spin-current-DFT. This is based on the introduction of four potentials via minimal substitution

that can be performed on existing functionals: The scalar xc potential  $v_{xc} = \delta E_{xc}/\delta n(\mathbf{r})$ , the Abelian xc vector gauge potential  $A_{xc,i} = \delta E_{xc}/\delta j_i(\mathbf{r})$ , the non-Abelian xc vector potential  $A_{xc,ij}^{\sigma\sigma'} = \delta E_{xc}/\delta J_{ij}^{\sigma\sigma'}$  and the xc magnetic field  $B_{xc,i} = \delta E_{xc}/\delta m_i^{(s)}(\mathbf{r})$ . However, they mention that in their formulation these fields do not behave as standard Maxwellian fields, in the sense that  $\mathbf{B}_{xc} \neq (\nabla \times \mathbf{A}_{xc})$ .

A year later, in 2018, S. Sharma, E. K. U. Gross, A. Sanna and J. K. Dewhurst propose a simple method to avoid unphysical xc magnetic fields  $\mathbf{B}_{xc}$  by removing the sources. In periodic systems the energy functional is then given in terms of the density  $n(\mathbf{r})$ , the curl of the spin-magnetization  $\nabla \times \mathbf{m}^{(s)}(\mathbf{r})$  and the total magnetization  $\mathbf{M}$ , which appear as boundary terms:

$$E_{xc}[n(\mathbf{r}), \mathbf{m}^{(s)}(\mathbf{r})] \mapsto E_{xc}^{sf}[n(\mathbf{r}), \nabla \times \mathbf{m}^{(s)}(\mathbf{r}), \mathbf{M}]. \quad (5.5)$$

In this source-free formulation the xc gauge field appears formally as  $A_{xc,i}^{sf} = \delta E_{xc}^{sf}/\delta(\nabla \times \mathbf{m}^{(s)}(\mathbf{r}))_i$ . The source-free xc magnetic field hence satisfies  $\mathbf{B}_{xc}^{sf} = \nabla \times \mathbf{A}_{xc}^{sf}$ . The variable conjugate to the boundary term  $\mathbf{M}$  is the external gauge field  $\mathbf{A}_{ext}$ , which therefore has to be included in the calculation. The new constraint can be readily implemented by means of shifting the original xc magnetic field by the divergence of a scalar field:

$$\mathbf{B}_{xc}^{sf} = \mathbf{B}_{xc} + \frac{1}{4\pi} \nabla \Phi, \quad (5.6)$$

where the scalar field  $\Phi$  is given by the Poisson equation

$$\nabla^2 \Phi(\mathbf{r}) = -4\pi \nabla \cdot \mathbf{B}_{xc}(\mathbf{r}). \quad (5.7)$$

An implementation is freely available in the ELK code [181] and has been applied to at least 11 compounds, which are mainly pnictides. The results show that the removal of the source term enhances the noncollinearity in  $\mathbf{B}_{xc}^{sf}$  compared to  $\mathbf{B}_{xc}$ . In their work, they have decided to introduce an intra-orbital Coulomb interaction  $U$  within the  $f$ -orbitals, in order to obtain an on-site magnetic dipole moment comparable to the experiment.

The current challenge seems to be that extensive tests are run on GGA functionals<sup>2</sup> and meta-GGA functionals [378], those applicability is limited to systems with no divergence of the static spin-current. This seems to be equivalent to the suppression of on-site magnetic multipole moments as formulated in Chapter 3. The community working towards the formulation of xc functionals that appropriately accounts for the xc magnetic field seems to be in pursuit of including electron–electron correlation effects directly into the xc functional [334–337, 379, 380]. This includes extensions employing the Hubbard model as well as new formulations of the xc functional including dipole–dipole interaction terms based on the Hartree energy functional.

Finally, let us create a connection to our results. We employ a similar trick as we used in Section B.5 in order to obtain the relation between the convective orbital current operator and the

---

<sup>2</sup>For instance the present work.

orbital angular momentum operator. That is we take the cross product of  $\mathbf{r}$  with the spin-current operator and yield

$$\mathbf{r} \times \hat{\mathbf{J}} = \frac{\mu_B^2}{e} \sum_{i=1}^N [\mathbf{l} \otimes \boldsymbol{\sigma} \delta(\mathbf{r} - \mathbf{r}_i) + \delta(\mathbf{r} - \mathbf{r}_i) \boldsymbol{\sigma} \otimes \mathbf{l}]. \quad (5.8)$$

Then, let us recall the general expression for the spin-orbit term, which is discussed in Section 2.5 and Section A.4, and reads

$$\mathcal{H}_{SO} = \frac{1}{c^2} \frac{K(r)}{r} \frac{dv^{\text{ion}}}{dr} \boldsymbol{\sigma} \cdot \mathbf{l}. \quad (5.9)$$

The spin-orbit coupling is the inner product of  $\boldsymbol{\sigma}$  and  $\mathbf{l}$ , so we can now see that the spin-orbit coupling is proportional to  $\text{Tr}\{\mathbf{r} \times \hat{\mathbf{J}}\} = \sum_{\alpha\beta\gamma} \epsilon_{\alpha\beta\gamma} r_\beta \times \hat{J}_{\alpha\gamma}$ , which corresponds to taking the trace over Equation (5.8). Hence, we have drawn a direct connection between the spin-orbit coupling and the static spin-current tensor. Based on Equation (5.2) and  $\mathbf{m}^{(s)}(\mathbf{r}) \parallel \mathbf{B}_{xc}(\mathbf{r})$ , we speculate that the spin-current tensor is not properly predicted and, thus, the spin-orbit coupling is not obtained correctly in our calculations. In fact, our results presented in Chapter 4 indicate that the prediction of the experimental magnetic ground state is particularly difficult in compounds exhibiting strong spin-orbit coupling compared to crystal field splitting.



## Chapter 6

# Summary and Outlook

The main goal of this thesis is to predict magnetic structures from first-principles to enable material design. We aim to be self-contained by deriving the multipole theory and introducing the cluster multipole (CMP) theory [173] in an easily digestible way. Then, the spin-density functional theory (SDFT) [28–30] is introduced with a particular focus on noncollinear magnetism and extensive benchmark calculations [176] are performed.

The noncollinear magnets at the heart of this work are  $\mathbf{q} = \mathbf{0}$  magnetic structures with transition metals, lanthanides and actinoides as magnetic sites. We show that the CMP basis is a natural choice for magnetic structures by a comparison to experimental data. The analysis prompts us to setup a heuristic rule: The magnetic ground state favors either pure CMPs or linear combinations of CMPs that combine equally weighted CMPs of the same expansion order and same irreducible representation. Based on this, we formulate a scheme to predict magnetic structures from first-principle calculations by

- creating an exhaustive list of candidate magnetic structures that is comprised of the CMP basis and linear combinations according to our heuristic rule, but omitting all magnetic structures that correspond to different magnetic domains of the same magnetic structure. That is we reject all candidates that are equivalent based on symmetry considerations.
- devising the generalized gradient approximation (GGA) in the form proposed by Perdew, Burke and Ernzerhof (PBE) [187] as implemented in VASP version 5.4 [80,81] for noncollinear magnetism [179] in the framework of SDFT proposed by J. Kübler [8,73] using experimentally determined lattice parameters and atomic positions.

The theoretical magnetic ground states of 131 compounds are computed without input of the experimentally known magnetic configurations. The comparison between the theoretical prediction and the experimental data revealed that in 90% of the materials one of the local minima in the total energy functional has the correct magnetic space group. The magnetic anisotropy is relatively well

predicted in compounds with magnetism emerging in  $3d$ -orbitals. In other words, there is a clear tendency that the lowest total energy in SDFT is assigned to the experimental magnetic ground state. On the other hand, the magnetic anisotropy lacks accuracy in compounds with  $4f$ -orbital magnetism, which are representative of systems with strong spin-orbit coupling. Furthermore, we compare the theoretical size of the on-site magnetic moment with the experimental one. Interestingly, we find no systematic over- or underestimations in PBE-GGA, which stands in contrast to the expectation due to the neglect of strong electronic correlation effects in the  $3d$  and  $4f$ -orbitals. The accuracy is approximately  $\pm 0.5 \mu_B$ . A smaller benchmark on 28 compounds containing Mn as magnetic sites and 4 compounds containing either Eu or Gd is employed to investigate the impact of intra-orbital Coulomb repulsion on the level of GGA+ $U$ . It shows that the on-site magnetic moment is enhanced by increasing  $U$ , particularly in frustrated systems and in the absence of oxygen, indifferent to whether the on-site magnetic moment is over- or underestimated at  $U = 0$ . Additionally, the magnetic anisotropy prediction of GGA+ $U$  seems to be lessened compared to GGA, which suggests that the current implementation cannot capture the sensitive balance between the energy scales of spin-orbit coupling, electronic correlation effects, and crystal field splitting.

Nevertheless, CMP+SDFT can successfully narrow down the possible magnetic configurations to a handful of computed configurations with minimal computational effort by creating an exhaustive list of candidate magnetic configurations. This presents a major step towards the prediction of the magnetic ground state as can be emphasized by a comparison with the, to the best of our knowledge, only other method attempting to predict the magnetic ground state from first-principles: The genetic algorithm by F. Zheng and P. Zhang [14]. While they need to perform about 900 calculations to find the theoretical ground state, CMP+SDFT needs on average 22.4 calculations per materials. Furthermore, they find *one* magnetic structure with the lowest total energy, and thus strongly depend on the accuracy of the devised first-principle method. CMP+SDFT on the other hand, obtains a well-defined set of local minima, which enabled us to point out shortcomings of the state-of-the-art SDFT implementations for noncollinear magnetism. Our analysis strengthened a dwelling criticism [325, 326] on a fundamental assumption widely employed in first-principles calculations, i.e., the exchange-correlation magnetic field is assumed to be locally aligned with the spin-magnetization. In this thesis, we review recent literature on exchange-correlation functionals treating noncollinear magnetism, which establishes a relation of the antisymmetric coupling of the exchange-correlation magnetic field with the spin-magnetization and the static spin-current tensor. We then formulate a direct connection to the spin-orbit coupling term in the effective Kohn-Sham Hamiltonian. Based on our benchmark calculation, we speculate that the magnetic anisotropy prediction might be significantly enhanced when devising an exchange-correlation functional that allows off-diagonal terms in the spin-density.

## 6.1 Future perspective

An immediate followup project is to test whether devising an exchange–correlation functional that allows off-diagonal terms in the spin-density improves the prediction of the magnetic ground state in our scheme. We hence need to either use a current implementation of an exchange–correlation functional that treats the exchange–correlation magnetic field on a more general footing, or we need to extend the current version of VASP to account for it. Finally, we can test if the magnetic anisotropy prediction is improved compared to the benchmark [176] presented in this thesis.

At that occasion, it would be interesting if we can use a source-free exchange–correlation magnetic field [328] and, thus, obtain the exchange–correlation gauge potential. That would allow us to obtain the on-site multipoles of the gauge field from first-principles. Conversely, it might be possible to combining the magnetic multipole description with the formulation of an exchange–correlation functionals. The extraction of multipoles of the gauge field from first-principles can be combined with recent attempts to promote magnetic multipoles to take on the role of a proper order parameter. It seems feasible to find explicit expressions to relate the multipoles of the gauge field with linear response of the system. Recent works [381, 382] that point in this direction are done by H. Kusunose, S. Hayami and coworkers. Intriguing questions in this context are (i) how do multipoles interact with each other, and (ii) how do multipoles on the atomic scale interact with multipoles on the inter-atomic scale, i.e., with cluster multipoles.

In fact, also cluster multipoles might be directly connected to the linear response, or at least to the shape of the linear response tensor as shown by the case study on  $\text{Mn}_3\text{Si}$  [48]. This can be done by exploiting the analysis provided by W. Kleiner, M. Seemann and coworkers [5, 6, 43, 159] based on the magnetic Laue group. Furthermore, we recall that in Section 3.3.2 we took on a simplified view, that ignores higher order magnetic moments and convective effects on the atomic scale. In contrast to the experiment, our calculations enabled us to separately consider the spin contribution to the on-site magnetic moment as a source for the cluster multipole and the orbital current as a source for the cluster multipole. In particular, in  $4f$ -materials it may be interesting to separately expand the bound spin and convective angular momentum in the cluster multipole expansion and ask in what linear combinations bound cluster multipoles and convective cluster multipoles appear. Yet another extension to the cluster multipole theory, that will greatly increase the applicability of the theory, is the generalization to the nonstatic case by formulating a Bloch-type wave of cluster multipoles. This could describe the spin-spiral wave as it appears in  $\gamma$ -Fe or, to put it more generally, open the possibility to discuss  $\mathbf{q} \neq \mathbf{0}$  magnetic structures.

Finally, let us recall that the main goal of this thesis has been to predict magnetic structures from first-principles *to enable material design*. It is paramount to formulate design criteria for new magnetic compounds that could find applications in spintronics or energy generation. These criteria may be based on insights acquired by answering questions raised in this section. Moreover, the present CMP+SDFT scheme should be extended to compute the electronic response, which requires tools commonly available to the DFT community to be adapted to the treatment of noncollinear

magnetism. In order to name one example, it would be highly desirable to compute symmetry-adapted Wannier orbitals to obtain a localized basis, that obeys the magnetic space group symmetry of the crystal. Currently, the generation of symmetry-adapted Wannier orbitals is only available for the paramagnetic space group symmetry of the crystal [383,384]. Furthermore, calculations at finite temperature would open the possibility to discuss phase transitions. This may be done by employing model calculations on top of the first-principles calculation, using for instance the Liechtenstein method [361–363] in order to compute the spin-wave dispersion and critical temperatures of magnetic phase transitions. This will be particularly useful when we create a computational database of magnetic materials. Preferably, the database should be based on crystals that are found in crystal structure optimization, instead of experimentally determined lattice parameters and atomic positions. This is to achieve independence of whether a material has already been experimentally realized, which can be highly challenging. The first project [385] to combine CMP+SDFT with the so-called minima hopping method [386], which is a crystal structure optimization method, is currently in its final stage: T. Yu and coworkers have proposed a design scheme for electrides<sup>1</sup> and this project shows how a previously unknown material could be designed step-wise by optimizing the crystal structure, predicting the magnetic ground state and finally computing specific material properties such as magnon spectra.

---

<sup>1</sup>Electrides are materials with interstitial electrons, which are not bound to a nuclei but form ionic bound within the crystal. Their very low work function and intriguing magnetic and topological nature make them very interesting potential functional materials.

# Appendices

# Appendix A

## Dirac theory

The time dependent Schrödinger equation

$$i\hbar \frac{\partial}{\partial t} |\Psi(t)\rangle = \mathcal{H} |\Psi(t)\rangle \quad (\text{A.1})$$

is not compatible with relativity due to the choice of the Hamiltonian and the fixed number of particles<sup>1</sup> it describes. In Dirac theory [21] time and space coordinates  $\mathbf{r} = (x^1, x^2, x^3)$  are put on equal footing by the ansatz

$$i\hbar \frac{\partial}{\partial t} \Psi = \mathcal{H}_D \Psi, \quad (\text{A.2})$$

$$\mathcal{H}_D = (-i\alpha_i \partial_i + \beta m), \quad (\text{A.3})$$

where the *relativistic dispersion relation*  $E = \sqrt{\mathbf{p}^2 c^2 + m^2 c^4}$  must be satisfied. Here,  $\partial_i = \partial / (\partial x^i)$  is the derivative and defines the momentum as usual via  $\mathbf{p} = -i\nabla$ .

A small calculation, that we will do in a moment, yields the *algebra* for  $\alpha_i$  and  $\beta$ :

$$\{\alpha_i, \alpha_j\} = 2\delta_{ij}, \quad (\text{A.4})$$

$$\{\alpha_i, \beta\} = 0, \quad (\text{A.5})$$

$$\beta^2 = 1, \quad (\text{A.6})$$

where  $\{\alpha_i, \alpha_j\} = \alpha_i \alpha_j + \alpha_j \alpha_i$  is the anticommutator and  $\delta_{ij} = 1$  if  $i = j$  and zero otherwise. For the sake of readability and simplicity let us switch to *natural units*  $\hbar = c = 1$  and derive above

---

<sup>1</sup>Klein's paradox shows that the Dirac equation can be interpreted as a single-particle theory only as long as there are no external forces and energies which are comparable to the mass scale  $m$ .

statements. The small calculation goes as follows:

$$E^2 = \mathbf{p}^2 + m^2 = -\partial_i \partial_i + m^2, \quad (\text{A.7})$$

$$\mathcal{H}_D^2 = (i\alpha_i \partial_i + \beta m) (i\alpha_j \partial_j + \beta m) \quad (\text{A.8})$$

$$= -\underbrace{\alpha_i \alpha_j \partial_i \partial_j}_{=\partial_i \partial_i} - i \underbrace{(\alpha_i \beta + \beta \alpha_i)}_{=0} m \partial_i + \underbrace{\beta^2}_{=1} m^2. \quad (\text{A.9})$$

By comparing the first and the last line we straightforwardly obtain Equations (A.4) and (A.5). Equation (A.6) on the other hand is obtained by exploiting that  $\partial_i \partial_j$  is symmetric in indices  $i, j$  and hence without loss of generality we can symmetrize  $\alpha_i \alpha_j = (\alpha_i \alpha_j + \alpha_j \alpha_i) / 2$ . We find

$$\alpha_i \alpha_j \partial_i \partial_j = \partial_i \partial_i \quad (\text{A.10})$$

$$\frac{1}{2} (\alpha_i \alpha_j + \alpha_j \alpha_i) \partial_i \partial_j = \delta_{ij} \partial_i \partial_j \quad (\text{A.11})$$

$$(\alpha_i \alpha_j + \alpha_j \alpha_i) \partial_i \partial_j = 2\delta_{ij} \partial_i \partial_j, \quad (\text{A.12})$$

$$(\alpha_i \alpha_j + \alpha_j \alpha_i) = \{\alpha_i, \alpha_j\} = 2\delta_{ij}. \quad (\text{A.13})$$

The last line corresponds to Equation (A.6).

The algebra defined in Equations (A.4) to (A.6) can be fulfilled by  $4 \times 4$  matrices and no lower dimension. The *Dirac spinor*  $\Psi$  consequently has 4 elements that are not corresponding to  $3 + 1$  dimensions of space-time. The interpretation of the elements  $\Psi_\nu$  with  $\nu = 1, 2, 3, 4$  depends on the chosen representation. In the non-relativistic limit—that we are interested in in the scope of this thesis—the appropriate representation of the matrices  $\alpha_i$  and  $\beta$  is the so-called *Dirac representation*:

$$\alpha_i = \begin{pmatrix} 0 & \sigma_i \\ \sigma_i & 0 \end{pmatrix}, \quad \beta = \begin{pmatrix} 1_{2 \times 2} & 0 \\ 0 & -1_{2 \times 2} \end{pmatrix}, \quad (\text{A.14})$$

$$\sigma_1 = \begin{pmatrix} 0 & 1 \\ 1 & 0 \end{pmatrix}, \sigma_2 = \begin{pmatrix} 0 & -i \\ i & 0 \end{pmatrix}, \sigma_3 = \begin{pmatrix} 1 & 0 \\ 0 & -1 \end{pmatrix}, 1_{2 \times 2} = \begin{pmatrix} 1 & 0 \\ 0 & 1 \end{pmatrix} \quad (\text{A.15})$$

with Pauli matrices  $\sigma_i$ .

## A.1 Solution of the Dirac equation

Let us now find the solution of the Dirac equation in order to gain a physical interpretation of  $\Psi_\nu$ . Starting point is a plane wave ansatz

$$\Psi_\nu^{(+)}(t, \mathbf{r}) = e^{-i(Et - \mathbf{p} \cdot \mathbf{r})} u_\nu(E, \mathbf{p}), \quad (\text{A.16})$$

$$\Psi_\nu^{(-)}(t, \mathbf{r}) = e^{i(Et - \mathbf{p} \cdot \mathbf{r})} v_\nu(E, \mathbf{p}). \quad (\text{A.17})$$

Here, the first line corresponds to a solution with positive energy corresponding to electrons propagating forward in time. The second line describes an unbound electron in vacuum with negative

energy, which was difficult to interpret at the time. Today, this is known to describe the antiparticle of electrons: positrons.

In the rest frame  $\mathbf{p} = 0$ ,  $E = m$  we obtain four solutions by plugging in Equations (A.16) and (A.17) in Equation (A.3)

$$\left(-i\frac{\partial}{\partial t} - i\alpha_{i,\mu\nu}\partial_i + \beta_{\mu\nu}m\right)\Psi_{\nu}^{(+/-)}(m, \mathbf{0}) = 0. \quad (\text{A.18})$$

Without normalization we find

$$u^1 = (1, 0, 0, 0)^T, u^2 = (0, 1, 0, 0)^T, v^1 = (0, 0, 1, 0)^T, v^2 = (0, 0, 0, 1)^T. \quad (\text{A.19})$$

In other words, in the rest frame electrons have nonzero components in  $\nu = 1, 2$  and positrons in  $\nu = 3, 4$ . The solutions in Equation (A.19)  $u^s$  and  $v^s$  gained an additional label  $s$ . A rotation about the  $z$ -axis shows that  $\nu = 1, 3$  correspond to spin up ( $s=1$ ), while  $\nu = 2, 4$  correspond to spin down in the rest frame ( $s=2$ ) in Equation (A.19).

The general solution of the non-interacting Dirac equation can finally be obtained by applying a Lorentz boost to the Dirac spinor of the rest frame. Normalization then leads to:

$$\Psi^{(+,s)}(t, \mathbf{r}) = e^{-i(Et - \mathbf{p}\cdot\mathbf{r})} \frac{1}{\sqrt{2m(m+E)}} \begin{pmatrix} (E+m)\varphi^s \\ \boldsymbol{\sigma}\cdot\mathbf{p} \varphi^s \end{pmatrix}, \quad (\text{A.20})$$

$$\Psi^{(-,s)}(t, \mathbf{r}) = e^{i(Et - \mathbf{p}\cdot\mathbf{r})} \frac{1}{\sqrt{2m(m+E)}} \begin{pmatrix} \boldsymbol{\sigma}\cdot\mathbf{p} \chi^s \\ (E+m)\chi^s \end{pmatrix}. \quad (\text{A.21})$$

Here, we introduce the two-component spinors  $\varphi^s$  and  $\chi^s$  with  $s = 1, 2$ . The so-called *large component spinor*  $\varphi^1 = (1, 0)^T$  and  $\varphi^2 = (0, 1)^T$ , and the *small component spinor*  $\chi^1 = (1, 0)^T$  and  $\chi^2 = (0, 1)^T$ . This description will become transparent by deriving the Pauli Hamiltonian in Section A.3.

## A.2 Electromagnetic coupling

The relativistic formulation of Maxwell's equations introduces the field tensor  $F^{\mu\nu}$ , which is composed of  $\mathbf{E}$  and  $\mathbf{B}$  and can be defined via the four-vector gauge field  $A^\mu = (\phi, \mathbf{A})$  as

$$F^{\mu\nu} = \partial^\mu A^\nu - \partial^\nu A^\mu. \quad (\text{A.22})$$

Then, the Maxwell's equations read

$$\partial^\mu F^{\mu\nu} = j^\nu, \quad (\text{A.23})$$

$$\partial^\mu \epsilon_{\mu\nu\sigma\rho} F_{\sigma\rho} = 0, \quad (\text{A.24})$$

where we combine the electric charge  $\rho$  and the electric current  $\mathbf{j}$  in  $j^\mu = (\rho, \mathbf{j})$ . In order to couple electrons to an electromagnetic field one would usually introduce a source term  $j^\nu A_\nu$  into the Hamiltonian. In the Dirac theory, the current reads

$$j^\nu(\mathbf{r}, t) = e(\Psi^\dagger(\mathbf{r}, t)\Psi(\mathbf{r}, t), \Psi^\dagger(\mathbf{r}, t)\boldsymbol{\alpha}\Psi(\mathbf{r}, t)). \quad (\text{A.25})$$



Conveniently, writing  $\mathcal{H}_D + j^\nu A_\mu$  yields exactly the same as performing the so-called *minimal substitution* in  $\mathcal{H}_D$ :

$$\frac{\partial}{\partial t} \rightarrow \frac{\partial}{\partial t} + ie\phi, \quad \partial_i \rightarrow \partial_i - ieA_i. \quad (\text{A.26})$$

Finally, the four-vector vector gauge field can be computed by means of the Poisson equations

$$\nabla^2 \phi = -4\pi\rho, \quad (\text{A.27})$$

$$\nabla^2 \mathbf{A} = -4\pi\mathbf{j}. \quad (\text{A.28})$$

Note that, performing minimal substitution on Equation (A.2), c.f. Equation (A.40), we can write

$$\Psi(\mathbf{r}, t) = \frac{1}{m} \left[ \beta \left( i\beta \frac{\partial}{\partial t} - e\phi \right) - \beta \boldsymbol{\alpha} (-i\nabla - e\mathbf{A}) \right] \Psi(\mathbf{r}, t). \quad (\text{A.29})$$

By defining the Dirac adjoint spinor

$$\bar{\Psi} = \Psi^\dagger \beta, \quad (\text{A.30})$$

we can obtain an analogous expression from the adjoint of the Dirac equation and perform the Gordon decomposition, see Ref. [8] p. 44 ff, to obtain new expressions for the density and current based on the original definition. Both are split into the convective term<sup>2</sup>, which are reminiscent of the current and density of spinless, nonrelativistic electrons, and the internal (or bound) contributions. The density reads

$$\rho = \rho_{\text{conv}} + \rho_{\text{int}}, \quad (\text{A.31a})$$

$$\rho_{\text{conv}} = -i\mu_B \left[ \bar{\Psi} \frac{\partial \Psi}{\partial t} - \left( \frac{\partial \bar{\Psi}}{\partial t} \right) \Psi \right] + \frac{e^2 \phi}{m} \bar{\Psi} \Psi, \quad (\text{A.31b})$$

$$\rho_{\text{int}} = -\nabla \cdot \mathbf{P}, \quad (\text{A.31c})$$

and the current reads

$$\mathbf{j} = \mathbf{j}_{\text{conv}} + \mathbf{j}_{\text{int}}, \quad (\text{A.32})$$

$$\mathbf{j}_{\text{conv}} = i\mu_B \left[ \bar{\Psi} \nabla \Psi - (\nabla \bar{\Psi}) \Psi \right] + \frac{e^2 \mathbf{A}}{m} \bar{\Psi} \Psi, \quad (\text{A.33})$$

$$\mathbf{j}_{\text{int}} = \nabla \times \mathbf{M} + \frac{\partial \mathbf{P}}{\partial t}, \quad (\text{A.34})$$

where  $\mu_B = e/(2m)$  is the Bohr magneton, and we defined the magnetization  $\mathbf{M}$  and polarization  $\mathbf{P}$

$$\mathbf{M} = \frac{e}{2m} \bar{\Psi} \boldsymbol{\Sigma} \Psi = -|g_s| \bar{\Psi} \frac{1}{2} \boldsymbol{\Sigma} \Psi \mu_B, \quad (\text{A.35a})$$

$$\mathbf{P} = -\bar{\Psi} (-i\boldsymbol{\alpha}) \Psi \mu_B, \quad (\text{A.35b})$$

---

<sup>2</sup>From Latin *convehere*, to carry together. The convective term includes the dynamic, unbound contributions to the density and the current. In Section 3.1, it appears as orbital angular momentum current to obtain ??.

with  $|g_s| \approx 2$  and the  $4 \times 4$  matrix

$$\Sigma_i = \begin{pmatrix} \sigma_i & 0 \\ 0 & \sigma_i \end{pmatrix}. \quad (\text{A.36})$$

### A.3 Pauli Hamiltonian

The Pauli Hamiltonian is the non-relativistic limit of Equation (A.3) when electromagnetic coupling is introduced. The final result reads

$$i \frac{\partial}{\partial t} \varphi = \mathcal{H}_{Pauli} \varphi, \quad (\text{A.37})$$

$$\mathcal{H}_{Pauli} = -\frac{\nabla^2}{2m} + e\phi - \mu_B (\mathbf{L} + 2\mathbf{S}) \cdot \mathbf{B}. \quad (\text{A.38})$$

Without further ado, let us introduce electromagnetic coupling by *minimal substitution*:

$$\frac{\partial}{\partial t} \rightarrow \frac{\partial}{\partial t} + ie\phi, \quad \partial_i \rightarrow \partial_i - ieA_i, \quad (\text{A.39})$$

$$i \frac{\partial}{\partial t} \Psi = \mathcal{H}_D \Psi + \mathcal{H}_{int} \Psi, \quad (\text{A.40})$$

$$\mathcal{H}_{int} = -e\alpha_i A_i + e\phi \quad (\text{A.41})$$

This defines the interacting problem with interacting Dirac Hamiltonian  $\mathcal{H}_D + \mathcal{H}_{int}$ .

Next, we go to the non-relativistic limit by assuming  $E - m \ll m$ . It is reasonable to split off the rest mass and start with the ansatz:

$$\Psi(t, \mathbf{r}) = e^{-it} \begin{pmatrix} \varphi(t, \mathbf{r}) \\ \chi(t, \mathbf{r}) \end{pmatrix} \quad (\text{A.42})$$

With Equation (A.40) we find two equations:

$$i \frac{\partial \varphi}{\partial t} = -i\sigma_i \partial_i \chi - e\sigma_i A_i \chi + e\phi \varphi, \quad (\text{A.43})$$

$$i \frac{\partial \chi}{\partial t} = -i\sigma_i \partial_i \varphi + 2m\chi - e\sigma_i A_i \varphi + e\phi \chi \quad (\text{A.44})$$

In Equation (A.44), we can neglect  $i \frac{\partial \chi}{\partial t} \propto E\chi \ll 2m\chi$  and assume weak potential  $e\phi \ll m$  and yield

$$\chi(t, \mathbf{r}) \approx \frac{1}{2m} \boldsymbol{\sigma} \cdot (-i\nabla - e\mathbf{A}) \varphi(t, \mathbf{r}) \ll \varphi(t, \mathbf{r}). \quad (\text{A.45})$$

Here, we see the justification to call  $\chi$  small component spinor and  $\varphi$  large component spinor. This can be plugged into Equation (A.43) to obtain:

$$i \frac{\partial \varphi}{\partial t} = \frac{1}{2m} [\boldsymbol{\sigma} \cdot (-i\nabla - e\mathbf{A})]^2 \varphi + e\phi \varphi \quad (\text{A.46})$$

$$= \frac{1}{2m} [(-i\nabla - e\mathbf{A})^2 - e\boldsymbol{\sigma} \cdot \mathbf{B}] \varphi + e\phi \varphi. \quad (\text{A.47})$$

Here we used the identity  $\sigma_i \sigma_j = \delta_{ij} + i\epsilon_{ijk} \sigma_k$  with the antisymmetric Levi Cevita symbol  $\epsilon_{ijk}$  in the following steps

$$[\boldsymbol{\sigma} \cdot (-i\nabla - e\mathbf{A})]^2 = \quad (\text{A.48})$$

$$= \sigma_i \sigma_j (-i\partial_i - eA_i) (-i\partial_j - eA_j) \quad (\text{A.49})$$

$$= \delta_{ij} (-i\partial_i - eA_i) (-i\partial_j - eA_j) + i\epsilon_{ijk} \sigma_k (-i\partial_i - eA_i) (-i\partial_j - eA_j). \quad (\text{A.50})$$

Note that in the second term in the last line we can drop the symmetric part as  $\epsilon_{ijk}$  is fully antisymmetric

$$\begin{aligned} & (-i\partial_i - eA_i) (-i\partial_j - eA_j) f(r) \\ &= -\partial_i \partial_j f(r) + ie [A_i (\partial_j f(r)) + A_j (\partial_i f(r))] + ie f(r) (\partial_i A_j) + e^2 A_i A_j f(r) \end{aligned} \quad (\text{A.51})$$

$$\rightarrow (-i\partial_i - eA_i) (-i\partial_j - eA_j) \stackrel{\text{a.s.}}{=} ie (\partial_i A_j). \quad (\text{A.52})$$

And then we introduce the magnetic field  $\mathbf{B} = \nabla \times \mathbf{A}$  in order to write its components as

$$B_k = \epsilon_{ijk} \partial_i A_j. \quad (\text{A.53})$$

With this we can write Equation (A.50) as Equation (A.47).

Finally, we assume a constant magnetic field to write  $\mathbf{A} = (\mathbf{B} \times \mathbf{r})/2$  and let  $\mathbf{A}$  be weak and fulfill Coulomb gauge  $\nabla \cdot \mathbf{A} = 0$  in order to write:

$$(-i\nabla - e\mathbf{A})^2 \approx -\nabla^2 - e(\mathbf{r} \times \mathbf{p}) \cdot \mathbf{B}. \quad (\text{A.54})$$

This approximation is obtained by the following steps

$$(-i\nabla - e\mathbf{A})^2 f(r) \quad (\text{A.55})$$

$$= -\nabla^2 f(r) + ie\nabla(\mathbf{A}f(r)) + ie\mathbf{A}\nabla(f(r)) + e^2 \underbrace{\mathbf{A}^2}_{\approx 0} f(r) \quad (\text{A.56})$$

$$= -\nabla^2 f(r) + ie \underbrace{2\mathbf{A}}_{\mathbf{B} \times \mathbf{r}} \cdot \nabla(f(r)) + ie \underbrace{\nabla(\mathbf{A})}_{=0} f(r) \quad (\text{A.57})$$

$$= -\nabla^2 f(r) + ie \underbrace{(\mathbf{B} \times \mathbf{r}) \cdot \nabla(f(r))}_{(\mathbf{r} \times \nabla(f(r))) \cdot \mathbf{B}}. \quad (\text{A.58})$$

The last step is possible because  $\mathbf{B}$  is constant. Using  $\mathbf{p} = -i\nabla$  we obtain Equation (A.54).

The weak constant field approximation Equation (A.54) can be plugged into Equation (A.47). Considering the definition of the *Bohr magneton*  $\mu_B = e/(2m)$  as well as introducing angular momentum  $\mathbf{L} = (\mathbf{r} \times \mathbf{p})$  and spin  $\mathbf{S} = 2\boldsymbol{\sigma}$  we obtain the final result. That is the Pauli Hamiltonian

for the large component  $\varphi(t, \mathbf{r})$ :

$$i\frac{\partial}{\partial t}\varphi(t, \mathbf{r}) = \frac{1}{2m} [-\nabla^2 - e(\mathbf{r} \times \mathbf{p}) \cdot \mathbf{B} - e\boldsymbol{\sigma} \cdot \mathbf{B}] \varphi(t, \mathbf{r}) + e\phi\varphi(t, \mathbf{r}) \quad (\text{A.59})$$

$$= \left[ -\frac{\nabla^2}{2m} + e\phi - \underbrace{\frac{e}{2m}(\mathbf{r} \times \mathbf{p}) \cdot \mathbf{B}}_{\mu_B \mathbf{L}} - \underbrace{\frac{e}{2m}\boldsymbol{\sigma} \cdot \mathbf{B}}_{\mu_B 2\mathbf{S}} \right] \varphi(t, \mathbf{r}) \quad (\text{A.60})$$

$$= \mathcal{H}_{Pauli} \varphi(t, \mathbf{r}) \quad (\text{A.61})$$

$$\mathcal{H}_{Pauli} = -\frac{\nabla^2}{2m} + e\phi - \mu_B (\mathbf{L} + 2\mathbf{S}) \cdot \mathbf{B}. \quad (\text{A.62})$$

## A.4 Relativistic corrections

In the preceding section we have seen how decoupling the large and small components of a Dirac spinor in the nonrelativistic limit can lead to the Pauli Hamiltonian. This enabled us to highlight some of its physical content. The systematic expansion in a series of powers of  $E_{\text{kin}}/m$  has been worked out by Foldy and Wouthuysen [72]. Here,  $E_{\text{kin}} = \sqrt{m^2 + p^2} - m$ . The goal is to find a block-diagonal  $\mathcal{H}'$  by use of a unitary transformation  $\Psi' = e^{iS}\Psi$  such that

$$i\frac{\partial}{\partial t}\Psi' = e^{iS} \left( \mathcal{H}e^{-iS} - i\frac{\partial}{\partial t}e^{-iS} \right) \Psi' = \mathcal{H}'\Psi'. \quad (\text{A.63})$$

For  $\mathcal{H} = \mathcal{H}_D + \mathcal{H}_{int}$  this can be done iteratively, where systematically the remainder is on the order of  $\mathcal{O}(\frac{1}{m^n})$  in iteration  $n$ . In other words, the Hamiltonian after iteration  $n$  has the form  $\mathcal{H}^{(n)} = \beta m + \mathcal{E}^{(n)} + \mathcal{O}^{(n)}$ , where  $\mathcal{O}^{(n)} = \mathcal{O}(\frac{1}{m^n})$ . After 3 iterations one finds

$$\mathcal{H}^{(3)} = \beta \left[ m + \frac{(\mathbf{p} - e\mathbf{A})^2}{2m} - \frac{\mathbf{p}^4}{8m^3} \right] + e\phi - \beta \mu_B \boldsymbol{\sigma} \cdot \mathbf{B} \quad (\text{A.64})$$

$$+ \left( -i\frac{e}{8m^2} \boldsymbol{\sigma} \cdot (\nabla \times \mathbf{E}) - \frac{1}{2m} \mu_B \boldsymbol{\sigma} \cdot (\mathbf{E} \times \mathbf{p}) \right) \quad (\text{A.65})$$

$$+ \frac{e}{8m^2} \nabla \cdot \mathbf{E} + \mathcal{O}^{(3)}. \quad (\text{A.66})$$

The first line yields the Pauli Hamiltonian in the weak constant field limit, where Equation (A.54) holds, plus a relativistic correction of the kinetic energy. The second line reduces to the spin-orbit coupling term, when focusing on static spherical potentials  $V(r)$  yielding  $\mathbf{E} = -\frac{dV}{dr} \frac{\mathbf{r}}{r}$  and  $(\nabla \times \mathbf{E}) = 0$ . Then  $(\mathbf{r} \times \mathbf{p})$  becomes  $\mathbf{L}$ . The last term arises as a correction due to the fluctuations of the position of an electron<sup>3</sup> and is called Darwin term.

<sup>3</sup>Consider an electron at  $\mathbf{x}$  with  $\langle \delta\mathbf{r} \rangle = 0$  but  $\langle (\delta\mathbf{r})^2 \rangle > 0$ . This entails a shift in the electrostatic energy according to

$$e\langle \phi(\mathbf{x} + \delta\mathbf{x}) \rangle = e\phi(\mathbf{r}) + \frac{e}{2} \nabla^2 \phi \frac{1}{3} \langle (\delta\mathbf{r})^2 \rangle \approx e\phi(\mathbf{r}) + \frac{e}{2} \nabla \cdot \mathbf{E} \frac{1}{3} \frac{1}{m^2}. \quad (\text{A.67})$$

In the last step we used that the fundamental uncertainty is of the order of the Compton wavelength  $\langle (\delta\mathbf{r})^2 \rangle \approx 1/m^2$ .

We summarize the Hamiltonian with all relativistic corrections in the weak constant field limit with a static spherical potential:

$$i \frac{\partial}{\partial t} \Psi' = [\mathcal{H}_{kin} + \mathcal{H}_{mag} + \mathcal{H}_V + \mathcal{H}_{SO} + \mathcal{H}_{Darwin}] \Psi', \quad (\text{A.68a})$$

$$\mathcal{H}_{kin} = \beta \left[ m - \frac{\nabla^2}{2m} - \frac{\mathbf{p}^4}{8m^3} \right], \quad (\text{A.68b})$$

$$\mathcal{H}_{mag} = -\beta \mu_B (\mathbf{L} + 2\mathbf{S}) \cdot \mathbf{B}, \quad (\text{A.68c})$$

$$\mathcal{H}_V = eV, \quad (\text{A.68d})$$

$$\mathcal{H}_{SO} = \frac{\mu_B}{2mr} \left( \frac{dV}{dr} \right) \mathbf{L} \cdot \boldsymbol{\sigma}, \quad (\text{A.68e})$$

$$\mathcal{H}_{Darwin} = \frac{e}{8m^2} \left( \frac{d^2V}{dr^2} \right). \quad (\text{A.68f})$$

Although this is the traditional way to obtain relativistic corrections, there are some works claiming  $E_{kin}/m$  cannot be guaranteed to be small everywhere in space for Coulomb potentials. Indeed, for  $r \rightarrow \infty$  we find  $E_{kin}$  becomes a large positive number. In principle, a bound electron would only render a finite expectation value at  $\mathbf{r} = 0$  for  $\mathbf{l} = 0$ , i.e. the  $s$ -orbital, for which there is no spin-orbit coupling. Nevertheless, it is numerically not a well-posed problem, if the Hamilton operator is regularized by the wave function. Hence, as discussed in Ref. [90] it is better to expand in  $\frac{E_{kin}+V}{2m-V}$ .

## A.5 Radial Dirac equation and spinor harmonics

Let us discuss the which operators commute with

$$\mathcal{H}_r = \mathcal{H}_D + \mathcal{H}_V = \boldsymbol{\alpha} \cdot \mathbf{p} + \beta m + eV(r). \quad (\text{A.69})$$

One finds the *total angular momentum operator*

$$[\mathcal{H}_r, \mathbf{J}^2] = 0, \quad (\text{A.70})$$

$$[\mathcal{H}_r, J_3] = 0, \quad (\text{A.71})$$

$$\mathbf{J} = \mathbf{L} + \mathbf{S}, \quad (\text{A.72})$$

gives rise to such constants of motion, but not  $\mathbf{L}$  and  $\mathbf{S}$  individually. The eigenvalue of  $\mathbf{J}^2$  and  $J_3$  are denoted by  $j(j+1)$  and  $m_j$ , respectively. One less often discussed operator is the *spin-orbit operator*  $\mathbf{K}$ , that defines a further conserved quantity:

$$[\mathcal{H}_r, \mathbf{K}] = 0, \quad (\text{A.73})$$

$$\mathbf{K} = \beta (\boldsymbol{\Sigma} \cdot \mathbf{L} + 1) = \begin{pmatrix} \boldsymbol{\sigma} \cdot \mathbf{L} + 1 & 0 \\ 0 & -\boldsymbol{\sigma} \cdot \mathbf{L} - 1 \end{pmatrix}, \quad (\text{A.74})$$

$$\Sigma_i = \sigma_i \oplus \sigma_i \quad (\text{A.75})$$

The eigenvalue of  $\mathbf{K}$  is given as

$$\kappa = \pm(j + \frac{1}{2}), \quad (\text{A.76})$$

where qualitatively the sign of  $\kappa$  relates to antiparallel ( $\kappa > 0$ ) or parallel ( $\kappa < 0$ ) alignment of the spin to the angular momentum in the nonrelativistic limit. In other words  $\text{sign}(\kappa)$  also determines the sign in  $j = l \pm \frac{1}{2}$

The eigenspinors of  $\mathcal{H}_r$  are thus characterized by three quantum numbers:  $j$ ,  $m_j$  and  $\text{sign}(\kappa)$ . It is possible to write these eigenspinors in terms of linear combinations of products of the eigenvectors  $\xi_{s,m_s}$  of spin with  $s = \frac{1}{2}$

$$\xi_{\frac{1}{2},+\frac{1}{2}} = \begin{pmatrix} 1 \\ 0 \end{pmatrix}, \quad \xi_{\frac{1}{2},-\frac{1}{2}} = \begin{pmatrix} 0 \\ 1 \end{pmatrix} \quad (\text{A.77})$$

and the spherical harmonics  $Y_{lm}(\Omega)$  with the relevant Clebsch-Gordan coefficients

$$\mathbf{Y}_{jm_j}^{l\frac{1}{2}}(\Omega) = \sum_{m_s=-s}^s \sum_{m_l=-l}^l \langle lm_l \frac{1}{2} m_s | jm_j \rangle Y_{lm_l}(\Omega) \xi_{\frac{1}{2},m_s}, \quad (\text{A.78})$$

$$\mathbf{y}_{jm_j}^{[+]} = \mathbf{Y}_{jm_j}^{l\frac{1}{2}}(\Omega)|_{j=l+\frac{1}{2}}, \quad (\text{A.79})$$

$$\mathbf{y}_{jm_j}^{[-]} = \mathbf{Y}_{jm_j}^{l\frac{1}{2}}(\Omega)|_{j=l-\frac{1}{2}}. \quad (\text{A.80})$$

Here, we introduce the so-called *spinor harmonics*  $\mathbf{y}_{jm_j}^{[\text{sign}(\kappa)]}$ . These stand in exact analogy to vector spherical harmonics, which we will use extensively in multipole theory. In a nutshell, for vector spherical harmonics we obtain linear combinations of products of the spherical basis  $\mathbf{e}_{1m'}$  and the spherical harmonics  $Y_{lm}(\Omega)$  with the relevant Clebsch-Gordan coefficients, see Equation (B.4). One useful property of the spinor harmonics is that

$$\boldsymbol{\sigma} \cdot \hat{\mathbf{r}} \mathbf{y}_{jm_j}^{[\text{sign}(\kappa)]} = \mathbf{y}_{jm_j}^{[-\text{sign}(\kappa)]} \quad (\text{A.81})$$

We can now separate the angular- and the radial-dependence of the Dirac spinor, that satisfies

$$\mathcal{H}_r \Psi_{jm_j}^{\text{sign}(\kappa)}(\mathbf{r}) = E_{jm_j}^{\text{sign}(\kappa)} \Psi_{jm_j}^{\text{sign}(\kappa)}(\mathbf{r}), \quad (\text{A.82})$$

by the ansatz

$$\Psi_{jm_j}^{\text{sign}(\kappa)}(\mathbf{r}) = \begin{pmatrix} \varphi_{jm_j}^{\text{sign}(\kappa)}(\mathbf{r}) \\ \chi_{jm_j}^{-\text{sign}(\kappa)}(\mathbf{r}) \end{pmatrix} = \begin{pmatrix} g(r) \mathbf{y}_{jm_j}^{[\text{sign}(\kappa)]}(\Omega) \\ i f(r) \mathbf{y}_{jm_j}^{[-\text{sign}(\kappa)]}(\Omega) \end{pmatrix}. \quad (\text{A.83})$$

Plugging eq into eq with eq. this yields

$$[\boldsymbol{\alpha} \cdot \mathbf{p} + \beta m + eV(r)] \begin{pmatrix} g(r) \mathbf{y}_{jm_j}^{[\text{sign}(\kappa)]}(\Omega) \\ i f(r) \mathbf{y}_{jm_j}^{[-\text{sign}(\kappa)]}(\Omega) \end{pmatrix} = E_{jm_j}^{\text{sign}(\kappa)} \begin{pmatrix} g(r) \mathbf{y}_{jm_j}^{[\text{sign}(\kappa)]}(\Omega) \\ i f(r) \mathbf{y}_{jm_j}^{[-\text{sign}(\kappa)]}(\Omega) \end{pmatrix}. \quad (\text{A.84})$$

It is possible to rewrite  $\boldsymbol{\sigma} \cdot \mathbf{p}$  by inserting  $(\boldsymbol{\sigma} \cdot \hat{\mathbf{r}})^2 = 1_{2 \times 2}$  and obtain

$$\boldsymbol{\sigma} \cdot \mathbf{p} = (\boldsymbol{\sigma} \cdot \hat{\mathbf{r}})^2 \boldsymbol{\sigma} \cdot \mathbf{p} \quad (\text{A.85})$$

$$= \boldsymbol{\sigma} \cdot \hat{\mathbf{r}} \left( \mathbf{r} \cdot \mathbf{p} + i \boldsymbol{\sigma} \cdot \frac{\mathbf{L}}{r} \right) \quad (\text{A.86})$$

$$= \boldsymbol{\sigma} \cdot \hat{\mathbf{r}} \frac{1}{r} \left( -i \frac{\partial}{\partial r} - i \boldsymbol{\sigma} \cdot \mathbf{L} \right) \quad (\text{A.87})$$

$$= \boldsymbol{\sigma} \cdot \hat{\mathbf{r}} \frac{i}{r} \left[ -\frac{\partial}{\partial r} r + \underbrace{(\boldsymbol{\sigma} \cdot \mathbf{L} + 1)}_{\pm \kappa \text{ for } \mathbf{y}^{[\pm]}} \right] \quad (\text{A.88})$$

Here, we used  $\mathbf{L} = \mathbf{r} \times \mathbf{p}$ ,  $\mathbf{p} = -i \nabla$  and  $\nabla = \hat{\mathbf{r}} \frac{\partial}{\partial r} - \frac{i}{r} (\hat{\mathbf{r}} \times \mathbf{L})$ , as well as  $\frac{\partial}{\partial r} = \frac{1}{r} \frac{\partial}{\partial r} r - \frac{1}{r}$ . Therefore the ansatz yields two differential equations

$$\begin{aligned} [eV(r) + m] g(r) \mathbf{y}_{jm_j}^{[\text{sign}(\kappa)]} + \boldsymbol{\sigma} \cdot \hat{\mathbf{r}} \frac{i}{r} \left[ -\frac{\partial}{\partial r} r + (\boldsymbol{\sigma} \cdot \mathbf{L} + 1) \right] i f(r) \mathbf{y}_{jm_j}^{[-\text{sign}(\kappa)]} \\ = E_{jm_j}^{\text{sign}(\kappa)} g(r) \mathbf{y}_{jm_j}^{[\text{sign}(\kappa)]} \end{aligned} \quad (\text{A.89})$$

$$\begin{aligned} \boldsymbol{\sigma} \cdot \hat{\mathbf{r}} \frac{i}{r} \left[ -\frac{\partial}{\partial r} r + (\boldsymbol{\sigma} \cdot \mathbf{L} + 1) \right] g(r) \mathbf{y}_{jm_j}^{[\text{sign}(\kappa)]} + [eV(r) - m] i f(r) \mathbf{y}_{jm_j}^{[-\text{sign}(\kappa)]} \\ = E_{jm_j}^{\text{sign}(\kappa)} i f(r) \mathbf{y}_{jm_j}^{[-\text{sign}(\kappa)]} \end{aligned} \quad (\text{A.90})$$

which simplify to

$$\left[ -\frac{1}{r} \frac{\partial}{\partial r} r - \frac{\kappa}{r} \right] f(r) = \left[ m - E_{jm_j}^{\text{sign}(\kappa)} + eV(r) \right] g(r) \quad (\text{A.91})$$

$$\left[ -\frac{1}{r} \frac{\partial}{\partial r} r + \frac{\kappa}{r} \right] g(r) = \left[ m + E_{jm_j}^{\text{sign}(\kappa)} - eV(r) \right] f(r) \quad (\text{A.92})$$

for the radial dependence. These coupled equations can now be solved numerically. For a comparison of such a fully relativistic calculation, with the first order relativistic corrections discussed in Section A.4 see Ref. [90].

## Appendix B

# Details of solving the vector Poisson equation

We want to solve the *vector Poisson equation*

$$\nabla^2 \mathbf{A}(\mathbf{r}) = -4\pi \mathbf{j}(\mathbf{r}), \quad (\text{B.1})$$

in *Coulomb gauge*

$$\nabla \cdot \mathbf{A} = 0. \quad (\text{B.2})$$

Here,  $\mathbf{j}(\mathbf{r})$  is the static current, that could for instance arise due to the orbital angular momentum or spin.

### B.1 General form of the vector gauge field

We want to shown that any solution of Equation (B.1) must have the form

$$\mathbf{A}(\mathbf{r}) = \sum_{p=1}^{\infty} \sum_{q=-p}^p \left[ M_{pq}^{p1} \frac{1}{r^{p+1}} \mathbf{Y}_{pq}^{p1}(\Omega) + T_{pq}^{p+1,1} \frac{1}{r^{p+2}} \mathbf{Y}_{pq}^{p+1,1}(\Omega) \right], \quad (\text{B.3})$$

where  $M_{pq}^{p1}$  are *magnetic* (M) multipole coefficients,  $T_{pq}^{p+1,1}$  are *magnetic toroidal* (MT) multipole coefficients and  $\mathbf{Y}_{pq}^{l1}(\Omega)$  are the *vector spherical harmonics*, defined as

$$\mathbf{Y}_{pq}^{l1}(\Omega) = \sum_{m=-l}^l \sum_{m'=-1}^1 \langle lm1m'|pq \rangle Y_{lm}(\Omega) \mathbf{e}_{1m'}, \quad (\text{B.4})$$

$$l^2 \mathbf{Y}_{pq}^{l1}(\Omega) = l(l+1) \mathbf{Y}_{pq}^{l1}(\Omega). \quad (\text{B.5})$$

Here,  $Y_{lm}(\Omega)$  are *spherical harmonics* and  $\mathbf{e}_{1m'}$  are *spherical unit vectors*, which are coupled to each other via the *Clebsch–Gordon coefficient*  $\langle lm1m'|pq \rangle$ . Note that by construction the *angular*



momentum quantum number  $l = p - 1, p, p + 1$ . A closer look at the Clebsch–Gordon coefficient reveals that  $p$  is a sort of total angular momentum arising from coupling of the angular momentum  $l$  with an intrinsic angular momentum of value  $\mathbf{1}$ .<sup>1</sup>

Let us begin by solving the homogeneous vector Poisson equation:

$$\nabla^2 \mathbf{A}(\mathbf{r}) = 0, \quad (\text{B.6})$$

We note that  $\mathbf{A} = (A^x, A^y, A^z)^T$  has three components. Here, it is better to write  $\mathbf{A}$  in terms of rank 1 spherical tensors, because  $\nabla^2$  satisfies rotational symmetry. We hence write

$$\mathbf{A} = A^{1m'} \mathbf{e}_{1m'} \quad (\text{B.7})$$

with contravariant components

$$A^{11} = -\frac{1}{\sqrt{2}} (A^x - iA^y), \quad (\text{B.8a})$$

$$A^{10} = A^z, \quad (\text{B.8b})$$

$$A^{1-1} = \frac{1}{\sqrt{2}} (A^x + iA^y) \quad (\text{B.8c})$$

and *spherical unit vectors* given by Cartesian unit vectors as

$$\mathbf{e}_{11} = -\frac{1}{\sqrt{2}} (\mathbf{e}_x + i\mathbf{e}_y), \quad (\text{B.9a})$$

$$\mathbf{e}_{10} = \mathbf{e}_z, \quad (\text{B.9b})$$

$$\mathbf{e}_{1-1} = \frac{1}{\sqrt{2}} (\mathbf{e}_x - i\mathbf{e}_y). \quad (\text{B.9c})$$

Inversely *Cartesian components* are given in terms of spherical components as

$$A^x = \frac{1}{\sqrt{2}} (A^{1-1} - A^{11}), \quad (\text{B.10a})$$

$$A^y = -\frac{i}{\sqrt{2}} (A^{1-1} + A^{11}), \quad (\text{B.10b})$$

$$A^z = A^{10}. \quad (\text{B.10c})$$

The implications of Equation (B.6) for the spherical component  $A^{1m'}$  become clear by inserting Equation (B.10):

$$\nabla^2 A^x = 0 \quad \rightarrow \quad \nabla^2 (A^{1-1} - A^{11}) = 0, \quad (\text{B.11a})$$

$$\nabla^2 A^y = 0 \quad \rightarrow \quad \nabla^2 (A^{1-1} + A^{11}) = 0, \quad (\text{B.11b})$$

$$\nabla^2 A^z = 0 \quad \rightarrow \quad \nabla^2 A_{10} = 0. \quad (\text{B.11c})$$

---

<sup>1</sup>This intrinsic angular momentum is often called spin, although it has no connection to the electronic spin. In fact, it merely reflects the 3 linearly independent directions of coordinate space by means of  $m' = -1, 0, 1$ .

Since  $\nabla^2$  is a linear operator, it is ok to add and subtract Equation (B.11a) and Equation (B.11b). This yields

$$\nabla^2 A^{1m'} = 0 \quad (\text{B.12})$$

for all  $m = -1, 0, 1$  independently.

Next, we follow a *separation ansatz* for each component

$$A^{1m'}(\mathbf{r}) = R^{1m'}(r)Y^{1m'}(\Omega), \quad (\text{B.13})$$

where  $R^{1m'}(r)$  describes the radial dependency of the component  $A^{1m'}$  and  $Y^{1m'}(\Omega)$  the angular dependency. The operator  $\nabla^2$  can be written in radial and angular contributions as

$$\nabla^2 = \nabla_r^2 + \frac{1}{r^2} \nabla_\Omega^2, \quad (\text{B.14a})$$

$$\nabla_r^2 = \frac{1}{r} \frac{\partial^2}{\partial r^2} r = \frac{1}{r^2} \frac{\partial}{\partial r} r^2 \frac{\partial}{\partial r}, \quad (\text{B.14b})$$

$$\nabla_\Omega^2 = \frac{1}{\sin(\theta)} \frac{\partial}{\partial \theta} \sin(\theta) \frac{\partial}{\partial \theta} + \frac{1}{\sin^2(\theta)} \frac{\partial^2}{\partial \varphi^2} \quad (\text{B.14c})$$

We plug the separation ansatz of Equation (B.13) and Equation (B.14) component-wise into the homogeneous Poisson equation Equation (B.11) and obtain

$$\left[ \nabla_r^2 + \frac{1}{r^2} \nabla_\Omega^2 \right] R^{1m'}(r)Y^{1m'}(\Omega) = 0, \quad (\text{B.15a})$$

$$r^2 \frac{\nabla_r^2 R^{1m'}(r)}{R^{1m'}(r)} = - \frac{\nabla_\Omega^2 Y^{1m'}(\Omega)}{Y^{1m'}(\Omega)} = C_1. \quad (\text{B.15b})$$

Since the first term in Equation (B.15b) depends only on  $r$  and the second only on  $\Omega$ , this can only hold for all  $r$  and  $\Omega$ , if the terms equal a constant  $C_1$ . This yields two separate differential equations:

$$r^2 \nabla_r^2 R^{1m'}(r) = C_1 R^{1m'}(r), \quad (\text{B.16})$$

$$\nabla_\Omega^2 Y^{1m'}(\Omega) = -C_1 Y^{1m'}(\Omega). \quad (\text{B.17})$$

First let us solve for the radial dependence  $R^{1m'}(r)$ . Equation (B.16) has two solutions, which we find by following the ansatz

$$R_l^{1m'}(r) = A_l^{1m'} r^l : \quad (\text{B.18a})$$

$$\frac{1}{r} \frac{\partial^2}{\partial r^2} r A_l^{1m'} r^l = l(l+1) A_l^{1m'} r^l, \quad (\text{B.18b})$$

$$\rightarrow C_1 = l(l+1) \quad (\text{B.18c})$$

and

$$R_l^{1m'}(r) = \frac{B_l^{1m'}}{r^{l+1}} : \quad (\text{B.19a})$$

$$\frac{1}{r} \frac{\partial^2}{\partial r^2} r \frac{B_l^{1m'}}{r^{l+1}} = l(l+1) \frac{B_l^{1m'}}{r^{l+1}} \quad (\text{B.19b})$$

$$\rightarrow C_1 = l(l+1). \quad (\text{B.19c})$$

Next, we solve Equation (B.17), once again by a separation ansatz

$$Y_l^{1m'} = X_l^{1m'}(\theta) \Phi_l^{1m'}(\varphi), \quad (\text{B.20})$$

that separate the polar angle  $\theta$  and azimuthal angle  $\varphi$ :

$$\nabla_{\Omega}^2 Y_l^{1m'}(\Omega) = -l(l+1) Y_l^{1m'}, \quad (\text{B.21a})$$

$$\begin{aligned} & \left[ \frac{1}{\sin(\theta)} \frac{\partial}{\partial \theta} \sin(\theta) \frac{\partial}{\partial \theta} + \frac{1}{\sin^2(\theta)} \frac{\partial^2}{\partial \varphi^2} \right] X_l^{1m'}(\theta) \Phi_l^{1m'}(\varphi) \\ & = -l(l+1) X_l^{1m'}(\theta) \Phi_l^{1m'}(\varphi), \end{aligned} \quad (\text{B.21b})$$

$$\begin{aligned} & \sin^2(\theta) \frac{1}{X_l^{1m'}(\theta)} \left[ \frac{1}{\sin(\theta)} \frac{\partial}{\partial \theta} \sin(\theta) \frac{\partial}{\partial \theta} \right] X_l^{1m'}(\theta) \\ & + l(l+1) \sin^2(\theta) = -\frac{1}{\Phi_l^{1m'}(\varphi)} \frac{\partial^2}{\partial \varphi^2} \Phi_l^{1m'}(\varphi) = C_2. \end{aligned} \quad (\text{B.21c})$$

We obtain two differential equations, that read:

$$\frac{\partial^2}{\partial \varphi^2} \Phi_l^{1m'}(\varphi) = -C_2 \Phi_l^{1m'}(\varphi), \quad (\text{B.22})$$

$$\begin{aligned} & \left[ \frac{1}{\sin(\theta)} \frac{\partial}{\partial \theta} \sin(\theta) \frac{\partial}{\partial \theta} \right] X_l^{1m'}(\theta) + l(l+1) X_l^{1m'}(\theta) \\ & = \frac{1}{\sin^2(\theta)} C_2 X_l^{1m'}(\theta). \end{aligned} \quad (\text{B.23})$$

We can solve Equation (B.22) with an educated guess:

$$\Phi_l^{1m'}(\varphi) = e^{i\sqrt{C_2}\varphi}. \quad (\text{B.24})$$

Additionally we know the boundary condition

$$\Phi_l^{1m'}(\varphi) = \Phi_l^{1m'}(\varphi + 2\pi), \quad (\text{B.25})$$

which puts further constraints on  $C_2$ :

$$i\sqrt{C_2}2\pi = \pm im2\pi \quad m \in Z \quad (\text{B.26a})$$

$$\rightarrow \sqrt{C_2} = m. \quad (\text{B.26b})$$

Finally, the polar differential equation given in Equation (B.23) must be solved. We substitute with  $x = \cos(\theta)$  and use

$$\sin^2(\theta) = 1 - \cos^2(\theta) = 1 - x^2, \quad (\text{B.27a})$$

$$-\frac{\partial}{\partial x} = \frac{1}{\sin(\theta)} \frac{\partial}{\partial \theta}, \quad (\text{B.27b})$$

$$\sin(\theta) \frac{\partial}{\partial \theta} = \sin^2(\theta) \frac{\partial}{\partial x} = (1 - x^2) \frac{\partial}{\partial x}. \quad (\text{B.27c})$$

This yields

$$\left[ \frac{\partial}{\partial x} (1 - x^2) \frac{\partial}{\partial x} - \frac{m^2}{(1 - x^2)} \right] P_{lm}^{1m'}(x) = -l(l+1) P_{lm}^{1m'}(x), \quad (\text{B.28})$$

which is a differential equation known to be solved by the *Legendre polynomials*  $P_{lm}^{1m'}(x)$ . Jointly the spherical dependence is written in terms of *spherical harmonics*

$$Y_{lm}^{1m'}(\Omega) = \Phi_{lm}^{1m'}(\varphi) P_{lm}^{1m'}(\cos^2(\theta)) \quad (\text{B.29})$$

for each component  $A^{1m'}$ . Thus, any solution of Equation (B.6) can be written as

$$\mathbf{A}(\mathbf{r}) = \sum_{m'=-1}^1 A^{1m'}(r, \Omega) \mathbf{e}_{1m'} \quad (\text{B.30a})$$

$$= \sum_{l=0}^{\infty} \sum_{m=-l}^l \sum_{m'=-1}^1 \left[ A_{lm}^{1m'} r^l Y_{lm}(\Omega) \mathbf{e}_{1m'} + \frac{B_{lm}^{1m'}}{r^{l+1}} Y_{lm}(\Omega) \mathbf{e}_{1m'} \right] \quad (\text{B.30b})$$

Here we note that, physically we expect  $\mathbf{A}(\mathbf{r})$  to vanish when  $r \rightarrow \infty$ , as well as for  $r \rightarrow 0$ . Therefore the first (second) term in Equation (B.30b) describes  $\mathbf{A}(\mathbf{r})$  within (outside) the current  $\mathbf{j}(\mathbf{r})$ . We are interested in the latter and set  $A_{lm}^{1m'} \equiv 0$ .

We have mentioned that the spherical unit vectors  $\mathbf{e}_{1m'}$  are spherical tensors of rank 1. This means the product  $Y_{lm}(\Omega) \mathbf{e}_{1m'}$  can be treated as if two angular momenta  $\mathbf{1}$  and  $\mathbf{l}$  are coupling. As is known for instance from the coupling of spin and orbital angular momentum, the coupling is formally done via Clebsch–Gordon coefficients:

$$Y_{lm}(\Omega) \mathbf{e}_{1m'} = \sum_{p=0}^{\infty} \sum_{q=-p}^p \langle lm1m' | pq \rangle \mathbf{Y}_{pq}^{l1}(\Omega). \quad (\text{B.31})$$

Here, vector valued eigenfunctions  $\mathbf{Y}_{pq}^{l1}(\Omega)$  of the angular momentum operator  $\mathbf{l}$  are introduced. The inverse relation of Equation (B.31) serves as a definition of these so-called *vector spherical harmonics*:

$$\mathbf{Y}_{pq}^{l1}(\Omega) = \sum_{m=-l}^l \sum_{m'=-1}^1 \langle lm1m' | pq \rangle Y_{lm}(\Omega) \mathbf{e}_{1m'}, \quad (\text{B.32})$$

$$\mathbf{l}^2 \mathbf{Y}_{pq}^{l1}(\Omega) = l(l+1) \mathbf{Y}_{pq}^{l1}(\Omega). \quad (\text{B.33})$$

as was stated in Equation (B.4) and Equation (B.5).

In addition to introducing vector spherical harmonics, we redefine the expansion coefficients in Equation (B.30b), in order to swallow the Clebsch–Gordan coefficients:

$$\sum_{l=0}^{\infty} \sum_{m'=-1}^1 B_{lm'}^{1m'} \langle lm1m'|pq\rangle = M_{pq}^{l1} (\delta_{l,p-1} + \delta_{l,p} + \delta_{l,p+1}). \quad (\text{B.34})$$

Here, we used that  $|l \pm 1| < p$ , which is a property of  $\langle lm1m'|pq\rangle$ . Thus,  $\mathbf{A}(\mathbf{r})$  can be written as:

$$\mathbf{A}(\mathbf{r}) = \sum_{p=0}^{\infty} \sum_{q=-p}^p \sum_{l=0}^{\infty} \sum_{m=-l}^l \sum_{m'=-1}^1 \left[ \frac{B_{lm'}^{1m'}}{r^{l+1}} \langle lm1m'|pq\rangle \mathbf{Y}_{pq}^{l1}(\Omega) \right] \quad (\text{B.35a})$$

$$= \sum_{p=0}^{\infty} \sum_{q=-p}^p \sum_{l=0}^{\infty} \left[ M_{pq}^{l1} (\delta_{l,p-1} + \delta_{l,p} + \delta_{l,p+1}) \frac{1}{r^{l+1}} \mathbf{Y}_{pq}^{l1}(\Omega) \right] \quad (\text{B.35b})$$

$$= \sum_{p=0}^{\infty} \sum_{q=-p}^p \left[ M_{pq}^{p-1,1} \frac{1}{r^p} \mathbf{Y}_{pq}^{p-1,1}(\Omega) + M_{pq}^{p1} \frac{1}{r^{p+1}} \mathbf{Y}_{pq}^{p1}(\Omega) + M_{pq}^{p+1,1} \frac{1}{r^{p+2}} \mathbf{Y}_{pq}^{p+1,1}(\Omega) \right]. \quad (\text{B.35c})$$

We will now proof that only the terms containing the M multipole coefficient  $M_{pq}^{p1}$  and the MT multipole coefficient  $M_{pq}^{p+1,1}$ , which we will denote by  $T_{pq}^{p+1,1}$  to highlight the difference, are actually compatible with the Coulomb gauge given in Equation (B.2). To this end, we will use the following three relations that can be derived from Equation (B.4) [140]:

$$\mathbf{Y}_{pq}^{p-1,1}(\Omega) = \frac{1}{\sqrt{p(2p+1)}} (p\hat{\mathbf{r}} - \mathbf{i}\hat{\mathbf{r}} \times \mathbf{l}) Y_{p,q}(\Omega), \quad (\text{B.36})$$

$$\mathbf{Y}_{pq}^{p,1}(\Omega) = \frac{1}{\sqrt{p(p+1)}} \mathbf{l} Y_{p,q}(\Omega), \quad (\text{B.37})$$

$$\mathbf{Y}_{pq}^{p+1,1}(\Omega) = \frac{-1}{\sqrt{(p+1)(2p+1)}} ((p+1)\hat{\mathbf{r}} + \mathbf{i}\hat{\mathbf{r}} \times \mathbf{l}) Y_{p,q}(\Omega), \quad (\text{B.38})$$

where  $\hat{\mathbf{r}}$  has unit length. These are derived step-by-step in Section B.7. Furthermore, we recall

some useful identities:

$$\nabla = \hat{\mathbf{r}} \frac{\partial}{\partial r} - \frac{\mathbf{i}}{r} (\hat{\mathbf{r}} \times \mathbf{l}), \quad (\text{B.39})$$

$$\hat{\mathbf{r}} = \frac{\mathbf{r}}{r}, \quad (\text{B.40})$$

$$r = \sqrt{\mathbf{r} \cdot \mathbf{r}}, \quad (\text{B.41})$$

$$\hat{\mathbf{r}} \cdot \hat{\mathbf{r}} = 1, \quad (\text{B.42})$$

$$\mathbf{l} = -\mathbf{i}\mathbf{r} \times \nabla, \quad (\text{B.43})$$

$$\hat{\mathbf{r}} \cdot (\hat{\mathbf{r}} \times \mathbf{l}) = 0, \quad (\text{B.44})$$

$$(\hat{\mathbf{r}} \times \mathbf{l}) \cdot \hat{\mathbf{r}} = 2\mathbf{i}, \quad (\text{B.45})$$

$$(\hat{\mathbf{r}} \times \mathbf{l}) \cdot (\hat{\mathbf{r}} \times \mathbf{l}) = \mathbf{l}^2, \quad (\text{B.46})$$

$$\hat{\mathbf{r}} \cdot \mathbf{l} = 0, \quad (\text{B.47})$$

$$(\hat{\mathbf{r}} \times \mathbf{l}) \cdot \mathbf{l} = 0 \quad (\text{B.48})$$

$$\hat{\mathbf{r}} \frac{\partial}{\partial r} f(r) = \frac{\partial}{\partial r} \hat{\mathbf{r}} f(r). \quad (\text{B.49})$$

The first factor in Equation (B.35c), namely  $M_{pq}^{p-1,1} \frac{1}{r^p} \mathbf{Y}_{pq}^{p-1,1}(\Omega)$ , can be investigated by applying  $\nabla$  onto  $f(r) \mathbf{Y}_{pq}^{p-1,1}(\Omega)$ , where  $f(r)$  is an arbitrary function of  $r$  that commutes with  $\mathbf{l}$ :

$$\begin{aligned} & \nabla \cdot (f(r) \mathbf{Y}_{pq}^{p-1,1}(\Omega)) \\ &= \left[ \hat{\mathbf{r}} \frac{\partial}{\partial r} - \frac{\mathbf{i}}{r} (\hat{\mathbf{r}} \times \mathbf{l}) \right] f(r) \frac{1}{\sqrt{p(2p+1)}} (p\hat{\mathbf{r}} - \mathbf{i}\hat{\mathbf{r}} \times \mathbf{l}) Y_{p,q}(\Omega) \\ &= \frac{1}{\sqrt{p(2p+1)}} \left[ \hat{\mathbf{r}} \frac{\partial}{\partial r} p\hat{\mathbf{r}} - \mathbf{i}\hat{\mathbf{r}} \frac{\partial}{\partial r} (\hat{\mathbf{r}} \times \mathbf{l}) - \frac{\mathbf{i}}{r} (\hat{\mathbf{r}} \times \mathbf{l}) \cdot \hat{\mathbf{r}} p - \frac{1}{r} (\hat{\mathbf{r}} \times \mathbf{l})^2 \right] f(r) Y_{p,q}(\Omega) \\ &= \sqrt{\frac{p}{2p+1}} Y_{p,q}(\Omega) \left[ \frac{\partial f(r)}{\partial r} - \frac{p-1}{r} f(r) \right] = 0. \end{aligned} \quad (\text{B.50})$$

The equality in the last line can only hold if

$$\frac{\partial f(r)}{\partial r} = \frac{p-1}{r} f(r) \quad (\text{B.51a})$$

$$\rightarrow f(r) = r^{p-1}. \quad (\text{B.51b})$$

However in Equation (B.35c) we see the radial dependence is  $r^{-p}$ . Hence,  $M_{pq}^{p-1,1}$  must be zero for all  $p$  and  $q$ , in order to be compatible with the gauge condition.

The next factor in Equation (B.35c) is  $M_{pq}^{p1} \frac{1}{r^{p+1}} \mathbf{Y}_{pq}^{p1}(\Omega)$ . We follow the same procedure:

$$\nabla \cdot (f(r) \mathbf{Y}_{pq}^{p1}(\Omega)) = \left[ \hat{\mathbf{r}} \frac{\partial}{\partial r} - \frac{\mathbf{i}}{r} (\hat{\mathbf{r}} \times \mathbf{l}) \right] f(r) \frac{1}{\sqrt{p(p+1)}} \mathbf{l} Y_{p,q}(\Omega) = 0$$

for all  $f(r)$  because  $\hat{\mathbf{r}} \cdot \mathbf{l} = 0$  and  $(\hat{\mathbf{r}} \times \mathbf{l}) \cdot \mathbf{l} = 0$ . This term can appear without any restrictions.

Finally, the factor  $T_{pq}^{p+1,1} \frac{1}{r^{p+2}} \mathbf{Y}_{pq}^{p+1,1}(\Omega)$  is investigated:

$$\begin{aligned} \nabla \cdot (f(r) \mathbf{Y}_{pq}^{p+1,1}(\Omega)) &= \left[ \hat{\mathbf{r}} \frac{\partial}{\partial r} - \frac{i}{r} (\hat{\mathbf{r}} \times \mathbf{l}) \right] f(r) \frac{-[(p+1)\hat{\mathbf{r}} + i\hat{\mathbf{r}} \times \mathbf{l}]}{\sqrt{(p+1)(2p+1)}} Y_{p,q}(\Omega) \\ &= \frac{-1}{\sqrt{(p+1)(2p+1)}} \left[ (p+1) \frac{\partial}{\partial r} + i \frac{\partial}{\partial r} \hat{\mathbf{r}} \cdot (\hat{\mathbf{r}} \times \mathbf{l}) \right. \\ &\quad \left. - \frac{i}{r} (\hat{\mathbf{r}} \times \mathbf{l}) \cdot \hat{\mathbf{r}} (p+1) + \frac{1}{r} (\hat{\mathbf{r}} \times \mathbf{l})^2 \right] f(r) Y_{p,q}(\Omega) \\ &= -\sqrt{\frac{(p+1)}{(2p+1)}} \left[ \frac{\partial}{\partial r} + \frac{p+2}{r} \right] f(r) Y_{p,q}(\Omega) = 0 \end{aligned} \quad (\text{B.52})$$

$$\rightarrow f(r) = \frac{1}{r^{p+2}}. \quad (\text{B.53})$$

This is consistent with the radial dependence in Equation (B.35c).

In summary, we have shown that

$$\nabla \cdot (r^{p-1} \mathbf{Y}_{pq}^{p-1,1}(\Omega)) = \nabla \cdot (f(r) \mathbf{Y}_{pq}^{p,1}(\Omega)) = \nabla \cdot \left( \frac{\mathbf{Y}_{pq}^{p+1,1}(\Omega)}{r^{p+2}} \right) = 0 \quad (\text{B.54})$$

is necessary to satisfy Coloumb gauge. Together with Equation (B.35c) this shows that that any solution of Equation (B.1) must have the form

$$\mathbf{A}(\mathbf{r}) = \sum_{p=0}^{\infty} \sum_{q=-p}^p \left[ M_{pq}^{p1} \frac{1}{r^{p+1}} \mathbf{Y}_{pq}^{p1}(\Omega) + T_{pq}^{p+1,1} \frac{1}{r^{p+2}} \mathbf{Y}_{pq}^{p+1,1}(\Omega) \right].$$

This is equivalent to Equation (B.3) at the beginning of this section, except for the range of  $p$ . We will see in the following that  $M_{00}^{01} \frac{1}{r^{p+1}} = T_{00}^{1,1} = 0$ . However, before we can move on to find explicit expressions for the coefficients  $M_{pq}^{p1} \frac{1}{r^{p+1}}$  and  $T_{pq}^{p+1,1}$ , we introduce the Green's function method.

## B.2 Green's function method

In this section we will show that the Green's function can be expanded in spherical harmonics as follows:

$$G(\mathbf{r}, \mathbf{r}') = \frac{1}{|\mathbf{r} - \mathbf{r}'|} = \sum_{p=0}^{\infty} \sum_{q=-p}^p \frac{4\pi}{2p+1} \frac{r_{<}^p}{r_{>}^{p+1}} Y_{pq}^*(\Omega') Y_{pq}(\Omega), \quad (\text{B.55})$$

where  $r_{<} = \min(r, r')$  and  $r_{>} = \max(r, r')$ . This is motivated by the scalar Poisson equation

$$\nabla^2 G(\mathbf{r}, \mathbf{r}') = -4\pi \delta^{(3)}(\mathbf{r} - \mathbf{r}'), \quad (\text{B.56})$$

with a point source

$$\delta^{(3)}(\mathbf{r} - \mathbf{r}') = \frac{1}{r'^2} \delta(r - r') \delta(\cos(\theta) - \cos(\theta')) \delta(\phi - \phi'), \quad (\text{B.57a})$$

$$\sum_{p=0}^{\infty} \sum_{q=-p}^p Y_{pq}^*(\Omega') Y_{pq}(\Omega) = \delta(\cos(\theta) - \cos(\theta')) \delta(\phi - \phi'). \quad (\text{B.57b})$$

In the subsequent section, we will in particular make use of the radial differential equation

$$(r^2 \nabla_r - p(p+1)) g_p(r, r') = -4\pi \delta(r - r'), \quad (\text{B.58})$$

with the solution

$$g_p(r, r') = \frac{4\pi}{2p+1} \frac{r_{<}^p}{r_{>}^{p+1}}, \quad (\text{B.59})$$

Starting point is the following ansatz:

$$G(\mathbf{r}, \mathbf{r}') = \sum_{p=0}^{\infty} \sum_{q=-p}^p G_{pq}(r, r', \Omega') Y_{pq}(\Omega), \quad (\text{B.60})$$

$$G_{pq}(r, r', \Omega') = \int d\Omega \frac{1}{|\mathbf{r} - \mathbf{r}'|} Y_{pq}^*(\Omega). \quad (\text{B.61})$$

Plugging this into Equation (B.56) yields

$$\begin{aligned} \left( \nabla_r^2 + \frac{1}{r^2} \nabla_{\Omega}^2 \right) \sum_{p=0}^{\infty} \sum_{q=-p}^p G_{pq}(r, r', \Omega') Y_{pq}(\Omega) = \\ -4\pi \frac{1}{r'^2} \delta(r - r') \sum_{p=0}^{\infty} \sum_{q=-p}^p Y_{pq}^*(\Omega') Y_{pq}(\Omega), \end{aligned} \quad (\text{B.62})$$

where we can compare for each  $p$  and  $q$  individually to obtain the differential equation

$$\left( \nabla_r^2 + \frac{1}{r^2} \nabla_{\Omega}^2 \right) G_{pq}(r, r', \Omega') = -4\pi \frac{1}{r'^2} \delta(r - r') Y_{pq}^*(\Omega'). \quad (\text{B.63})$$

Both sides of the equation should have the same angular dependence. Noting that the radial and angular contributions are separated on the right hand side, we yet again take a separation ansatz

$$G_{pq}(r, r', \Omega') = g_p(r, r') Y_{pq}^*(\Omega'), \quad (\text{B.64})$$

and plug it into Equation (B.63) to obtain Equation (B.58)

$$(r^2 \nabla_r^2 - p(p+1)) g_p(r, r') = -4\pi \delta(r - r').$$

For  $r \neq r'$  the solution is quickly determined, as we have seen in the homogeneous case from Equation (B.16) to Equation (B.19). It yields

$$\rightarrow g_p(r, r') = \begin{cases} A_p(r') \frac{1}{r^{p+1}} & , r < r' \\ B_p(r') r^p & , r' < r \end{cases}. \quad (\text{B.65})$$

The radial solutions are linked to the cases  $r > r'$  and  $r < r'$ , because of diverging behaviour that could occur when  $r \rightarrow \infty$  and  $r \rightarrow 0$ , respectively.



In contrast to the homogeneous equation discussed before, here we need to consider the case when  $r = r'$ , where  $\delta(r - r') = 1$ . First, we note that the dimension of  $g_p(r, r')$  is known to be  $[length^{-1}]$ . Therefore, the dependence on  $r'$  must compensate  $r$ , in order to obtain the correct dimensionality. Furthermore, we assume  $g_p(r, r')$  to be continuous:

$$A_p(r')r'^p = B_p(r')\frac{1}{r'^{p+1}} = C_p\frac{1}{r'} \quad (\text{B.66})$$

$$\rightarrow g_p(r, r') = C_p\frac{r_{<}^p}{r_{>}^{p+1}}. \quad (\text{B.67})$$

The constant  $C_p$  is determined by integrating Equation (B.58) from  $r' - \epsilon$  to  $r' + \epsilon$ , which yields  $r = r'$  in the limit  $\epsilon \rightarrow 0$ :

$$\lim_{\epsilon \rightarrow 0} \int_{r' - \epsilon}^{r' + \epsilon} dr [r^2 \nabla_r^2 - p(p+1)] g_p(r, r') = -4\pi \lim_{\epsilon \rightarrow 0} \int_{r' - \epsilon}^{r' + \epsilon} dr \delta(r - r'), \quad (\text{B.68a})$$

$$\lim_{\epsilon \rightarrow 0} \int_{r' - \epsilon}^{r' + \epsilon} dr \left[ \frac{\partial}{\partial r} r^2 \frac{\partial}{\partial r} - p(p+1) \right] g_p(r, r') = -4\pi, \quad (\text{B.68b})$$

$$\lim_{\epsilon \rightarrow 0} \left[ r^2 \frac{\partial}{\partial r} g_p(r, r') \right]_{r' - \epsilon}^{r' + \epsilon} = -4\pi, \quad (\text{B.68c})$$

$$C_p \lim_{\epsilon \rightarrow 0} \left[ r^2 \frac{\partial}{\partial r} \frac{r'^p}{r^{p+1}} \Big|_{r=r'+\epsilon} - r^2 \frac{\partial}{\partial r} \frac{r^p}{r'^{p+1}} \Big|_{r=r'-\epsilon} \right] = -4\pi, \quad (\text{B.68d})$$

$$C_p = \frac{4\pi}{2p+1}. \quad (\text{B.68e})$$

That yields Equation (B.59) and Equation (B.55) by using Equation (B.64)

$$g_p(r, r') = \frac{4\pi}{2p+1} \frac{r_{<}^p}{r_{>}^{p+1}},$$

$$G(\mathbf{r}, \mathbf{r}') = \sum_{p=0}^{\infty} \sum_{q=-p}^p \frac{4\pi}{2p+1} \frac{r_{<}^p}{r_{>}^{p+1}} Y_{pq}^*(\Omega') Y_{pq}(\Omega).$$

### B.3 General form of multipole coefficients

In this section we show that the magnetic (M) multipole coefficient  $M_{pq}^{p1}$  and the magnetic toroidal (MT) multipole coefficient  $T_{pq}^{p+1,1}$  can be written as

$$M_{pq}^{p1} = -\frac{4\pi i}{2p+1} \int d^3\mathbf{r} \nabla (r^p Y_{pq}^*(\Omega)) \cdot \left[ \frac{\mathbf{r} \times \mathbf{j}_{\text{orb}}(\mathbf{r})}{\sqrt{p(p+1)}} + \sqrt{\frac{p+1}{p}} \mathbf{M}(\mathbf{r}) \right], \quad (\text{B.69})$$

and

$$T_{pq}^{p+1,1} = \frac{-4\pi}{\sqrt{(p+1)(2p+1)}} \int d^3\mathbf{r} \nabla (r^p Y_{pq}^*(\Omega)) \cdot \left[ \mathbf{r} \times \frac{\mathbf{r} \times \mathbf{j}_{\text{orb}}(\mathbf{r})}{p+2} + \mathbf{r} \times \mathbf{M}(\mathbf{r}) \right]. \quad (\text{B.70})$$

From Section B.1 we know that any solution  $\mathbf{A}(\mathbf{r})$  of the vector Poisson equation in Equation (B.1) must have the form presented in Equation (B.3). Let us for the moment set

$$\xi(r; pq) = M_{pq}^{p1} \frac{1}{r^{p+1}}, \quad (\text{B.71a})$$

$$\zeta(r; pq) = T_{pq}^{p+1,1} \frac{1}{r^{p+2}}, \quad (\text{B.71b})$$

and start with the following educated guess:

$$\mathbf{A}(\mathbf{r}) = \sum_{p=0}^{\infty} \sum_{q=-p}^p [\xi(r; pq) \mathbf{Y}_{pq}^{p1}(\Omega) + \zeta(r; pq) \mathbf{Y}_{pq}^{p+1,1}(\Omega)]. \quad (\text{B.72})$$

We plug Equation (B.72) into Equation (B.1) and use Equation (B.14) for  $\nabla^2 = \nabla_r^2 + \frac{1}{r^2} \nabla_{\Omega}^2$  under consideration of Equation (B.21a), which allows us to determine the eigenvalue of  $\nabla_{\Omega}^2$  by means of  $\nabla_{\Omega}^2 \mathbf{Y}_{pq}^{l,1}(\Omega) = -l(l+1) \mathbf{Y}_{pq}^{l,1}(\Omega)$ :

$$\sum_{pq} \left\{ \left[ \nabla_r^2 - \frac{p(p+1)}{r^2} \right] \xi(r; pq) \mathbf{Y}_{pq}^{p1}(\Omega) + \left[ \nabla_r^2 - \frac{(p+1)(p+2)}{r^2} \right] \zeta(r; pq) \mathbf{Y}_{pq}^{p+1,1}(\Omega) \right\} = -4\pi \mathbf{j}(\mathbf{r}). \quad (\text{B.73})$$

By construction vector spherical harmonics satisfy the orthogonality relation

$$\int d\Omega \mathbf{Y}_{PQ}^{*L1}(\Omega) \cdot \mathbf{Y}_{pq}^{l1}(\Omega) = \delta_{Ll} \delta_{Pp} \delta_{Qq}. \quad (\text{B.74})$$

Hence, when we multiply  $\mathbf{Y}_{PQ}^{*L1}(\Omega)$  onto Equation (B.73) from the left and integrate over  $d\Omega$ , we can use Equation (B.74) in order to evaluate the sum over  $p$  and  $q$ . This yields

$$\left[ \nabla_r^2 - \frac{P(P+1)}{r^2} \right] \xi(r; PQ) \delta_{LP} + \left[ \nabla_r^2 - \frac{(P+1)(P+2)}{r^2} \right] \zeta(r; PQ) \delta_{L,P+1} = -4\pi \int d\Omega \mathbf{Y}_{PQ}^{*L1}(\Omega) \cdot \mathbf{j}(\mathbf{r}). \quad (\text{B.75})$$

The problem breaks up into the cases  $L = P$ ,

$$[r^2 \nabla_r^2 - P(P+1)] \xi(r; PQ) = -4\pi r^2 \int d\Omega \mathbf{Y}_{PQ}^{*P1}(\Omega) \cdot \mathbf{j}(\mathbf{r}), \quad (\text{B.76})$$

which corresponds to the magnetic multipole, and the case  $L = P + 1$ ,

$$[r^2 \nabla_r^2 - (P+1)(P+2)] \zeta(r; PQ) = -4\pi r^2 \int d\Omega \mathbf{Y}_{PQ}^{*P+1,1}(\Omega) \cdot \mathbf{j}(\mathbf{r}) \quad (\text{B.77})$$

which corresponds to the magnetic toroidal multipole.

The green's function method introduced in Section B.2 showed that

$$[r^2 \nabla_r^2 - p(p+1)] g_p(r, r') = -4\pi \delta(r - r'), \quad (\text{B.78})$$

$$g_p(r, r') = \frac{4\pi}{2p+1} \frac{r'^p}{r^{p+1}}, \quad (\text{B.79})$$

for  $r' < r$ , see Equation (B.58) and Equation (B.59). When we multiply Equation (B.78) with  $r'^2 \int d\Omega' \mathbf{Y}_{PQ}^{*P1}(\Omega') \cdot \mathbf{j}(\mathbf{r}')$ , we can integrate over  $\int dr'$  on the left and rewrite  $\int r'^2 dr' \int \Omega'$  as  $\int d^3 \mathbf{r}'$  on the left. Hence, we obtain

$$\begin{aligned} [r^2 \nabla_r^2 - p(p+1)] \frac{4\pi}{2p+1} \frac{1}{r^{p+1}} \int d^3 \mathbf{r}' r'^p \mathbf{Y}_{PQ}^{*P1}(\Omega') \cdot \mathbf{j}(\mathbf{r}') \\ = -4\pi r^2 \int d\Omega \mathbf{Y}_{PQ}^{*P1}(\Omega) \cdot \mathbf{j}(\mathbf{r}). \end{aligned} \quad (\text{B.80})$$

This can be compared with Equation (B.76) when  $p = P$  and  $q = Q$ . Thus, we find

$$\xi(r; pq) = \frac{1}{r^{p+1}} \frac{4\pi}{2p+1} \int d^3 \mathbf{r}' r'^p \mathbf{Y}_{pq}^{*p1}(\Omega') \cdot \mathbf{j}(\mathbf{r}'), \quad (\text{B.81})$$

$$M_{pq}^{p1} = \frac{4\pi}{2p+1} \int d^3 \mathbf{r} r^p \mathbf{Y}_{pq}^{*p1}(\Omega) \cdot \mathbf{j}(\mathbf{r}) \quad (\text{B.82})$$

In the last line we used Equation (B.71a)  $\xi(r; pq) = M_{pq}^{p1} \frac{1}{r^{p+1}}$ .

Similarly, after multiplying Equation (B.78) with  $r'^2 \int d\Omega' \mathbf{Y}_{PQ}^{*P+1,1}(\Omega') \mathbf{j}(\mathbf{r}')$  and integrating over  $\int dr'$ , a comparison with Equation (B.77) with  $p = P+1$  and  $q = Q$  yields

$$\zeta(r; pq) = \frac{1}{r^{p+2}} \frac{4\pi}{2p+3} \int d^3 \mathbf{r}' r'^{p+1} \mathbf{Y}_{pq}^{*p+1,1}(\Omega') \cdot \mathbf{j}(\mathbf{r}'), \quad (\text{B.83})$$

$$T_{pq}^{p+1,1} = \frac{4\pi}{2p+3} \int d^3 \mathbf{r} r^{p+1} \mathbf{Y}_{pq}^{*p+1,1}(\Omega) \cdot \mathbf{j}(\mathbf{r}), \quad (\text{B.84})$$

where we used Equation (B.71b), i.e.,  $\zeta(r; pq) = T_{pq}^{p+1,1} \frac{1}{r^{p+2}}$ .

Although Equation (B.82) and Equation (B.84) already present a path to compute the gauge field  $\mathbf{A}(\mathbf{r})$  for any current  $\mathbf{j}(\mathbf{r})$ , we will now make somewhat lengthy gymnastics to obtain the form of the coefficients proposed at the beginning of this section in Equation (B.69) and Equation (B.70). To this end we need the following identities:

$$-i \hat{\mathbf{r}} \times \mathbf{Y}_{pq}^{p-1,1} = \sqrt{\frac{p+1}{2p+1}} \mathbf{Y}_{pq}^{p1}, \quad (\text{B.85})$$

$$-i \nabla \times (r^{p+1} \mathbf{Y}_{pq}^{p+1,1}) = (2p+3) \sqrt{\frac{p}{2p+1}} r^p \mathbf{Y}_{pq}^{p,1}, \quad (\text{B.86})$$

$$(\mathbf{r} \times \mathbf{Y}_{pq}^{l1}) \cdot \mathbf{j} = -\mathbf{Y}_{pq}^{l1} \cdot (\mathbf{r} \times \mathbf{j}), \quad (\text{B.87})$$

$$(\mathbf{r} \times \mathbf{j}_m) = \mathbf{r} \times (\nabla \times \mathbf{M}) = \nabla (\mathbf{r} \cdot \mathbf{M}) - [1 + \mathbf{r} \cdot \nabla] \mathbf{M}, \quad (\text{B.88})$$

$$\nabla (r^p Y_{pq}) = \sqrt{p(2p+1)} r^{p-1} \mathbf{Y}_{pq}^{p-1,1}, \quad (\text{B.89})$$

where  $\mathbf{j}_m = \nabla \times \mathbf{M}$ .

We start to compute the M multipole coefficient by using the complex conjugate of Equation (B.85) in Equation (B.82), and subsequently we rewrite  $r^p \hat{\mathbf{r}} = r^{p-1} \hat{\mathbf{r}}$  and use Equation (B.87) to interchange the cross product. Lastly, Equation (B.89) is used to obtain the first term in Equation (B.69):

$$M_{pq}^{p1} = \frac{4\pi}{2p+1} \int d^3\mathbf{r} r^p \mathbf{Y}_{pq}^{*p1}(\Omega) \cdot \mathbf{j}(\mathbf{r}) \quad (\text{B.90a})$$

$$= i \frac{4\pi}{\sqrt{(2p+1)(p+1)}} \int d^3\mathbf{r} r^p (\hat{\mathbf{r}} \times \mathbf{Y}_{pq}^{*p-1,1}(\Omega)) \cdot \mathbf{j}(\mathbf{r}) \quad (\text{B.90b})$$

$$= -i \frac{4\pi}{\sqrt{(2p+1)(p+1)}} \int d^3\mathbf{r} r^{p-1} \mathbf{Y}_{pq}^{*p-1,1}(\Omega) \cdot (\mathbf{r} \times \mathbf{j}(\mathbf{r})) \quad (\text{B.90c})$$

$$= -i \frac{4\pi}{2p+1} \frac{1}{\sqrt{p(p+1)}} \int d^3\mathbf{r} \nabla (r^p Y_{pq}) \cdot (\mathbf{r} \times \mathbf{j}(\mathbf{r})). \quad (\text{B.90d})$$

Starting again from Equation (B.90c), we use Equation (B.88) to obtain

$$M_{pq}^{p1} = -i \frac{4\pi}{\sqrt{(2p+1)(p+1)}} \int d^3\mathbf{r} r^{p-1} \mathbf{Y}_{pq}^{*p-1,1}(\Omega) \cdot (\mathbf{r} \times \mathbf{j}_m(\mathbf{r})), \quad (\text{B.91a})$$

$$= -i \frac{4\pi}{\sqrt{(2p+1)(p+1)}} \int d^3\mathbf{r} r^{p-1} \mathbf{Y}_{pq}^{*p-1,1}(\Omega) \cdot [\nabla (\mathbf{r} \cdot \mathbf{M}(\mathbf{r})) - [1 + \mathbf{r} \cdot \nabla] \mathbf{M}(\mathbf{r})] \quad (\text{B.91b})$$

By means of partial integration we find that

$$\int d^3\mathbf{r} r^{p-1} \mathbf{Y}_{pq}^{*p-1,1}(\Omega) \cdot \nabla (\mathbf{r} \cdot \mathbf{M}(\mathbf{r})) = - \int d^3\mathbf{r} \nabla (r^{p-1} \mathbf{Y}_{pq}^{*p-1,1}(\Omega)) \cdot \mathbf{r} \cdot \mathbf{M}(\mathbf{r}) \quad (\text{B.92a})$$

$$= 0 \quad (\text{B.92b})$$

due to Equation (B.54). And similarly, through partial integration we find that

$$(p-1) \int d^3\mathbf{r} r^{p-1} \mathbf{Y}_{pq}^{*p-1,1}(\Omega) \cdot \mathbf{M}(\mathbf{r}) = - \int d^3\mathbf{r} r^{p-1} \mathbf{Y}_{pq}^{*p-1,1}(\Omega) \cdot [3\mathbf{M}(\mathbf{r}) + (\mathbf{r} \cdot \nabla) \mathbf{M}(\mathbf{r})]. \quad (\text{B.93})$$

This renders

$$M_{pq}^{p1} = -i \frac{4\pi(p+1)}{\sqrt{(2p+1)(p+1)}} \int d^3\mathbf{r} r^{p-1} \mathbf{Y}_{pq}^{*p-1,1}(\Omega) \cdot \mathbf{M}(\mathbf{r}). \quad (\text{B.94})$$

Lastly, Equation (B.89) is used to obtain the second term in Equation (B.69):

$$M_{pq}^{p1} = -\frac{4\pi i}{2p+1} \sqrt{\frac{p+1}{p}} \int d^3\mathbf{r} \nabla (r^p Y_{pq}^*(\Omega)) \cdot \mathbf{M}(\mathbf{r}). \quad (\text{B.95})$$

Next, we compute the MT multipole coefficient starting from Equation (B.84). By means of partial integration, we find

$$\int d^3\mathbf{r} r^{p+1} \mathbf{Y}_{pq}^{*p+1,1}(\Omega) \cdot (\nabla \times \mathbf{M}(\mathbf{r})) = \int d^3\mathbf{r} \mathbf{M}(\mathbf{r}) \cdot (\nabla \times r^{p+1} \mathbf{Y}_{pq}^{*p+1,1}(\Omega)). \quad (\text{B.96})$$

The curl of the vector spherical harmonic can further be evaluated by means of Equation (B.86). Subsequently we can use Equation (B.85) and  $r^p \hat{\mathbf{r}} = r^{p-1} \hat{\mathbf{r}}$  once again to obtain the following expression:

$$T_{pq}^{p+1,1} = \frac{4\pi}{2p+3} \int d^3\mathbf{r} r^{p+1} \mathbf{Y}_{pq}^{*p+1,1}(\Omega) \cdot \mathbf{j}(\mathbf{r}) \quad (\text{B.97})$$

$$= \frac{4\pi}{2p+3} \int d^3\mathbf{r} \mathbf{M}(\mathbf{r}) \cdot (\nabla \times r^{p+1} \mathbf{Y}_{pq}^{*p+1,1}(\Omega)) \quad (\text{B.98})$$

$$= -4\pi i \sqrt{\frac{p}{2p+1}} \int d^3\mathbf{r} r^p \mathbf{Y}_{pq}^{*p,1}(\Omega) \cdot \mathbf{M}(\mathbf{r}) \quad (\text{B.99})$$

$$= 4\pi \sqrt{\frac{p}{p+1}} \int d^3\mathbf{r} r^{p-1} (\mathbf{r} \times \mathbf{Y}_{pq}^{*p-1,1}(\Omega)) \cdot \mathbf{M}(\mathbf{r}) \quad (\text{B.100})$$

Interchanging the cross product renders a minus and using Equation (B.89) yields the second term in Equation (B.70):

$$\begin{aligned} T_{pq}^{p+1,1} &= -4\pi \sqrt{\frac{p}{p+1}} \int d^3\mathbf{r} r^{p-1} \mathbf{Y}_{pq}^{*p-1,1}(\Omega) \cdot (\mathbf{r} \times \mathbf{M}(\mathbf{r})) \quad (\text{B.101}) \\ &= \frac{-4\pi}{\sqrt{(p+1)(2p+1)}} \int d^3\mathbf{r} \nabla (r^p Y_{pq}^*(\Omega)) \cdot (\mathbf{r} \times \mathbf{M}(\mathbf{r})). \end{aligned}$$

Finally, we will derive the first term in Equation (B.70). First, we find

$$\mathbf{r} \times \mathbf{M} = \frac{1}{2} \{ \mathbf{r} \times (\mathbf{r} \times \mathbf{j}_m) + \mathbf{r} [\nabla \cdot (\mathbf{r} \times \mathbf{M})] + \nabla \times (r^2 \mathbf{M}) \}. \quad (\text{B.102})$$

Let us highlight that the vector spherical harmonics are no operators and therefore do not act on anything to the right<sup>2</sup>. Thus, by use of Equation (B.36), we find

$$\mathbf{Y}_{pq}^{*p-1,1} \cdot \mathbf{r} = r \hat{\mathbf{r}} \cdot \mathbf{Y}_{pq}^{*p-1,1} \quad (\text{B.103})$$

$$= \frac{r}{\sqrt{p(2p+1)}} \hat{\mathbf{r}} \cdot [p \hat{\mathbf{r}} + i(\hat{\mathbf{r}} \times \mathbf{l})] Y_{pq}^* \quad (\text{B.104})$$

$$= \sqrt{\frac{p}{2p+1}} Y_{pq}^* \quad (\text{B.105})$$

We plug in Equation (B.102) into Equation (B.101), whereby the last term is a vanishing boundary term. Then, we use Equation (B.105), before we once again device partial integration and use

<sup>2</sup>In particular, here we shall not use Equation (B.45), which here reads  $(\hat{\mathbf{r}} \times \mathbf{l}) \cdot \mathbf{r} = 2ir$ .

Equation (B.89) in the last step:

$$\begin{aligned} T_{pq}^{p+1,1} &= -4\pi \sqrt{\frac{p}{p+1}} \int d^3\mathbf{r} r^{p-1} \mathbf{Y}_{pq}^{*p-1,1}(\Omega) \cdot (\mathbf{r} \times \mathbf{M}(\mathbf{r})) \\ &= -4\pi \sqrt{\frac{p}{p+1}} \int d^3\mathbf{r} r^{p-1} \mathbf{Y}_{pq}^{*p-1,1}(\Omega) \\ &\quad \cdot \frac{1}{2} \{ \mathbf{r} \times (\mathbf{r} \times \mathbf{j}_m(\mathbf{r})) + \mathbf{r} [\nabla \cdot (\mathbf{r} \times \mathbf{M}(\mathbf{r}))] \} \end{aligned} \quad (\text{B.106})$$

$$\begin{aligned} &= -\frac{4\pi}{2} \sqrt{\frac{p}{p+1}} \int d^3\mathbf{r} r^{p-1} \mathbf{Y}_{pq}^{*p-1,1}(\Omega) \cdot [\mathbf{r} \times (\mathbf{r} \times \mathbf{j}_m(\mathbf{r}))] \\ &\quad - \frac{4\pi}{2} \sqrt{\frac{p}{p+1}} \sqrt{\frac{p}{2p+1}} \int d^3\mathbf{r} r^p Y_{pq}^*(\Omega) [\nabla \cdot (\mathbf{r} \times \mathbf{M})] \end{aligned} \quad (\text{B.107})$$

$$\begin{aligned} &= -\frac{4\pi}{2} \sqrt{\frac{p}{p+1}} \int d^3\mathbf{r} r^{p-1} \mathbf{Y}_{pq}^{*p-1,1}(\Omega) \cdot [\mathbf{r} \times (\mathbf{r} \times \mathbf{j}_m(\mathbf{r}))] \\ &\quad + \frac{4\pi}{2} \sqrt{\frac{p}{p+1}} \sqrt{\frac{p}{2p+1}} \int d^3\mathbf{r} \nabla (r^p Y_{pq}^*(\Omega)) \cdot (\mathbf{r} \times \mathbf{M}(\mathbf{r})) \end{aligned} \quad (\text{B.108})$$

$$\begin{aligned} &= -\frac{4\pi}{2} \sqrt{\frac{p}{p+1}} \int d^3\mathbf{r} r^{p-1} \mathbf{Y}_{pq}^{*p-1,1}(\Omega) \cdot [\mathbf{r} \times (\mathbf{r} \times \mathbf{j}_m(\mathbf{r}))] \\ &\quad + \frac{4\pi}{2} \sqrt{\frac{p}{p+1}} p \int d^3\mathbf{r} r^{p-1} \mathbf{Y}_{pq}^{*p-1,1}(\Omega) \cdot (\mathbf{r} \times \mathbf{M}(\mathbf{r})) \end{aligned} \quad (\text{B.109})$$

A comparison of Equation (B.109) and Equation (B.101) yields

$$\int d^3\mathbf{r} r^{p-1} \mathbf{Y}_{pq}^{*p-1,1}(\Omega) \cdot (\mathbf{r} \times \mathbf{M}(\mathbf{r})) = \frac{1}{p+2} \int d^3\mathbf{r} r^{p-1} \mathbf{Y}_{pq}^{*p-1,1}(\Omega) \cdot [\mathbf{r} \times (\mathbf{r} \times \mathbf{j}_m(\mathbf{r}))]. \quad (\text{B.110})$$

Using Equation (B.110) directly in Equation (B.101) we find

$$\begin{aligned} T_{pq}^{p+1,1} &= -4\pi \sqrt{\frac{p}{p+1}} \int d^3\mathbf{r} r^{p-1} \mathbf{Y}_{pq}^{*p-1,1}(\Omega) \cdot (\mathbf{r} \times \mathbf{M}(\mathbf{r})) \\ &= -4\pi \sqrt{\frac{p}{p+1}} \frac{1}{p+2} \int d^3\mathbf{r} r^{p-1} \mathbf{Y}_{pq}^{*p-1,1}(\Omega) \cdot [\mathbf{r} \times (\mathbf{r} \times \mathbf{j}_m(\mathbf{r}))]. \end{aligned} \quad (\text{B.111})$$

Finally, once more using Equation (B.89) in the inverse direction and replacing  $\mathbf{j}_m(\mathbf{r})$  by  $\mathbf{j}_{\text{orb}}(\mathbf{r})$ , we obtain the first term of Equation (B.70):

$$T_{pq}^{p+1,1} = -\frac{4\pi}{\sqrt{(p+1)(2p+1)}} \frac{1}{p+2} \int d^3\mathbf{r} \nabla (r^p Y_{pq}^*(\Omega)) \cdot [\mathbf{r} \times (\mathbf{r} \times \mathbf{j}_{\text{orb}}(\mathbf{r}))].$$

## B.4 Why there are no monopole gauge fields or monopole magnetic fields

Here, we argue why we can drop  $p = 0$  in Equation (B.3). First, we note that in both, Equations (B.69) and (B.70), the integrand contains a factor  $\nabla (r^0 Y_{00}^*)$ , which is zero because  $Y_{00}$  is a

constant. Then, perhaps one is skeptic of the divergence  $1/\sqrt{0}$  in  $M_{00}^{01}$  in Equation (B.69). However in Equation (B.3), we see that  $\mathbf{Y}_{00}^{01}$  appears at  $p = 0$ . And  $\mathbf{Y}_{00}^{01} \equiv \mathbf{0}$  and hence independent of the M multipole coefficient for  $p = 0$   $\mathbf{A}(\mathbf{r})$  is always zero, i.e.,  $M_{00}^{01} \equiv 0$ . Later in Section B.6 it is easily possible to check that the magnetic field also vanishes at  $p = 0$ . Thus, without loss of generality we can drop  $p = 0$ .

## B.5 Multipole coefficients for an electron cloud

Next, we want to express the magnetic (M) multipole coefficient and the magnetic toroidal (MT) multipole coefficient of a many-body wave function of  $N$  electrons. So first we recall the formalism introduced in Section 2.1. Specifically, we need the spin-magnetization of a many-body state given in Equation (2.34), i.e.

$$\hat{\mathbf{m}}^{(s)}(\mathbf{r}) = -\mu_B \sum_{i=1}^N \delta(\mathbf{r} - \mathbf{r}_i) \boldsymbol{\sigma}.$$

This allows us to define the spin-magnetization current as

$$\hat{\mathbf{j}}_m(\mathbf{r}) = \nabla \times \hat{\mathbf{m}}^{(s)}(\mathbf{r}) \quad (\text{B.112})$$

The orbital current operator would read<sup>3</sup>

$$\hat{\mathbf{j}}_{\text{orb}}(\mathbf{r}) = i\mu_B \sum_{i=1}^N [\nabla \delta(\mathbf{r} - \mathbf{r}_i) + \delta(\mathbf{r} - \mathbf{r}_i) \nabla], \quad (\text{B.115})$$

which relates to the orbital angular momentum through

$$\mathbf{r} \times \hat{\mathbf{j}}_{\text{orb}}(\mathbf{r}) = -\mu_B \sum_{i=1}^N [\mathbf{l} \delta(\mathbf{r} - \mathbf{r}_i) + \delta(\mathbf{r} - \mathbf{r}_i) \mathbf{l}]. \quad (\text{B.116})$$

Thus, we can obtain the static current using

$$\mathbf{j}(\mathbf{r}) = \text{Tr} \left\{ \rho \hat{\mathbf{j}}(\mathbf{r}) \right\}, \quad (\text{B.117})$$

$$\hat{\mathbf{j}}(\mathbf{r}) = \hat{\mathbf{j}}_m(\mathbf{r}) + \hat{\mathbf{j}}_{\text{orb}}(\mathbf{r}). \quad (\text{B.118})$$

The next step is defining the quantum mechanical operator for the M and MT multipole coefficients. Let us use Equation (B.69) and Equation (B.70), which were derived in the previous

<sup>3</sup>One may want to consider the following simplified picture:

$$\mathbf{j}_{\text{orb}}(\mathbf{r}) = e\mathbf{v}(\mathbf{r}) = \frac{e}{2m} 2\mathbf{p}(\mathbf{r}) = -\frac{|e|\hbar}{2m} \frac{2}{\hbar} \mathbf{p}(\mathbf{r}). \quad (\text{B.113})$$

Note that  $\mu_B = \frac{|e|\hbar}{2m}$ ,  $\hbar = 1$  and  $\mathbf{l}(\mathbf{r}) = \mathbf{r} \times \mathbf{p}(\mathbf{r})$  to obtain

$$\mathbf{r} \times \mathbf{j}_{\text{orb}}(\mathbf{r}) = -2\mu_B \mathbf{l}(\mathbf{r}). \quad (\text{B.114})$$

section:

$$M_{pq}^{p1} = -\frac{4\pi i}{2p+1} \int d^3\mathbf{r} \nabla (r^p Y_{pq}^*(\Omega)) \cdot \left[ \frac{\mathbf{r} \times \mathbf{j}_{\text{orb}}(\mathbf{r})}{\sqrt{p(p+1)}} + \sqrt{\frac{p+1}{p}} \mathbf{M}(\mathbf{r}) \right],$$

$$T_{pq}^{p+1,1} = \frac{-4\pi}{\sqrt{(p+1)(2p+1)}} \int d^3\mathbf{r} \nabla (r^p Y_{pq}^*(\Omega)) \cdot \left[ \mathbf{r} \times \frac{\mathbf{r} \times \mathbf{j}_{\text{orb}}(\mathbf{r})}{p+2} + \mathbf{r} \times \mathbf{M}(\mathbf{r}) \right].$$

We replace the classical expressions with the appropriate quantum mechanical operators and yield:

$$\hat{M}_{pq}^{p1} = \frac{4\pi i \mu_B}{2p+1} \sqrt{\frac{p+1}{p}} \int d^3\mathbf{r} \nabla (r^p Y_{pq}^*(\Omega)) \cdot \sum_{i=1}^N \left[ \frac{[\mathbf{l}\delta(\mathbf{r}-\mathbf{r}_i) + \delta(\mathbf{r}-\mathbf{r}_i)\mathbf{l}]}{p+1} + \delta(\mathbf{r}-\mathbf{r}_i)\boldsymbol{\sigma} \right], \quad (\text{B.119})$$

$$\hat{T}_{pq}^{p+1,1} = \frac{4\pi \mu_B}{\sqrt{(p+1)(2p+1)}} \int d^3\mathbf{r} \nabla (r^p Y_{pq}^*(\Omega)) \cdot \sum_{i=1}^N \left[ \mathbf{r} \times \frac{[\mathbf{l}\delta(\mathbf{r}-\mathbf{r}_i) + \delta(\mathbf{r}-\mathbf{r}_i)\mathbf{l}]}{p+2} + \mathbf{r} \times \delta(\mathbf{r}-\mathbf{r}_i)\boldsymbol{\sigma} \right]. \quad (\text{B.120})$$

This can be used to obtain the expectation value of the multipole coefficients by means of

$$M_{pq}^{p1} = \text{Tr} \left\{ \rho \hat{M}_{pq}^{p1} \right\}, \quad (\text{B.121})$$

$$T_{pq}^{p+1,1} = \text{Tr} \left\{ \rho \hat{T}_{pq}^{p+1,1} \right\}. \quad (\text{B.122})$$

Note that  $\nabla (r^p Y_{pq}^*(\Omega))$  contains an operator that has not been applied. Thus, it would be a misleading notation to execute  $\int d^3\mathbf{r}$  and write  $\nabla (r_i^p Y_{pq}^*(\Omega_i))$ . Together with Equation (B.3),

$$\mathbf{A}(\mathbf{r}) = \sum_{p=1}^{\infty} \sum_{q=-p}^p \left[ M_{pq}^{p1} \frac{1}{r^{p+1}} \mathbf{Y}_{pq}^{p1}(\Omega) + T_{pq}^{p+1,1} \frac{1}{r^{p+2}} \mathbf{Y}_{pq}^{p+1,1}(\Omega) \right],$$

this yields a general expression for the vector gauge field of an electron cloud.

## B.6 Magnetic field of a general vector gauge field

The original assumption to obtain the vector Poisson equation from the Maxwell equations states that

$$\mathbf{B} = \nabla \times \mathbf{A}. \quad (\text{B.123})$$

We found the vector gauge field in Coulomb gauge  $\nabla \cdot \mathbf{A} = 0$  generally has the form given in Equation (B.3), that reads

$$\mathbf{A}(\mathbf{r}) = \sum_{p=0}^{\infty} \sum_{q=-p}^p \left[ M_{pq}^{p1} \frac{1}{r^{p+1}} \mathbf{Y}_{pq}^{p1}(\Omega) + T_{pq}^{p+1,1} \frac{1}{r^{p+2}} \mathbf{Y}_{pq}^{p+1,1}(\Omega) \right],$$



where here we start from  $p = 0$  in order not to presume that the magnetic field has no monopole contribution. But the argument in Section B.4 can be followed to see that every contribution at  $p = 0$  always vanishes.

It is also generally true that

$$\begin{aligned} \nabla \times [f(r)\mathbf{Y}_{pq}^{p1}] &= i\mathbf{Y}_{pq}^{p-1,1} \sqrt{\frac{p+1}{2p+1}} \left[ \frac{\partial}{\partial r} + \frac{p+1}{r} \right] f(r) \\ &\quad - i\mathbf{Y}_{pq}^{p+1,1} \sqrt{\frac{p}{2p+1}} \left[ \frac{p}{r} - \frac{\partial}{\partial r} \right] f(r) \end{aligned} \quad (\text{B.124a})$$

$$\nabla \times [f(r)\mathbf{Y}_{pq}^{p+1,1}] = i\mathbf{Y}_{pq}^{p1} \sqrt{\frac{p}{2p+1}} \left[ \frac{\partial}{\partial r} + \frac{p+2}{r} \right] f(r), \quad (\text{B.124b})$$

for arbitrary function  $f(r)$ . We hence see that

$$\nabla \times \left[ \frac{1}{r^{p+1}} \mathbf{Y}_{pq}^{p+1,1} \right] \equiv 0 \quad (\text{B.125})$$

and the magnetic field must be given in terms of magnetic multipoles only. The *general form of the magnetic field* reads

$$\mathbf{B} = \sum_{p=0}^{\infty} \sum_{q=-p}^p M_{pq}^{p1} \nabla \times \left[ \frac{1}{r^{p+1}} \mathbf{Y}_{pq}^{p1}(\Omega) \right] \quad (\text{B.126})$$

$$= -i \sum_{p=0}^{\infty} \sum_{q=-p}^p \sqrt{p(2p+1)} M_{pq}^{p1} \frac{1}{r^{p+2}} \mathbf{Y}_{pq}^{p+1,1}(\Omega). \quad (\text{B.127})$$

Here, again the M multipole coefficients are given by

$$M_{pq}^{p1} = -\frac{4\pi i}{2p+1} \int d^3\mathbf{r} \nabla (r^p Y_{pq}^*(\Omega)) \cdot \left[ \frac{\mathbf{r} \times \mathbf{j}_{\text{orb}}(\mathbf{r})}{\sqrt{p(p+1)}} + \sqrt{\frac{p+1}{p}} \mathbf{M}(\mathbf{r}) \right],$$

as derived in Section B.3. Finally, we see that  $\sqrt{p(2p+1)} M_{pq}^{p1}$  is zero at  $p = 0$ .

## B.7 Generating vector spherical harmonics

In this section, we derive

$$\hat{\mathbf{r}} Y_{pq} = \sqrt{\frac{p}{2p+1}} \mathbf{Y}_{pq}^{p-1,1} - \sqrt{\frac{p+1}{2p+1}} \mathbf{Y}_{pq}^{p+1,1} \quad (\text{B.128a})$$

$$\boldsymbol{\ell} Y_{pq} = \sqrt{p(p+1)} \mathbf{Y}_{pq}^{p1} \quad (\text{B.128b})$$

$$(\hat{\mathbf{r}} \times \boldsymbol{\ell}) Y_{pq} = i(p+1) \sqrt{\frac{p}{2p+1}} \mathbf{Y}_{pq}^{p-1,1} + ip \sqrt{\frac{p+1}{2p+1}} \mathbf{Y}_{pq}^{p+1,1}. \quad (\text{B.128c})$$

$$\hat{\mathbf{r}} Y_{pq} = \sqrt{\frac{4\pi}{3}} \sum_m (-1)^m Y_{1,-m} \mathbf{e}_m Y_{pq} \quad (\text{B.129a})$$

$$= - \sum_{L,M,m} \langle 10p0|L0 \rangle \langle LM1m|pq \rangle Y_{LM} \mathbf{e}_m \quad (\text{B.129b})$$

$$= - \sum_L \langle 10p0|L0 \rangle \mathbf{Y}_{pq}^{L1} \quad (\text{B.129c})$$

$$= - \langle 10p0|(p-1)0 \rangle \mathbf{Y}_{pq}^{p-1,1} - \langle 10p0|p0 \rangle \mathbf{Y}_{pq}^{p1} - \langle 10p0|(p+1)0 \rangle \mathbf{Y}_{pq}^{p+1,1} \quad (\text{B.129d})$$

$$= \sqrt{\frac{p}{2p+1}} \mathbf{Y}_{pq}^{p-1,1} - \sqrt{\frac{p+1}{2p+1}} \mathbf{Y}_{pq}^{p+1,1} \quad (\text{B.129e})$$

For the first equal sign, we used the definition of  $\hat{\mathbf{r}}$  in

$$\hat{\mathbf{r}} = \frac{\mathbf{r}}{|\mathbf{r}|} = \frac{\mathbf{r}}{r} = \sqrt{\frac{4\pi}{3}} \sum_q (-1)^q Y_{1,-q} \mathbf{e}_q. \quad (\text{B.130})$$

To get to the second line, we used the product of two spherical harmonics, i.e.,

$$Y_{\ell m} Y_{pq} = (-1)^{1+m} \sum_{L=0}^{\infty} \sum_{M=-L}^L \sqrt{\frac{(2\ell+1)}{4\pi}} \langle \ell 0 p 0 | L 0 \rangle \langle LM \ell(-m) | pq \rangle Y_{LM}. \quad (\text{B.131a})$$

In the third line, we use the definition of vector spherical harmonics, eq. (B.4). In the fourth line, we explicitly write down the sum over  $L$ , since it can only go over the values  $p \pm 1$  and  $p$ , due to the rules of angular momentum coupling. Finally, in the last line, we evaluate the three Clebsch–Gordan coefficients, one of which is zero. Next, we see that

$$\boldsymbol{\ell} Y_{pq} = \sum_m \ell^m Y_{pq} \mathbf{e}_m \quad (\text{B.132a})$$

$$= \sum_m \sqrt{p(p+1)} \langle p(q-m)1m|pq \rangle Y_{p,q-m} \mathbf{e}_m \quad (\text{B.132b})$$

$$= \sqrt{p(p+1)} \mathbf{Y}_{pq}^{p1}. \quad (\text{B.132c})$$

For the first equal sign, we simply write  $\boldsymbol{\ell}$  in terms of its spherical components. In the second line, we use the fact that this angular momentum acts like a ladder operator, i.e.,

$$\ell_m Y_{pq} = (-1)^m \sqrt{p(p+1)} \langle p(q+m)1(-m)|pq \rangle Y_{p,q+m} \quad (\text{B.133a})$$

$$\ell^m Y_{pq} = \sqrt{p(p+1)} \langle p(q-m)1m|pq \rangle Y_{p,q-m}. \quad (\text{B.133b})$$

eq. (B.133b) Finally, in the last line we use the definition of a vector spherical harmonics.

In order to derive  $(\hat{\mathbf{r}} \times \boldsymbol{\ell}) Y_{pq}$ , eq. (B.128c), we look at the components of the resulting vector  $\mathbf{V}$ :

$$(\hat{\mathbf{r}} \times \boldsymbol{\ell}) Y_{pq} \equiv \mathbf{V} = V^- \mathbf{e}_- + V^0 \mathbf{e}_0 + V^+ \mathbf{e}_+ \quad (\text{B.134})$$

We can start by investigating  $V^-$ :

$$V^- = i(\hat{r}^0 \ell^- - \hat{r}^- \ell^0) Y_{pq} = i(\hat{r}_0 \ell^- + \hat{r}_+ \ell^0) Y_{pq} \quad (\text{B.135})$$

where we pull down the index of  $\hat{r}$ . Next, we write  $\hat{r}_q$  in terms of spherical harmonics, which reads

$$\hat{r}^q = \sqrt{\frac{4\pi}{3}} Y_{1q}^* = \sqrt{\frac{4\pi}{3}} (-1)^q Y_{1,-q} \quad \hat{r}_q = \sqrt{\frac{4\pi}{3}} Y_{1q}, \quad (\text{B.136})$$

as well as evaluate how  $\ell^m$  acts on  $Y_{pq}$ , as written in eq. (B.133b):

$$\begin{aligned} V^- &= i\sqrt{\frac{4\pi}{3}} \sqrt{p(p+1)} \langle p(q+1)1(-1)|pq \rangle Y_{10} Y_{p,q+1} \\ &\quad + i\sqrt{\frac{4\pi}{3}} \sqrt{p(p+1)} \langle pq10|pq \rangle Y_{11} Y_{p,q} \end{aligned} \quad (\text{B.137})$$

Now we evaluate the product of two spherical harmonics, as detailed in eq. (B.131a):

$$\begin{aligned} V^- &= i\sqrt{p(p+1)} \sum_{L=0}^{\infty} \sum_{M=-L}^L \left[ -\langle 10p0|L0 \rangle \langle LM10|p(q+1) \rangle \langle p(q+1)1(-1)|pq \rangle Y_{LM} \right. \\ &\quad \left. + \langle 10p0|L0 \rangle \langle LM1(-1)|pq \rangle \langle pq10|pq \rangle Y_{LM} \right] \end{aligned} \quad (\text{B.138})$$

We can now perform the sum over both  $L$  and  $M$ . First, since the magnetic quantum numbers have to match in each Clebsch–Gordan coefficient,  $M$  is uniquely determined (and if the necessary value for  $M$  should lie outside its range of  $-L \leq M \leq L$ , the corresponding Clebsch–Gordan coefficient is zero anyway):

$$\begin{aligned} V^- &= i\sqrt{p(p+1)} \sum_{L=0}^{\infty} \left[ -\langle 10p0|L0 \rangle \langle L(q+1)10|p(q+1) \rangle \langle p(q+1)1(-1)|pq \rangle Y_{L,q+1} \right. \\ &\quad \left. + \langle 10p0|L0 \rangle \langle L(q+1)1(-1)|pq \rangle \langle pq10|pq \rangle Y_{L,q+1} \right] \end{aligned} \quad (\text{B.139})$$

Second, due to the first Clebsch–Gordan coefficient in each term, the value of  $L$  is constrained to be either  $L = p \pm 1$  or  $L = p$ . However, by actually calculating those Clebsch–Gordan coefficients, we see that the one for  $L = p$  actually vanishes. Therefore, we can perform the sum over  $L$  simply by using two values,  $p \pm 1$ :

$$\begin{aligned} V^- &= i\sqrt{p(p+1)} \left[ -\langle 10p0|(p-1)0 \rangle \langle (p-1)(q+1)10|p(q+1) \rangle \langle p(q+1)1(-1)|pq \rangle Y_{p-1,q+1} \right. \\ &\quad + \langle 10p0|(p-1)0 \rangle \langle (p-1)(q+1)1(-1)|pq \rangle \langle pq10|pq \rangle Y_{p-1,q+1} \\ &\quad - \langle 10p0|(p+1)0 \rangle \langle (p+1)(q+1)10|p(q+1) \rangle \langle p(q+1)1(-1)|pq \rangle Y_{p+1,q+1} \\ &\quad \left. + \langle 10p0|(p+1)0 \rangle \langle (p+1)(q+1)1(-1)|pq \rangle \langle pq10|pq \rangle Y_{p+1,q+1} \right] \end{aligned} \quad (\text{B.140})$$

The next step is to evaluate the Clebsch–Gordan coefficients. As we already mentioned, the first one in each row only exists for  $L = p \pm 1$ :

$$\langle 10p0|L0\rangle = \begin{cases} -\sqrt{\frac{p}{2p+1}}, & L = p - 1 \\ 0, & L = p \\ \sqrt{\frac{p+1}{2p+1}}, & L = p + 1 \end{cases} \quad (\text{B.141})$$

This means we can write:

$$\begin{aligned} V^- = i\sqrt{\frac{p(p+1)}{2p+1}} & \left[ \sqrt{p} \langle (p-1)(q+1)10|p(q+1)\rangle \langle p(q+1)1(-1)|pq\rangle Y_{p-1,q+1} \right. \\ & - \sqrt{p} \langle (p-1)(q+1)1(-1)|pq\rangle \langle pq10|pq\rangle Y_{p-1,q+1} \\ & - \sqrt{p+1} \langle (p+1)(q+1)10|p(q+1)\rangle \langle p(q+1)1(-1)|pq\rangle Y_{p+1,q+1} \\ & \left. + \sqrt{p+1} \langle (p+1)(q+1)1(-1)|pq\rangle \langle pq10|pq\rangle Y_{p+1,q+1} \right] \end{aligned} \quad (\text{B.142})$$

Since the first two Clebsch–Gordan coefficients are multiplied by a spherical harmonic  $Y_{p-1,q+1}$ , the allowed values for  $q$  are:  $-(p-1) \leq q+1 \leq p-1$ . Otherwise, the spherical harmonic vanishes. Under this assumption, we can evaluate the first two lines of coefficients:

$$\begin{aligned} & \langle (p-1)(q+1)10|p(q+1)\rangle \langle p(q+1)1(-1)|pq\rangle \quad (\text{B.143}) \\ & - \langle (p-1)(q+1)10|p(q+1)\rangle \langle p(q+1)1(-1)|pq\rangle = \frac{p+1}{p} \sqrt{\frac{(p-q-1)(p-q)}{2(2p-1)(p+1)}} \end{aligned}$$

In the third and fourth line, we have Clebsch–Gordan coefficients multiplied by a spherical harmonic of type  $Y_{p+1,q+1}$ . This means, the allowed values for  $q$  are:  $-(p+1) \leq q+1 \leq p+1$ . Under this assumption, we can again evaluate the coefficients:

$$\begin{aligned} & \langle (p+1)(q+1)10|p(q+1)\rangle \langle p(q+1)1(-1)|pq\rangle \quad (\text{B.144}) \\ & - \sqrt{p+1} \langle (p+1)(q+1)1(-1)|pq\rangle \langle pq10|pq\rangle = -\frac{1}{p+1} \sqrt{\frac{p(p+q+1)(p+q+2)}{2(2p+3)}} \end{aligned}$$

This drastically simplifies the expression for  $V^-$ :

$$V^- = i(p+1) \sqrt{\frac{(p-q-1)(p-q)}{2(2p+1)(2p-1)}} Y_{p-1,q+1} + ip \sqrt{\frac{(p+q+1)(p+q+2)}{2(2p+1)(2p+3)}} Y_{p+1,q+1} \quad (\text{B.145})$$

Now we perform a rather unintuitive step, which will however lead to a nice result: we pull out

certain factors from underneath the square root:

$$\begin{aligned} V^- &= i(p+1)\sqrt{\frac{p}{2p+1}}\sqrt{\frac{(p-q-1)(p-q)}{2p(2p-1)}}Y_{p-1,q+1} \\ &\quad + ip\sqrt{\frac{p+1}{2p+1}}\sqrt{\frac{(p+q+1)(p+q+2)}{2(p+1)(2p+3)}}Y_{p+1,q+1} \end{aligned} \quad (\text{B.146})$$

The reason for this is that now we can write the large square root again as a Clebsch–Gordan coefficient:

$$\langle (p-1)(q+1)1(-1)|pq \rangle^{-\underline{(p-1) \leq q+1 \leq p-1}} \sqrt{\frac{(p-q-1)(p-q)}{2p(2p-1)}} \quad (\text{B.147a})$$

$$\langle (p+1)(q+1)1(-1)|pq \rangle^{-\underline{(p+1) \leq q+1 \leq p+1}} \sqrt{\frac{(p+q+1)(p+q+2)}{2(p+1)(2p+3)}} \quad (\text{B.147b})$$

which leads to:

$$\begin{aligned} V^- &= i(p+1)\sqrt{\frac{p}{2p+1}}\langle (p-1)(q+1)1(-1)|pq \rangle Y_{p-1,q+1} \\ &\quad + ip\sqrt{\frac{p+1}{2p+1}}\langle (p+1)(q+1)1(-1)|pq \rangle Y_{p+1,q+1} \end{aligned} \quad (\text{B.148})$$

To see why this is useful, let us list the components of a vector spherical harmonic:

$$(\mathbf{Y}_{pq}^{\ell 1})^{m'} = \begin{cases} \langle \ell(q+1)1(-1)|pq \rangle Y_{\ell,q+1}, & m' = -1 \\ \langle \ell q 1 0 | pq \rangle Y_{\ell q}, & m' = 0 \\ \langle \ell(q-1)1 1 | pq \rangle Y_{\ell,q-1}, & m' = 1 \end{cases} \quad (\text{B.149})$$

This means, the minus-component of  $(\hat{\mathbf{r}} \times \boldsymbol{\ell})Y_{pq}$ , which we denoted as  $V^-$ , is exactly the minus-component of two vector spherical harmonics! In particular, we find

$$V^- = i(p+1)\sqrt{\frac{p}{2p+1}}(\mathbf{Y}_{pq}^{p-1,1})^- + ip\sqrt{\frac{p+1}{2p+1}}(\mathbf{Y}_{pq}^{p+1,1})^- \quad (\text{B.150})$$

With a similar, albeit tedious, calculation, we can calculate the other components of  $(\hat{\mathbf{r}} \times \boldsymbol{\ell})Y_{pq}$  as well:

$$\begin{aligned} V^0 &= i(p+1)\sqrt{\frac{p}{2p+1}}\langle (p-1)q 1 0 | pq \rangle Y_{p-1,q} \\ &\quad + ip\sqrt{\frac{p+1}{2p+1}}\langle (p+1)q 1 0 | pq \rangle Y_{p+1,q} \end{aligned} \quad (\text{B.151})$$

$$\begin{aligned} V^+ &= i(p+1)\sqrt{\frac{p}{2p+1}}\langle (p-1)(q-1)1 1 | pq \rangle Y_{p-1,q-1} \\ &\quad + ip\sqrt{\frac{p+1}{2p+1}}\langle (p+1)(q-1)1 1 | pq \rangle Y_{p+1,q-1} \end{aligned} \quad (\text{B.152})$$

This means, our final result is:

$$\begin{aligned}
 (\hat{\mathbf{r}} \times \boldsymbol{\ell})Y_{pq} &= V^- \mathbf{e}_- + V^0 \mathbf{e}_0 + V^+ \mathbf{e}_+ \\
 &= i(p+1) \sqrt{\frac{p}{2p+1}} \mathbf{Y}_{pq}^{p-1,1} + ip \sqrt{\frac{p+1}{2p+1}} \mathbf{Y}_{pq}^{p+1,1}
 \end{aligned} \tag{B.153}$$

which completes the proof.

# Appendix C

## Experimental data

Table 1 contains a list of MAGNDATA [15] entries used in this study. Each `0.xxx.mcif` label is linked to its web-entry [387] and the corresponding experimental reference. The purpose of Table 1 is to allow quick access to the experimental data. Furthermore, the inequivalent magnetic sites that constitute magnetic clusters are listed as well. For each cluster, the experimental on-site magnetic moment  $\mu_{\text{exp}}$ , the LSDA+CMP on-site magnetic moment  $\mu_{\text{th}}$  and the individual contribution from spin and orbital angular momentum in LSDA+CMP  $\mu_s$  and  $\mu_l$  are presented. The number of degrees of freedom, that is directly related to the number of magnetic configurations in the CMP basis, is given, as well as the number of active CMPs in the experimental magnetic configuration.

Note that some entries either lack  $\mu_{\text{exp}}$  or the number of active CMPs. This is because following the experimental references we could not validate some of the information due to various reasons. Some examples, where  $\mu_{\text{exp}}$  could not be confirmed, include among others: `0.110.mcif`  $\text{Cr}_2\text{O}_3$ —here, the order was determined using second harmonic generation—`0.113.mcif`  $\text{NiCO}_3$ , `0.114.mcif`  $\text{MnCO}_3$ —here, the magnetic moment was given an arbitrary value. On the other hand, there are entries, where the exact magnetic order could not be confirmed. For instance, `0.154.mcif`  $\text{Er}_2\text{Ru}_2\text{O}_7$ , where MAGNDATA commented that not all possible alternative models seem to have been checked, or `0.155.mcif`  $\text{CaMnGe}_2\text{O}_6$ , where there is some controversy around the proposed magnetic order [227, 228].

Table 1: Experimental data.

0.1.mcif LaMnO <sub>3</sub> Ref. [191]						
cluster	$\mu_{\text{exp}}$	$\mu_{\text{th}}$	$\mu_s$	$\mu_l$	active CMP	dgr. of freedom
Mn	3.87	3.51	3.53	0.01	2	12
0.3.mcif LiCa <sub>3</sub> OsO <sub>6</sub> Ref. [282]						
cluster	$\mu_{\text{exp}}$	$\mu_{\text{th}}$	$\mu_s$	$\mu_l$	active CMP	dgr. of freedom
O	0.0	0.10	0.09	0.01	0	24
Os	2.2	1.59	1.68	0.09	1	6
0.4.mcif Cr <sub>2</sub> NiO <sub>4</sub> Ref. [292]						
cluster	$\mu_{\text{exp}}$	$\mu_{\text{th}}$	$\mu_s$	$\mu_l$	active CMP	dgr. of freedom
Cr	1.40	2.67	2.69	0.02	2	12
Ni	1.64	1.42	1.25	0.17	2	6
0.5.mcif Cr <sub>2</sub> S <sub>3</sub> Ref. [293]						
cluster	$\mu_{\text{exp}}$	$\mu_{\text{th}}$	$\mu_s$	$\mu_l$	active CMP	dgr. of freedom
Cr	1.19	2.64	2.66	0.02	2	3
Cr	1.19	2.63	2.65	0.01	2	3
Cr	1.19	2.64	2.66	0.02	2	6
0.6.mcif YMnO <sub>3</sub> Ref. [297]						
cluster	$\mu_{\text{exp}}$	$\mu_{\text{th}}$	$\mu_s$	$\mu_l$	active CMP	dgr. of freedom
Mn	2.90	3.45	3.47	0.02	2	18
0.7.mcif ScMnO <sub>3</sub> Ref. [297]						
cluster	$\mu_{\text{exp}}$	$\mu_{\text{th}}$	$\mu_s$	$\mu_l$	active CMP	dgr. of freedom
Mn	3.03	3.37	3.39	0.02	2	18
0.9.mcif GdB <sub>4</sub> Ref. [174]						
cluster	$\mu_{\text{exp}}$	$\mu_{\text{th}}$	$\mu_s$	$\mu_l$	active CMP	dgr. of freedom
Gd	7.14	6.91	6.83	0.07	1	12



0.10.mcif DyFeO <sub>3</sub> Ref. [192]						
cluster	$\mu_{\text{exp}}$	$\mu_{\text{th}}$	$\mu_s$	$\mu_l$	active CMP	dgr. of freedom
Dy	1.0	---	---	---	0	24
Fe	1.04	---	---	---	0	24
0.12.mcif U <sub>3</sub> (Al <sub>3</sub> Ru) <sub>4</sub> Ref. [207]						
cluster	$\mu_{\text{exp}}$	$\mu_{\text{th}}$	$\mu_s$	$\mu_l$	active CMP	dgr. of freedom
U	2.50	1.09	1.50	2.59	5	18
0.13.mcif Ca <sub>3</sub> MnCoO <sub>6</sub> Ref. [212]						
cluster	$\mu_{\text{exp}}$	$\mu_{\text{th}}$	$\mu_s$	$\mu_l$	active CMP	dgr. of freedom
Co	0.66	0.02	0.02	0.0	1	6
Mn	1.93	2.49	2.47	0.01	1	6
0.15.mcif MnF <sub>2</sub> Ref. [224]						
cluster	$\mu_{\text{exp}}$	$\mu_{\text{th}}$	$\mu_s$	$\mu_l$	active CMP	dgr. of freedom
Mn	4.6	4.53	4.53	0.00	1	6
0.16.mcif EuTiO <sub>3</sub> Ref. [232]						
cluster	$\mu_{\text{exp}}$	$\mu_{\text{th}}$	$\mu_s$	$\mu_l$	active CMP	dgr. of freedom
Eu	6.92	6.29	6.63	0.33	2	6
0.17.mcif FePO <sub>4</sub> Ref. [239]						
cluster	$\mu_{\text{exp}}$	$\mu_{\text{th}}$	$\mu_s$	$\mu_l$	active CMP	dgr. of freedom
Fe	4.15	3.98	3.96	0.01	3	12
O	0.0	0.13	0.13	0.00	0	12
O	0.0	0.12	0.12	0.0	0	12
0.18.mcif Ba(MnAs) <sub>2</sub> Ref. [244]						
cluster	$\mu_{\text{exp}}$	$\mu_{\text{th}}$	$\mu_s$	$\mu_l$	active CMP	dgr. of freedom
Mn	3.88	3.63	3.61	0.01	1	6

0.19.mcif TiMnO <sub>3</sub> Ref. [248]						
cluster	$\mu_{\text{exp}}$	$\mu_{\text{th}}$	$\mu_s$	$\mu_l$	active CMP	dgr. of freedom
Mn	4.55	4.34	4.34	0.00	1	6
0.20.mcif MnTe <sub>2</sub> Ref. [255]						
cluster	$\mu_{\text{exp}}$	$\mu_{\text{th}}$	$\mu_s$	$\mu_l$	active CMP	dgr. of freedom
Mn	4.27	4.07	4.03	0.03	1	12
0.21.mcif NiPbO <sub>3</sub> Ref. [258]						
cluster	$\mu_{\text{exp}}$	$\mu_{\text{th}}$	$\mu_s$	$\mu_l$	active CMP	dgr. of freedom
Ni	1.69	---	---	---	0	12
0.22.mcif DyB <sub>4</sub> Ref. [263]						
cluster	$\mu_{\text{exp}}$	$\mu_{\text{th}}$	$\mu_s$	$\mu_l$	active CMP	dgr. of freedom
Dy	9.8	8.45	4.65	3.79	1	12
0.23.mcif Ca <sub>3</sub> Mn <sub>2</sub> O <sub>7</sub> Ref. [269]						
cluster	$\mu_{\text{exp}}$	$\mu_{\text{th}}$	$\mu_s$	$\mu_l$	active CMP	dgr. of freedom
Mn	2.67	2.54	2.56	0.02	1	12
0.24.mcif LiMnPO <sub>4</sub> Ref. [276]						
cluster	$\mu_{\text{exp}}$	$\mu_{\text{th}}$	$\mu_s$	$\mu_l$	active CMP	dgr. of freedom
Mn	3.9	4.49	4.49	0.0	2	12
0.25.mcif NaOsO <sub>3</sub> Ref. [277]						
cluster	$\mu_{\text{exp}}$	$\mu_{\text{th}}$	$\mu_s$	$\mu_l$	active CMP	dgr. of freedom
Os	1.0	0.87	0.93	0.06	2	12
0.26.mcif TmAgGe Ref. [278]						
cluster	$\mu_{\text{exp}}$	$\mu_{\text{th}}$	$\mu_s$	$\mu_l$	active CMP	dgr. of freedom
Tm	6.44	---	---	---	0	24

0.27.mcif Y(Fe <sub>2</sub> Ge) <sub>2</sub> Ref. [279]						
cluster	$\mu_{\text{exp}}$	$\mu_{\text{th}}$	$\mu_s$	$\mu_l$	active CMP	dgr. of freedom
Fe	0.63	1.98	1.92	0.05	2	12
Fe	0.63	1.96	1.90	0.06	2	12
0.28.mcif LiFe(SiO <sub>3</sub> ) <sub>2</sub> Ref. [280]						
cluster	$\mu_{\text{exp}}$	$\mu_{\text{th}}$	$\mu_s$	$\mu_l$	active CMP	dgr. of freedom
Fe	4.67	4.07	4.05	0.01	3	12
O	0.0	0.15	0.15	0.0	0	12
O	0.0	0.14	0.14	0.0	0	12
O	0.0	0.14	0.14	0.00	0	12
O	0.0	0.14	0.13	0.00	0	12
0.30.mcif YbMnO <sub>3</sub> Ref. [283]						
cluster	$\mu_{\text{exp}}$	$\mu_{\text{th}}$	$\mu_s$	$\mu_l$	active CMP	dgr. of freedom
Yb	0.0	1.15	0.36	0.79	0	12
Mn	3.25	3.30	3.32	0.01	2	18
0.36.mcif NiF <sub>2</sub> Ref. [286]						
cluster	$\mu_{\text{exp}}$	$\mu_{\text{th}}$	$\mu_s$	$\mu_l$	active CMP	dgr. of freedom
Ni	2.00	1.76	1.57	0.18	2	6
0.37.mcif U <sub>3</sub> Al <sub>2</sub> Si <sub>3</sub> Ref. [287]						
cluster	$\mu_{\text{exp}}$	$\mu_{\text{th}}$	$\mu_s$	$\mu_l$	active CMP	dgr. of freedom
U	0.16	0.18	1.52	1.70	1	3
U	0.16	0.16	1.49	1.64	1	3
U	1.29	0.44	1.76	2.20	4	12
0.39.mcif NaNd <sub>2</sub> RuO <sub>6</sub> Ref. [288]						
cluster	$\mu_{\text{exp}}$	$\mu_{\text{th}}$	$\mu_s$	$\mu_l$	active CMP	dgr. of freedom
Nd	2.24	0.82	2.75	3.51	3	12
Ru	1.61	1.53	1.46	0.07	2	6

0.43.mcif HoMnO <sub>3</sub> Ref. [285]						
cluster	$\mu_{\text{exp}}$	$\mu_{\text{th}}$	$\mu_s$	$\mu_l$	active CMP	dgr. of freedom
Ho	4.17	9.35	3.73	5.62	1	6
Ho	1.31	9.32	3.75	5.57	1	12
Mn	3.31	3.47	3.49	0.02	2	18
0.45.mcif La <sub>2</sub> NiO <sub>4</sub> Ref. [291]						
cluster	$\mu_{\text{exp}}$	$\mu_{\text{th}}$	$\mu_s$	$\mu_l$	active CMP	dgr. of freedom
Ni	1.68	1.28	1.15	0.12	2	12
0.50.mcif TiMnO <sub>3</sub> Ref. [294]						
cluster	$\mu_{\text{exp}}$	$\mu_{\text{th}}$	$\mu_s$	$\mu_l$	active CMP	dgr. of freedom
Mn	3.9	4.34	4.34	0.00	1	6
0.56.mcif Ba <sub>2</sub> CoGe <sub>2</sub> O <sub>7</sub> Ref. [295]						
cluster	$\mu_{\text{exp}}$	$\mu_{\text{th}}$	$\mu_s$	$\mu_l$	active CMP	dgr. of freedom
Co	2.89	2.74	2.52	0.21	2	6
0.58.mcif Al <sub>2</sub> CoO <sub>4</sub> Ref. [296]						
cluster	$\mu_{\text{exp}}$	$\mu_{\text{th}}$	$\mu_s$	$\mu_l$	active CMP	dgr. of freedom
Co	1.9	2.68	2.50	0.18	1	6
0.64.mcif MnV <sub>2</sub> O <sub>4</sub> Ref. [298]						
cluster	$\mu_{\text{exp}}$	$\mu_{\text{th}}$	$\mu_s$	$\mu_l$	active CMP	dgr. of freedom
Mn	4.2	4.21	4.20	0.00	1	6
V	1.29	1.63	1.67	0.04	3	12
0.66.mcif Fe <sub>2</sub> O <sub>3</sub> Ref. [299]						
cluster	$\mu_{\text{exp}}$	$\mu_{\text{th}}$	$\mu_s$	$\mu_l$	active CMP	dgr. of freedom
Fe	4.22	3.58	3.56	0.02	2	12

0.72.mcif CaMnBi <sub>2</sub> Ref. [300]						
cluster	$\mu_{\text{exp}}$	$\mu_{\text{th}}$	$\mu_s$	$\mu_l$	active CMP	dgr. of freedom
Mn	3.73	3.95	3.86	0.09	1	6
0.73.mcif SrMnBi <sub>2</sub> Ref. [300]						
cluster	$\mu_{\text{exp}}$	$\mu_{\text{th}}$	$\mu_s$	$\mu_l$	active CMP	dgr. of freedom
Mn	3.75	4.01	3.91	0.09	1	6
0.74.mcif Mn <sub>3</sub> CuN Ref. [301]						
cluster	$\mu_{\text{exp}}$	$\mu_{\text{th}}$	$\mu_s$	$\mu_l$	active CMP	dgr. of freedom
Mn	2.47	2.91	2.90	0.01	---	---
0.76.mcif Cr <sub>2</sub> TeO <sub>6</sub> Ref. [302]						
cluster	$\mu_{\text{exp}}$	$\mu_{\text{th}}$	$\mu_s$	$\mu_l$	active CMP	dgr. of freedom
Cr	2.45	2.64	2.68	0.03	1	12
0.77.mcif Tb <sub>2</sub> Ti <sub>2</sub> O <sub>7</sub> Ref. [304]						
cluster	$\mu_{\text{exp}}$	$\mu_{\text{th}}$	$\mu_s$	$\mu_l$	active CMP	dgr. of freedom
Tb	---	---	---	---	7	12
0.78.mcif Ni(NO <sub>3</sub> ) <sub>2</sub> Ref. [303]						
cluster	$\mu_{\text{exp}}$	$\mu_{\text{th}}$	$\mu_s$	$\mu_l$	active CMP	dgr. of freedom
Ni	1.33	---	---	---	0	24
Ni	1.33	---	---	---	0	24
0.79.mcif CaIrO <sub>3</sub> Ref. [305]						
cluster	$\mu_{\text{exp}}$	$\mu_{\text{th}}$	$\mu_s$	$\mu_l$	active CMP	dgr. of freedom
Ir	---	---	---	---	1	6
0.80.mcif U <sub>2</sub> InPd <sub>2</sub> Ref. [306]						
cluster	$\mu_{\text{exp}}$	$\mu_{\text{th}}$	$\mu_s$	$\mu_l$	active CMP	dgr. of freedom
U	1.40	1.10	1.60	2.70	1	12

0.81.mcif U <sub>2</sub> SnPd <sub>2</sub> Ref. [306]						
cluster	$\mu_{\text{exp}}$	$\mu_{\text{th}}$	$\mu_s$	$\mu_l$	active CMP	dgr. of freedom
U	1.89	1.06	1.66	2.73	1	12
0.83.mcif LiFeP <sub>2</sub> O <sub>7</sub> Ref. [239]						
cluster	$\mu_{\text{exp}}$	$\mu_{\text{th}}$	$\mu_s$	$\mu_l$	active CMP	dgr. of freedom
Fe	4.62	4.09	4.07	0.01	2	6
O	0.0	0.10	0.10	0.00	0	6
0.88.mcif LiNiPO <sub>4</sub> Ref. [307]						
cluster	$\mu_{\text{exp}}$	$\mu_{\text{th}}$	$\mu_s$	$\mu_l$	active CMP	dgr. of freedom
Ni	2.22	1.72	1.53	0.19	2	12
0.89.mcif Ba(MnBi) <sub>2</sub> Ref. [308]						
cluster	$\mu_{\text{exp}}$	$\mu_{\text{th}}$	$\mu_s$	$\mu_l$	active CMP	dgr. of freedom
Mn	3.83	3.97	3.88	0.09	1	6
0.95.mcif LiFePO <sub>4</sub> Ref. [239]						
cluster	$\mu_{\text{exp}}$	$\mu_{\text{th}}$	$\mu_s$	$\mu_l$	active CMP	dgr. of freedom
Fe	4.19	3.72	3.55	0.17	1	12
0.96.mcif CoSO <sub>4</sub> Ref. [309]						
cluster	$\mu_{\text{exp}}$	$\mu_{\text{th}}$	$\mu_s$	$\mu_l$	active CMP	dgr. of freedom
Co	3.21	2.82	2.59	0.23	3	12
0.97.mcif Fe(SbO <sub>2</sub> ) <sub>2</sub> Ref. [310]						
cluster	$\mu_{\text{exp}}$	$\mu_{\text{th}}$	$\mu_s$	$\mu_l$	active CMP	dgr. of freedom
Fe	3.68	3.70	3.55	0.14	3	12
0.101.mcif Mn <sub>2</sub> GeO <sub>4</sub> Ref. [193]						
cluster	$\mu_{\text{exp}}$	$\mu_{\text{th}}$	$\mu_s$	$\mu_l$	active CMP	dgr. of freedom
Mn	3.02	4.43	4.43	0.0	2	12
Mn	4.5	4.44	4.44	0.0	1	12

0.105.mcif ErVO <sub>3</sub> Ref. [194]						
cluster	$\mu_{\text{exp}}$	$\mu_{\text{th}}$	$\mu_s$	$\mu_l$	active CMP	dgr. of freedom
Er	8.2	6.89	2.41	4.47	1	12
V	1.47	0.07	0.08	0.03	2	12
0.106.mcif DyVO <sub>3</sub> Ref. [194]						
cluster	$\mu_{\text{exp}}$	$\mu_{\text{th}}$	$\mu_s$	$\mu_l$	active CMP	dgr. of freedom
Dy	7.76	8.43	4.65	3.77	2	12
V	1.45	1.68	1.70	0.03	2	12
0.107.mcif Ho <sub>2</sub> Ge <sub>2</sub> O <sub>7</sub> Ref. [195]						
cluster	$\mu_{\text{exp}}$	$\mu_{\text{th}}$	$\mu_s$	$\mu_l$	active CMP	dgr. of freedom
Ho	9.05	9.12	3.75	5.38	3	24
0.109.mcif Mn <sub>3</sub> Pt Ref. [196]						
cluster	$\mu_{\text{exp}}$	$\mu_{\text{th}}$	$\mu_s$	$\mu_l$	active CMP	dgr. of freedom
Mn	2.93	3.12	3.09	0.02	3	9
0.110.mcif Cr <sub>2</sub> O <sub>3</sub> Ref. [197]						
cluster	$\mu_{\text{exp}}$	$\mu_{\text{th}}$	$\mu_s$	$\mu_l$	active CMP	dgr. of freedom
Cr	---	---	---	---	1	12
0.111.mcif Nb <sub>2</sub> Co <sub>4</sub> O <sub>9</sub> Ref. [198]						
cluster	$\mu_{\text{exp}}$	$\mu_{\text{th}}$	$\mu_s$	$\mu_l$	active CMP	dgr. of freedom
Co	3.0	2.62	2.43	0.19	1	12
Co	3.0	2.77	2.38	0.38	1	12
0.112.mcif FeBO <sub>3</sub> Ref. [199]						
cluster	$\mu_{\text{exp}}$	$\mu_{\text{th}}$	$\mu_s$	$\mu_l$	active CMP	dgr. of freedom
Fe	4.7	3.91	3.89	0.02	1	6

0.113.mcif NiCO <sub>3</sub> Ref. [200]						
cluster	$\mu_{\text{exp}}$	$\mu_{\text{th}}$	$\mu_s$	$\mu_l$	active CMP	dgr. of freedom
Ni	---	---	---	---	1	6
0.114.mcif CoCO <sub>3</sub> Ref. [201]						
cluster	$\mu_{\text{exp}}$	$\mu_{\text{th}}$	$\mu_s$	$\mu_l$	active CMP	dgr. of freedom
Co	---	---	---	---	1	6
0.115.mcif MnCO <sub>3</sub> Ref. [202]						
cluster	$\mu_{\text{exp}}$	$\mu_{\text{th}}$	$\mu_s$	$\mu_l$	active CMP	dgr. of freedom
Mn	---	---	---	---	1	6
0.116.mcif FeCO <sub>3</sub> Ref. [203]						
cluster	$\mu_{\text{exp}}$	$\mu_{\text{th}}$	$\mu_s$	$\mu_l$	active CMP	dgr. of freedom
Fe	---	---	---	---	1	6
0.117.mcif LuFeO <sub>3</sub> Ref. [204]						
cluster	$\mu_{\text{exp}}$	$\mu_{\text{th}}$	$\mu_s$	$\mu_l$	active CMP	dgr. of freedom
Fe	2.90	3.64	3.61	0.05	2	18
O	0.0	0.12	0.12	0.00	0	18
0.118.mcif Ba <sub>5</sub> Co <sub>5</sub> ClO <sub>13</sub> Ref. [205]						
cluster	$\mu_{\text{exp}}$	$\mu_{\text{th}}$	$\mu_s$	$\mu_l$	active CMP	dgr. of freedom
Co	0.61	0.69	0.63	0.05	1	12
Co	2.21	2.67	2.59	0.08	1	12
Co	0.35	0.23	0.19	0.04	1	6
O	0.0	0.26	0.26	0.00	0	36
0.119.mcif CoSe <sub>2</sub> O <sub>5</sub> Ref. [206]						
cluster	$\mu_{\text{exp}}$	$\mu_{\text{th}}$	$\mu_s$	$\mu_l$	active CMP	dgr. of freedom
Co	3.20	2.82	2.55	0.27	2	12



0.121.mcif $\text{Li}_2\text{Co}(\text{SO}_4)_2$ Ref. [208]						
cluster	$\mu_{\text{exp}}$	$\mu_{\text{th}}$	$\mu_s$	$\mu_l$	active CMP	dgr. of freedom
Co	3.33	2.90	2.62	0.28	3	6
0.122.mcif $\text{Li}_2\text{Mn}(\text{SO}_4)_2$ Ref. [208]						
cluster	$\mu_{\text{exp}}$	$\mu_{\text{th}}$	$\mu_s$	$\mu_l$	active CMP	dgr. of freedom
Mn	4.58	4.52	4.52	0.0	3	6
0.125.mcif $\text{MnGeO}_3$ Ref. [209]						
cluster	$\mu_{\text{exp}}$	$\mu_{\text{th}}$	$\mu_s$	$\mu_l$	active CMP	dgr. of freedom
Ge	0.0	0.10	0.10	0.00	0	6
Mn	4.6	3.65	3.66	0.00	1	6
0.126.mcif $\text{NpCo}_2$ Ref. [210]						
cluster	$\mu_{\text{exp}}$	$\mu_{\text{th}}$	$\mu_s$	$\mu_l$	active CMP	dgr. of freedom
Np	0.5	0.04	1.35	1.31	1	6
0.128.mcif $\text{FeSO}_4\text{F}$ Ref. [211]						
cluster	$\mu_{\text{exp}}$	$\mu_{\text{th}}$	$\mu_s$	$\mu_l$	active CMP	dgr. of freedom
Fe	4.32	4.06	4.04	0.01	1	6
0.130.mcif $\text{Cu}_3\text{Mo}_2\text{O}_9$ Ref. [213]						
cluster	$\mu_{\text{exp}}$	$\mu_{\text{th}}$	$\mu_s$	$\mu_l$	active CMP	dgr. of freedom
Cu	0.08	---	---	---	2	12
Cu	0.62	0.62	0.52	0.09	2	12
Cu	0.62	0.55	0.51	0.03	2	12
O	0.0	0.22	0.22	0.00	0	12
0.131.mcif $\text{Mn}(\text{C}_2\text{N}_3)_2$ Ref. [214]						
cluster	$\mu_{\text{exp}}$	$\mu_{\text{th}}$	$\mu_s$	$\mu_l$	active CMP	dgr. of freedom
Mn	5.01	4.41	4.42	0.00	1	6

0.132.mcif Fe(C <sub>2</sub> N <sub>3</sub> ) <sub>2</sub> Ref. [214]						
cluster	$\mu_{\text{exp}}$	$\mu_{\text{th}}$	$\mu_s$	$\mu_l$	active CMP	dgr. of freedom
Fe	4.11	3.73	3.51	0.22	2	6
0.133.mcif Ni <sub>3</sub> B <sub>7</sub> ClO <sub>13</sub> Ref. [215]						
cluster	$\mu_{\text{exp}}$	$\mu_{\text{th}}$	$\mu_s$	$\mu_l$	active CMP	dgr. of freedom
Ni	1.65	1.79	1.56	0.23	1	12
Ni	0.79	1.70	1.47	0.23	1	12
Ni	0.79	0.16	0.11	0.07	1	12
0.137.mcif V <sub>2</sub> Cu <sub>2</sub> O <sub>7</sub> Ref. [216]						
cluster	$\mu_{\text{exp}}$	$\mu_{\text{th}}$	$\mu_s$	$\mu_l$	active CMP	dgr. of freedom
Cu	0.93	0.54	0.48	0.06	2	12
0.138.mcif CrBiO <sub>3</sub> Ref. [217]						
cluster	$\mu_{\text{exp}}$	$\mu_{\text{th}}$	$\mu_s$	$\mu_l$	active CMP	dgr. of freedom
Cr	2.04	2.63	2.67	0.04	1	6
Cr	2.04	2.64	2.68	0.04	1	6
0.140.mcif Lu(Fe <sub>2</sub> Ge) <sub>2</sub> Ref. [218]						
cluster	$\mu_{\text{exp}}$	$\mu_{\text{th}}$	$\mu_s$	$\mu_l$	active CMP	dgr. of freedom
Fe	0.44	1.93	1.86	0.06	2	12
Fe	0.44	1.79	1.73	0.05	2	12
0.141.mcif TbGe <sub>2</sub> Ref. [219]						
cluster	$\mu_{\text{exp}}$	$\mu_{\text{th}}$	$\mu_s$	$\mu_l$	active CMP	dgr. of freedom
Tb	7.55	7.73	5.74	1.99	1	6
Tb	9.45	7.73	5.81	1.92	1	6
0.142.mcif Fe <sub>2</sub> TeO <sub>6</sub> Ref. [220]						
cluster	$\mu_{\text{exp}}$	$\mu_{\text{th}}$	$\mu_s$	$\mu_l$	active CMP	dgr. of freedom
Fe	4.19	3.82	3.79	0.02	1	12

0.143.mcif Cr <sub>2</sub> TeO <sub>6</sub> Ref. [220]						
cluster	$\mu_{\text{exp}}$	$\mu_{\text{th}}$	$\mu_s$	$\mu_l$	active CMP	dgr. of freedom
Cr	2.45	2.64	2.68	0.03	1	12
0.146.mcif EuZrO <sub>3</sub> Ref. [221]						
cluster	$\mu_{\text{exp}}$	$\mu_{\text{th}}$	$\mu_s$	$\mu_l$	active CMP	dgr. of freedom
Eu	7.3	6.67	6.75	0.08	2	12
0.148.mcif LiLa <sub>2</sub> RuO <sub>6</sub> Ref. [222]						
cluster	$\mu_{\text{exp}}$	$\mu_{\text{th}}$	$\mu_s$	$\mu_l$	active CMP	dgr. of freedom
Ru	2.20	1.82	1.84	0.01	2	6
O	0.0	0.12	0.11	0.00	0	12
O	0.0	0.11	0.11	0.00	0	12
O	0.0	0.10	0.10	0.00	0	12
0.149.mcif Nd <sub>3</sub> (Al <sub>3</sub> Ru) <sub>4</sub> Ref. [223]						
cluster	$\mu_{\text{exp}}$	$\mu_{\text{th}}$	$\mu_s$	$\mu_l$	active CMP	dgr. of freedom
Nd	2.09	0.19	3.22	3.41	2	18
Ru	0.0	0.13	0.11	0.01	0	18
0.150.mcif NiS <sub>2</sub> Ref. [225]						
cluster	$\mu_{\text{exp}}$	$\mu_{\text{th}}$	$\mu_s$	$\mu_l$	active CMP	dgr. of freedom
Ni	0.98	0.47	0.44	0.03	1	12
0.154.mcif Er <sub>2</sub> Ru <sub>2</sub> O <sub>7</sub> Ref. [226]						
cluster	$\mu_{\text{exp}}$	$\mu_{\text{th}}$	$\mu_s$	$\mu_l$	active CMP	dgr. of freedom
Er	4.5	7.56	2.66	4.89	---	---
Ru	2.0	1.36	1.23	0.12	---	---
0.155.mcif CaMn(GeO <sub>3</sub> ) <sub>2</sub> Ref. [228]						
cluster	$\mu_{\text{exp}}$	$\mu_{\text{th}}$	$\mu_s$	$\mu_l$	active CMP	dgr. of freedom
Mn	4.18	4.43	4.43	0.0	---	---

0.157.mcif Yb <sub>2</sub> Sn <sub>2</sub> O <sub>7</sub> Ref. [229]						
cluster	$\mu_{\text{exp}}$	$\mu_{\text{th}}$	$\mu_s$	$\mu_l$	active CMP	dgr. of freedom
O	0.0	0.09	0.12	0.02	0	6
Yb	1.04	1.54	0.53	1.01	2	12
0.158.mcif Yb <sub>2</sub> Ti <sub>2</sub> O <sub>7</sub> Ref. [230]						
cluster	$\mu_{\text{exp}}$	$\mu_{\text{th}}$	$\mu_s$	$\mu_l$	active CMP	dgr. of freedom
Yb	0.89	1.54	0.53	1.00	2	12
0.159.mcif DyCoO <sub>3</sub> Ref. [231]						
cluster	$\mu_{\text{exp}}$	$\mu_{\text{th}}$	$\mu_s$	$\mu_l$	active CMP	dgr. of freedom
Dy	9.08	8.83	4.73	4.12	2	12
0.160.mcif TbCoO <sub>3</sub> Ref. [231]						
cluster	$\mu_{\text{exp}}$	$\mu_{\text{th}}$	$\mu_s$	$\mu_l$	active CMP	dgr. of freedom
Tb	8.26	7.69	5.74	1.95	2	12
Co	0.0	0.15	0.14	0.00	0	12
0.163.mcif MnPS <sub>3</sub> Ref. [233]						
cluster	$\mu_{\text{exp}}$	$\mu_{\text{th}}$	$\mu_s$	$\mu_l$	active CMP	dgr. of freedom
Mn	4.43	4.25	4.25	0.00	2	6
0.164.mcif Y <sub>2</sub> MnCoO <sub>6</sub> Ref. [234]						
cluster	$\mu_{\text{exp}}$	$\mu_{\text{th}}$	$\mu_s$	$\mu_l$	active CMP	dgr. of freedom
Mn	---	---	---	---	3	6
Co	---	---	---	---	3	6
0.165.mcif SrMnVHO <sub>5</sub> Ref. [235]						
cluster	$\mu_{\text{exp}}$	$\mu_{\text{th}}$	$\mu_s$	$\mu_l$	active CMP	dgr. of freedom
Mn	3.31	4.34	4.34	0.00	3	6
Mn	3.31	4.34	4.34	0.00	3	6

0.167.mcif Nd <sub>3</sub> Mg <sub>2</sub> Sb <sub>3</sub> O <sub>14</sub> Ref. [236]						
cluster	$\mu_{\text{exp}}$	$\mu_{\text{th}}$	$\mu_s$	$\mu_l$	active CMP	dgr. of freedom
Nd	1.78	0.73	2.96	3.69	4	9
0.168.mcif Fe <sub>2</sub> H <sub>4</sub> NF <sub>6</sub> Ref. [237]						
cluster	$\mu_{\text{exp}}$	$\mu_{\text{th}}$	$\mu_s$	$\mu_l$	active CMP	dgr. of freedom
Fe	4.12	3.93	3.81	0.12	3	12
Fe	3.12	4.09	3.92	0.16	1	12
0.169.mcif U <sub>3</sub> As <sub>4</sub> Ref. [238]						
cluster	$\mu_{\text{exp}}$	$\mu_{\text{th}}$	$\mu_s$	$\mu_l$	active CMP	dgr. of freedom
U	1.90	0.66	1.69	2.36	6	18
0.170.mcif U <sub>3</sub> P <sub>4</sub> Ref. [238]						
cluster	$\mu_{\text{exp}}$	$\mu_{\text{th}}$	$\mu_s$	$\mu_l$	active CMP	dgr. of freedom
U	1.47	0.43	1.61	2.04	6	18
0.171.mcif DyScO <sub>3</sub> Ref. [240]						
cluster	$\mu_{\text{exp}}$	$\mu_{\text{th}}$	$\mu_s$	$\mu_l$	active CMP	dgr. of freedom
Dy	9.46	8.88	4.77	4.12	2	12
0.173.mcif Pr <sub>3</sub> (Al <sub>3</sub> Ru) <sub>4</sub> Ref. [241]						
cluster	$\mu_{\text{exp}}$	$\mu_{\text{th}}$	$\mu_s$	$\mu_l$	active CMP	dgr. of freedom
Pr	---	---	---	---	2	18
0.177.mcif Mn <sub>3</sub> GaN Ref. [242]						
cluster	$\mu_{\text{exp}}$	$\mu_{\text{th}}$	$\mu_s$	$\mu_l$	active CMP	dgr. of freedom
Mn	1.17	2.59	2.57	0.01	3	9
0.178.mcif CoF <sub>2</sub> Ref. [243]						
cluster	$\mu_{\text{exp}}$	$\mu_{\text{th}}$	$\mu_s$	$\mu_l$	active CMP	dgr. of freedom
Co	2.6	2.91	2.62	0.29	1	6

0.180.mcif MnPSe <sub>3</sub> Ref. [245]						
cluster	$\mu_{\text{exp}}$	$\mu_{\text{th}}$	$\mu_s$	$\mu_l$	active CMP	dgr. of freedom
Mn	4.74	4.22	4.20	0.01	1	6
0.187.mcif CeMnAsO Ref. [246]						
cluster	$\mu_{\text{exp}}$	$\mu_{\text{th}}$	$\mu_s$	$\mu_l$	active CMP	dgr. of freedom
Ce	0.7	0.41	0.60	1.01	1	6
Mn	3.3	3.53	3.48	0.05	1	6
0.189.mcif CeMn <sub>2</sub> (GeO <sub>3</sub> ) <sub>4</sub> Ref. [247]						
cluster	$\mu_{\text{exp}}$	$\mu_{\text{th}}$	$\mu_s$	$\mu_l$	active CMP	dgr. of freedom
Mn	4.61	4.41	4.41	0.00	2	12
0.191.mcif BaCuF <sub>4</sub> Ref. [249]						
cluster	$\mu_{\text{exp}}$	$\mu_{\text{th}}$	$\mu_s$	$\mu_l$	active CMP	dgr. of freedom
Cu	0.83	---	---	---	0	6
0.192.mcif RbFe <sub>2</sub> F <sub>6</sub> Ref. [250]						
cluster	$\mu_{\text{exp}}$	$\mu_{\text{th}}$	$\mu_s$	$\mu_l$	active CMP	dgr. of freedom
Fe	3.99	4.06	3.93	0.12	1	12
Fe	4.29	3.93	3.84	0.10	3	12
0.193.mcif LiCoPO <sub>4</sub> Ref. [251]						
cluster	$\mu_{\text{exp}}$	$\mu_{\text{th}}$	$\mu_s$	$\mu_l$	active CMP	dgr. of freedom
Co	---	---	---	---	1	12
0.194.mcif U(SiPt) <sub>2</sub> Ref. [252]						
cluster	$\mu_{\text{exp}}$	$\mu_{\text{th}}$	$\mu_s$	$\mu_l$	active CMP	dgr. of freedom
U	1.67	0.86	1.66	2.52	1	6
0.198.mcif GdVO <sub>4</sub> Ref. [253]						
cluster	$\mu_{\text{exp}}$	$\mu_{\text{th}}$	$\mu_s$	$\mu_l$	active CMP	dgr. of freedom
Gd	7.0	6.87	6.83	0.03	1	6

0.199.mcif Mn <sub>3</sub> Sn Ref. [254]						
cluster	$\mu_{\text{exp}}$	$\mu_{\text{th}}$	$\mu_s$	$\mu_l$	active CMP	dgr. of freedom
Mn	2.99	3.18	3.15	0.03	3	18
0.203.mcif Mn <sub>3</sub> Ge Ref. [256]						
cluster	$\mu_{\text{exp}}$	$\mu_{\text{th}}$	$\mu_s$	$\mu_l$	active CMP	dgr. of freedom
Mn	2.99	2.74	2.71	0.02	---	---
0.204.mcif Ca <sub>2</sub> MnReO <sub>6</sub> Ref. [257]						
cluster	$\mu_{\text{exp}}$	$\mu_{\text{th}}$	$\mu_s$	$\mu_l$	active CMP	dgr. of freedom
Mn	4.33	4.17	4.14	0.05	3	6
Re	0.21	0.20	0.46	0.25	2	6
0.211.mcif Ca <sub>2</sub> MnO <sub>4</sub> Ref. [259]						
cluster	$\mu_{\text{exp}}$	$\mu_{\text{th}}$	$\mu_s$	$\mu_l$	active CMP	dgr. of freedom
Mn	2.4	2.54	2.56	0.02	1	12
0.212.mcif Sr <sub>2</sub> Mn <sub>3</sub> (AsO) <sub>2</sub> Ref. [260]						
cluster	$\mu_{\text{exp}}$	$\mu_{\text{th}}$	$\mu_s$	$\mu_l$	active CMP	dgr. of freedom
Mn	3.4	3.55	3.53	0.01	1	6
0.215.mcif BaNi <sub>2</sub> (PO <sub>4</sub> ) <sub>2</sub> Ref. [261]						
cluster	$\mu_{\text{exp}}$	$\mu_{\text{th}}$	$\mu_s$	$\mu_l$	active CMP	dgr. of freedom
Ni	2.00	1.72	1.55	0.17	2	6
0.219.mcif Co <sub>2</sub> SiO <sub>4</sub> Ref. [262]						
cluster	$\mu_{\text{exp}}$	$\mu_{\text{th}}$	$\mu_s$	$\mu_l$	active CMP	dgr. of freedom
Co	3.87	2.59	2.40	0.18	3	12
Co	3.35	2.76	2.54	0.22	1	12
O	0.0	0.12	0.12	0.0	0	12

0.220.mcif Mn <sub>2</sub> SiO <sub>4</sub> Ref. [264]						
cluster	$\mu_{\text{exp}}$	$\mu_{\text{th}}$	$\mu_s$	$\mu_l$	active CMP	dgr. of freedom
Mn	3.84	4.44	4.44	0.0	3	12
Mn	4.67	4.45	4.45	0.0	2	12
0.221.mcif Fe <sub>2</sub> SiO <sub>4</sub> Ref. [265]						
cluster	$\mu_{\text{exp}}$	$\mu_{\text{th}}$	$\mu_s$	$\mu_l$	active CMP	dgr. of freedom
Fe	4.44	3.57	3.46	0.11	3	12
Fe	4.4	3.73	3.59	0.14	1	12
O	0.0	0.10	0.10	0.0	0	12
0.222.mcif MnCuAs Ref. [266]						
cluster	$\mu_{\text{exp}}$	$\mu_{\text{th}}$	$\mu_s$	$\mu_l$	active CMP	dgr. of freedom
Mn	3.6	3.68	3.67	0.01	1	6
0.228.mcif TbCo <sub>2</sub> Ref. [267]						
cluster	$\mu_{\text{exp}}$	$\mu_{\text{th}}$	$\mu_s$	$\mu_l$	active CMP	dgr. of freedom
Co	1.19	1.28	1.16	0.12	1	9
Co	1.3	1.28	1.11	0.17	1	3
Tb	8.3	7.10	5.61	1.49	1	6
0.229.mcif Ba <sub>2</sub> MnSi <sub>2</sub> O <sub>7</sub> Ref. [268]						
cluster	$\mu_{\text{exp}}$	$\mu_{\text{th}}$	$\mu_s$	$\mu_l$	active CMP	dgr. of freedom
Mn	4.1	4.39	4.39	0.0	1	6
0.230.mcif K <sub>2</sub> CoP <sub>2</sub> O <sub>7</sub> Ref. [270]						
cluster	$\mu_{\text{exp}}$	$\mu_{\text{th}}$	$\mu_s$	$\mu_l$	active CMP	dgr. of freedom
Co	3.03	2.77	2.55	0.21	1	12



0.235.mcif PrMn <sub>2</sub> SbO <sub>6</sub> Ref. [271]						
cluster	$\mu_{\text{exp}}$	$\mu_{\text{th}}$	$\mu_s$	$\mu_l$	active CMP	dgr. of freedom
Pr	2.2	1.63	1.93	3.56	1	12
Mn	5.1	4.43	4.43	0.0	1	6
Mn	5.1	4.44	4.44	0.00	1	6
Mn	5.1	4.41	4.40	0.00	1	12
0.236.mcif Ca(Al <sub>2</sub> Fe) <sub>4</sub> Ref. [272]						
cluster	$\mu_{\text{exp}}$	$\mu_{\text{th}}$	$\mu_s$	$\mu_l$	active CMP	dgr. of freedom
Fe	0.71	3.26	3.11	0.15	2	12
0.237.mcif Er <sub>2</sub> Sn <sub>2</sub> O <sub>7</sub> Ref. [273]						
cluster	$\mu_{\text{exp}}$	$\mu_{\text{th}}$	$\mu_s$	$\mu_l$	active CMP	dgr. of freedom
Er	4.38	7.87	2.72	5.14	1	12
0.238.mcif Er <sub>2</sub> Pt <sub>2</sub> O <sub>7</sub> Ref. [274]						
cluster	$\mu_{\text{exp}}$	$\mu_{\text{th}}$	$\mu_s$	$\mu_l$	active CMP	dgr. of freedom
Er	4.80	7.73	2.70	5.03	1	12
0.239.mcif LiCa <sub>3</sub> RuO <sub>6</sub> Ref. [275]						
cluster	$\mu_{\text{exp}}$	$\mu_{\text{th}}$	$\mu_s$	$\mu_l$	active CMP	dgr. of freedom
O	0.0	0.10	0.1	0.00	0	24
Ru	2.8	1.78	1.80	0.02	1	6
0.290.mcif CeCu <sub>2</sub> Ref. [281]						
cluster	$\mu_{\text{exp}}$	$\mu_{\text{th}}$	$\mu_s$	$\mu_l$	active CMP	dgr. of freedom
Ce	0.33	0.04	0.31	0.36	1	6
0.318.mcif Tm <sub>2</sub> MnCoO <sub>6</sub> Ref. [284]						
cluster	$\mu_{\text{exp}}$	$\mu_{\text{th}}$	$\mu_s$	$\mu_l$	active CMP	dgr. of freedom
Tm	2.17	5.03	1.62	3.40	3	12
Mn	2.82	3.35	3.38	0.03	2	6
Co	2.82	0.14	0.11	0.04	2	6

0.408.mcif PrSi Ref. [289]						
cluster	$\mu_{\text{exp}}$	$\mu_{\text{th}}$	$\mu_s$	$\mu_l$	active CMP	dgr. of freedom
Pr	2.80	0.11	2.23	2.15	2	12
0.409.mcif TmNi Ref. [290]						
cluster	$\mu_{\text{exp}}$	$\mu_{\text{th}}$	$\mu_s$	$\mu_l$	active CMP	dgr. of freedom
Tm	5.89	4.35	1.35	2.99	2	12

# Bibliography

- [1] G. R. Schleder, A. C. Padilha, C. M. Acosta, M. Costa, and A. Fazzio, “From dft to machine learning: recent approaches to materials science—a review,” *Journal of Physics: Materials*, vol. 2, no. 3, p. 032001, 2019.
- [2] H. Zhang, “High-throughput design of magnetic materials,” *Electronic Structure*, 2020.
- [3] V. Baltz, A. Manchon, M. Tsoi, T. Moriyama, T. Ono, and Y. Tserkovnyak, “Antiferromagnetic spintronics,” *Reviews of Modern Physics*, vol. 90, p. 015005, feb 2018.
- [4] T. Nomoto and R. Arita, “Cluster multipole dynamics in noncollinear antiferromagnets,” *Physical Review Research*, vol. 2, p. 012045, feb 2020.
- [5] W. Kleiner, “Space-time symmetry of transport coefficients,” *Physical Review*, vol. 142, no. 2, p. 318, 1966.
- [6] W. Kleiner, “Space-time symmetry restrictions on transport coefficients. ii. two theories compared,” *Physical Review*, vol. 153, no. 3, p. 726, 1967.
- [7] M. Seemann, D. Ködderitzsch, S. Wimmer, and H. Ebert, “Symmetry-imposed shape of linear response tensors,” *Physical Review B - Condensed Matter and Materials Physics*, vol. 92, no. 15, 2015.
- [8] J. Kübler, *Theory of itinerant electron magnetism*, vol. 106. Oxford University Press, 2017.
- [9] M. K. Horton, J. H. Montoya, M. Liu, and K. A. Persson, “High-throughput prediction of the ground-state collinear magnetic order of inorganic materials using Density Functional Theory,” *npj Computational Materials*, vol. 5, no. 1, pp. 1–11, 2019.
- [10] S. Sanvito, C. Oses, J. Xue, A. Tiwari, M. Zic, T. Archer, P. Tozman, M. Venkatesan, M. Coey, and S. Curtarolo, “Accelerated discovery of new magnets in the heusler alloy family,” *Science advances*, vol. 3, no. 4, p. e1602241, 2017.

- [11] V. Stevanović, S. Lany, X. Zhang, and A. Zunger, “Correcting density functional theory for accurate predictions of compound enthalpies of formation: Fitted elemental-phase reference energies,” *Physical Review B*, vol. 85, no. 11, p. 115104, 2012.
- [12] P. Gorai, E. S. Toberer, and V. Stevanović, “Thermoelectricity in transition metal compounds: the role of spin disorder,” *Physical Chemistry Chemical Physics*, vol. 18, no. 46, pp. 31777–31786, 2016.
- [13] Y. Xu, L. Elcoro, Z. Song, B. J. Wieder, M. G. Vergniory, N. Regnault, Y. Chen, C. Felser, and B. A. Bernevig, “High-throughput calculations of antiferromagnetic topological materials from magnetic topological quantum chemistry,” 2020.
- [14] F. Zheng and P. Zhang, “Maggene: A genetic evolution program for magnetic structure prediction,” *arXiv preprint arXiv:2003.05650*, 2020.
- [15] S. V. Gallego, J. M. Perez-Mato, L. Elcoro, E. S. Tasci, R. M. Hanson, M. I. Aroyo, and G. Madariaga, “MAGNDATA: Towards a database of magnetic structures,” *Journal of Applied Crystallography*, vol. 49, no. 6, pp. 1941–1956, 2016.
- [16] A. T. von Middendorff, *Die Isepiptesen Russlands: Grundlagen zur Erforschung der Zugzeiten und Zugrichtungen der Vögel Russlands*. Buchdruckerei der K. Akademie der Wissenschaften, 1855.
- [17] W. Wiltschko, “Über den einfluß statischer magnetfelder auf die zugorientierung der rotkehlchen (*erithacus rubecula*),” *Zeitschrift für Tierpsychologie*, vol. 25, no. 5, pp. 537–558, 1968.
- [18] P. J. Hore and H. Mouritsen, “The radical-pair mechanism of magnetoreception,” *Annual Review of Biophysics*, vol. 45, no. 1, pp. 299–344, 2016. PMID: 27216936.
- [19] C. X. Wang, I. A. Hilburn, D.-A. Wu, Y. Mizuhara, C. P. Cousté, J. N. Abrahams, S. E. Bernstein, A. Matani, S. Shimojo, and J. L. Kirschvink, “Transduction of the geomagnetic field as evidenced from alpha-band activity in the human brain,” *eneuro*, 2019.
- [20] S. Mühlbauer, D. Honecker, É. A. Périgo, F. Bergner, S. Disch, A. Heinemann, S. Erokhin, D. Berkov, C. Leighton, M. R. Eskildsen, *et al.*, “Magnetic small-angle neutron scattering,” *Reviews of Modern Physics*, vol. 91, no. 1, p. 015004, 2019.
- [21] P. A. M. Dirac, “The quantum theory of the electron,” *Proceedings of the Royal Society of London. Series A, Containing Papers of a Mathematical and Physical Character*, vol. 117, no. 778, pp. 610–624, 1928.
- [22] H. J. Van Leeuwen, *Vraagstukken uit de electronentheorie van het magnetisme*. Eduard Ijdo, 1919.

- [23] H.-J. Van Leeuwen, "Problemes de la théorie électronique du magnétisme," 1921.
- [24] P. A. Dirac, "Note on exchange phenomena in the thomas atom," in *Mathematical Proceedings of the Cambridge Philosophical Society*, vol. 26, pp. 376–385, Cambridge University Press, 1930.
- [25] P. Hohenberg and W. Kohn, "Inhomogeneous electron gas," *Physical review*, vol. 136, no. 3B, p. B864, 1964.
- [26] W. Kohn and L. J. Sham, "Self-consistent equations including exchange and correlation effects," *Physical review*, vol. 140, no. 4A, p. A1133, 1965.
- [27] R. Gaspar, "Über eine approximation des hartree-fockschen potentials durch eine universelle potentialfunktion," *Acta Physica Academiae Scientiarum Hungaricae*, vol. 3, no. 3-4, pp. 263–286, 1954.
- [28] L. Hedin and B. I. Lundqvist, "Explicit local exchange-correlation potentials," *Journal of Physics C: Solid state physics*, vol. 4, no. 14, p. 2064, 1971.
- [29] U. von Barth and L. Hedin, "A local exchange-correlation potential for the spin polarized case. i," *Journal of Physics C: Solid State Physics*, vol. 5, no. 13, p. 1629, 1972.
- [30] A. Rajagopal and J. Callaway, "Inhomogeneous electron gas," *Physical Review B*, vol. 7, no. 5, p. 1912, 1973.
- [31] K. Momma and F. Izumi, "Vesta 3 for three-dimensional visualization of crystal, volumetric and morphology data," *Journal of applied crystallography*, vol. 44, no. 6, pp. 1272–1276, 2011.
- [32] P. Mohn, "Magnetism in the solid state—an introduction, springer series," in *Solid-state sciences*, Springer Heidelberg, 2003.
- [33] J. M. Coey, *Magnetism and magnetic materials*. Cambridge university press, 2010.
- [34] S. F. A. Kettle. Springer, 2013.
- [35] A. Herpin and P. Meriel, "Étude de l'antiferromagnétisme helicoidal de  $\text{MnAu}_2$  par diffraction de neutrons," 1961.
- [36] Y. Yafet and C. Kittel, "Antiferromagnetic arrangements in ferrites," *Physical Review*, vol. 87, no. 2, p. 290, 1952.
- [37] W. Schmatz, T. Springer, J. t. Schelten, and K. Ibel, "Neutron small-angle scattering: experimental techniques and applications," *Journal of Applied Crystallography*, vol. 7, no. 2, pp. 96–116, 1974.

- [38] J. Glasbrenner, K. Bussmann, and I. Mazin, “Magnetic spiral induced by strong correlations in  $\text{MnAu}$ ,” *Physical Review B*, vol. 90, no. 14, p. 144421, 2014.
- [39] F. Keffer, “Encyclopedia of physics,” *Springer-Verlag, Berlin, Germany*, vol. 18, p. 139, 1966.
- [40] J. Coey, “Noncollinear spin structures,” *Canadian journal of physics*, vol. 65, no. 10, pp. 1210–1232, 1987.
- [41] B. Campbell, J. M. Perez-Mato, V. Petricek, J. Rodriguez-Carvajal, and W. Sikora, “Magnetic CIF Dictionary,” 2020.
- [42] M. Fiebig, D. Fröhlich, B. Krichevtsov, and R. V. Pisarev, “Second harmonic generation and magnetic-dipole-electric-dipole interference in antiferromagnetic  $\text{Cr}_2\text{O}_3$ ,” *Physical Review Letters*, vol. 73, no. 15, p. 2127, 1994.
- [43] W. Kleiner, “Space-time symmetry restrictions on transport coefficients. iii. thermogalvanomagnetic coefficients,” *Physical Review*, vol. 182, no. 3, p. 705, 1969.
- [44] J. K. LL.D., “Xliii. on rotation of the plane of polarization by reflection from the pole of a magnet,” *The London, Edinburgh, and Dublin Philosophical Magazine and Journal of Science*, vol. 3, no. 19, pp. 321–343, 1877.
- [45] S. Nakatsuji, N. Kiyohara, and T. Higo, “Large anomalous hall effect in a non-collinear antiferromagnet at room temperature,” *Nature*, vol. 527, no. 7577, pp. 212–215, 2015.
- [46] M. Ikhlas, T. Tomita, T. Koretsune, M.-T. Suzuki, D. Nishio-Hamane, R. Arita, Y. Otani, and S. Nakatsuji, “Large anomalous nernst effect at room temperature in a chiral antiferromagnet,” *Nature Physics*, vol. 13, no. 11, pp. 1085–1090, 2017.
- [47] T. Higo, H. Man, D. B. Gopman, L. Wu, T. Koretsune, O. M. vanâ Erve, Y. P. Kabanov, D. Rees, Y. Li, M.-T. Suzuki, *et al.*, “Large magneto-optical kerr effect and imaging of magnetic octupole domains in an antiferromagnetic metal,” *Nature photonics*, vol. 12, no. 2, p. 73, 2018.
- [48] M.-T. Suzuki, T. Koretsune, M. Ochi, and R. Arita, “Cluster multipole theory for anomalous hall effect in antiferromagnets,” *Physical Review B*, vol. 95, no. 9, p. 094406, 2017.
- [49] M. Martsenyuk and N. Martsenyuk, “Origin of aromagnetism,” *JETP Lett*, vol. 53, no. 5, 1991.
- [50] I. E. Dzyaloshinskii, “On the magneto-electrical effects in antiferromagnets,” *Soviet Physics JETP*, vol. 10, pp. 628–629, 1960.
- [51] D. Astrov, “The magnetoelectric effect in antiferromagnetics,” *Sov. Phys. JETP*, vol. 11, no. 3, pp. 708–709, 1960.

- [52] D. Astrov, “Magnetoelectric effect in chromium oxide,” *Sov. Phys. JETP*, vol. 13, no. 4, pp. 729–733, 1961.
- [53] Y. F. Popov, A. Kadomtseva, D. Belov, G. Vorobâev, and A. Zvezdin, “Magnetic-field-induced toroidal moment in the magnetoelectric  $\text{Cr}_2\text{O}_3$ ,” *Journal of Experimental and Theoretical Physics Letters*, vol. 69, no. 4, pp. 330–335, 1999.
- [54] E. Fischer, G. Gorodetsky, and R. Hornreich, “A new family of magnetoelectric materials:  $\text{A}_2\text{M}_4\text{O}_9$  ( $\text{A} = \text{Ta}, \text{Nb}; \text{M} = \text{Mn}, \text{Co}$ ),” *Solid State Communications*, vol. 10, no. 12, pp. 1127–1132, 1972.
- [55] N. Khanh, N. Abe, H. Sagayama, A. Nakao, T. Hanashima, R. Kiyonagi, Y. Tokunaga, and T. Arima, “Magnetoelectric coupling in the honeycomb antiferromagnet  $\text{Co}_4\text{Nb}_2\text{O}_9$ ,” *Physical Review B*, vol. 93, no. 7, p. 075117, 2016.
- [56] N. Khanh, N. Abe, S. Kimura, Y. Tokunaga, and T. Arima, “Manipulation of electric polarization with rotating magnetic field in a honeycomb antiferromagnet  $\text{Co}_4\text{Nb}_2\text{O}_9$ ,” *Physical Review B*, vol. 96, no. 9, p. 094434, 2017.
- [57] Y. Yanagi, S. Hayami, and H. Kusunose, “Manipulating the magnetoelectric effect: Essence learned from  $\text{Co}_4\text{Nb}_2\text{O}_9$ ,” *Physical Review B*, vol. 97, no. 2, p. 020404, 2018.
- [58] Y. Yanagi, S. Hayami, and H. Kusunose, “Theory of magnetoelectric response in  $\text{Co}_4\text{Nb}_2\text{O}_9$ ,” *Physica B: Condensed Matter*, vol. 536, pp. 107–110, 2018.
- [59] S. Hayami, H. Kusunose, and Y. Motome, “Toroidal order in metals without local inversion symmetry,” *Physical Review B*, vol. 90, no. 2, p. 024432, 2014.
- [60] S. Hayami, H. Kusunose, and Y. Motome, “Toroidal order in a partially disordered state on a layered triangular lattice: implication to  $\text{uni4b}$ ,” in *Journal of Physics: Conference Series*, vol. 592, p. 012101, IOP Publishing, 2015.
- [61] H. Saito, K. Uenishi, N. Miura, C. Tabata, H. Hidaka, T. Yanagisawa, and H. Amitsuka, “Evidence of a new current-induced magnetoelectric effect in a toroidal magnetic ordered state of  $\text{uni4b}$ ,” *Journal of the Physical Society of Japan*, vol. 87, no. 3, p. 033702, 2018.
- [62] X. Li, T. Cao, Q. Niu, J. Shi, and J. Feng, “Coupling the valley degree of freedom to antiferromagnetic order,” *Proceedings of the National Academy of Sciences*, vol. 110, no. 10, pp. 3738–3742, 2013.
- [63] T. Ideue, K. Hamamoto, S. Koshikawa, M. Ezawa, S. Shimizu, Y. Kaneko, Y. Tokura, N. Nagasawa, and Y. Iwasa, “Bulk rectification effect in a polar semiconductor,” *Nature Physics*, vol. 13, no. 6, pp. 578–583, 2017.

- [64] G. Gitgeatpong, Y. Zhao, M. Avdeev, R. Piltz, T. Sato, and K. Matan, “Magnetic structure and dzyaloshinskii-moriya interaction in the  $s=1/2$  helical-honeycomb antiferromagnet  $\alpha$ - $\text{Cu}_2\text{V}_2\text{O}_7$ ,” *Physical Review B*, vol. 92, no. 2, p. 024423, 2015.
- [65] S. Hayami, H. Kusunose, and Y. Motome, “Asymmetric magnon excitation by spontaneous toroidal ordering,” *Journal of the Physical Society of Japan*, vol. 85, no. 5, p. 053705, 2016.
- [66] G. Gitgeatpong, M. Suewattana, S. Zhang, A. Miyake, M. Tokunaga, P. Chanlert, N. Kurita, H. Tanaka, T. Sato, Y. Zhao, *et al.*, “High-field magnetization and magnetic phase diagram of  $\alpha$ - $\text{Cu}_2\text{V}_2\text{O}_7$ ,” *Physical Review B*, vol. 95, no. 24, p. 245119, 2017.
- [67] G. Gitgeatpong, Y. Zhao, P. Piyawongwatthana, Y. Qiu, L. W. Harriger, N. P. Butch, T. Sato, and K. Matan, “Nonreciprocal magnons and symmetry-breaking in the noncentrosymmetric antiferromagnet,” *Physical review letters*, vol. 119, no. 4, p. 047201, 2017.
- [68] R. Takashima, Y. Shiomi, and Y. Motome, “Nonreciprocal spin seebeck effect in antiferromagnets,” *Physical Review B*, vol. 98, no. 2, p. 020401, 2018.
- [69] N. L. Schryer and L. R. Walker, “The motion of 180 domain walls in uniform dc magnetic fields,” *Journal of Applied Physics*, vol. 45, no. 12, pp. 5406–5421, 1974.
- [70] M. Born and R. Oppenheimer, “Zur quantentheorie der molekeln,” *Annalen der physik*, vol. 389, no. 20, pp. 457–484, 1927.
- [71] K. Capelle, “A bird’s-eye view of density-functional theory,” *Brazilian journal of physics*, vol. 36, no. 4A, pp. 1318–1343, 2006.
- [72] L. L. Foldy and S. A. Wouthuysen, “On the dirac theory of spin  $1/2$  particles and its non-relativistic limit,” *Physical Review*, vol. 78, no. 1, p. 29, 1950.
- [73] J. Kübler, K.-H. Höck, J. Sticht, and A. Williams, “Local spin-density functional theory of noncollinear magnetism,” *Journal of applied physics*, vol. 63, no. 8, pp. 3482–3486, 1988.
- [74] J. Kubler, K.-H. Hock, J. Sticht, and A. Williams, “Density functional theory of non-collinear magnetism,” *Journal of Physics F: Metal Physics*, vol. 18, no. 3, p. 469, 1988.
- [75] S. Kurth, J. P. Perdew, and P. Blaha, “Molecular and solid-state tests of density functional approximations: Lsd, ggas, and meta-ggas,” *International journal of quantum chemistry*, vol. 75, no. 4-5, pp. 889–909, 1999.
- [76] D. Hobbs, G. Kresse, and J. Hafner, “Fully unconstrained noncollinear magnetism within the projector augmented-wave method,” *Physical Review B*, vol. 62, no. 17, p. 11556, 2000.
- [77] J. F. Dobson, G. Vignale, and M. P. Das, *Electronic density functional theory: recent progress and new directions*. Springer Science & Business Media, 2013.



- [78] J. P. Perdew, K. Burke, and M. Ernzerhof, "Generalized gradient approximation made simple," *Physical review letters*, vol. 77, no. 18, p. 3865, 1996.
- [79] J. P. Perdew and K. Burke, "Comparison shopping for a gradient-corrected density functional," *International journal of quantum chemistry*, vol. 57, no. 3, pp. 309–319, 1996.
- [80] G. Kresse and J. Hafner, "Ab initio molecular dynamics for liquid metals," *Physical Review B*, vol. 47, no. 1, pp. 558–561, 1993.
- [81] G. Kresse and J. Hafner, "Ab initio molecular-dynamics simulation of the liquid-metalamorphous-semiconductor transition in germanium," *Physical Review B*, vol. 49, no. 20, pp. 14251–14269, 1994.
- [82] V. Heine and D. Weaire, "Pseudopotential theory of cohesion and structure," in *Solid state physics*, vol. 24, pp. 249–463, Elsevier, 1970.
- [83] G. Kresse and D. Joubert, "From ultrasoft pseudopotentials to the projector augmented-wave method," *Physical review b*, vol. 59, no. 3, p. 1758, 1999.
- [84] D. Vanderbilt, "Soft self-consistent pseudopotentials in a generalized eigenvalue formalism," *Physical review B*, vol. 41, no. 11, p. 7892, 1990.
- [85] G. Kresse and J. Hafner, "Norm-conserving and ultrasoft pseudopotentials for first-row and transition elements," *Journal of Physics: Condensed Matter*, vol. 6, no. 40, p. 8245, 1994.
- [86] O. K. Andersen, "Linear methods in band theory," *Physical Review B*, vol. 12, no. 8, p. 3060, 1975.
- [87] P. E. Blöchl, "Projector augmented-wave method," *Physical review B*, vol. 50, no. 24, p. 17953, 1994.
- [88] S. Steiner, S. Khmelevskiy, M. Marsmann, and G. Kresse, "Calculation of the magnetic anisotropy with projected-augmented-wave methodology and the case study of disordered Fe<sub>1-x</sub>Co<sub>x</sub> alloys," *Physical Review B*, vol. 93, no. 22, p. 224425, 2016.
- [89] W. Kutzelnigg, "Perturbation theory of relativistic corrections," *Zeitschrift für Physik D Atoms, Molecules and Clusters*, vol. 15, no. 1, pp. 27–50, 1990.
- [90] E. v. Lenthe, E.-J. Baerends, and J. G. Snijders, "Relativistic regular two-component hamiltonians," *The Journal of chemical physics*, vol. 99, no. 6, pp. 4597–4610, 1993.
- [91] T. Leung, X. Wang, and B. Harmon, "Band-theoretical study of magnetism in Sr<sub>2</sub>CuO<sub>4</sub>," *Physical Review B*, vol. 37, no. 1, p. 384, 1988.
- [92] L. Mattheiss, "Electronic structure of the 3d transition-metal monoxides. i. energy-band results," *Physical Review B*, vol. 5, no. 2, p. 290, 1972.

- [93] R. Kaneko, M.-T. Huebsch, S. Sakai, R. Arita, H. Shinaoka, K. Ueda, Y. Tokura, and J. Fujioka, “Enhanced thermopower in the correlated semimetallic phase of hole-doped pyrochlore iridates,” *Physical Review B*, vol. 99, no. 16, p. 161104, 2019.
- [94] N. F. Mott, “The basis of the electron theory of metals, with special reference to the transition metals,” *Proceedings of the Physical Society. Section A*, vol. 62, no. 7, p. 416, 1949.
- [95] N. F. Mott, “Metal-insulator transition,” *Reviews of Modern Physics*, vol. 40, no. 4, p. 677, 1968.
- [96] F. Gebhard, “Metal-insulator transitions,” *The Mott Metal-Insulator Transition*, pp. 1–48, 1997.
- [97] J. Hubbard, “Electron correlations in narrow energy bands,” *Proceedings of the Royal Society of London. Series A. Mathematical and Physical Sciences*, vol. 276, no. 1365, pp. 238–257, 1963.
- [98] V. I. Anisimov, J. Zaanen, and O. K. Andersen, “Band theory and mott insulators: Hubbard u instead of stoner i,” *Physical Review B*, vol. 44, no. 3, p. 943, 1991.
- [99] W. Metzner and D. Vollhardt, “Correlated lattice fermions in  $d=\hat{a}$  dimensions,” *Physical review letters*, vol. 62, no. 3, p. 324, 1989.
- [100] E. Müller-Hartmann, “Correlated fermions on a lattice in high dimensions,” *Zeitschrift für Physik B Condensed Matter*, vol. 74, no. 4, pp. 507–512, 1989.
- [101] A. Georges and G. Kotliar, “Hubbard model in infinite dimensions,” *Physical Review B*, vol. 45, no. 12, p. 6479, 1992.
- [102] M. Jarrell, “Hubbard model in infinite dimensions: A quantum monte carlo study,” *Physical review letters*, vol. 69, no. 1, p. 168, 1992.
- [103] A. Georges, G. Kotliar, W. Krauth, and M. J. Rozenberg, “Dynamical mean-field theory of strongly correlated fermion systems and the limit of infinite dimensions,” *Reviews of Modern Physics*, vol. 68, no. 1, p. 13, 1996.
- [104] G. Kotliar and D. Vollhardt, “Strongly correlated materials: Insights from dynamical mean-field theory,” *Physics today*, vol. 57, no. 3, pp. 53–60, 2004.
- [105] V. Anisimov, A. Poteryaev, M. Korotin, A. Anokhin, and G. Kotliar, “First-principles calculations of the electronic structure and spectra of strongly correlated systems: dynamical mean-field theory,” *Journal of Physics: Condensed Matter*, vol. 9, no. 35, p. 7359, 1997.
- [106] A. Lichtenstein and M. Katsnelson, “Ab initio calculations of quasiparticle band structure in correlated systems: Lda++ approach,” *Physical Review B*, vol. 57, no. 12, p. 6884, 1998.

- [107] K. Held, I. Nekrasov, G. Keller, V. Eyert, N. Blümer, A. McMahan, R. Scalettar, T. Pruschke, V. Anisimov, and D. Vollhardt, “Realistic investigations of correlated electron systems with lda+ dmft,” *physica status solidi (b)*, vol. 243, no. 11, pp. 2599–2631, 2006.
- [108] K. Held, O. Andersen, M. Feldbacher, A. Yamasaki, and Y. Yang, “Bandstructure meets many-body theory: the lda+ dmft method,” *Journal of Physics: Condensed Matter*, vol. 20, no. 6, p. 064202, 2008.
- [109] N. Marzari and D. Vanderbilt, “Maximally localized generalized wannier functions for composite energy bands,” *Physical review B*, vol. 56, no. 20, p. 12847, 1997.
- [110] P. Anderson, *In Moment formation in solids edited by W. J. L. Buyers*. Springer, 1984.
- [111] A. C. Hewson, *The Kondo problem to heavy fermions*, vol. 2. Cambridge university press, 1997.
- [112] L. Hedin, “New method for calculating the one-particle green’s function with application to the electron-gas problem,” *Physical Review*, vol. 139, no. 3A, p. A796, 1965.
- [113] S. Biermann, F. Aryasetiawan, and A. Georges, “First-principles approach to the electronic structure of strongly correlated systems: Combining the g w approximation and dynamical mean-field theory,” *Physical review letters*, vol. 90, no. 8, p. 086402, 2003.
- [114] S. Biermann, F. Aryasetiawan, and A. Georges, “Electronic structure of strongly correlated materials: towards a first principles scheme,” in *Physics of Spin in Solids: Materials, Methods and Applications*, pp. 43–65, Springer, 2004.
- [115] F. Aryasetiawan, M. Imada, A. Georges, G. Kotliar, S. Biermann, and A. Lichtenstein, “Frequency-dependent local interactions and low-energy effective models from electronic structure calculations,” *Physical Review B*, vol. 70, no. 19, p. 195104, 2004.
- [116] M. Cococcioni and S. De Gironcoli, “Linear response approach to the calculation of the effective interaction parameters in the lda+ u method,” *Physical Review B*, vol. 71, no. 3, p. 035105, 2005.
- [117] E. Şaşıoğlu, C. Friedrich, and S. Blügel, “Effective coulomb interaction in transition metals from constrained random-phase approximation,” *Physical Review B*, vol. 83, no. 12, p. 121101, 2011.
- [118] E. Gull, A. J. Millis, A. I. Lichtenstein, A. N. Rubtsov, M. Troyer, and P. Werner, “Continuous-time monte carlo methods for quantum impurity models,” *Reviews of Modern Physics*, vol. 83, no. 2, p. 349, 2011.

- [119] G. Rohringer, H. Hafermann, A. Toschi, A. Katanin, A. Antipov, M. Katsnelson, A. Lichtenstein, A. Rubtsov, and K. Held, “Diagrammatic routes to nonlocal correlations beyond dynamical mean field theory,” *Reviews of Modern Physics*, vol. 90, no. 2, p. 025003, 2018.
- [120] Y. Vilk and A.-M. Tremblay, “Non-perturbative many-body approach to the hubbard model and single-particle pseudogap,” *Journal de Physique I*, vol. 7, no. 11, pp. 1309–1368, 1997.
- [121] P. Kent, M. Jarrell, T. Maier, and T. Pruschke, “Efficient calculation of the antiferromagnetic phase diagram of the three-dimensional hubbard model,” *Physical Review B*, vol. 72, no. 6, p. 060411, 2005.
- [122] G. Rohringer, A. Toschi, A. Katanin, and K. Held, “Critical properties of the half-filled hubbard model in three dimensions,” *Physical review letters*, vol. 107, no. 25, p. 256402, 2011.
- [123] E. Kozik, E. Burovski, V. W. Scarola, and M. Troyer, “Néel temperature and thermodynamics of the half-filled three-dimensional hubbard model by diagrammatic determinant monte carlo,” *Physical Review B*, vol. 87, no. 20, p. 205102, 2013.
- [124] D. Hirschmeier, H. Hafermann, E. Gull, A. I. Lichtenstein, and A. E. Antipov, “Mechanisms of finite-temperature magnetism in the three-dimensional hubbard model,” *Physical Review B*, vol. 92, no. 14, p. 144409, 2015.
- [125] M.-T. D. Philipp, *The temperature dependence of the scattering rate in cuprates : insights from strong-coupling diagrammatic methods*. 2017.
- [126] J. Kaufmann, C. Eckhardt, M. Pickem, M. Kitatani, A. Kauch, and K. Held, “Self-consistent ab initio d $\gamma$ a approach,” 2020.
- [127] W. Hansen, “A new type of expansion in radiation problems,” *Physical review*, vol. 47, no. 2, p. 139, 1935.
- [128] W. Heitler, “On the radiation emitted by a multipole and its angular momentum,” in *Mathematical Proceedings of the Cambridge Philosophical Society*, vol. 32, pp. 112–126, Cambridge University Press, 1936.
- [129] H. Corben and J. Schwinger, “The electromagnetic properties of mesotrons,” *Physical Review*, vol. 58, no. 11, p. 953, 1940.
- [130] G. Goertzel, “Angular correlation of gamma-rays,” *Physical review*, vol. 70, no. 11-12, p. 897, 1946.
- [131] V. Berestetskii, “\* vnutrennyaya konversiya izlucheniya magnitnogo multipolya,” *ZHURNAL EKSPERIMENTALNOI I TEORETICHESKOI FIZIKI*, vol. 18, no. 12, pp. 1057–1069, 1948.

- [132] E. Feenberg and G. Goertzel, “Theory of nuclear coulomb energy,” *Physical Review*, vol. 70, no. 9-10, p. 597, 1946.
- [133] J. M. Blatt and V. F. Weisskopf, *Theoretical nuclear physics*. Wiley, New York, 1952.
- [134] V. Dubovik and A. Cheshkov, “Form factors and multipoles in electromagnetic interactions,” *Sov. Phys. JETP*, vol. 24, pp. 924–926, 1967.
- [135] V. Dubovik and A. Cheshkov, “Multipole expansion in classical and quantum field theory and radiation,” *Sov. J. Part. Nucl*, vol. 5, no. 3, pp. 318–337, 1975.
- [136] V. Dubovik and L. Tosunyan, “Toroidal moments in the physics of electromagnetic and weak interactions,” *Soviet Journal of Particles and Nuclei*, vol. 14, no. 5, pp. 504–519, 1983.
- [137] V. Dubovik, L. Tosunyan, and V. Tugushev, “Axial toroidal moments in electrodynamics and solid-state physics,” *Zh. Eksp. Teor. Fiz*, vol. 90, no. 2, pp. 590–605, 1986.
- [138] V. Dubovik and V. Tugushev, “Toroid moments in electrodynamics and solid-state physics,” *Physics reports*, vol. 187, no. 4, pp. 145–202, 1990.
- [139] V. Dubovik, M. Martsenyuk, and B. Saha, “Material equations for electromagnetism with toroidal polarizations,” *Physical Review E*, vol. 61, no. 6, p. 7087, 2000.
- [140] H. Kusunose, “Description of multipole in f-electron systems,” *Journal of the Physical Society of Japan*, vol. 77, no. 6, pp. 1–18, 2008.
- [141] Y. Kuramoto, “Electronic higher multipoles in solids,” *Progress of Theoretical Physics Supplement*, vol. 176, pp. 77–96, 2008.
- [142] N. A. Spaldin, M. Fiebig, and M. Mostovoy, “The toroidal moment in condensed-matter physics and its relation to the magnetoelectric effect,” *Journal of Physics: Condensed Matter*, vol. 20, no. 43, p. 434203, 2008.
- [143] P. Santini, S. Carretta, G. Amoretti, R. Caciuffo, N. Magnani, and G. H. Lander, “Multipolar interactions in f-electron systems: The paradigm of actinide dioxides,” *Reviews of Modern Physics*, vol. 81, no. 2, p. 807, 2009.
- [144] Y. Kuramoto, H. Kusunose, and A. Kiss, “Multipole orders and fluctuations in strongly correlated electron systems,” *Journal of the Physical Society of Japan*, vol. 78, no. 7, p. 072001, 2009.
- [145] M.-T. Suzuki, H. Ikeda, and P. M. Oppeneer, “First-principles theory of magnetic multipoles in condensed matter systems,” *Journal of the Physical Society of Japan*, vol. 87, no. 4, p. 041008, 2018.

- [146] T. Kaelberer, V. Fedotov, N. Papasimakis, D. Tsai, and N. Zheludev, “Toroidal dipolar response in a metamaterial,” *Science*, vol. 330, no. 6010, pp. 1510–1512, 2010.
- [147] V. A. Fedotov, A. Rogacheva, V. Savinov, D. P. Tsai, and N. I. Zheludev, “Resonant transparency and non-trivial non-radiating excitations in toroidal metamaterials,” *Scientific reports*, vol. 3, no. 1, pp. 1–5, 2013.
- [148] Y. Fan, Z. Wei, H. Li, H. Chen, and C. M. Soukoulis, “Low-loss and high-q planar metamaterial with toroidal moment,” *Physical Review B*, vol. 87, no. 11, p. 115417, 2013.
- [149] V. Savinov, V. Fedotov, and N. I. Zheludev, “Toroidal dipolar excitation and macroscopic electromagnetic properties of metamaterials,” *Physical Review B*, vol. 89, no. 20, p. 205112, 2014.
- [150] N. Papasimakis, V. Fedotov, V. Savinov, T. Raybould, and N. Zheludev, “Electromagnetic toroidal excitations in matter and free space,” *Nature materials*, vol. 15, no. 3, pp. 263–271, 2016.
- [151] W. R. Inc., “Mathematica, Version 12.1.” Champaign, IL, 2020.
- [152] D. Park, “Introduction to quantum mechanics,” *New York: McGraw-Hill1964*, 1964.
- [153] M. Bartelmann, B. Feuerbacher, T. Krüger, D. Lüst, A. Rebhan, and A. Wipf, *Theoretische Physik 3— Quantenmechanik*. Springer, 2018.
- [154] A. R. Edmonds, *Angular momentum in quantum mechanics*. Princeton university press, 1996.
- [155] S. Hayami, M. Yatsushiro, Y. Yanagi, and H. Kusunose, “Classification of atomic-scale multipoles under crystallographic point groups and application to linear response tensors,” *Physical Review B*, vol. 98, no. 16, p. 165110, 2018.
- [156] Y. Aharonov and D. Bohm, “Significance of electromagnetic potentials in the quantum theory,” *Phys. Rev.*, vol. 115, pp. 485–491, Aug 1959.
- [157] A. N. Bogdanov and D. Yablonskii, “Thermodynamically stable  $\hat{a}$ vortices in magnetically ordered crystals. the mixed state of magnets,” *Zh. Eksp. Teor. Fiz*, vol. 95, no. 1, p. 178, 1989.
- [158] B. Göbel, I. Mertig, and O. A. Tretiakov, “Beyond skyrmions: Review and perspectives of alternative magnetic quasiparticles,” *Physics Reports*, 2020.
- [159] M. Seemann, D. Ködderitzsch, S. Wimmer, and H. Ebert, “Symmetry-imposed shape of linear response tensors,” *Physical Review B*, vol. 92, no. 15, p. 155138, 2015.
- [160] T. Inui, Y. Tanabe, and Y. Onodera, *Group theory and its applications in physics*, vol. 78. Springer Science & Business Media, 2012.

- [161] R. Conte, J. Raynal, and E. Soulié, “Determination of point group harmonics for arbitrary  $j$  by a projection method. i. cubic group, quantization along an axis of order 4,” *Journal of mathematical physics*, vol. 25, no. 5, pp. 1176–1186, 1984.
- [162] H. Bethe, “Termaufspaltung in kristallen,” *Annalen der Physik*, vol. 395, no. 2, pp. 133–208, 1929.
- [163] K. Fox and B. J. Krohn, “Computation of cubic harmonics,” *Journal of Computational Physics*, vol. 25, no. 4, pp. 386–408, 1977.
- [164] H. Jahn, “A new coriolis perturbation in the methane spectrum i. vibrational-rotational hamiltonian and wave functions,” *Proceedings of the Royal Society of London. Series A. Mathematical and Physical Sciences*, vol. 168, no. 935, pp. 469–495, 1938.
- [165] D. Betts, A. Bhatia, and M. Wyman, “Houston’s method and its application to the calculation of characteristic temperatures of cubic crystals,” *Physical Review*, vol. 104, no. 1, p. 37, 1956.
- [166] K. Lea, M. Leask, and W. Wolf, “The raising of angular momentum degeneracy of f-electron terms by cubic crystal fields,” *Journal of Physics and Chemistry of Solids*, vol. 23, no. 10, pp. 1381–1405, 1962.
- [167] J. Moret-Bailly, L. Gautier, and J. Montagutelli, “Clebsch-gordan coefficients adapted to cubic symmetry,” *Journal of Molecular Spectroscopy*, vol. 15, no. 3, pp. 355–377, 1965.
- [168] H. Puff, “Contribution to the theory of cubic harmonics,” *physica status solidi (b)*, vol. 41, no. 1, pp. 11–22, 1970.
- [169] J. Muggli, “Cubic harmonics as linear combinations of spherical harmonics,” *Zeitschrift für angewandte Mathematik und Physik ZAMP*, vol. 23, no. 2, pp. 311–317, 1972.
- [170] S. Altmann and C. Bradley, “Lattice harmonics ii. hexagonal close-packed lattice,” *Reviews of Modern Physics*, vol. 37, no. 1, p. 33, 1965.
- [171] K. Stevens, “Matrix elements and operator equivalents connected with the magnetic properties of rare earth ions,” *Proceedings of the Physical Society. Section A*, vol. 65, no. 3, p. 209, 1952.
- [172] T. Hahn and H. Klapper, “Crystallographic and noncrystallographic point groups,” *International Tables for Crystallography*, pp. 762–803, 2006.
- [173] M. T. Suzuki, T. Nomoto, R. Arita, Y. Yanagi, S. Hayami, and H. Kusunose, “Multipole expansion for magnetic structures: A generation scheme for a symmetry-adapted orthonormal basis set in the crystallographic point group,” *Physical Review B*, vol. 99, no. 17, p. 174407, 2019.

- [174] J. A. Blanco, P. J. Brown, A. Stunault, K. Katsumata, F. Iga, and S. Michimura, “Magnetic structure of  $\text{GdB}_4$  from spherical neutron polarimetry,” *Physical Review B*, vol. 73, p. 212411, jun 2006.
- [175] M. I. Aroyo, J. M. Perez-Mato, D. Orobengoa, E. Tasci, G. De La Flor, and A. Kirov, “Crystallography online: Bilbao Crystallographic Server,” *Bulgarian Chemical Communications*, vol. 43, no. 2, pp. 183–197, 2011.
- [176] M.-T. Huebsch, T. Nomoto, M.-T. Suzuki, and R. Arita, “Benchmark for *Ab Initio* prediction of magnetic structures based on cluster-multipole theory,” *Phys. Rev. X*, vol. 11, p. 011031, Feb 2021.
- [177] V. T. N. Huyen, M.-T. Suzuki, K. Yamauchi, and T. Oguchi, “Topology analysis for anomalous hall effect in the noncollinear antiferromagnetic states of  $\text{mn}_3\text{a}_n$  ( $\text{a}=\text{ni, cu, zn, ga, ge, pd, in, sn, ir, pt}$ ),” *Physical Review B*, vol. 100, no. 9, p. 094426, 2019.
- [178] U. von Barth and L. Hedin, “A local exchange-correlation potential for the spin polarized case,” *Journal of Physics C: Solid State Physics*, vol. 5, pp. 1629–1642, jul 1972.
- [179] D. Hobbs and J. Hafner, “Ab initio density functional study of phase stability and noncollinear magnetism in Mn,” *Journal of Physics: Condensed Matter*, vol. 13, pp. L681–L688, jul 2001.
- [180] A. D. Corso and A. M. Conte, “Spin-orbit coupling with ultrasoft pseudopotentials: Application to Au and Pt,” *Physical Review B*, vol. 71, p. 115106, mar 2005.
- [181] “The Elk FP-LAPW Code,” 2020.
- [182] F. G. Eich and E. K. U. Gross, “Transverse Spin-Gradient Functional for Noncollinear Spin-Density-Functional Theory,” *Physical Review Letters*, vol. 111, p. 156401, oct 2013.
- [183] J. K. Dewhurst, S. Sharma, and C. Ambrosch-Draxl, “EXITING code,” 2020.
- [184] S. Sharma, J. K. Dewhurst, C. Ambrosch-Draxl, S. Kurth, N. Helbig, S. Pittalis, S. Shallcross, L. Nordström, and E. K. U. Gross, “First-Principles Approach to Noncollinear Magnetism: Towards Spin Dynamics,” *Physical Review Letters*, vol. 98, p. 196405, may 2007.
- [185] L. Nordström and D. J. Singh, “Noncollinear Intra-atomic Magnetism,” *Physical Review Letters*, vol. 76, pp. 4420–4423, jun 1996.
- [186] H. Eschrig and V. D. P. Servedio, “Relativistic density functional approach to open shells,” *Journal of Computational Chemistry*, vol. 20, pp. 23–30, jan 1999.
- [187] J. P. Perdew, K. Burke, and M. Ernzerhof, “Generalized Gradient Approximation Made Simple,” *Physical Review Letters*, vol. 77, pp. 3865–3868, oct 1996.



- [188] S. P. Ong, W. D. Richards, A. Jain, G. Hautier, M. Kocher, S. Cholia, D. Gunter, V. L. Chevrier, K. A. Persson, and G. Ceder, "Python Materials Genomics (pymatgen): A robust, open-source python library for materials analysis," *Computational Materials Science*, vol. 68, pp. 314–319, 2013.
- [189] A. Togo and I. Tanaka, "SpgLib: a software library for crystal symmetry search," 2018.
- [190] A. Yanase, "Fortran Program for Space Group," 1985.
- [191] F. Moussa, M. Hennion, J. Rodriguez-Carvajal, H. Moudden, L. Pinsard, and A. Revcolevschi, "Spin waves in the antiferromagnet perovskite  $\text{LaMnO}_3$  : A neutron-scattering study," *Physical Review B*, vol. 54, pp. 15149–15155, dec 1996.
- [192] Y. Tokunaga, S. Iguchi, T. Arima, and Y. Tokura, "Magnetic-Field-Induced Ferroelectric State in  $\text{DyFeO}_3$ ," *Physical Review Letters*, vol. 101, p. 097205, aug 2008.
- [193] J. S. White, T. Honda, K. Kimura, T. Kimura, C. Niedermayer, O. Zaharko, A. Poole, B. Roessli, and M. Kenzelmann, "Coupling of Magnetic and Ferroelectric Hysteresis by a Multicomponent Magnetic Structure in  $\text{Mn}_2\text{GeO}_4$ ," *Physical Review Letters*, vol. 108, p. 077204, feb 2012.
- [194] M. Reehuis, C. Ulrich, K. Prokeš, S. Mat'áš, J. Fujioka, S. Miyasaka, Y. Tokura, and B. Keimer, "Structural and magnetic phase transitions of the orthovanadates  $R\text{VO}_3$  ( $R = \text{Dy}, \text{Ho}, \text{Er}$ ) as seen via neutron diffraction," *Physical Review B*, vol. 83, p. 064404, feb 2011.
- [195] E. Morosan, J. A. Fleitman, Q. Huang, J. W. Lynn, Y. Chen, X. Ke, M. L. Dahlberg, P. Schiffer, C. R. Craley, and R. J. Cava, "Structure and magnetic properties of the  $\text{Ho}_2\text{Ge}_2\text{O}_7$  pyrogermanate," *Physical Review B*, vol. 77, p. 224423, jun 2008.
- [196] E. Krén, G. Kádár, L. Pál, and P. Szabó, "Investigation of the First-Order Magnetic Transformation in  $\text{Mn}_3\text{Pt}$ ," *Journal of Applied Physics*, vol. 38, pp. 1265–1266, mar 1967.
- [197] M. Fiebig, D. Fröhlich, and H. J. Thiele, "Determination of spin direction in the spin-flop phase of  $\text{Cr}_2\text{O}_3$ ," *Physical Review B*, vol. 54, pp. R12681–R12684, nov 1996.
- [198] E. Bertaut, L. Corliss, F. Forrat, R. Aleonard, and R. Pauthenet, "Étude de niobates et tantalates de métaux de transition bivalents," *Journal of Physics and Chemistry of Solids*, vol. 21, pp. 234–251, dec 1961.
- [199] M. Pernet, D. Elmale, and J.-C. Joubert, "Structure magnétique du métaborate de fer  $\text{FeBO}_3$ ," *Solid State Communications*, vol. 8, pp. 1583–1587, oct 1970.
- [200] R. Plumier, M. Sougi, and R. Saint-James, "Neutron-diffraction reinvestigation of  $\text{NiCO}_3$ ," *Physical Review B*, vol. 28, pp. 4016–4020, oct 1983.

- [201] P. J. Brown, P. J. Welfordt, and J. B. Forsyth, "Magnetization density and the magnetic structure of cobalt carbonate," *J. Phys. C : Solid State Phys*, vol. 6, 1973.
- [202] P. J. Brown and J. B. Forsyth, "The spatial distribution of ferromagnetic moment in  $\text{MnCO}_3$ ," *Proceedings of the Physical Society*, vol. 92, pp. 125–135, sep 1967.
- [203] R. A. Alikhanov, "Neutron diffraction investigation of the antiferromagnetism of the carbonates of manganese and iron," *Sov. Phys. JETP*, vol. 9, p. 1204, 1959.
- [204] S. M. Disseler, J. A. Borchers, C. M. Brooks, J. A. Mundy, J. A. Moyer, D. A. Hillsberry, E. L. Thies, D. A. Tenne, J. Heron, M. E. Holtz, J. D. Clarkson, G. M. Stiehl, P. Schiffer, D. A. Muller, D. G. Schlom, and W. D. Ratcliff, "Magnetic Structure and Ordering of Multiferroic Hexagonal  $\text{LuFeO}_3$ ," *Physical Review Letters*, vol. 114, p. 217602, may 2015.
- [205] O. Mentré, M. Kauffmann, G. Ehora, S. Daviero-Minaud, F. Abraham, and P. Roussel, "Structure, dimensionality and magnetism of new cobalt oxyhalides," *Solid State Sciences*, vol. 10, pp. 471–475, apr 2008.
- [206] B. C. Melot, B. Paden, R. Seshadri, E. Suard, G. Nénert, A. Dixit, and G. Lawes, "Magnetic structure and susceptibility of  $\text{CoSe}_2\text{O}_5$ : An antiferromagnetic chain compound," *Physical Review B*, vol. 82, p. 014411, jul 2010.
- [207] R. Troć, M. Pasturel, O. Tougait, A. P. Sazonov, A. Gukasov, C. Sulkowski, and H. Noël, "Single-crystal study of the kagome antiferromagnet U," *Physical Review B - Condensed Matter and Materials Physics*, vol. 85, no. 6, pp. 1–9, 2012.
- [208] M. Reynaud, G. Rousse, J.-N. Chotard, J. Rodríguez-Carvajal, and J.-M. Tarascon, "Marinite  $\text{Li}_2M(\text{SO}_4)_2$  ( $M = \text{Co}, \text{Fe}, \text{Mn}$ ) and  $\text{Li}_1\text{Fe}(\text{SO}_4)_2$ : Model Compounds for Super-Super-Exchange Magnetic Interactions," *Inorganic Chemistry*, vol. 52, pp. 10456–10466, sep 2013.
- [209] K. Tsuzuki, Y. Ishikawa, N. Watanabe, and S. Akimoto, "Neutron Diffraction and Paramagnetic Scattering from a High Pressure Phase of  $\text{MnGeO}_3$  (Ilmenite)," *Journal of the Physical Society of Japan*, vol. 37, pp. 1242–1247, nov 1974.
- [210] A. T. Aldred, B. D. Dunlap, D. J. Lam, G. H. Lander, M. H. Mueller, and I. Nowik, "Magnetic properties of neptunium Laves phases:  $\text{NpMn}_2$ ,  $\text{NpFe}_2$ ,  $\text{NpCo}_2$  and  $\text{NpNi}_2$ ," *Physical Review B*, vol. 11, pp. 530–544, jan 1975.
- [211] B. C. Melot, G. Rousse, J.-N. Chotard, M. Ati, J. Rodríguez-Carvajal, M. C. Kemei, and J.-M. Tarascon, "Magnetic Structure and Properties of the Li-Ion Battery Materials  $\text{FeSO}_4\text{F}$  and  $\text{LiFeSO}_4\text{F}$ ," *Chemistry of Materials*, vol. 23, pp. 2922–2930, jun 2011.
- [212] Y. J. Choi, H. T. Yi, S. Lee, Q. Huang, V. Kiryukhin, and S.-W. Cheong, "Ferroelectricity in an Ising Chain Magnet," *Physical Review Letters*, vol. 100, p. 047601, jan 2008.

- [213] M. Hase, H. Kuroe, V. Y. Pomjakushin, L. Keller, R. Tamura, N. Terada, Y. Matsushita, A. Dönni, and T. Sekine, “Magnetic structure of the spin- $\frac{1}{2}$  frustrated quasi-one-dimensional antiferromagnet  $\text{Cu}_3\text{Mo}_2\text{O}_9$ : Appearance of a partially disordered state,” *PHYSICAL REVIEW B*, vol. 92, p. 54425, 2015.
- [214] A. Lappas, A. S. Wills, M. A. Green, K. Prassides, and M. Kurmoo, “Magnetic ordering in the rutile molecular magnets,” *Physical Review B*, vol. 67, p. 144406, apr 2003.
- [215] Z.-G. Y, P. Schobinger-Papamantellos, S.-Y. Mao, C. Ritter, E. Suard, M. Sato, and H. Schmid, “A neutron diffraction study of the magnetic structure and phase transition in  $\text{Ni}_3^{11}\text{B}_7\text{O}_{13}\text{Cl}$  boracite,” *Ferroelectrics*, vol. 204, pp. 83–95, dec 1997.
- [216] G. Gitgeatpong, Y. Zhao, M. Avdeev, R. O. Piltz, T. J. Sato, and K. Matan, “Magnetic structure and Dzyaloshinskii-Moriya interaction in the  $S = \frac{1}{2}$  helical-honeycomb antiferromagnet  $\alpha - \text{Cu}_2\text{V}_2\text{O}_7$ ,” *Physical Review B*, vol. 92, p. 024423, jul 2015.
- [217] C. Darie, C. Goujon, M. Bacia, H. Klein, P. Toulemonde, P. Bordet, and E. Suard, “Magnetic and crystal structures of  $\text{BiCrO}_3$ ,” *Solid State Sciences*, vol. 12, pp. 660–664, may 2010.
- [218] P. Schobinger-Papamantellos, K. H. Buschow, and J. Rodríguez-Carvajal, “Magnetoelastic phase transitions in the  $\text{LuFe}_4\text{Ge}_2$  and  $\text{YFe}_4\text{Si}_2$  compounds: A neutron diffraction study,” *Journal of Magnetism and Magnetic Materials*, vol. 324, no. 22, pp. 3709–3715, 2012.
- [219] P. Schobinger-Papamantellos, D. De Mooij, and K. Buschow, “Crystallographic and magnetic structure of  $\text{TbGe}_2$ ,” *Journal of the Less Common Metals*, vol. 144, pp. 265–274, dec 1988.
- [220] W. Kunmann, S. La Placa, L. Corliss, J. Hastings, and E. Banks, “Magnetic structures of the ordered trirutiles  $\text{Cr}_2\text{WO}_6$ ,  $\text{Cr}_2\text{TeO}_6$  and  $\text{Fe}_2\text{TeO}_6$ ,” *Journal of Physics and Chemistry of Solids*, vol. 29, pp. 1359–1364, aug 1968.
- [221] M. Avdeev, B. J. Kennedy, and T. Kolodiazhnyi, “Neutron powder diffraction study of the magnetic structure of  $\text{EuZrO}_3$ ,” *Journal of Physics: Condensed Matter*, vol. 26, p. 095401, mar 2014.
- [222] P. D. Battle, C. P. Grey, M. Hervieu, C. Martin, C. A. Moore, and Y. Paik, “Structural chemistry and magnetic properties of  $\text{La}_2\text{LiRuO}_6$ ,” *Journal of Solid State Chemistry*, vol. 175, pp. 20–26, oct 2003.
- [223] D. I. Gorbunov, M. S. Henriques, A. V. Andreev, V. Eigner, A. Gukasov, X. Fabrèges, Y. Skourski, V. Petříček, and J. Wosnitza, “Magnetic anisotropy and reduced neodymium magnetic moments in  $\text{Nd}_3\text{Ru}_4\text{Al}_2$ ,” *Physical Review B*, vol. 93, p. 024407, jan 2016.
- [224] Z. Yamani, Z. Tun, and D. H. Ryan, “Neutron scattering study of the classical antiferromagnet  $\text{MnF}_2$  : a perfect hands-on neutron scattering teaching courseSpecial issue on Neutron Scattering in Canada.,” *Canadian Journal of Physics*, vol. 88, pp. 771–797, oct 2010.

- [225] S. Yano, D. Louca, J. Yang, U. Chatterjee, D. E. Bugaris, D. Y. Chung, L. Peng, M. Grayson, and M. G. Kanatzidis, “Magnetic structure of  $\text{NiS}_{2-x}\text{Se}_x$ ,” *Physical Review B*, vol. 93, p. 024409, jan 2016.
- [226] N. Taira, M. Wakeshima, Y. Hinatsu, A. Tobo, and K. Ohoyama, “Magnetic structure of pyrochlore-type  $\text{Er}_2\text{Ru}_2\text{O}_7$ ,” *Journal of Solid State Chemistry*, vol. 176, pp. 165–169, nov 2003.
- [227] L. Ding, C. V. Colin, C. Darie, J. Robert, F. Gay, and P. Bordet, “One-dimensional short-range magnetic correlations in the magnetoelectric pyroxene  $\text{CaMnGe}_2\text{O}_6$ ,” *Physical Review B*, vol. 93, p. 064423, feb 2016.
- [228] G. J. Redhammer, G. Roth, W. Treutmann, W. Paulus, G. André, C. Pietzonka, and G. Amthauer, “Magnetic ordering and spin structure in Ca-bearing clinopyroxenes  $\text{CaM}_{2+}(\text{Si}, \text{Ge})_2\text{O}_6$ ,  $M=\text{Fe}, \text{Ni}, \text{Co}, \text{Mn}$ ,” *Journal of Solid State Chemistry*, vol. 181, pp. 3163–3176, nov 2008.
- [229] A. Yaouanc, P. Dalmas de Réotier, P. Bonville, J. A. Hodges, V. Glazkov, L. Keller, V. Sikolenko, M. Bartkowiak, A. Amato, C. Baines, P. J. C. King, P. C. M. Gubbens, and A. Forget, “Dynamical Splayed Ferromagnetic Ground State in the Quantum Spin Ice  $\text{Yb}_2\text{Sn}_2\text{O}_7$ ,” *Physical Review Letters*, vol. 110, p. 127207, mar 2013.
- [230] J. Gaudet, K. A. Ross, E. Kermarrec, N. P. Butch, G. Ehlers, H. A. Dabkowska, and B. D. Gaulin, “Gapless quantum excitations from an icelike splayed ferromagnetic ground state in stoichiometric  $\text{Yb}_2\text{Ti}_2\text{O}_7$ ,” *Physical Review B*, vol. 93, p. 064406, feb 2016.
- [231] K. Knížek, Z. Jirák, P. Novák, and C. de la Cruz, “Non-collinear magnetic structures of  $\text{TbCoO}_3$  and  $\text{DyCoO}_3$ ,” *Solid State Sciences*, vol. 28, pp. 26–30, feb 2014.
- [232] V. Scagnoli, M. Allieta, H. Walker, M. Scavini, T. Katsufuji, L. Sagarna, O. Zaharko, and C. Mazzoli, “ $\text{EuTiO}_3$  magnetic structure studied by neutron powder diffraction and resonant x-ray scattering,” *Physical Review B*, vol. 86, p. 094432, sep 2012.
- [233] E. Ressouche, M. Loire, V. Simonet, R. Ballou, A. Stunault, and A. Wildes, “Magnetoelectric  $\text{MnPS}_3$  as a candidate for ferrotoroidicity,” *Physical Review B*, vol. 82, p. 100408, sep 2010.
- [234] J. Blasco, J. García, G. Subías, J. Stankiewicz, J. A. Rodríguez-Velamazán, C. Ritter, J. L. García-Muñoz, and F. Fauth, “Magnetoelectric and structural properties of  $\text{Y}_2\text{CoMnO}_6$ : The role of antisite defects,” *Physical Review B*, vol. 93, p. 214401, jun 2016.
- [235] L. D. Sanjeewa, V. O. Garlea, M. A. McGuire, C. D. McMillen, H. Cao, and J. W. Kolis, “Structural and magnetic characterization of the one-dimensional  $S = \frac{5}{2}$  antiferromagnetic chain system  $\text{SrMn}(\text{VO}_4)(\text{OH})$ ,” *Physical Review B*, vol. 93, p. 224407, jun 2016.

- [236] A. Scheie, M. Sanders, J. Krizan, Y. Qiu, R. J. Cava, and C. Broholm, “Effective spin- $\frac{1}{2}$  scalar chiral order on kagome lattices in  $\text{Nd}_3\text{Sb}_3\text{Mg}_2\text{O}_{14}$ ,” *Physical Review B*, vol. 93, p. 180407, may 2016.
- [237] G. Ferey, M. Leblanc, R. De Pape, and J. Pannetier, “Frustrated magnetic structures: II. Antiferromagnetic structure of the ordered modified pyrochlore  $\text{NH}_4\text{Fe}^{II}\text{Fe}^{III}\text{F}_6$  at  $4.2 \sim K$ ,” *Solid State Communications*, vol. 53, pp. 559–563, feb 1985.
- [238] P. Burlet, J. Rossat-Mignod, R. Troć, and Z. Henkie, “Non-collinear magnetic structure of  $\text{U}_3\text{P}_4$  and  $\text{U}_3\text{As}_4$ ,” *Solid State Communications*, vol. 39, pp. 745–749, aug 1981.
- [239] G. Rousse, J. Rodriguez-Carvajal, S. Patoux, and C. Masquelier, “Magnetic Structures of the Triphylite  $\text{LiFePO}_4$  and of Its Delithiated Form  $\text{FePO}_4$ ,” *Chemistry of Materials*, vol. 15, no. 21, pp. 4082–4090, 2003.
- [240] L. S. Wu, S. E. Nikitin, M. Frontzek, A. I. Kolesnikov, G. Ehlers, M. D. Lumsden, K. A. Shaykhutdinov, E.-J. Guo, A. T. Savici, Z. Gai, A. S. Sefat, and A. Podlesnyak, “Magnetic ground state of the Ising-like antiferromagnet  $\text{DyScO}_3$ ,” *Physical Review B*, vol. 96, p. 144407, oct 2017.
- [241] M. S. Henriques, D. I. Gorbunov, A. V. Andreev, X. Fabrèges, A. Gukasov, M. Uhlarz, V. PetÁíček, B. Ouladdiaf, and J. Wosnitza, “Complex magnetic order in the kagome ferromagnet  $\text{Pr}_3\text{Ru}_4\text{Al}_{12}$ ,” *Physical Review B*, vol. 97, p. 014431, jan 2018.
- [242] D. Fruchart and E. F. Bertaut, “Magnetic Studies of the Metallic Perovskite-Type Compounds of Manganese,” *Journal of the Physical Society of Japan*, vol. 44, pp. 781–791, mar 1978.
- [243] W. Jauch, M. Reehuis, A. J. Schultz, and IUCr, “ $\gamma$ -ray and neutron diffraction studies of  $\text{CoF}_2$  : magnetostriction, electron density and magnetic moments,” *Acta Crystallographica Section A Foundations of Crystallography*, vol. 60, pp. 51–57, jan 2004.
- [244] Y. Singh, M. A. Green, Q. Huang, A. Kreyssig, R. J. McQueeney, D. C. Johnston, and A. I. Goldman, “Magnetic order in  $\text{BaMn}_2\text{As}_2$  from neutron diffraction measurements,” *Physical Review B*, vol. 80, p. 100403, sep 2009.
- [245] A. Wiedenmann, J. Rossat-Mignod, A. Louisy, R. Brec, and J. Rouxel, “Neutron diffraction study of the layered compounds  $\text{MnPSe}_3$  and  $\text{FePSe}_3$ ,” *Solid State Communications*, vol. 40, pp. 1067–1072, dec 1981.
- [246] Q. Zhang, W. Tian, S. G. Peterson, K. W. Dennis, and D. Vaknin, “Spin reorientation and Ce-Mn coupling in antiferromagnetic oxypnictide  $\text{CeMnAsO}$ ,” *Physical Review B*, vol. 91, p. 064418, feb 2015.

- [247] D. Xu, M. Avdeev, P. D. Battle, and X.-Q. Liu, "Magnetic Properties of  $\text{CeMn}_{2-x}\text{Co}_x\text{Ge}_4\text{O}_{12}$  ( $0 \leq x \leq 2$ ) as a Function of Temperature and Magnetic Field," *Inorganic Chemistry*, vol. 56, pp. 2750–2762, mar 2017.
- [248] G. Shirane, S. J. Pickart, and Y. Ishikawa, "Neutron Diffraction Study of Antiferromagnetic  $\text{MnTiO}_3$  and  $\text{NiTiO}_3$ ," *Journal of the Physical Society of Japan*, vol. 14, pp. 1352–1360, oct 1959.
- [249] A. C. Garcia-Castro, W. Ibarra-Hernandez, E. Bousquet, and A. H. Romero, "Direct Magnetization-Polarization Coupling in  $\text{BaCuF}_4$ ," *PHYSICAL REVIEW LETTERS*, vol. 121, p. 117601, 2018.
- [250] S. W. Kim, S.-H. Kim, P. S. Halasyamani, M. A. Green, K. P. Bhatti, C. Leighton, H. Das, and C. J. Fennie, " $\text{RbFe}^{2+}\text{Fe}^{3+}\text{F}_6$ : Synthesis, structure, and characterization of a new charge-ordered magnetically frustrated pyrochlore-related mixed-metal fluoride," *Chem. Sci.*, vol. 3, pp. 741–751, feb 2012.
- [251] R. Santoro, D. Segal, and R. Newnham, "Magnetic properties of  $\text{LiCoPO}_4$  and  $\text{LiNiPO}_4$ ," *Journal of Physics and Chemistry of Solids*, vol. 27, pp. 1192–1193, jun 1966.
- [252] R. A. Steeman, E. Frikkee, S. A. M. Mentink, A. A. Menovsky, G. J. Nieuwenhuys, and J. A. Mydosh, "Hybridisation effects in  $\text{UPt}_2\text{Si}_2$ ," *Journal of Physics: Condensed Matter*, vol. 2, pp. 4059–4066, may 1990.
- [253] E. Palacios, M. Evangelisti, R. Sáez-Puche, A. J. Dos Santos-García, F. Fernández-Martínez, C. Cascales, M. Castro, R. Burriel, O. Fabelo, and J. A. Rodríguez-Velamazán, "Magnetic structures and magnetocaloric effect in  $\text{RVO}_4$  ( $\text{R} = \text{Gd}, \hat{\text{A}} \text{Nd}$ )," *Physical Review B*, vol. 97, p. 214401, jun 2018.
- [254] P. J. Brown, V. Nunezt, F. Tassett, J. B. Forsytht, and P. Radhakrishnao, "Determination of the magnetic structure of  $\text{Mn}_3\text{Sn}$  using generalized neutron polarization analysis," *J. Phys.: Condens. Matter*, vol. 2, pp. 9409–9422, 1990.
- [255] P. Burlet, E. Ressouche, B. Malaman, R. Welter, J. P. Sanchez, and P. Vulliet, "Noncollinear magnetic structure of  $\text{MnTe}_2$ ," *Physical Review B*, vol. 56, pp. 14013–14018, dec 1997.
- [256] A. S. Sukhanov, S. Singh, L. Caron, T. Hansen, A. Hoser, V. Kumar, H. Borrmann, A. Fitch, P. Devi, K. Manna, C. Felser, and D. S. Inosov, "Gradual pressure-induced change in the magnetic structure of the noncollinear antiferromagnet  $\text{Mn}_3\text{Ge}$ ," *Physical Review B*, vol. 97, p. 214402, jun 2018.
- [257] A. S. Cavichini, M. T. Orlando, J. B. Depianti, J. L. Passamai, F. Damay, F. Porcher, and E. Granado, "Exotic magnetism and spin-orbit-assisted Mott insulating state in a  $3d - 5d$  double perovskite," *Physical Review B*, vol. 97, p. 054431, feb 2018.

- [258] X. F. Hao, A. Stroppa, S. Picozzi, A. Filippetti, and C. Franchini, "Exceptionally large room-temperature ferroelectric polarization in the  $\text{PbNiO}_3$  multiferroic nickelate: First-principles study," *Physical Review B*, vol. 86, p. 014116, jul 2012.
- [259] C. Autret, C. Martin, M. Hervieu, R. Retoux, B. Raveau, G. André, and F. Bourée, "Structural investigation of  $\text{Ca}_2\text{MnO}_4$  by neutron powder diffraction and electron microscopy," *Journal of Solid State Chemistry*, vol. 177, pp. 2044–2052, jun 2004.
- [260] S. L. Brock, N. Raju, J. Greedan, and S. M. Kauzlarich, "The magnetic structures of the mixed layer pnictide oxide compounds  $\text{Sr}_2\text{Mn}_3\text{Pn}_2\text{O}_{12}$  ( $\text{Pn} = \text{As}, \text{Sb}$ )," *Journal of Alloys and Compounds*, vol. 237, pp. 9–19, apr 1996.
- [261] L. Regnault, J. Henry, J. Rossat-Mignod, and A. De Combarieu, "Magnetic properties of the layered nickel compounds  $\text{BaNi}_2(\text{PO}_4)_2$  and  $\text{BaNi}_2(\text{AsO}_4)_2$ ," *Journal of Magnetism and Magnetic Materials*, vol. 15-18, pp. 1021–1022, jan 1980.
- [262] A. Sazonov, M. Meven, V. Hutanu, G. Heger, T. Hansen, A. Gukasov, and IUCr, "Magnetic behaviour of synthetic  $\text{Co}_2\text{SiO}_4$ ," *Acta Crystallographica Section B Structural Science*, vol. 65, pp. 664–675, dec 2009.
- [263] G. Will and W. Schafer, "Neutron diffraction and the magnetic structures of some rare earth diborides and tetraborides," *Journal of the Less Common Metals*, vol. 67, pp. 31–39, sep 1979.
- [264] W. Lottermoser and H. Fuess, "Magnetic structure of the orthosilicates  $\text{Mn}_2\text{SiO}_4$  and  $\text{Co}_2\text{SiO}_4$ ," *Physica Status Solidi (a)*, vol. 109, pp. 589–595, oct 1988.
- [265] W. Lottermoser, R. Müller, and H. Fuess, "Antiferromagnetism in synthetic olivines," *Journal of Magnetism and Magnetic Materials*, vol. 54-57, pp. 1005–1006, feb 1986.
- [266] P. Wadley, V. Hills, M. R. Shahedkhah, K. W. Edmonds, R. P. Champion, V. Novák, B. Oulad-diaf, D. Khalyavin, S. Langridge, V. Saidl, P. Nemeč, A. W. Rushforth, B. L. Gallagher, S. S. Dhesi, F. Maccherozzi, J. Železný, and T. Jungwirth, "Antiferromagnetic structure in tetragonal  $\text{CuMnAs}$  thin films," *Scientific Reports*, vol. 5, p. 17079, dec 2015.
- [267] Z. Ouyang, F. Wang, Q. Hang, W. Liu, G. Liu, J. Lynn, J. Liang, and G. Rao, "Temperature dependent neutron powder diffraction study of the Laves phase compound  $\text{TbCo}_2$ ," *Journal of Alloys and Compounds*, vol. 390, pp. 21–25, mar 2005.
- [268] M. Sale, Q. Xia, M. Avdeev, and C. D. Ling, "Crystal and Magnetic Structures of Melilite-Type  $\text{Ba}_2\text{MnSi}_2\text{O}_7$ ," *Inorganic Chemistry*, vol. 58, pp. 4164–4172, apr 2019.
- [269] M. V. Lobanov, M. Greenblatt, E. a. N. Caspi, J. D. Jorgensen, D. V. Sheptyakov, B. H. Toby, C. E. Botez, and P. W. Stephens, "Crystal and magnetic structure of the  $\text{Ca}_3\text{Mn}_2\text{O}_7$

- Ruddlesden-Popper phase: neutron and synchrotron x-ray diffraction study,” *Journal of Physics: Condensed Matter*, vol. 16, pp. 5339–5348, jul 2004.
- [270] M. Sale, M. Avdeev, Z. Mohamed, C. D. Ling, and P. Barpanda, “Magnetic structure and properties of centrosymmetric twisted-melilite  $K_2CoP_2O_7$ ,” *Dalton Transactions*, vol. 46, pp. 6409–6416, may 2017.
- [271] E. Solana-Madruga, Á. M. Arévalo-López, A. J. Dos Santos-García, C. Ritter, C. Cascales, R. Sáez-Puche, and J. P. Attfield, “Anisotropic magnetic structures of the  $MnRMnSbO_6$  high-pressure doubly ordered perovskites ( $R = La, Pr, \text{ and } Nd$ )  $MnRMnSbO_6$  high-pressure doubly ordered perovskites,” *PHYSICAL REVIEW B*, vol. 97, p. 134408, 2018.
- [272] V. Gvozdetskyi, A. Senyshyn, R. Gladyshevskii, and V. Hlukhyy, “Crystal and Magnetic Structures of the Chain Antiferromagnet  $CaFe_4Al_8$ ,” *Inorganic Chemistry*, vol. 57, no. 10, pp. 5820–5829, 2018.
- [273] S. Petit, E. Lhotel, F. Damay, P. Boutrouille, A. Forget, and D. Colson, “Long-Range Order in the Dipolar X Y Antiferromagnet  $Er_2Sn_2O_7$ ,” *Physical Review Letters*, vol. 119, p. 187202, oct 2017.
- [274] A. M. Hallas, J. Gaudet, N. P. Butch, G. Xu, M. Tachibana, C. R. Wiebe, G. M. Luke, and B. D. Gaulin, “Phase Competition in the Palmer-Chalker XY Pyrochlore  $Er_2Pt_2O_7$ ,” *Physical Review Letters*, vol. 119, p. 187201, oct 2017.
- [275] S. Calder, D. J. Singh, V. O. Garlea, M. D. Lumsden, Y. G. Shi, K. Yamaura, and A. D. Christianson, “Interplay of spin-orbit coupling and hybridization in  $Ca_3LiOsO_6$  and  $Ca_3LiRuO_6$ ,” *Physical Review B*, vol. 96, p. 184426, nov 2017.
- [276] R. Toft-Petersen, N. H. Andersen, H. Li, J. Li, W. Tian, S. L. Bud’ko, T. B. S. Jensen, C. Niedermayer, M. Laver, O. Zaharko, J. W. Lynn, and D. Vaknin, “Magnetic phase diagram of magnetoelectric  $LiMnPO_4$ ,” *Physical Review B*, vol. 85, p. 224415, jun 2012.
- [277] S. Calder, V. O. Garlea, D. F. McMorrow, M. D. Lumsden, M. B. Stone, J. C. Lang, J.-W. Kim, J. A. Schlueter, Y. G. Shi, K. Yamaura, Y. S. Sun, Y. Tsujimoto, and A. D. Christianson, “Magnetically Driven Metal-Insulator Transition in  $NaOsO_3$ ,” *Physical Review Letters*, vol. 108, p. 257209, jun 2012.
- [278] S. Baran, D. Kaczorowski, A. Arulraj, B. Penc, and A. Szytuła, “Frustrated magnetic structure of  $TmAgGe$ ,” *Journal of Magnetism and Magnetic Materials*, vol. 321, no. 19, pp. 3256–3261, 2009.
- [279] P. Schobinger-Papamantellos, J. Rodriguez-Carvajal, G. André, N. Duong, K. Buschow, and P. Tolédano, “Simultaneous structural and magnetic transitions in  $YFe_4Ge_2$  studied by neu-



- tron diffraction and magnetic measurements,” *Journal of Magnetism and Magnetic Materials*, vol. 236, pp. 14–27, oct 2001.
- [280] G. J. Redhammer, G. Roth, W. Treutmann, M. Hoelzel, W. Paulus, G. André, C. Pietzonka, and G. Amthauer, “The magnetic structure of clinopyroxene-type LiFeGe<sub>2</sub>O<sub>6</sub> and revised data on multiferroic LiFeSi<sub>2</sub>O<sub>6</sub>,” *Journal of Solid State Chemistry*, vol. 182, pp. 2374–2384, sep 2009.
- [281] R. Trump, S. Thierfeldt, M. Loewenhaupt, and T. Chattopadhyay, “Magnetic structure of the Kondo lattice compound CeCu<sub>2</sub>,” *Journal of Applied Physics*, vol. 69, pp. 4699–4701, apr 1991.
- [282] S. Calder, M. D. Lumsden, V. O. Garlea, J. W. Kim, Y. G. Shi, H. L. Feng, K. Yamaura, and A. D. Christianson, “Magnetic structure determination of Ca<sub>3</sub>LiOsO<sub>6</sub> using neutron and x-ray scattering,” *Physical Review B*, vol. 86, p. 054403, aug 2012.
- [283] X. Fabrèges, I. Mirebeau, P. Bonville, S. Petit, G. Lebras-Jasmin, A. Forget, G. André, and S. Pailhès, “Magnetic order in YbMnO<sub>3</sub> studied by neutron diffraction and Mössbauer spectroscopy,” *Physical Review B*, vol. 78, p. 214422, dec 2008.
- [284] J. Blasco, J. L. García-Muñoz, J. García, G. Subías, J. Stankiewicz, J. A. Rodríguez-Velamazán, and C. Ritter, “Magnetic order and magnetoelectric properties of R<sub>2</sub>CoMnO<sub>6</sub> perovskites (R = Ho, Tm, Yb, and Lu),” *PHYSICAL REVIEW B*, vol. 96, p. 24409, 2017.
- [285] P. J. Brown and T. Chatterji, “Neutron diffraction and polarimetric study of the magnetic and crystal structures of HoMnO<sub>3</sub> and YMnO<sub>3</sub>,” *Journal of Physics Condensed Matter*, vol. 18, no. 44, pp. 10085–10096, 2006.
- [286] P. J. Brown and J. B. Forsyth, “A neutron diffraction study of weak ferromagnetism in nickel fluoride,” *Journal of Physics C: Solid State Physics*, vol. 14, pp. 5171–5184, nov 1981.
- [287] A. G. Gukasov, P. Rogl, P. J. Brown, M. Mihalik, and A. Menovsky, “Site susceptibility tensors and magnetic structure of U<sub>3</sub>Al<sub>2</sub>Si<sub>3</sub>: a polarized neutron diffraction study,” *Journal of Physics: Condensed Matter*, vol. 14, pp. 8841–8851, sep 2002.
- [288] A. A. Aczel, D. E. Bugaris, J. Yeon, C. de la Cruz, H.-C. zur Loye, and S. E. Nagler, “Coupled Nd and B′ spin ordering in the double perovskites Nd<sub>2</sub>NaB′O<sub>6</sub> (B′ = Ru, Os),” *Physical Review B*, vol. 88, p. 014413, jul 2013.
- [289] V. Nguyen, F. Tchéou, and J. Rossat-Mignod, “Magnetic structures of PrSi and NdSi intermetallic alloys,” *Solid State Communications*, vol. 23, pp. 821–823, sep 1977.
- [290] D. Gignoux, J. Rossat-Mignod, and F. Tcheou, “Magnetic structure of the TmNi compound crystal field effect,” *Physica Status Solidi (a)*, vol. 14, pp. 483–488, dec 1972.

- [291] J. Rodriguez-Carvajal, M. T. Fernandez-Diaz, and J. L. Martinez, “Neutron diffraction study on structural and magnetic properties of  $\text{La}_2\text{NiO}_4$ ,” *Journal of Physics: Condensed Matter*, vol. 3, pp. 3215–3234, may 1991.
- [292] K. Tomiyasu and I. Kagomiya, “Magnetic Structure of  $\text{NiCr}_2\text{O}_4$  Studied by Neutron Scattering and Magnetization Measurements,” *Journal of the Physical Society of Japan*, vol. 73, pp. 2539–2542, sep 2004.
- [293] E. Bertaut, J. Cohen, B. Lambert-Andron, and P. Mollard, “Étude de  $\text{Cr}_2\text{S}_3$  rhomboédrique par diffraction neutronique et mesures magnétiques,” *Journal de Physique*, vol. 29, pp. 813–824, aug 1968.
- [294] A. M. Arévalo-López and J. P. Attfield, “Weak ferromagnetism and domain effects in multiferroic  $\text{LiNbO}_3$ -type  $\text{MnTiO}_3$ -II,” *Physical Review B*, vol. 88, p. 104416, sep 2013.
- [295] V. Hutanu, A. Sazonov, M. Meven, H. Murakawa, Y. Tokura, S. Bordács, I. Kézsmárki, and B. Náfrádi, “Determination of the magnetic order and the crystal symmetry in the multiferroic ground state of  $\text{Ba}_2\text{CoGe}_2\text{O}_7$ ,” *Physical Review B*, vol. 86, p. 104401, sep 2012.
- [296] B. Roy, A. Pandey, Q. Zhang, T. W. Heitmann, D. Vaknin, D. C. Johnston, and Y. Furukawa, “Experimental evidence of a collinear antiferromagnetic ordering in the frustrated  $\text{CoAl}_2\text{O}_4$  spinel,” *Physical Review B*, vol. 88, p. 174415, nov 2013.
- [297] A. Muñoz, J. A. Alonso, M. J. Martínez-Lope, M. T. Casáis, J. L. Martínez, and M. T. Fernández-Díaz, “Magnetic structure of hexagonal  $\text{RMnO}_3$  ( $R = \text{Y}, \text{Sc}$ ): Thermal evolution from neutron powder diffraction data,” *Physical Review B*, vol. 62, pp. 9498–9510, oct 2000.
- [298] V. O. Garlea, R. Jin, D. Mandrus, B. Roessli, Q. Huang, M. Miller, A. J. Schultz, and S. E. Nagler, “Magnetic and Orbital Ordering in the Spinel  $\text{MnV}_2\text{O}_4$ ,” *Physical Review Letters*, vol. 100, p. 066404, feb 2008.
- [299] A. H. Hill, F. Jiao, P. G. Bruce, A. Harrison, W. Kockelmann, and C. Ritter, “Neutron Diffraction Study of Mesoporous and Bulk Hematite,  $\alpha\text{-Fe}_2\text{O}_3$ ,” *Chemistry of Materials*, vol. 20, pp. 4891–4899, aug 2008.
- [300] Y. F. Guo, A. J. Princep, X. Zhang, P. Manuel, D. Khalyavin, I. I. Mazin, Y. G. Shi, and A. T. Boothroyd, “Coupling of magnetic order to planar Bi electrons in the anisotropic Dirac metals  $\text{AMnBi}_2$  ( $A = \text{Sr}, \text{Ca}$ ),” *Physical Review B*, vol. 90, p. 075120, aug 2014.
- [301] S. Iikubo, K. Kodama, K. Takenaka, H. Takagi, and S. Shamoto, “Magnetovolume effect in  $\text{Mn}_3\text{Cu}_{1-x}\text{Ge}_x\text{N}$  related to the magnetic structure: Neutron powder diffraction measurements,” *Physical Review B*, vol. 77, p. 020409, jan 2008.

- [302] M. Zhu, D. Do, C. R. Dela Cruz, Z. Dun, H. D. Zhou, S. D. Mahanti, and X. Ke, “Tuning the Magnetic Exchange via a Control of Orbital Hybridization in  $\text{Cr}_2(\text{Te}_{1-x}\text{W}_x)\text{O}_6$ ,” *Physical Review Letters*, vol. 113, p. 076406, aug 2014.
- [303] O. S. Volkova, V. V. Mazurenko, I. V. Solovyev, E. B. Deeva, I. V. Morozov, J.-Y. Lin, C. K. Wen, J. M. Chen, M. Abdel-Hafez, and A. N. Vasiliev, “Noncollinear ferrimagnetic ground state in  $\text{Ni}(\text{NO}_3)_2$ ,” *Physical Review B*, vol. 90, p. 134407, oct 2014.
- [304] A. P. Sazonov, A. Gukasov, H. B. Cao, P. Bonville, E. Ressouche, C. Decorse, and I. Mirebeau, “Magnetic structure in the spin liquid  $\text{Tb}_2\text{Ti}_2\text{O}_7$  induced by a [111] magnetic field: Search for a magnetization plateau,” *Physical Review B*, vol. 88, p. 184428, nov 2013.
- [305] K. Ohgushi, J. I. Yamaura, H. Ohsumi, K. Sugimoto, S. Takeshita, A. Tokuda, H. Takagi, M. Takata, and T. H. Arima, “Resonant X-ray diffraction study of the strongly spin-orbit-coupled mott insulator  $\text{CaIrO}_3$ ,” *Physical Review Letters*, vol. 110, no. 21, pp. 1–5, 2013.
- [306] A. Purwanto, R. A. Robinson, L. Havela, V. Sechovský, P. Svoboda, H. Nakotte, K. Prokeš, F. R. de Boer, A. Seret, J. M. Winand, J. Rebizant, and J. C. Spirlet, “Magnetic ordering in  $\text{U}_2\text{Pd}_2\text{In}$  and  $\text{U}_2\text{Pd}_2\text{Sn}$ ,” *Physical Review B*, vol. 50, pp. 6792–6801, sep 1994.
- [307] T. B. S. Jensen, N. B. Christensen, M. Kenzelmann, H. M. Rønnow, C. Niedermayer, N. H. Andersen, K. Lefmann, J. Schefer, M. v. Zimmermann, J. Li, J. L. Zarestky, and D. Vaknin, “Field-induced magnetic phases and electric polarization in  $\text{LiNiPO}_4$ ,” *Physical Review B*, vol. 79, p. 092412, mar 2009.
- [308] S. Calder, B. Saporov, H. B. Cao, J. L. Niedziela, M. D. Lumsden, A. S. Sefat, and A. D. Christianson, “Magnetic structure and spin excitations in  $\text{BaMn}_2\text{Bi}_2$ ,” *Physical Review B*, vol. 89, p. 064417, feb 2014.
- [309] P. J. Brown and B. C. Frazer, “Magnetic Structure of  $\text{CoSO}_4$ ,” *Physical Review*, vol. 129, pp. 1145–1147, feb 1963.
- [310] J. A. Gonzalo, D. E. Cox, and G. Shirane, “The Magnetic Structure of  $\text{FeSb}_2\text{O}_4$ ,” *Physical Review*, vol. 147, pp. 415–418, jul 1966.
- [311] M. B. WILK and R. GNANADESIKAN, “Probability plotting methods for the analysis for the analysis of data,” *Biometrika*, vol. 55, pp. 1–17, mar 1968.
- [312] M. El-Batanouny, *Advanced quantum condensed matter*. Cambridge University Press, 2020.
- [313] O. P. Vajk, M. Kenzelmann, J. W. Lynn, S. B. Kim, and S.-W. Cheong, “Magnetic Order and Spin Dynamics in Ferroelectric  $\text{HoMnO}_3$ ,” *Physical Review Letters*, vol. 94, p. 087601, mar 2005.

- [314] T. Lottermoser, T. Lonkai, U. Amann, D. Hohlwein, J. Ihringer, and M. Fiebig, “Magnetic phase control by an electric field,” *Nature*, vol. 430, pp. 541–544, jul 2004.
- [315] A. Muñoz, J. A. Alonso, M. J. Martínez-Lope, M. T. Casáis, J. L. Martínez, and M. T. Fernández-Díaz, “Evolution of the Magnetic Structure of Hexagonal  $\text{HoMnO}_3$  from Neutron Powder Diffraction Data,” *Chemistry of Materials*, vol. 13, pp. 1497–1505, may 2001.
- [316] M. Fiebig, D. Fröhlich, K. Kohn, S. Leute, T. Lottermoser, V. V. Pavlov, and R. V. Pisarev, “Determination of the Magnetic Symmetry of Hexagonal Manganites by Second Harmonic Generation,” *Physical Review Letters*, vol. 84, pp. 5620–5623, jun 2000.
- [317] J. An, S. Barabash, V. Ozolins, M. van Schilfgaarde, and K. D. Belashchenko, “First-principles study of phase stability of gd-doped euo and eus,” *Physical Review B*, vol. 83, no. 6, p. 064105, 2011.
- [318] M. Schlipf, M. Betzinger, M. Ležaić, C. Friedrich, and S. Blügel, “Structural, electronic, and magnetic properties of the europium chalcogenides: A hybrid-functional dft study,” *Physical Review B*, vol. 88, no. 9, p. 094433, 2013.
- [319] A. Pulkkinen, B. Barbiellini, J. Nokelainen, V. Sokolovskiy, D. Baigutlin, O. Miroshkina, M. Zagrebin, V. Buchelnikov, C. Lane, R. S. Markiewicz, *et al.*, “Coulomb correlation in noncollinear antiferromagnetic  $\alpha$ -mn,” *Physical Review B*, vol. 101, no. 7, p. 075115, 2020.
- [320] R. O. Jones and O. Gunnarsson, “The density functional formalism, its applications and prospects,” *Reviews of Modern Physics*, vol. 61, no. 3, p. 689, 1989.
- [321] D. C. Patton, D. V. Porezag, and M. R. Pederson, “Simplified generalized-gradient approximation and anharmonicity: Benchmark calculations on molecules,” *Physical Review B*, vol. 55, no. 12, p. 7454, 1997.
- [322] B. Hammer, L. B. Hansen, and J. K. Nørskov, “Improved adsorption energetics within density-functional theory using revised perdue-burke-ernzerhof functionals,” *Physical review B*, vol. 59, no. 11, p. 7413, 1999.
- [323] L. Wang, T. Maxisch, and G. Ceder, “Oxidation energies of transition metal oxides within the gga+ u framework,” *Physical Review B*, vol. 73, no. 19, p. 195107, 2006.
- [324] P. Liu, J. He, B. Kim, S. Khmelevskiy, A. Toschi, G. Kresse, and C. Franchini, “Comparative ab initio study of the structural, electronic, magnetic, and dynamical properties of lioso 3 and naoso 3,” *Physical Review Materials*, vol. 4, no. 4, p. 045001, 2020.
- [325] L. Kleinman, “Density functional for noncollinear magnetic systems,” *Physical Review B*, vol. 59, no. 5, p. 3314, 1999.

- [326] K. Capelle, G. Vignale, and B. Györfy, “Spin currents and spin dynamics in time-dependent density-functional theory,” *Physical review letters*, vol. 87, no. 20, p. 206403, 2001.
- [327] M. Katsnelson and V. Antropov, “Spin angular gradient approximation in the density functional theory,” *Physical Review B*, vol. 67, no. 14, p. 140406, 2003.
- [328] S. Sharma, J. Dewhurst, C. Ambrosch-Draxl, S. Kurth, N. Helbig, S. Pittalis, S. Shallcross, L. Nordström, and E. Gross, “First-principles approach to noncollinear magnetism: Towards spin dynamics,” *Physical review letters*, vol. 98, no. 19, p. 196405, 2007.
- [329] G. Scalmani and M. J. Frisch, “A new approach to noncollinear spin density functional theory beyond the local density approximation,” *Journal of chemical theory and computation*, vol. 8, no. 7, pp. 2193–2196, 2012.
- [330] I. W. Bulik, G. Scalmani, M. J. Frisch, and G. E. Scuseria, “Noncollinear density functional theory having proper invariance and local torque properties,” *Physical Review B*, vol. 87, no. 3, p. 035117, 2013.
- [331] F. Eich and E. Gross, “Transverse spin-gradient functional for noncollinear spin-density-functional theory,” *Physical review letters*, vol. 111, no. 15, p. 156401, 2013.
- [332] F. Eich, S. Pittalis, and G. Vignale, “Transverse and longitudinal gradients of the spin magnetization in spin-density-functional theory,” *Physical Review B*, vol. 88, no. 24, p. 245102, 2013.
- [333] S. Pittalis, G. Vignale, and F. Eich, “ $U(1) \times su(2)$  gauge invariance made simple for density functional approximations,” *Physical Review B*, vol. 96, no. 3, p. 035141, 2017.
- [334] J. J. Goings, F. Egidi, and X. Li, “Current development of noncollinear electronic structure theory,” *International Journal of Quantum Chemistry*, vol. 118, no. 1, p. e25398, 2018.
- [335] C. A. Ullrich, “Density-functional theory for systems with noncollinear spin: Orbital-dependent exchange-correlation functionals and their application to the hubbard dimer,” *Physical Review B*, vol. 98, no. 3, p. 035140, 2018.
- [336] C. A. Ullrich, “(spin-) density-functional theory for open-shell systems: Exact magnetization density functional for the half-filled hubbard trimer,” *Physical Review A*, vol. 100, no. 1, p. 012516, 2019.
- [337] E. A. Pluhar III and C. A. Ullrich, “Exchange-correlation magnetic fields in spin-density-functional theory,” *Physical Review B*, vol. 100, no. 12, p. 125135, 2019.
- [338] G. Bergerhoff, R. Hundt, R. Sievers, and I. D. Brown, “The inorganic crystal structure data base,” *Journal of Chemical Information and Modeling*, vol. 23, pp. 66–69, may 1983.

- [339] P. Villars, N. Onodera, and S. Iwata, "The Linus Pauling file (LPF) and its application to materials design," *Journal of Alloys and Compounds*, vol. 279, pp. 1–7, sep 1998.
- [340] P. S. White, J. R. Rodgers, Y. Le Page, and IUCr, "CRYSTMET: a database of the structures and powder patterns of metals and intermetallics," *Acta Crystallographica Section B Structural Science*, vol. 58, pp. 343–348, jun 2002.
- [341] P. Villars and K. Cenzual, "Pearsons crystal data: Crystal structure database for inorganic compounds," *ASM International/Material Phases Data System, Vitznau, Switzerland*, 2010.
- [342] "SpringerMaterials: The Landolt-Börnstein database.," 2020.
- [343] C. Bale, E. Bélisle, P. Chartrand, S. Deckerov, G. Eriksson, K. Hack, I.-H. Jung, Y.-B. Kang, J. Melançon, A. Pelton, C. Robelin, and S. Petersen, "FactSage thermochemical software and databases — recent developments," *Calphad*, vol. 33, pp. 295–311, jun 2009.
- [344] P. Linstrom and W. Mallard, "NIST Chemistry WebBook, NIST Standard Reference Database Number 69," *National Institute of Standards and Technology, Gaithersburg MD 20899*, 2015.
- [345] "MatWeb: Material property data, Data base of materials data sheets," 2020.
- [346] "MatNavi: NIMS materials database.," 2014.
- [347] H. Okamoto, P. Villars, and A. Prince, *Handbook of ternary alloy phase diagrams*. ASM international Materials Park, OH, 1995.
- [348] G. Hautier, C. Fischer, V. Ehlacher, A. Jain, and G. Ceder, "Data Mined Ionic Substitutions for the Discovery of New Compounds," *Inorg. Chem*, vol. 50, pp. 656–663, 2011.
- [349] R. F. Berger and J. B. Neaton, "Computational design of low-band-gap double perovskites," *PHYSICAL REVIEW B*, vol. 86, p. 165211, 2012.
- [350] L. Cheng, R. S. Assary, X. Qu, A. Jain, S. P. Ong, N. N. Rajput, K. Persson, and L. A. Curtiss, "Accelerating Electrolyte Discovery for Energy Storage with High-Throughput Screening," *The Journal of Physical Chemistry Letters*, vol. 6, pp. 283–291, jan 2015.
- [351] J. Carrete, N. Mingo, S. Wang, and S. Curtarolo, "Nanograined Half-Heusler Semiconductors as Advanced Thermoelectrics: An Ab Initio High-Throughput Statistical Study," *Advanced Functional Materials*, vol. 24, pp. 7427–7432, dec 2014.
- [352] H. Zhu, G. Hautier, U. Aydemir, Z. M. Gibbs, G. Li, S. Bajaj, J.-H. Pöhls, D. Broberg, W. Chen, A. Jain, M. A. White, M. Asta, G. J. Snyder, K. Persson, and G. Ceder, "Computational and experimental investigation of  $\text{TmAgTe}_2$  and  $\text{XYZ}_2$  compounds, a new group of thermoelectric materials identified by first-principles high-throughput screening," *Journal of Materials Chemistry C*, vol. 3, no. 40, pp. 10554–10565, 2015.

- [353] M. T. Dunstan, A. Jain, W. Liu, S. P. Ong, T. Liu, J. Lee, K. A. Persson, S. A. Scott, J. S. Dennis, and C. P. Grey, “Large scale computational screening and experimental discovery of novel materials for high temperature CO<sub>2</sub> capture,” *Energy & Environmental Science*, vol. 9, no. 4, pp. 1346–1360, 2016.
- [354] W. Chen, J.-H. Pö, G. Hautier, D. Broberg, S. Bajaj, U. Aydemir, Z. M. Gibbs, H. Zhu, M. Asta, G. J. Snyder, B. Meredig, M. A. White, K. Persson, and A. Jain, “Understanding thermoelectric properties from high-throughput calculations: trends, insights, and comparisons with experiment,” *J. Mater. Chem. C*, vol. 4, p. 4414, 2016.
- [355] I. Petousis, D. Mrdjenovich, E. Ballouz, M. Liu, D. Winston, W. Chen, T. Graf, T. D. Schladt, K. A. Persson, and F. B. Prinz, “High-throughput screening of inorganic compounds for the discovery of novel dielectric and optical materials,” *Scientific Data*, vol. 4, p. 160134, dec 2017.
- [356] J. Dagdelen, J. Montoya, M. de Jong, and K. Persson, “Computational prediction of new auxetic materials,” *Nature Communications*, vol. 8, p. 323, dec 2017.
- [357] Y. Umeda, H. Hayashi, H. Moriwake, and I. Tanaka, “Materials informatics for dielectric materials,” *Japanese Journal of Applied Physics*, vol. 57, p. 11UB01, nov 2018.
- [358] A. Mansouri Tehrani, A. O. Oliynyk, M. Parry, Z. Rizvi, S. Couper, F. Lin, L. Miyagi, T. D. Sparks, and J. Brgoch, “Machine Learning Directed Search for Ultraincompressible, Superhard Materials,” *Journal of the American Chemical Society*, vol. 140, pp. 9844–9853, aug 2018.
- [359] R. Chen, H. C. Po, J. B. Neaton, and A. Vishwanath, “Topological materials discovery using electron filling constraints,” *Nature Physics*, vol. 14, pp. 55–61, jan 2018.
- [360] J. A. Flores-Livas, L. Boeri, A. Sanna, G. Profeta, R. Arita, and M. Eremets, “A perspective on conventional high-temperature superconductors at high pressure: Methods and materials,” *Physics Reports*, vol. 856, pp. 1–78, apr 2020.
- [361] A. I. Liechtenstein, M. Katsnelson, V. Antropov, and V. Gubanov, “Local spin density functional approach to the theory of exchange interactions in ferromagnetic metals and alloys,” *Journal of Magnetism and Magnetic Materials*, vol. 67, no. 1, pp. 65–74, 1987.
- [362] L. Udvardi, L. Szunyogh, K. Palotás, and P. Weinberger, “First-principles relativistic study of spin waves in thin magnetic films,” *Physical Review B*, vol. 68, no. 10, p. 104436, 2003.
- [363] I. Turek, J. Kudrnovský, V. Drchal, and P. Bruno, “Exchange interactions, spin waves, and transition temperatures in itinerant magnets,” *Philosophical Magazine*, vol. 86, no. 12, pp. 1713–1752, 2006.

- [364] M. Uhl, L. Sandratskii, and J. Kübler, “Electronic and magnetic states of  $\gamma$ -fe,” *Journal of magnetism and magnetic materials*, vol. 103, no. 3, pp. 314–324, 1992.
- [365] M. Körling and J. Ergon, “Gradient-corrected ab initio calculations of spin-spiral states in fcc-fe and the effects of the atomic-spheres approximation,” *Physical Review B*, vol. 54, no. 12, p. R8293, 1996.
- [366] D. Bylander and L. Kleinman, “Full potential ab initio calculations of spiral spin density waves in fcc fe,” *Physical Review B*, vol. 58, no. 14, p. 9207, 1998.
- [367] D. Bylander and L. Kleinman, “Full-potential generalized gradient approximation calculations of spiral spin-density waves in  $\gamma$ -fe,” *Physical Review B*, vol. 59, no. 9, p. 6278, 1999.
- [368] K. Capelle and L. Oliveira, “Density-functional theory for spin-density waves and antiferromagnetic systems,” *Physical Review B*, vol. 61, no. 22, p. 15228, 2000.
- [369] K. Capelle and E. Gross, “Spin-density functionals from current-density functional theory and vice versa: a road towards new approximations,” *Physical review letters*, vol. 78, no. 10, p. 1872, 1997.
- [370] E. Sjöstedt and L. Nordström, “Noncollinear full-potential studies of  $\gamma$ - fe,” *Physical Review B*, vol. 66, no. 1, p. 014447, 2002.
- [371] K. Capelle and B. L. Gyorffy, “Exploring dynamical magnetism with time-dependent density-functional theory: from spin fluctuations to gilbert damping,” *EPL (Europhysics Letters)*, vol. 61, no. 3, p. 354, 2003.
- [372] K. Bencheikh, “Spin-orbit coupling in the spin-current-density-functional theory,” *Journal of Physics A: Mathematical and General*, vol. 36, no. 48, p. 11929, 2003.
- [373] S. Rohra and A. Görling, “Exact-exchange spin-current density-functional theory,” *Physical review letters*, vol. 97, no. 1, p. 013005, 2006.
- [374] J. E. Peralta, G. E. Scuseria, and M. J. Frisch, “Noncollinear magnetism in density functional calculations,” *Physical Review B*, vol. 75, no. 12, p. 125119, 2007.
- [375] N. I. Gidopoulos, “Potential in spin-density-functional theory of noncollinear magnetism determined by the many-electron ground state,” *Physical Review B*, vol. 75, no. 13, p. 134408, 2007.
- [376] L. Ortenzi, I. Mazin, P. Blaha, and L. Boeri, “Accounting for spin fluctuations beyond local spin density approximation in the density functional theory,” *Physical Review B*, vol. 86, no. 6, p. 064437, 2012.



- [377] D. C. Ralph and M. D. Stiles, “Spin transfer torques,” *Journal of Magnetism and Magnetic Materials*, vol. 320, no. 7, pp. 1190–1216, 2008.
- [378] F. Tran, G. Baudesson, J. Carrete, G. K. Madsen, P. Blaha, K. Schwarz, and D. J. Singh, “Shortcomings of meta-gga functionals when describing magnetism,” *arXiv preprint arXiv:2004.04543*, 2020.
- [379] N. Singh, P. Elliott, T. Nautiyal, J. Dewhurst, and S. Sharma, “Adiabatic generalized gradient approximation kernel in time-dependent density functional theory,” *Physical Review B*, vol. 99, no. 3, p. 035151, 2019.
- [380] C. Pellegrini, T. Müller, J. K. Dewhurst, S. Sharma, A. Sanna, and E. K. Gross, “Density functional theory of magnetic dipolar interactions,” *Physical Review B*, vol. 101, no. 14, p. 144401, 2020.
- [381] M. Yatsushiro and S. Hayami, “Nqr and nmr spectra in the odd-parity multipole material cecosi,” *Physical Review B*, vol. 102, no. 19, p. 195147, 2020.
- [382] S. Hayami, Y. Yanagi, and H. Kusunose, “Spontaneous antisymmetric spin splitting in non-collinear antiferromagnets without spin-orbit coupling,” *Physical Review B*, vol. 101, no. 22, p. 220403, 2020.
- [383] R. Sakuma, “Symmetry-adapted wannier functions in the maximal localization procedure,” *Physical Review B*, vol. 87, no. 23, p. 235109, 2013.
- [384] G. Pizzi, V. Vitale, R. Arita, S. Blügel, F. Freimuth, G. Géranton, M. Gibertini, D. Gresch, C. Johnson, T. Koretsune, *et al.*, “Wannier90 as a community code: new features and applications,” *Journal of Physics: Condensed Matter*, vol. 32, no. 16, p. 165902, 2020.
- [385] T. Yu, M. Hirayama, J. A. Flores-Livas, T. Nomoto, and R. Arita, “First-principles design of halide-reduced electriles: Magnetism and topological phases,” 2020.
- [386] S. Goedecker, “Minima hopping: An efficient search method for the global minimum of the potential energy surface of complex molecular systems,” *The Journal of chemical physics*, vol. 120, no. 21, pp. 9911–9917, 2004.
- [387] “MAGNDATA,” 2020.

# Curriculum Vitae

<b>Name</b>	Marie-Therese Huebsch (born: Philipp)
<b>Nationality</b>	German
<b>Born</b>	June 3, 1992 in Hamburg, Germany
<b>Marital status</b>	married
<b>Email</b>	mt.huebsch@pm.me
<b>Languages</b>	German (native), English (proficient), Japanese (intermediate)

## Academic degrees

Mar 19, 2021 (expected)	Doctor of Philosophy	University of Tokyo, Japan
Jan 11, 2018	Master of Science	TU Wien, Austria
Feb 24, 2016	Bachelor of Science	TU Wien, Austria

## List of publications

- [1] T. Yu, M. Hirayama, J. A. Flores-Livas, M.-T. Huebsch, T. Nomoto, M.-T. Suzuki, and R. Arita, *First-principles design of Halide-reduced electrides: magnetism and topological phases* (2020), arXiv:2011.01595 [cond-mat.mtrl-sci].
- [2] M.-T. Huebsch, T. Nomoto, M.-T. Suzuki, and R. Arita, *Benchmark for Ab Initio Prediction of Magnetic Structures Based on Cluster-Multipole Theory*, Phys. Rev. X **11**, 011031, (2021).
- [3] R. Kaneko, M.-T. Huebsch<sup>1</sup>, S. Sakai, R. Arita, H. Shinaoka, K. Ueda, Y. Tokura, and J. Fujioka, *Enhanced thermopower in the correlated semimetallic phase of hole-doped pyrochlore iridates*, Phys. Rev. B **99**, 161104(R) (2019).
- [4] M.-T. D. Philipp, *The temperature dependence of the scattering rate in cuprates: insights from strong-coupling diagrammatic methods*, TU Wien, thesis, (2017).
- [5] M.-T. Philipp, M. Wallerberger, P. Gunacker, and K. Held, *Mott-Hubbard transition in the mass-imbalance Hubbard model*, Eur. Phys. J. B **90**, 114 (2017).

---

<sup>1</sup>Two first authors.

## Research experience

current	<b>project</b>	<i>Magnetic structure prediction on <math>Ca_2Ru_2O_7</math></i>
	Supervisor	Ryotaro Arita
	Collaborators	Y. Tokura, K. Ueda and R. Kaneko
	Institute	Center for Emergent Matter Science, RIKEN, Wako, Saitama 351-0198, Japan
Aug 2020	<b>project</b>	<i>Benchmark for ab initio prediction of magnetic structures based on cluster multipole theory</i>
	Supervisor	Ryotaro Arita
	Collaborators	Takuya Nomoto and Michi-To Suzuki
	Institute	Center for Emergent Matter Science, RIKEN, Wako, Saitama 351-0198, Japan
Mar 2019	<b>project</b>	<i>DFT+DMFT calculations on doped <math>Eu_2Ir_2O_7</math></i>
	Supervisor	Shiro Sakai and Ryotaro Arita
	Institute	Center for Emergent Matter Science, RIKEN, Wako, Saitama 351-0198, Japan
Dec 2017	<b>Master thesis</b>	<i>The temperature dependence of the scattering rate in cuprates</i>
	Supervisor	Thomas Schäfer and Alessandro Toschi
	Institute	Institute of Solid State Physics, TU Wien, 1040, Vienna, Austria
Dec 2016	<b>research intern</b>	<i>Padé approximation on DGA self-energies</i>
	Supervisor	Georg Rohringer and Alexey Rubtsov
	Institute	Russian Quantum Center, Skolkovo 143025, Russia
Dec 2015	<b>Bachelor thesis</b>	<i>Mott-Hubbard Transition in the Mass-Imbalanced Hubbard Model</i>
	Supervisor	Markus Wallerberger and Karsten Held
	Institute	Institute of Solid State Physics, TU Wien, 1040, Vienna, Austria
Aug 2015	<b>research intern</b>	<i>Labwork: Interfacing Rydberg Atoms with Superconducting Circuits</i>
	Supervisor	Tobias Thiele and Andreas Wallraff
	Institute	Department of Physics, ETH Zürich, CH-8093 Zürich, Switzerland
Jan 2015	<b>project work</b>	<i>Initiation of the Fabrication of Superconducting Quantum bits at the Atomic Institute of Vienna</i>
	Supervisor	Johannes Majer and Jörg Schmiedmayer
	Institute	Vienna Center for Quantum Science and Technology, Atominstitut, TU Wien, 1020 Vienna, Austria
Sep 2014	<b>project work</b>	<i>Ultra-short Laser Pulses: Methods for Characterizing the Duration and Carrier-Envelope Phase</i>
	Supervisor	Markus Kitzler-Zeiler
	Institute	Photonics Institute, TU Wien, 1040 Vienna, Austria

## Conferences and proceedings

Dec, 2020	<i>participant</i>	CEMS Topical Meeting: “Complex Magnetism meets Topology: New Coupling Mechanisms and Responses” RIKEN, online
Sep, 2020	<i>talk</i>	Autumn meeting Physical Society of Japan (JPS), online
Sep, 2020	<i>participant</i>	Autumn School on Correlated Electrons: Topology, Entanglement, and Strong Correlations Forschungszentrum Jülich, online
Aug, 2020	<i>participant</i>	CEMS Topical Meeting: “Magnon-Phonon Coupling” RIKEN, online
Jun, 2020	<i>talk</i>	Condensed Matter Physics in All the Cities University of Kent, online
Oct, 2019	<i>poster</i>	Deep Learning and Physics Yukawa Institute for Theoretical Physics, Kyoto, Japan
Sep, 2018	<i>poster</i>	Novel Quantum States in Condensed Matter Yukawa Institute for Theoretical Physics, Kyoto, Japan
Sep, 2018	<i>poster</i>	CEMS Symposium on Trends in Condensed Matter Physics RIKEN, Wako, Japan
Jul, 2018	<i>participant</i>	Bandstructure meets quantum field theory Institute for Solid State Physics, TU Wien, Austria
Nov, 2017	<i>poster</i>	RIKEN summer school Tsukuba International Congress Center, Tsukuba, Japan
Mar, 2017	<i>talk, poster</i>	DPG March Meeting Deutsche Physikalische Gesellschaft, Dresden, Germany
Mar, 2015	<i>participant</i>	DPG March Meeting Deutsche Physikalische Gesellschaft, Berlin, Germany

## Fellowships and awards

Apr 1, 2018 – Mar 19, 2021	International Program Associate fellowship awarded by RIKEN, Japan
Jun, 2011	Dr. Hans Riegel-Fachpreis awarded by the University of Graz, Austria

## Extracurricular

since 2017    Pretty Much Physics    Graduate-level educational YouTube channel